Spatiotemporal dynamics of the DNA double strand break marker 53BP1 after exposure to ionising radiation.

A thesis submitted for the degree of

Doctor of Philosophy

by

Andrew Duncan McVean

School of Health Sciences and Social Care

Brunel University

2011

Abstract

53BP1 is known to be involved in the DNA damage response and has been shown to localise into discrete foci at the site of DNA double strand breaks (DSBs) after exposure to ionising radiation (IR). Quantification of radiation induced foci (RIF) at varying times after exposure has been used to assess the induction of DSB and kinetics of their decline, suggestive of repair. In addition, the size and relative nuclear distribution of foci, observed at different times after IR, could provide insights into the dynamics of these foci that may be relevant for understanding mechanisms of chromosome exchange.

To assess this human bronchial epithelial (HBEp) cells, which are the primary target for 50% of our average annual radiation exposure, have been irradiated with low linear energy transfer (LET) ^{60}Co γ-rays (0- 2.0 Gy) or ^{238}Pu high LET α-particles (~1α-particle/nucleus LET 121-235 keV/µm). DSB were quantified at various time points (0-24hrs) after IR, stained for 53BP1 and categorised into three sizes (<0.5µm, 0.5 µm-1.0 µm and >1.0µm in diameter).The data generated was used to ask questions on the radiobiological DSB response of HBEp cells (chapter 4), the recruitment of 53BP1 to DSB and the possible dynamics of DSB for repair. In addition, immortalised HBEp cells transfected with 53BP1-GFP fusion protein were irradiated with ^{60}Co γ-rays and analysed to further assess the spatio-temporal aspects of DSB in live cells. After exposure to 2Gy γ-rays peak induction of 53BP1 was observed within 30 min (22foci) with a subsequent decline to sham levels (2 foci) after 24hrs.

For the quantification of spatiotemporal dynamics (chapter 5), a bespoke foci analysis tool was developed (chapter 3) to provide detailed measurements of RIF number, size and relative location with greater speed and reliability than manual counting and categorising method. This novel approach to foci analysis provides evidence for limited (<1µm) movement of foci is presented that may support the ICN model for chromosomal exchange aberrations.

Forward / Acknowledgments

I would like to thank Dr Rhona Anderson, my PhD supervisor for the dedication and enthusiasm she has shown throughout my PhD and for affording me the opportunity to perform this research. I would also like to thank Dr Mike Themis for his support as my second supervisor.

I would especially like to acknowledge the contributions of several collaborative parties: Dr Simon Kent and Mr Alexei Bakanov from Department of Information Systems and Computing, at Brunel University for their assistance in the development of our software.
Dr Mark Hill and David Stevens, Professor Boris Vojnovic and Dr Paul Barber of the Gray Cancer Institute (Oxford), for all aspects relating to the irradiation of HBEp cells on Mylar dishes and for the use of a customised automated microscope. Dr Sylvain Costes and Dr Charlie Chen of the Life Sciences Division at the Lawrence Berkeley National Laboratory, (USA) for the use of their automated analysis system. Professor Kevin Prise, Dr Giuseppe Schettino and Dr Luca Severino of the Centre for Cancer Research and Cell Biology (Belfast) for the optimiations for the irradiation of HBEp cells on glass with α-particles.

During my time at Brunel University I have had the privilege to work with some outstanding scientists and above all good friends. In particular I would like to thank Dr Matthew Themis for his advice, moral support and encouragement, I would also like to thank Dr Lauren Godwin and Elisa Garimberti for their advice, support and good humour which have been invaluable.

As a final note, I must express deep gratitude to my wife and family for understanding my commitments. The fact that they feel so proud of what I have achieved and what I intend to achieve, has driven me to succeed.

Declaration

I declare that all the work presented in this thesis is my own. Development of the methodology of automated analysis software was performed in collaboration with Dr Simon Kent and Mr Alexi Bakanov and can be found in the appendix.

Andrew Duncan McVean
BSc.

Abbreviations

~	Approximately
^{223}Rn	Radon isotope
^{226}Ra	Radium isotope
^{238}U	Uranium isotope
2D	Two-dimensional (X & Y axis)
3D	Three-dimensional (X,Y & Z axis)
4D	Four-dimensional (X, Y, Z and time)
53BP1	p53 binding protein 1
AF555	Alexa Fluor 555
AG01522	Human dermal fibroblast cells
BRCT	Breast cancer 1 (BRCA1) C-terminal domain
BSA	Bovine serum albumin
BSS	Buffered saline solution
CLSM	Confocal Laser Scanning Microscopy
CO_2	Carbon dioxide
CT	Chromosome territory
DAPI	4'-6-diamidino-2-phenyl-lindole
DiOC-$_6$	3,3'-dihexyloxacarbocyanine iodide dye
DMSO	Dimethyl sulfoxide
DNA	Deoxyribonucleic acid
DNA-PK	DNA-dependent protein kinase
DOP	Degenerate oligonucleotide polymerase chain reaction
DSB	Double strand break
EDTA	Ethylenediaminetetraacetic acid
FDA	US Food and Drug Administration
FISH	Fluorescence in-situ hybridisation
FITC	Fluorescein isothiocyanate
GFP	Green fluorescent protein
Gy	Gray
HBEp	Human bronchial epithelial cells
He^{2+}	α-particle
HeLa	Henrietta Lacks (cervical cancer cell line)

HEPES	4-(2-hydroxyethyl)-1-piperazineethanesulfonic acid
HR	Homologous recombination
hr(s)	Hour(s)
ICD	Inter-chromatin domain
IF	Immunofluorescence
IMS	Industrial Methylated Spirit
IOD	Integrated optical density
IR	Ionising radiation
Kb	Kilobase
KCi	Kilocurie
KeV	Kiloelectron volts
kg	kilogram
LET	Linear energy transfer
MAR	Matrix attachment region
MCF-7	Breast cancer cell line
MIP	Maximum intensity projection
NaOH	Sodium hydroxide solution
NHEJ	Non-homologous end-joining
NLS	Nuclear localisation sequence
nm	nanometre
NOR	Nucleolar organizing region
NSCLC	Non-small cell lung cancer
PBS	Phosphate-buffered saline
PCR	Polymerase chain reaction
PET	Polyethylene terephthalate (Mylar)
PNK	Polynucleotide kinase
RBE	Relative biological effectiveness
RGB	Red green blue
RIF	Radiation-induced foci
RNA	Ribonucleic acid
RT	Room temperature
SCLC	Small cell lung cancer
SI	International System of Units

SSC	Saline sodium citrate buffer
Sv	Sievert
TIFF	Tagged image file format
TNS	Trypsin neutralization solution
U2OS	Human osteosarcoma cell line
μm	micrometre

Table of contents

Table of figures

1 Introduction

In 1895 Wilhelm Röntgen discovered X-rays by experimentation with electrical apparatus, since then mankind has been working with radiation to understand its physical attributes and its biological effects. Units of radiation echo the names of eminent physicists and biologists; Roentgen, Becquerel and possibly most famous of all, Curie who is credited with the term radioactivity. It did not take long for scientists to realize the possible diagnostic uses for both man-made and radioactive elements in conjunction with photographic film, as exposure enabled mass (e.g. bones) to be observed through soft tissue. We now understand that radiation acts as a double edged sword, whereby the properties that make radiation a vital asset in modern-day diagnostics may also cause disease through damage to the genome. The irony of this is that we use radiation to treat the very same diseases that can result from radiation exposure.

The clinical effects of radiation have been correlated from a range of theoretical, experimental and epidemiological data. For example, our understanding of the physics of radiation informs us of the interactions of radiation with biological matter, while biological advances (e.g. molecular pathways of the damage response) are shedding light on the biological consequences at the cellular, tissue and organism level and, estimations of human cancer risk have been determined from A-bomb survival data. We are all constantly exposed to radiation as a consequence of environmental and occupational exposures and, increasingly through medical diagnostic and therapeutic procedures. Therefore, the impact of all of this research has been and will continue to improve understanding of human health risks to inform both radiation protection policies and novel radiotherapeutic regimes.

1.1 What is Radiation

The electromagnetic spectrum encompasses wave forms of energy with varying frequencies (Figure 1-1).
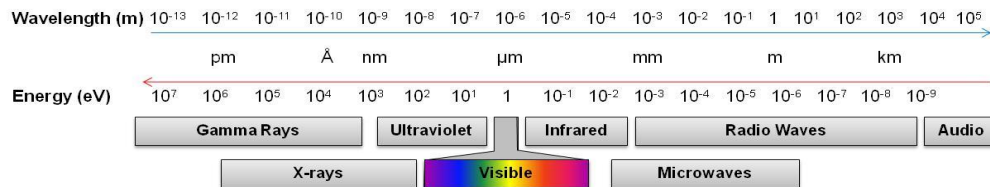
Figure 1-1 Electromagnetic spectrum of radiation.
(McVean 2011)

Energy and frequency are linked, with higher frequency radiation containing more energy per unit. For example hard γ-rays have approximately ten times more energy than x-rays and ten-thousand times more energy than visible light (Figure 1-1). Radiation can be broadly categorized into two sub-types, ionising and non-ionising. Ionising radiation is defined as any form of radiation capable of removing electrons from atoms to leave ions. In addition to electromagnetic ionising radiation (gamma rays and X-rays) particle radiation is also capable of ionising atoms. Particulate radiation is emitted during radioactive decay and can consist of fast ions, protons or neutrons, see Figure 1-2.
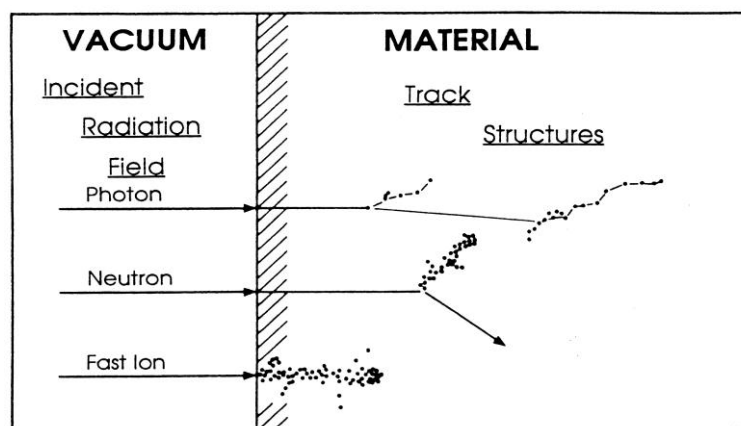
Figure 1-2 Track structures for high and low LET radiations.
(Image courtesy of Dr Mark Hill 2010)

To quantify the energy deposition from different track structures the energy per unit mass (Joules/kg) is used, known as the absorbed dose; the SI unit for absorbed dose is the Gray (Gy). The amount of energy that radiation deposits per unit length is measured as Linear Energy transfer (LET), which is expressed in terms of kiloelectron Volts/µm. Gamma rays (γ) and x-rays typically have low LETs in the region of 0.2 to 2 keV/µm compared to α-particles which have up to 166 keV/µm whilst fast Fe ions can have LETs up to 1000 keV/µm. These LET differences are determined by the structure of the radiation tracks and therefore the spatial deposition of energy; for γ-rays, electron ionisations are sparse and essentially isolated whilst for α-particles and fast ions, ionisations are localised and very densely packed along a linear axis. Importantly, different radiation qualities with differing track structures and LETs result in differing biological effects. For example, the energy deposition of γ-rays is homogenous through the irradiated volume producing a reduced spectrum of damage when compared to the densely ionising tracks of α-particles, of the same absorbed dose (Figure 1-3).
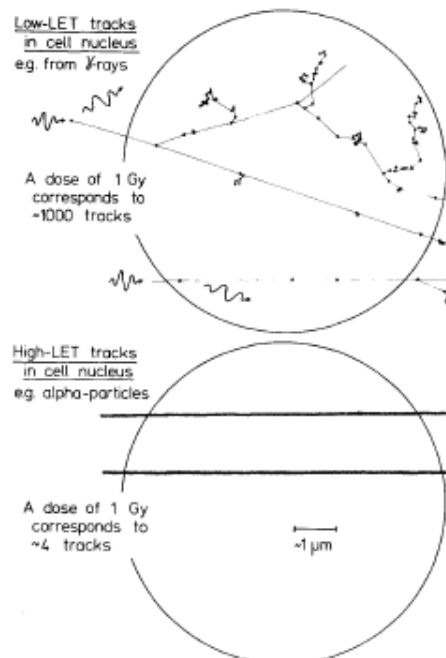
Figure 1-3 Scale illustration of ionisation events through the cell nucleus
(Goodhead, 1989)

To measure the effects of radiation on whole organisms or tissues it is necessary to normalise the differences in radiation qualities. X-rays are used as a benchmark and are defined as having a relative biological effectiveness (RBE) of 1, to which other qualities of radiation are then compared to this. For example, if 1Gy of α-particles has ~20x greater effect in the formation of damage than 1Gy γ-rays from a ^{60}Cobalt γ-source, then α-particles will have an RBE of 20 for that particular damage measure. The RBE can then be used in conjunction with the dose to calculate the equivalent dose for entire organisms or with weighting factors for different tissues within organisms.

1.2 Radiation exposure and human health

The majority of our understanding of exposure to radiation and human health effects, including cancer risk, originates from the survivors of the atom bomb (A-Bomb) strikes of the Second World War at Hiroshima and Nagasaki. More recently data has been obtained from individuals present at the Chernobyl radiation accident in Russia (Saenko et al., 2011). Information is also being generated on risks after radiotherapy (Sachs et al., 2007), for example, the upper torso is often exposed to radiation for diagnostic and therapeutic purposes, whereby large volumes of normal tissue receive varying amounts of dose. The secondary consequences of such exposure remain unclear but there is evidence of an elevated risk of lung cancer in breast cancer survivors after receiving radiotherapy (Neugut et al., 1994).

For the average individual, radiation exposure is largely dependent on geographic location and occupation. For instance, the average individual in the UK would expect to be exposed to 2.7 mSV/year, of this 2.2 mSv is from natural sources (Fig 1-4).
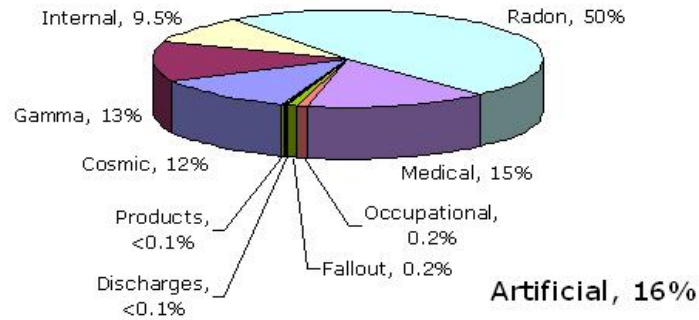
Figure 1-4 Breakdown of average radiation exposure within the
(NRPB, UK)

Of the natural background radiation types, Radon gas contributes approximately 1.3mSV/year (Watson et al., 2005). Radon gas (^{222}Rn) is one product of the decay chain of Uranium (^{238}U) that is present naturally in the ground and which decays through the emission of an α-particle (He^{2+}). Radon gas can also be produced from the decay chain for Thorium but is less stable and has a shorter half life overall. Radon gas measurements show that certain regions within the UK are more likely to have elevated exposures to Radon gas compared to others e.g. Cornwall verses Norfolk (Fig 1-5).
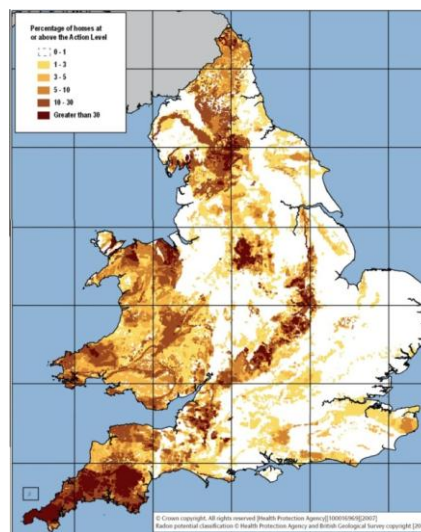
Figure 1-5 Indicative map of Radon in England and Wales
(Miles et al., 2007)

5
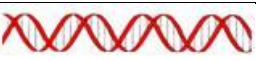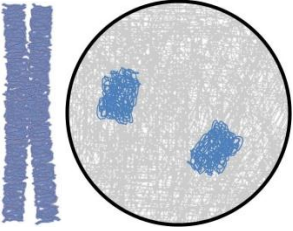
The gaseous nature of Radon means that it can concentrate within well-insulated buildings, thereby providing a mechanism for inhalation and subsequent exposure of internal tissues. For instance, the epithelial cells of the bronchioles are primary targets for inhaled gases, and recent epidemiological evidence shows a causal association between domestic exposure to Radon gas and lung cancer (Darby et al., 2005).

Occupations where the risk of exposure is increased above background levels are those which involve mineral extraction or processing (e.g Uranium miners exposed to high levels of Radon gas), airline personnel (e.g. cosmic rays) and healthcare professionals (e.g. x-rays). There are reports showing detrimental health effects due to working environments but modern monitoring and control measures are in-place to reduce such risks. One area that spans both occupational and domestic exposure is our exposure to cosmic radiation, primarily from high energy charged particles from the solar system. At ground level the atmosphere and shielding effects of buildings reduce the average environmental dose from cosmic radiation but for air crew, especially those who fly at high altitudes and for regular fliers, there is reduced protection. For example, a 15hr flight to New York has been estimated to have an additional dose of 0.1mSv (Watson et al., 2005).

1.3 Structure of chromatin

In 1868 Freidrich Miescher found two chemically distinct components within the nuclei of cells; a phosphorus-containing substance with an acidic portion and several proteins, but it was not until 1944 that nucleic acid was proven to be the vehicle of genetic information (Avery et al., 1944). Thanks to the work of Watson, Crick and Franklin the structure of deoxyribonucleic acid (DNA) is known to be a double stranded helix with strands organized in opposing directions (Fig 1-6a). DNA does not exist in isolation as naked DNA but is associated with proteins, termed as histones. It was Albrecht Kossel in 1884 who first purified and named histones after the German for 'unknown origin', and who subsequently fractionated individual subunits identified as H1, H2A, H2B, H3 and H4.

These proteins have since been shown to form an octamer (H2A, H2B, H3 and H4) core (Kornberg, 1974, Johnson et al., 1995) and comprise a high proportion of positively charged lysine and arginine amino acid residues, known as tails, that facilitate binding to the negatively charged phosphate backbone of DNA, with Histone H1 acting as a linker outside the core octamer. This model of chromatin loosely representing beads (histones) on a string (DNA), termed nucleosomes (Arents et al., 1991) (Figure 1-6b), is further condensed into the theoretical 30nm fibre (Figure 1-6c) (Finch and Klug, 1976, Woodcock et al., 1993).

(a)	DNA double helix of diameter ~2nm
(b)	Nucleosomes form beads on a string which are compacted into the 30nm chromatin fibre.
(c)	Compacted chromatin fibres are suggested to be organized into looped domains.
(d)	In interphase, chromosomes exist as distinct territories of chromatin fibres. During mitosis chromatin condenses into metaphase chromosomes.

Figure 1-6 Hierarchical organisation of chromatin.
(McVean 2011)

Histone tails are important for the physical organisation of chromatin. In addition to facilitating DNA binding, acetylation or methylation of residues is known to alter the conformation of the nucleosome (Olins and Olins, 1974, Oudet et al., 1975, Strahl and Allis, 2000, Zhang and Reinberg, 2001), for example, methylation is associated with gene silencing and condensation of chromatin (heterochromatin). The organisation of chromatin above this 30nm fibre scale is yet to be determined but possibly comprises looped domains of chromatin and have been suggested to be linked to a scaffold or matrix by regions within the genome termed as

matrix attachment regions (MARs) (Rollini et al., 1999). (Figure 1-6c). What is known is that individual molecules of chromatin exist as discrete chromosome territories within the nuclear space throughout the whole of interphase before subsequently undergoing further compaction to form metaphase chromosomes that are ultimately visible by light microscopy during mitosis (Figure 1-6d). Interestingly, cytogenetic stains such as G-banding have contributed to our understanding of how chromatin is organised revealing relationships between highly condensed (heterochromatin) and more open (euchromatin) with particular physical attributes, such as sensitivity to enzymes, see Table 1-1.

Table 1-1 Comparison of Giemsa light and dark bands of chromosomes

Giemsa-light (R-bands)	Giemsa-dark bands
Guanine – Cytosine rich	Adenosine – Thymine rich
Early replicating	Late replicating
Gene rich	Gene poor
Housekeeping genes	Tissue specific genes
High proportion of CpG islands	Low ratio of CpG islands
Nuclear interior associated	Nuclear periphery associated
Open chromatin (DNase sensitive)	Condensed chromatin (DNase insensitive)
GC-rich & poor isochores	GC-poor isochores only

A relative comparison of the attributes of Giemsa light and dark staining regions of chromosomes. This table has been extrapolated from (Gardiner, 1995, Niimura and Gojobori, 2002)

The territorial organisation of chromosomes and sub-chromosomal domains is not believed to be random, instead chromosomes have been shown to occupy preferential positions within the nucleus (van Dekken et al., 1989, Zirbel et al., 1993), and that the relative location of these territories is influenced by gene density (Boyle et al., 2001, Mahy et al., 2002a, Mahy et al., 2002b, Boei et al., 2006), chromosomes size (Sun et al., 2000, Bolzer et al., 2005), chromatin density (Radulescu et al., 2004, Costes et al., 2007), gene expression (Croft et al., 1999, Kozubek et al., 2002, Parada et al., 2004), cellular proliferative state (Parada et al., 2004,

Mehta et al., 2008), or a combination of the above. Thus, to date there remains a great deal of controversy in the field as to what determines territorial organisation, although the relationship between organisation and function is emerging as being important (Elcock and Bridger, 2010).
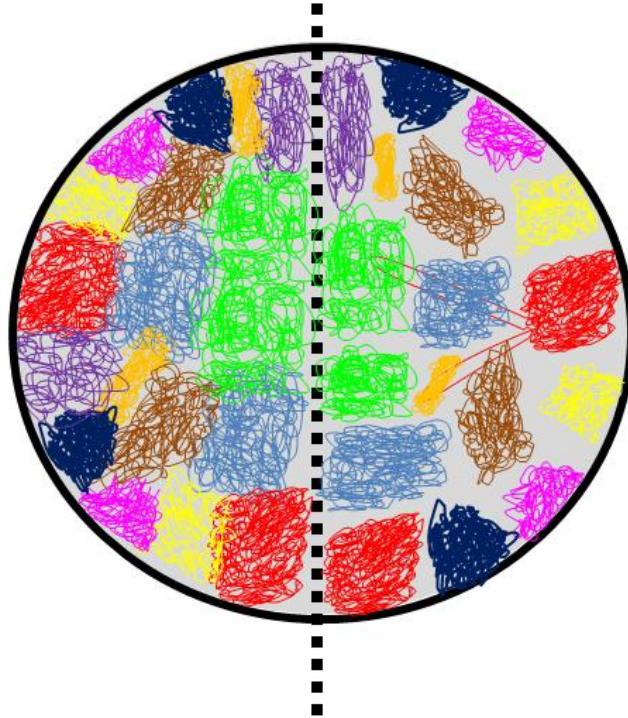
Figure 1-7 Proposed models for organisation of chromosome territories
Chromosomes territories (shown in different colours) occupy discrete, preferential positions within the nucleus that vary depending on cell type, stage of differentiation and disease status. Models have been proposed whereby neighbouring territories exist in very close proximity or intermingle (ICN) (Branco and Pombo) (left side of nucleus in cartoon) or whether a distinct channel (ICD) separates them (right side of nucleus in cartoon). A chromosome with looped domains has also been included (right, red chromosome).

Another aspect of nuclear organisation that remains controversial is how close neighbouring chromosome territories are from each other (Figure 1-7). Two principle models have been proposed; the inter-chromatin domain model (ICD) which proposes channels exist between territories that have functional roles in nuclear function e.g. transcription factories, PML bodies etc (Cremer et al., 1993, Zirbel et al., 1993, Kurz et al., 1996, Bridger et al., 1998, Costes et al., 2007) (Figure 1-7 right) and the inter-chromosomal network (ICN) (Branco and Pombo, 2006) (Figure 1-7 left) which suggests that neighbouring chromosome territories intermingle, invoking chromosome contact at territory interfaces. In addition to this, evidence exists for gene loci to loop out of territories and extend over large nuclear

distances for interaction with gene promoters or co-expressed genes (Volpi et al., 2000, Mahy et al., 2002a, Mahy et al., 2002b), see Figure 1-7 (red chromosome). Limited resolution and technology mean that to date neither model can be fully validated however there is an emerging acceptance that the ICN more closely reflects nuclear organisation. The relevance of such arguments as to the proximity of neighbouring chromosomes will be explored later.

1.4 Ionising radiation induced damage

DNA double strand breaks and their illegitimate repair are the link between ionising radiation and cancer (Lobrich and Jeggo, 2007). Hütterman *et al* (1978) described the chain of events following exposure to ionising radiation: 1) Energy is deposited and dissipated, the distribution and density of the energy deposition are dependant on radiation quality and dose. 2) The primary products undergo secondary reactions, for example, photons from X-rays strip electrons from atoms which then go onto deposit their energy. 3) Chemical imbalances arise, the ionisation of water results in the generation of free radicals, H^+ and OH^+, with a range of ~4nm (deLara et al., 1995). 4) Biological effects occur, which can result in cancer through ineffective repair of the lesions.

The direct effects from step 2, where electrons directly interact with the atoms of DNA, are capable of inducing breaks in the sugar phosphate backbone. The frequency of these events and their proximity is defined largely by the track structure of the radiation. The indirect effects (step 3) primarily originate from the hydrolysis of water and have a limited range for the induction of damage (<10nm) (Roots and Okada, 1975). The combination of direct and indirect effects can lead to genomic lesions including; base damage, single strand breaks and double strand breaks (DSBs) (Weterings et al., 2003, Boei et al., 2006), see Figure 1-8.

A small 'clustered damage' (simple dsb)
resulting from a local cluster of
ionizations within a single track:

electron

Direct Break

'Indirect' Break

Radical diffusion distances in cells
are very small (< 4 nanometres).
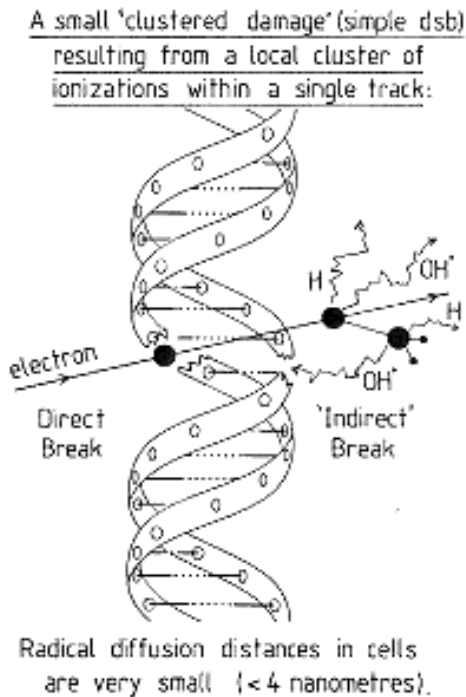
Figure 1-8 Direct and indirect effects of ionising radiation on DNA
DNA double strand beak occurring from primary products (left) and from secondary
reaction of free radicals (right) (Goodhead, 1989)

The track structure will directly influence the type, frequency, distribution and complexity of damage. For high LET radiation 70% of the damage induced is via direct effects, whilst for low LET radiation this only constitutes 30% of the damage. With High LET radiation the higher density of ionisation events leads to a non-random distribution of damage in relation to the genome (Heussen et al., 1987, Oleinick et al., 1994, Holley and Chatterjee, 1996, Rydberg et al., 1998, Sak et al., 2000, Rydberg et al., 2002). Chromatin structure is also likely to influence the complexity of damage and its relative distribution. In fact, the distribution of damage caused by higher energy α-particles has been used to hypothesise the structure of the theoretical 30nm chromatin fibre (Lobrich et al., 1996, Rydberg et al., 1998). The solenoid model for compacted chromatin shows how the distribution of ionisation events for low and high LET radiations (top and bottom respectively) can have different biological consequences, see Figure 1-9.
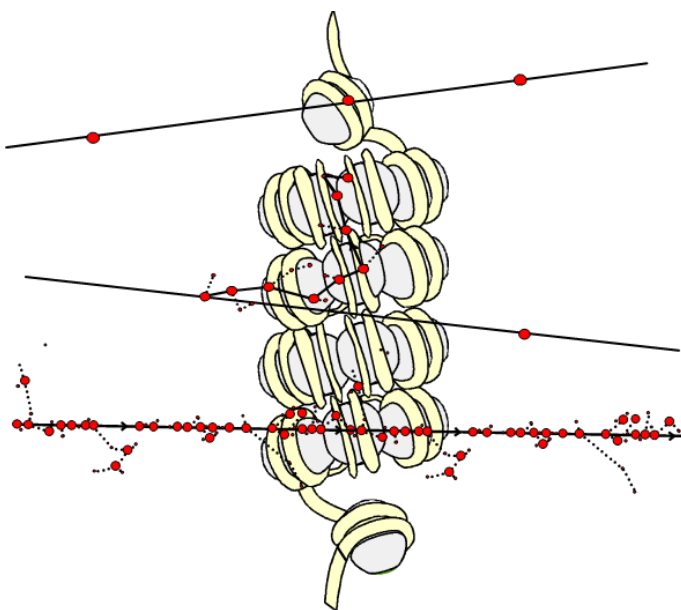
Figure 1-9 Interactions of radiation tracks with solenoid chromatin model
(Image courtesy of Dr Mark Hill)

Numerous authors have asked if certain regions of the genome are more or less likely to be damaged by ionising radiation. The density of chromatin has been implicated as an important factor in defining susceptibility of DNA to DSBs, where dense regions are hypothesised to correspond to gene poor heterochromatin (Radulescu et al., 2004, Costes et al., 2007) and have been hypothesised to have different susceptibilities to euchromatin. This led to the conclusion that chromatin and its relative conformation is responsible for the non-random distribution of breaks and that nucleic proteins offer protection against DSBs. Arguments that support this suggest that condensed chromatin is less accessible to H_2O and therefore free radicals and that histones or bound proteins may sequester radicals (Falk et al., 2008). Alternatively, the increased sensitivity of compacted metaphase chromosomes to radiation has been suggested to be the result of a lack of access for repair enzymes (Heussen et al., 1987). Therefore it can be assumed that there may be an optimal level of compaction that affords a level of protection from varying levels of radiation exposure, for various cell types (Nakano and Shinohara, 1994). Indeed conformation changes that occur after damage induction may contribute to the efficiency of repair (Huyen et al., 2004, Sy et al., 2010).

The measurement of DSB induction and subsequent decline has classically been measured using pulse field gel-electrophoresis but this method is not capable of resolving smaller numbers of breaks and therefore requires a large dose (1-5Gy) to induce a visible response (Nevaldine et al., 1994, Schultz et al., 2000). This method is also not cell specific and will only show the induction of DSBs in a population of cells. An improvement of this is the Comet assay, in which the volume of DSBs can be detected in single cells. However, as with electrophoresis, resolution is limited and spatiotemporal dynamics within the nucleus cannot be detected (Calini et al., 2002).

1.5 Cellular response to DNA DSBs

A normal competent cell can respond to the DNA lesions through cell cycle arrest, repair or programmed cell death (apoptosis) (Figure 1-10). After induction of damage, signalling occurs and transduction of the signal is used to promote repair and prevent cell division.
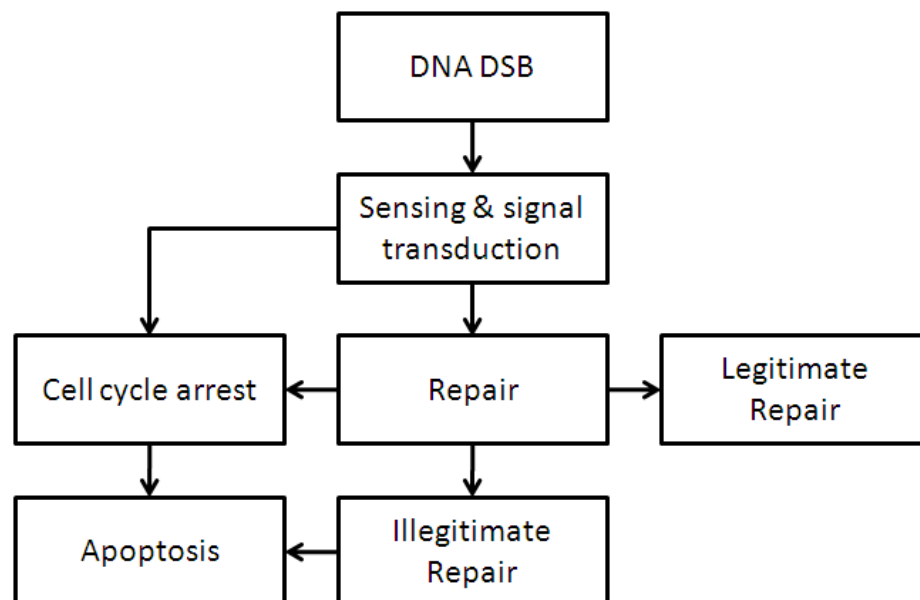
Figure 1-10 Flow diagram for cellular responses to DSBs

The pathway for cell cycle arrest involves sensors and effectors cascading signals at checkpoints in the cell cycle (G_1, G_2 and metaphase). Cells that are held at checkpoints or disposed of through apoptosis will not result in pathology and so will not be discussed in any more detail. The process of repair however, can and does result in the illegitimate rejoining of DSBs, which can result in pathogenesis. Therefore, it is important to understand the upstream events that sense and signal the presence of a DSB.

The key signalling proteins associated with DSBs and possible models for their recruitment have been proposed but no definitive model has yet been established (Bekker-Jensen et al., 2005, Wilson and Stern, 2008, Eliezer et al., 2009, Goodarzi and Jeggo, 2009, Nakamura et al., 2010, Goodarzi and Jeggo, 2011). The key proteins known to be associated with the chromatin at a DSB are the MRN complex, MDC1, and 53BP1. Chromatin modifications to H2AX, H3 and H4 are also associated with the sites of DSBs. A model for the recruitment of proteins and chromatin medications is shown in Figure 1-11.
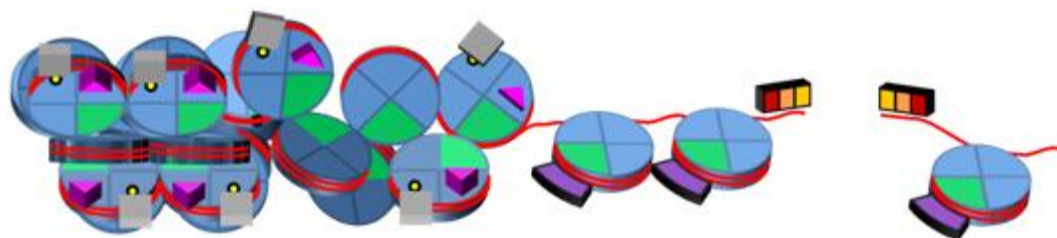
Figure 1-11 Protein interactions with chromatin at the site of a DSB
MRN complex (▯) senses DSB and activates ATM which phosphorylates serine 139 of H2AX (⊙) to generate γ-H2AX. MDC1 (NFBD1) binds to γ-H2AX (◖) and γ-H2AX is then ubiquniated (◄) by RNF8, RNF168 and RAP80 chromatin and re-modeling factors are recruited. Localisation of 53BP1(◣) has been linked to binding of the exposed lysine 79 of histone 3 (◤).

The initial damage sensor for DSBs is believed to be the MRN protein complex, consisting of Mre11, Rad50 and Nijmegen Breakage Syndrome 1 (NBS1) (Petrini and Stracker, 2003), which is capable of activating the ataxia-telangiectasia mutated (ATM) kinase at the damaged site (Uziel et al., 2003, So et al., 2009). The components of MRN have been shown to form discrete foci after exposure to DSB inducing agents (Maser et al., 1997), which have been used as markers of DSBs (Nelms et al., 1998).

Histone 2AX (H2AX) is then believed to become phosphorylated on serine 139 by activated ATM or DNA-PK (Stiff et al., 2004, Savic et al., 2009), these overlapping pathways may highlight the importance of this event. This phosphorylation event has been shown to take place within minutes (Rogakou et al., 1998) but is not localized to the site of the DSB, instead phosphorylation has been shown to extend along the length of chromatin in either direction of the DSB (Nakamura et al., 2010). The phosphorylation of H2AX has also been hypothesised to be involved in the re-modelling of chromatin for repair (Paull et al., 2000). The mediator of damage Cceckpoint 1 protein (MDC1) has been shown to bind to γ–H2AX (Stucki et al., 2005). Further modifications to chromatin are made, including ubiqutination of H2A and methylation of H3 and H4 by RAP8 and Rnf80.

The tumour-suppressor protein 53 Binding Protein 1 (p53BP1 / 53BP1) has been shown to rapidly form foci after exposure to ionising radiation (Schultz et al., 2000, Anderson et al., 2001) and to co-localise with other DSB associated proteins, however the mechanism for its recruitment is still debated (FitzGerald et al., 2009, Goodarzi and Jeggo, 2009). For instance, 53PB1 has been hypothesised to be recruited by MDC1 (Bekker-Jensen et al., 2005, Xie et al., 2007), γH2AX, (Ward et al., 2003), the MRN complex (Lee et al., 2010) and through conformation changes to chromatin at lysine 79 of histone 3 and lysine 20 of histone 4 (Huyen et al., 2004, Botuyan et al., 2006). 53BP1 is as a highly conserved protein with several functional regions including a nuclear localisation sequence (NLS) and tandem tudor domains that have been identified as the essential units for the localisation of 53BP1 to DSBs after irradiation (Zgheib et al., 2009). 53BP1 has been implicated as a transducer for the activation of ATM and subsequent phosphorylation of Chk2 in the cell cycle arrest pathways (Wang et al., 2002, Uziel et al., 2003, Mochan et al., 2004, van Vugt et al., 2010). The roles of 53BP1 can therefore be considered multifaceted (Fitz and Goodarzi) and although it is generally accepted that 53BP1 is a downstream marker of DSBs it is still rapidly re-localised within minutes (Anderson et al., 2001, Rappold et al., 2001). The

signalling pathway for DSBs have been summarised in Table 1-2. It has been suggested that the signalling pathway is required to permit access of the repair machinery to condensed chromatin but, not all repair is dependant on signalling (Misteli and Soutoglou, 2009, Goodarzi et al., 2010).

Table 1-2 Proposed signalling cascade for DSB
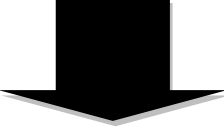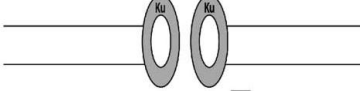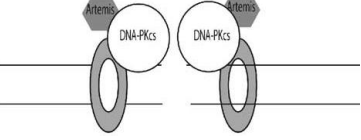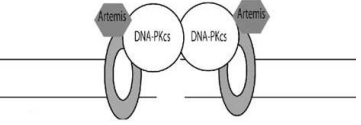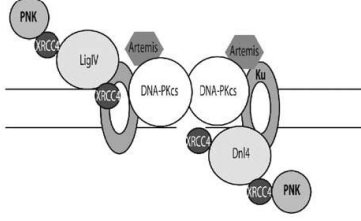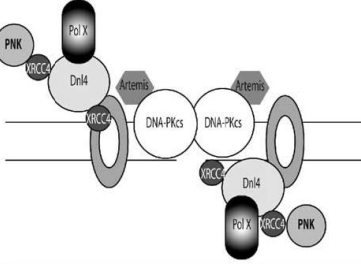
Upstream events	MRN detects break through direct binding
	ATM recruited and activated
	H2AX phosphorylated (by ATM)
	MDC1 binding to γ-H2AX
	Chromatin remodelling factors recruited
Downstream event	53BP1 and BRCA1 recruited

Table adapted from (Misteli and Soutoglou, 2009)

There are two principal pathways for the repair of DSBs; the high fidelity homologous recombination (HR) and the error-prone non-homologous end joining (NHEJ). Homologous Recombination (HR) repair is activated through the protein Rad52 which binds to damaged DNA, activating Rad51 and resulting in activation of the HR pathway (Karran, 2000, Takata et al., 2001). This pathway is dependent on a homologous sequence to use as a template, therefore HR is generally accepted to be restricted to the late S and early G2 phases of the cell cycle, meaning that NHEJ is the predominant repair pathway for DSBs in a population of normal cycling cells (Rothkamm et al., 2003). The core machinery involved in NHEJ have been identified principally through 'knockdown' experiments, see Table 1-3 and include DNA-PKcs, artemis, xrcc4, ligase IV. DNA-dependant protein kinase (DNA-PK) activity was first observed in HeLa cells (Walker et al., 1985, Carter et al., 1988) and subsequently shown to interact with DNA using electron microscopy (DeFazio et al., 2002), binding was significantly improved with the presence of DNA binding proteins ku70 and ku80 (Mimori et al., 1986, Gu et al., 1997, West et al., 1998). We now know that DNA-PKcs forms a signalling complex that causes a cascade of other signalling proteins to initiate NHEJ (Table 1-3).

Table 1-3 Core machinery of NHEJ repair pathway.

ACTIVITY	DESCRIPTION	REFERENCES
	Double Stranded break occurs.	
	Ku heterodimer encercles dsDNA ends.	(Smider et al 1994) Ku80 (Gu et al., 1997) Ku70
	Bound ku recruits DNA-PKcs and Artemis.	(Riballo et al., 2004) (Calsou et al., 2003) DNAPKcs
	DNA-PK bridges ends and phosphorylates Artemis.	(Weterings et al., 2003) (DeFazio et al., 2002) (Yaneva et al., 1997) synapse bridge (Riballo et al., 2004) Artemis phosphorylation)
	DNA/DNA-PK complex recruits LigaseIV-XRCC4 complex and polynucleotide kinase (PNK).	(Frank et al., 1998) LigaseIV (Li et al., 1995) XRCC4 (Chappell et al., 2002) PNK
	Processing and gap filling by polymerase and PNK allows ligaseIV to seal the nic.	(Mahajan et al., 2002) Polymerase

1.6 Dynamics of DNA DSBs for repair

Chromosome rearrangements are one consequence of the cellular repair processes, whereby different DSB 'ends' are illegitimately rejoined instead of the faithful repair of paired DSBs. Factors that are likely to influence this incorrect DSB repair include the spatial deposition of energy (ionisation events), complexity of lesions initially-induced and the organisation of nucleus / chromatin at the sites of this damage. It is known that chromosomes occupy distinct territories within the nucleus and that chromosome rearrangements are effectively induced after exposure to radiation, therefore for exchanges to occur, chromatin from different chromosome territories must either be in contact at the time of damage (contact first model) and/or damaged chromatin must migrate to become in relative close proximity for an illegitimate repair/exchange event to occur (breakage and re-union model).

The contact first model suggests chromosomes are already proximal for functional purposes at the time of damage induction (e.g. transcription factories, (Volpi et al., 2000, Mahy et al., 2002a) or due to intermingling of chromosomes (ICN) (Branco and Pombo, 2006), and that their subsequent rejoining is a chance event due to proximity. This theory relies on multiple chromosomes being consistently within the same nuclear volume as cytogenetic evidence shows high frequencies of translocations between specific regions (e.g. BRC-ABL).
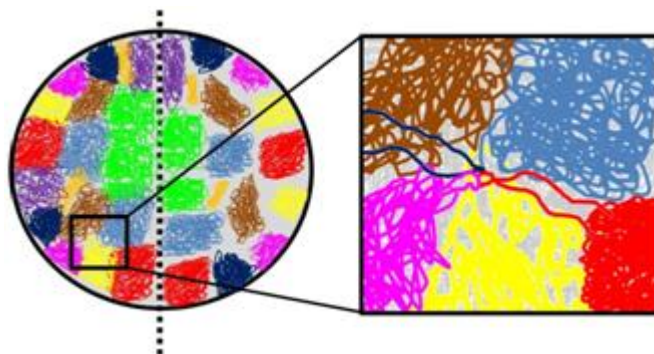
Figure 1-12 Illustration of contact first theory for exchange aberrations
In the contact first model complex exchanges occur where DSBs are induced in multiple chromosomes that are already in close proximity. The formation of exchanges, including complex exchanges, involving 3 or more chromosomes could be the result of genes looping out of their territories (insert).

However, there must be an underlying cause for the chromosomal exchanges that are frequently observed in metaphase chromosomes (Anderson et al., 2006), for which the contact first theory does not account. In yeast, the migration of DSBs can occur over large distances to sites of repair (Lisby et al., 2003, Lisby and Rothstein, 2004). Experiments in human fixed cells have provided evidence that the number of foci within a nucleus reduces with time but area remains constant, suggesting that foci are clustering together for repair (i.e. migrating), which would lead to increased probability of exchange (Aten et al., 2004, Desai et al., 2005, Markova et al., 2007). These observations are consistent with the breakage and re-union model whereby DSBs move over a given distance before rejoining. This process may be undirected, through relaxation of the super structure of chromatin, along concentration gradients or it may be a directed and dynamic process. Evidence thus far for migration of DSB in mammalian cells suggests that large scale movements are rare but limited movement over distances (<2µm) are thought to occur (Anderson et al., 2002, Savage, 2002, Sachs et al., 2007).

The ability to create fusion proteins of 53BP1 and green fluorescent protein (GFP) has allowed real time measurement of RIF dynamics (Pryde et al., 2005, Falk et al., 2007, Asaithamby and Chen, 2009, Cao et al., 2010, Giunta et al., 2010). Live cell experiments with mammalian cells have shown movement of DSB markers (53BP1) to be restricted to within 1um, (Falk et al., 2007, Jakob et al., 2009), consistent with previous models. This level of movement has been suggested to be the uncontrolled migration of DSBs from high to low density regions within the nucleus and in-line with the theory that chromatin remodelling factors allow de-condensation of chromatin flanking DSBs (Nelms et al., 1998, Kruhlak et al., 2006). Indeed RIF have been demonstrated to preferentially exist at the interface of high and low density chromatin, which in itself could be considered evidence of limited diffusion of DSBs from high density chromatin to lower density chromatin (Costes et al., 2007).The density of chromatin may not be the only contributing factor defining marginal movement. Gene density has been implicated in the directed acetylation of histones and by proxy accessibility of chromatin for repair (Surralles et al.,

1997a, Surralles et al., 1997b). Thus, there is no consensus on which model best describes the mechanism of chromosome exchange.

1.7 Quantification of radiation induced foci

The measurement of DSB induction and subsequent decline has classically been measured using pulse field gel-electrophoresis but this method is not capable of resolving smaller numbers of breaks and therefore requires a large dose (1-5 Gy) to induce a visible response (Nevaldine et al., 1994, Schultz et al., 2000). This method is also not cell specific and will only show the induction of DSBs in a population of cells. An improvement of this assay is the Comet assay, in which the volume of DSBs can be detected in single cells. However, as with electrophoresis, resolution is limited and spatiotemporal dynamics within the nucleus cannot be detected (Calini et al., 2002). Microscopy has been a fundamental tool to biologists for hundreds of years. During the mid nineteenth century George G Stokes coined the term "fluorescence" to describe the light emitted from organic and inorganic matter when excited with specific ranges (ultra violet) of sunlight. Stokes also observed that the emitted light was of a shorter wavelength than the exciting light, this is known as the 'Stokes shift' or 'Stokes' Law' and is one of the fundamental principals of fluorescence microscopy. By the mid-twentieth century the familiar setup of the fluorescence microscope had been established and a multitude of fluorescent dyes and stains were available (Masters, 2010). In 1950 Coons and Kaplan used antibodies conjugated with fluorescent dyes to specifically label proteins, which ultimately led to the field of immunofluorescence.

The use of markers, such as the phosphorylated variant of histone 2A (γ-H2AX), for the detection of radiation induced double strand breaks (DSBs) is now standard practice for investigating biologically relevant doses of radiation (for a review of the field see Lobrich et al 2009). For instance, the induction and subsequent repair kinetics of DSBs have been determined in a range of cell types upon exposure to varying qualities and radiation doses (Falk et al., 2008, Rube et al., 2008). Additionally, the development of antibodies specific to other relevant proteins in the DNA

damage response (DDR) pathway has revolutionised our ability to investigate mechanistic aspects of DSB processing in interphase nuclei (Maser et al., 1997, Rogakou et al., 1999, Schultz et al., 2000).

Radiation-induced foci (RIF) assays are now being applied to assess the clinical outcome to radiation (Banath et al., 2010), as well as evaluating risk complications associated with radiotherapies and diagnostics (Lassmann et al., 2010, Beels et al., 2011). RIF are also being exploited as biomarkers for dosimetric purposes to identify individuals exposed to unknown levels of radiation (Redon et al., 2010) and for the assessment of cellular sensitivity, which could be utilised for pre-screening of patients prior to radiotherapy or diagnostics (Bourton et al., 2011). Detailed quantification and measurement of foci has, until recently, been limited to visual observations and counting by eye on the microscope. The benefits and caveats of this method are listed in Table 1-4.

Table 1-4 Benefits and caveats of manual foci counting

Benefit	Caveat
Rapid counts of foci in real time	No measure of size
No knowledge of computing or image analysis required	Operator bias (reduced with blind scoring)
Provides an overview of the appearance of nuclei	Inter and intra operator reproducibility
	Accuracy for thick specimens
	No measure of spatial distribution of foci
	Live cell measurements not feasible

Of the caveats listed, reproducibility is the key factor for comparisons between labs as different operators will have different criteria and on a day to day basis and are likely to have different counts for the same data. This becomes more significant when analysing samples that require the operator to scan through the focal planes and remember which foci have already been counted. The development of integrated optical systems with sensitive digital cameras has enabled scientists to rapidly capture images and image stacks, that can be analysed downstream of the microscope room, but this methodology is far from standardised. The fundamental aspects of foci counting that determine the final number and size of foci in nuclei are defined by the resolution of the entire system; these aspects are listed in Table 1-5. Each facet of the system will be discussed.

Table 1-5 Factors affecting resolution of RIF assay

System element	Variable	Effectors
Sample	Thickness	2D / 3D fixation
	Mounting surface	Glass / Plastic
Microscope	Optics	Magnification and NA
	Type	Widefield / Confocal
	Illumination	Laser / lamp / LED
Image acquisition	Dynamic range	Bit depth
	Spatial resolution	
	Image type	Data compression
Analysis	Axial resolution	Step size
	Identification method	Segmentation
	Data transfer / entry	N/A

1.7.1 Sample preparation

The fixation method used will determine the efficacy of preservation of epitopes (antibody targets) and the morphology of the cell. The principal methods for fixation and permeabilisation are listed in Table 1-6.

Table 1-6 Comparison of sample fixation methods

Process	Agents	Remarks
Dehydration	Methanol, Ethanol, Acetone,	To preserve morphology Precipitation of proteins can strip epitopes of interest.
Cross linking	Aldehydes (formaldehyde, gluteraldehyde)	Most suitable for preservation of soluble proteins. Some aldehyde groups case autofluorescnce
Cryogenic	LN2 + Isopentant	Must be followed by additional fixation before staining
Embedding	Parafin wax	Less suitable for cultured cells
Permeabilisation	Detergent, saponin, snap freezing	Detergents are effective at removing lipids whilst Saponin sequesters cholesterols, snap freezing with LN2 can also permeate membranes in the presence of moisture.

Fixation using alcohols results in shrinkage of the sample, this can be counteracted with acetic acid, which also denatures the sample but causes swelling. This method does not preserve the morphology of the cell and often causes a flattening of the sample as the cytoskeleton is precipitated. Cross linking preserves the structure of the cell more faithfully as the cytoskeleton is preserved but this can make penetration of antibodies and DNA probes difficult and so additional permeabilisation steps are needed.

1.7.2 <u>Microscope resolution</u>

The resolution of a microscope describes the shortest resolvable distance between two independent objects as seen by the operator / camera. See Figure 1-13.
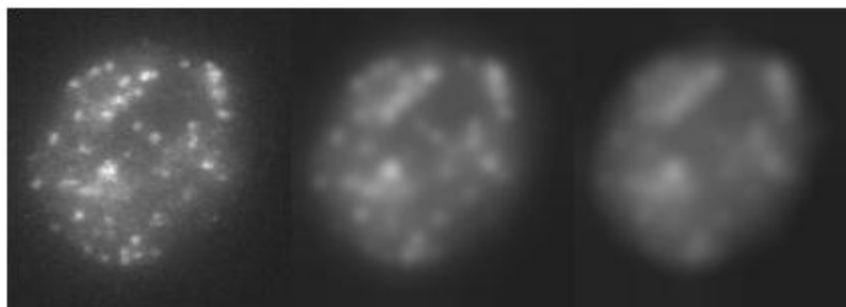
Figure 1-13 Example of decreasing optical resolution

Several formulas exist to define the absolute resolution of a microscope, these are based on the numerical aperture of the optics and the wavelength of light being used to visualise the sample. Theoretically two objects could be resolved with a separation of ~0.25µm but other factors decrease the resolution. The vertical resolution or 'depth of field' is also governed by the wavelength of light, Numerical Aperture and refractive index of the mounting media:

$$D = 2\lambda\eta/(NA)^2$$
$$937nm = 2 \times 550 \times 1.44 / (1.3)^2$$

The design of confocal microscopes improves axial resolution by only utilising light from a single focal plane. For both widefield and confocal, a 1.3 numerical aperture (NA) objective will have a depth of field of ~0.5µm, cultured monolayers of cells are typically in the region of 10µm thick. Therefore, to observe whole cells, information must be taken from multiple focal planes. Classically, this has been achieved by taking a series of images at known step sizes along the z-axis. This series of images can then be analysed as a stack or collapsed into a maximum intensity projection (MIP) to make a single image for analysis. Alternatively, the extended focus method can generate similar results (Barber, 2007).
The illumination method for confocal microscopy is dependant on lasers,

the even illumination and quality of images from confocal microscopes is largely due to the confocal unit that drives the scanning process. For widefield microscopy even illumination is important for the counting of foci as multiple nuclei are captured in a single field of view, the development of higher power lasers and even light emitting diodes has enabled widefield microscopy to utilise more even illumination than can be achieved using arc lamp technology.

1.7.3 <u>Image acquisition</u>

The sensor, camera or photomultiplier, is critical to obtaining images for analysis. The pixel resolution is determined by the sensor type, size and the magnification of the microscope. This is different to optical resolution, see Figure 1-14.
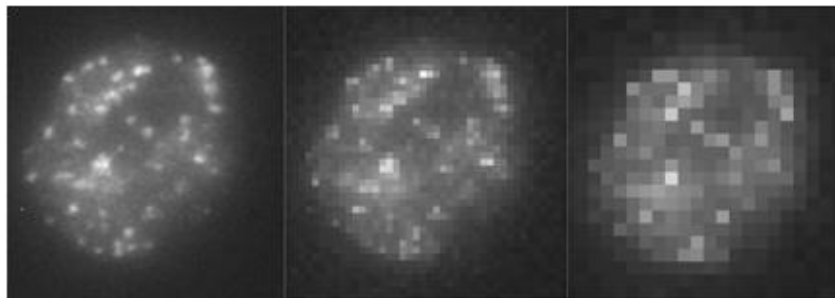
Figure 1-14 Example of decreasing digital resolution

The sensor will also define the signal to noise ratio, which describes the contrast between background (noise) and the fluorescence (signal). The dynamic range of a sensor will have a significant effect on image signal to noise ratio. This is sometimes referred to as Gray-level resolution or bit depth and is the number of shades of grey (monochrome sensor) each pixel can be. For example, a one bit image (2^1) can be either black or white whilst a three bit image (2^3) can encode eight shades. Modern scientific cameras often have bit depths in excess of 12 bits, allowing a larger range of intensities to be measured, see Table 1-7. Interestingly, the human eye is not directly comparable to a digital sensor but is far more sensitive at detecting contrast (range).

24

Table 1-7 Comparison of bit depths

Number of 'bits'	8	10	12	14	16
Grey Levels	256	1024	4096	16384	65535

In conjunction with the image bit depth, image files should be stored in a suitable way as to facilitate digital image analysis. The standard format for analysis is the Tagged Image File Format (TIFF), with each colour for a multicolour image being independent to enable the largest dynamic range of pixels. There is also the ability to code more information into the file about the image; commonly known as metadata. Typically this contains information on the acquisition settings and parameters. Other file formats specific to commercial products exist and each encode their metadata in their own ways but most rely on the TIFF for the image itself. The least favourable formats are those that compress the images and merge multiple colours as this will sacrifice data (e.g. JPEG, colour TIFF, bitmap).

1.7.4 Image analysis

Advances in digital technology have enabled the development of new methods in the quantification of radiation induced foci (Bocker and Iliakis, 2006, Barber, 2007, Gerashchenko and Dynlacht, 2009) and the use of computer aided scoring has also enabled detection of foci from as little as 1 cGy (Ishikawa et al., 2010, Su et al., 2010). Manual image analysis offers several benefits over counting foci on the microscope. However, the main drawback is that the dynamic range of the image cannot be portrayed effectively on the screen. The majority of liquid crystal display and cathode ray tube monitors use the same input from a computer, which is 24bit (truecolour). This covers three colours - red, green and blue - with 8 bits each and varying the ratios for each colour changes the pixel colour. Greyscale range is achieved by presenting all colours in equal proportions, therefore this is also limited to 8bit (256 shades). As a result, the initial setup of the display adjustment is critical to visualising the full dynamic range of the image for visual analysis.

Identifying foci in a digital image is often achieved simply by using

an intensity threshold determined by the operator. Providing there is no bias this can be an effective method for identifying foci. However, the method is labour intensive and the threshold will only apply to one focal plane. As intensity will be reduced with change in focal planes, it is therefore an ideal method for MIPs and single plane images but not suited for high throughput or complex 3D image stacks. Alternatively edge detection algorithms can be applied to detect foci in images where intensity alone cannot identify a focus (Figure 1-15).
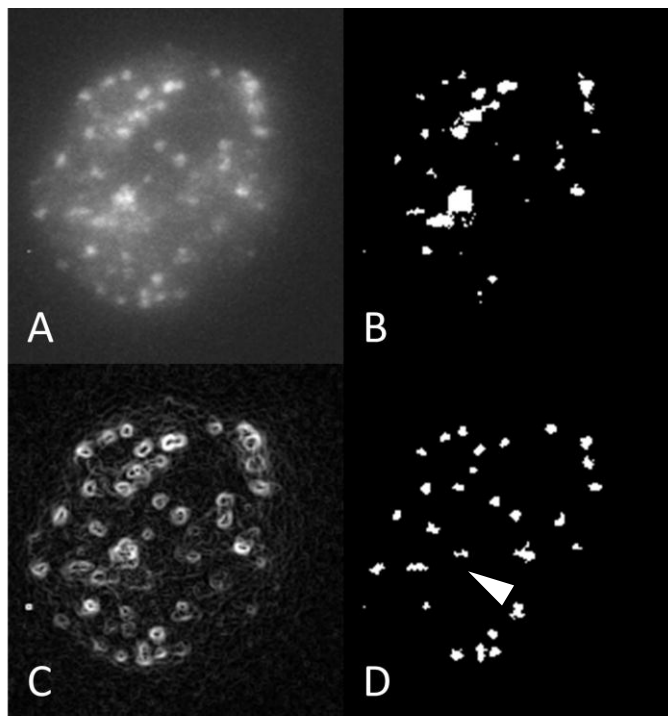
Figure 1-15 Comparison of foci detection techniques
Nucleus stained by IF to show discrete RIF (A). The same nucleus is then shown as a binary image based on manual threshold (B). Edge detection can identify changes in signal intensity (C) whilst the peaks of intensity with segmentation (D) can also be used to identify RIF (arrow indicates lack of specificity for size using peak intensity segmentation).

Filtering and smoothing of images is another image manipulation method that can improve the accuracy of a focus count. Smoothing is a particularly effective method of removing "salt and pepper" background common in Confocal images, and also reduces the local contrast of foci from other focal planes, minimising the number of erroneous foci counted.
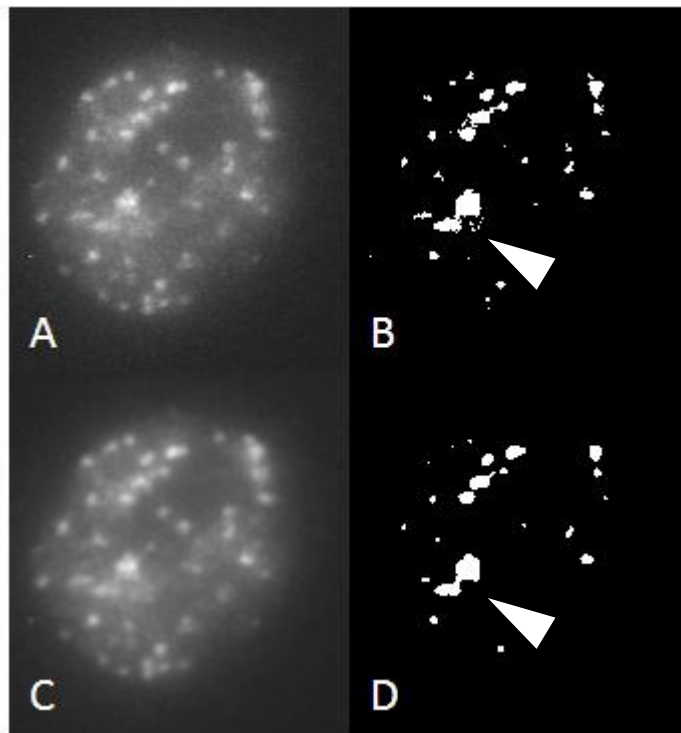
Figure 1-16 Effect of image smoothing on threshold
An intensity threshold is applied to an 8bit greyscale image (A) to generate a binary image (B), high intensity background has been included in the binary image (arrow). Smoothing the original image (C) results in the higher intensity background becoming less significant compared to the peaks of intensity of foci (D).

Generally thresholding alone is not effective at identifying foci as the threshold required to identify all foci will often include background that is not intended to be classified as a focus, see Figure 1-16. However excessive smoothing can result in loss of foci and merging of proximal foci. Therefore to accurately identify foci a combination of the methods described above must be employed.

1.7.1 <u>Live cell microscopy</u>

The labelling of radiation induced foci with antibodies relies on the sample being fixed, which can only provides a window on insight into the possible dynamics of radiation induced foci in a population of cells. To examine the dynamics of RIF in real time human bronchial epithelial cells have been genetically modified to express a fusion protein of green fluorescent protein (GFP) and 53BP1 (Asaithamby and Chen, 2009). To be able to stably transfect, clone and experiment on HBEp cells the number of population doublings must be increased. HBEp-3KT cells have been immortalised using human telomerase reverse transcriptase (hTERT) (Ramirez et al., 2004) to prevent differentiation and senescence. Using plasmid pCD3.1Hyg-EGFP-53BP1 cells with the transfection were selected in media containing Hygromycin-B (Asaithamby and Chen, 2009).

1.8 Aims

Radiation induced foci (RIF) are an important marker of radiation induced damage. They can let us visualise the amount and spatial deposition of damage in a cell nucleus and assess how this may alter as the cell initially senses the damage and then initiates processes to deal with the damage (repair). The induction and subsequent decline of RIF has been assessed in a range of cell types and after varying qualities and doses of ionising radiation (Schultz et al., 2000, Anderson et al., 2001, Rappold et al., 2001, Rothkamm et al., 2003, Costes et al., 2006, Leatherbarrow et al., 2006, Falk et al., 2007, Markova et al., 2007, Asaithamby and Chen, 2009, Banath et al., 2010)

Initial observations of RIF suggested an increase with time after irradiation (Aten et al., 2004), the biological relevance of this size change remains unclear. The tools for the accurate quantification of RIF size changes have only recently become readily available (van Veelen et al., 2005, Yamauchi et al., 2008, Cai et al., 2009, Schettino et al., 2010). So to address the question of foci size changes, a method of analysis was developed to accurately and reproducibly quantify and measure foci in nuclei of the target cells.

2 Materials and methods

2.1 Materials

The following materials were used for subculture, storage and experimentation of adherent cells:

35mm Petri dishes	Nunc
Bovine Pituitary Extract	Lonza
Bronchial Epithelial Cell Basal Medium	Lonza
Cryovials	Nunc
Dimethyl Sulfoxide	Sigma Aldrich
Eagle's Minimum Essential Medium with Earle's salts and non-essential amino acids	Sigma Aldrich
EDTA	Fisher Scientific
Epinephrine	Lonza
Foetal Bovine Serum	Sigma Aldrich
Gentamicin Sulfate and Amphotericin-B	Lonza
Glass coverslips (various)	Fisher Scientific
Glutamine	Gibco
HEPES Buffered Saline Solution	Lonza
Human bronchial epithelial (HBEp) cells (Primary)	Lonza
Human Epithelial Growth factor	Lonza
Hydrocortisone	Lonza
Industrial Methylated Spirits	Fisher Scientific
Insulin	Lonza
Penicillin & Streptomycin	Gibco
Phophate buffered saline	Gibco
QuadriPERM® culture dishes	Sigma Aldrich
Retinoic Acid	Lonza
SuperFrost glass microscope slides	Menzel
T75 and T25 culture flasks	Nunc
Transferrin	Lonza
Trypan Blue	Sigma Aldrich

Trypsin (for normal adherent cells)	Sigma Aldrich
Trypsin Neutralising Solution	Lonza
Trypsin/EDTA (for Human Bronchial Epithelial Cells)	Lonza

For fixation and immunofluorescence the follow materials were used:

Acetic Acid	VWR
Clear nail varnish	No. 7
Cow gum	Cow Proofings
$DiOC_6$	
Goat anti mouse IgG conjugated with AlexaFluor 555.	Invitrogen
Hydrochloric Acid	BDH
Immersol 518N (microscope immersion oil)	Zeiss
Methanol	Fisher Scientific
Mouse monoclonal anti-human 53BP1 Antibody (Clone 19)	BD
Para formaldehyde	Sigma Aldrich
Polyclonal Goat anti rabbit conjugated with FITC	Abcam
Rabbit anti-human γ-□H2AX Antibody (polyclonal).	Abcam
Saponin	Sigma Aldrich
Sodium Hydroxide	Arcos
Trion X-100	Invitrogen
Vecatashield + 4',6-diamidino-2-phenylindole	Vector Laboratories

For the generation of probes for use in Fluorescent In-Situ Hybridisation assays the following materials were used:

10x DOP PCR buffer	Sigma Aldrich
20X SSC	Fisher Scientific
AdenosineTp, CYtosineTp, GuanineTp, ThymidineTp	Invitrogen
Agarose	Fisher Scientific
Biotin DUTp	GE Healthcare
Bovine Serum Albumin	Invitrogen
Cot1 DNA	Roche
Dextran sulphate	Invitrogen
DOP Primers	Sigma Aldrich
Ethanol	Hayman
Formamide	Fisher Scientific
Herring/salmon sperm DNA	Invitrogen
Molecular grade water	Fisher Scientific
Sodium acetate	Arcos
Streptavidin	GE healthcare
Taq Supreme	Kapa Biosystems
Tris Buffer Elute	Fisher Scientific
Tween-20	Fisher Scientific
1000kb DNA ladder	New England Biolabs
Ethidium bromide	

2.2 Methods

2.2.1 Cell culture

All cell culture work was conducted in a class two laminar flow hood. All items were rinsed with 70% industrial Methylated Spirits (IMS) prior to use. The main cell type used throughout this study was primary human bronchial epithelial (HBEp) cells. These were supplied commercially by Lonza at passage (p)1, bulked to generate stocks from p2 onwards with batches of p4-8 used for experimentation. For various optimisations and also for comparison, human dermal fibroblasts (AG01522) (Coriell) were also used.

2.2.1.1 Subculture of Human Bronchial Epithelial cells

HBEp cells were routinely sub-cultured at ~80-90% confluence (see section 4.2.1 for details) by trypsinising according to the suppliers guide. Specifically for a standard T75 flask, medium was aspirated and the cell monolayer rinsed with 15ml pre-warmed HEPES-BSS before addition of 6ml Trypsin/EDTA solution. Cells were incubated at $37^{o}C$ & 5%CO2 in a humidified incubator until >90% of cells had rounded up and become detached (2-6min) before addition of 12ml Trypsin Neutralisation Solution (TNS). The cell suspension was then centrifuged at 220 x g for 5min, the supernatant removed and the pellet re-suspended in 2-3ml complete medium. Complete medium (Lonza BulletKit CC-3170) consists of bronchial epithelial cell basal medium (500ml/99%), bovine pituitary extract (2ml/0.2%), insulin (0.5ml/0.1%), hydrocortisone (0.5ml/0.1%), gentamicin sulfate and amphotericin-b (0.5ml/0.1%), retinoic acid (0.5ml/0.1%), transferrin (0.5ml/0.1%), epinephrine (0.5ml/0.1%) and human epithelial growth factor (0.5ml/0.1%). The viability of trypsinised cells was then estimated using trypan blue staining. Cells were either re-seeded for experimentation or for maintenance at a density of $3.5x10^{3}$ / cm^{2}. To ensure optimal growth of HBEp cells, complete medium was changed every 48hrs and additionally, fresh medium was added between passage in line with the approximate confluence of the cell sheet.

Cell sheet confluence <25% = 1.0ml/5cm^2 (15ml in T75)

Cell sheet confluence ~25 – 45% = 1.5ml/5cm2 (22.5ml in T75)

Cell sheet confluence >45% = 2.0ml/5cm2 (30ml in T75)

2.2.1.2 Subculture of AG01522 human dermal fibroblasts

Routine subculture of AG01522 human dermal fibroblasts (Coriell) was performed at 90-100% confluence. Cells were cultured in T75 culture flasks (nunc) at 37°C & 5%CO$_2$ in a humidified incubator. Complete medium containing Eagle's Minimum Essential Medium with Earle's salts and non-essential amino acids (Sigma Aldrich) (78%), Foetal Bovine Serum (FBS) (Sigma Aldrich) (20%), Penicillin & Streptomycin (Gibco) (1%) and Glutamine (Gibco) (1%) (v/v) was warmed to 37°C in a water bath. Existing medium from flasks was removed and the cell monolayer washed with versene (0.197g EDTA in 1000ml of PBS). Vessels were then incubated for between 1 and 5 min at 37°C in Trypsin solution (Trypsin diluted 100x in versene). Trypsin solution was then inactivated with 5ml complete medium. The cell suspension was centrifuged at ~200g for 5min in a sterile centrifuge tube. Supernatant was removed and cells were re-suspended in complete medium. A sample of the suspension was diluted in trypan blue and a viable cell count was made for each vessel using a haematocytometer. AG01522 fibroblasts were seeded at 5x10^5 cells/cm^2.

2.2.1.3 Freezing cells

The procedure for subculture was carried out and cell suspensions diluted in complete medium supplemented with 4-8% DMSO. Cell suspensions were aliquoted into 1ml cryogenic storage vials (nunc cryovials) at a density of ~1x10^6 cells/ml, frozen to -80°C for a minimum of 24hrs then transferred to liquid nitrogen (-196°C) long-term storage containers.

2.2.1.4 Thawing adherent cells

Complete medium was added to culture flasks (~0.26ml/cm^2) and allowed to equilibrate to 37°C in 95% air/5%CO$_2$ for 30min. Cryovials of frozen cells (~1x10^6/ml) in medium supplemented with 4-8% dimethyl sulfoxide (DMSO) were then removed from liquid nitrogen storage (-196°C) and thawed rapidly in a water bath (37°C). When 90% thawed, the contents of a cryovial were added to the equilibrated compete media and the flask returned immediately to the incubator. Media was replaced 24hrs after seeding to remove DMSO.

2.2.1.5 Subculture of adherent cells onto glass substrates:

For routine immunofluorescence (with or without γ-ray exposure), cells were seeded onto sterilised coverslips within 35mm Petri dishes or onto sterilised SuperFrost glass microscope slides in quadriPERM® dishes at 3.5x10^{3}cells/cm^2. Both coverslips and slides were prepared by washing in hydrochloric acid (1:10 in water) to remove any grease then rinsed in 10x dH$_2$O washes on a rotor rocker. Slides were stored at 4°C in 100% methanol until required. Immediately prior to use, slides were flamed to sterilise and left to dry in a Class II hood and placed into appropriate culture vessels, before seeding of cells as appropriate.

2.2.1.6 Subculture of adherent cells onto 'Mylar':

For α-particle exposure, cells were grown onto a 2.5µm thick substrate of polyethylene terephthalate (PET or 'Mylar') attached to glass irradiation dishes (Courtesey of Dr Mark Hill and Abdelrazek Abdelrazzak). Dishes were sterilised in an oven at 210°C (dry heat) overnight to preserve the adhesive holding the PET to the dish. To aid cell adhesion, dishes were pre-treated with complete medium for 1hr at 37°C before use.

2.2.2 Irradiation

Brunel University's high activity (1.9 KCi on June 24th 1999 with a half life of 63.24 months) and low activity (0.27 TBq) ^{60}Cobalt γ-sources were used throughout this study. In addition, cells were transported to both the Gray Institute, University of Oxford (in collaboration with Dr Mark Hill) and Queens University, Belfast (in collaboration with Dr Guiseppe Schetinno and Professor Kevin Prise) and exposed to α-particles from ^{238}Plutonium sources. For Sources at Brunel University and Oxford, Dr Mark Hill has calculated fluence for irradiations, incorporating travel doses. Fluence for irradiation with α-particles was estimated from exposures on CR-39 (Columbia Resin number 39) plates and subsequent etching with sodium hydroxide.

2.2.2.1 Low-LET γ-rays

Irradiations were performed using dose rates of 0.113 - 0.325 Gy/min (calculated by Dr Mark Hill). The radiation facility is a 5 minute walk from the cell culture facility. To minimise the effects of transit, cells were transported to the irradiation source at 37°C using a thermally insulated box with pre-heated liquid heat reservoir (gel packs pre-warmed in a waterbath). Cells were irradiated at room temperature or in a 37°C portable incubator, depending on the exposure length.
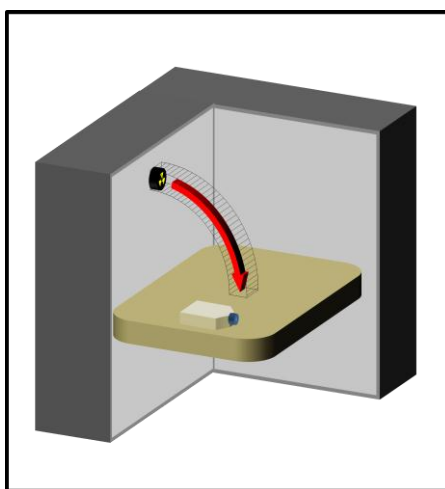
Figure 2-1 Schematic representation of setup for irradiation
Culture vessels are located 50-100cm from the source on a steel bench. The radiation source emerges from shielding via a tube and stops centrally on the bench

2.2.2.2 <u>High-LET α-particles</u>

In order to visualise 'tracks' of α-particle exposure through the nuclei of 'hit' cells, cells were exposed at two different facilities employing different irradiation rigs to achieve tracks along the horizontal plane.

2.2.2.2.1 Gray Institute, University of Oxford

To visualise transverse (x/y-axis) tracks, cells were grown on a 2.5µm or 0.9µm PET (Mylar) Mylar dishes. Cells were transported to Oxford in a 37°C incubator and allowed to settle for 2-3 days before being seeded onto the Mylar dishes. The cells were then left to reach ~90% confluence over a period of 3 days, then irradiated at an angle of 30° from vertical (Figure 2-2). Dishes were exposed for 18 seconds each to achieve a delivery of a fluence of ~1 α-particle per HBEp cell nucleus, based on the nuclear area as determined by DiOC-$_6$ staining (see section 2.2.3.2), then returned the sample to the incubator for varying lengths of time.
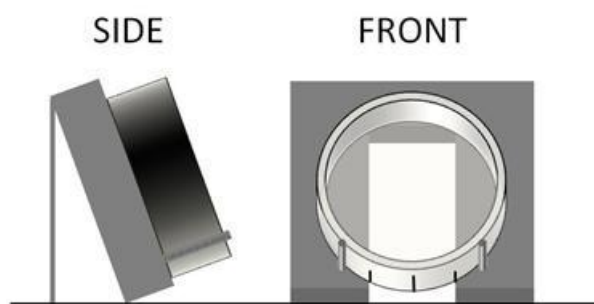
Figure 2-2 Schematic of irradiation with α-particles at a 30°C angle.
α-particles pass through a helium chamber directly beneath the dish and pass through a PET covered hole directly beneath the sample. The holder supports the dish and has a window to allow α-particles to pass through the base of the dish

2.2.2.2.2 Queens University, Belfast

The design of this source allowed cells to be cultured directly onto glass microscopic slides enabling greater flexibility for subsequent biological assay developments e.g. visualisation of 53BP1 foci within individual chromosome territories using fluorescence in situ hybridisation (FISH). Specifically, the plutonium source was mounted on a mock microscope objective in place of the lens with a series of acrylic rings that ensured exact and reproducible positioning of slides above the source (Figure 2-3).
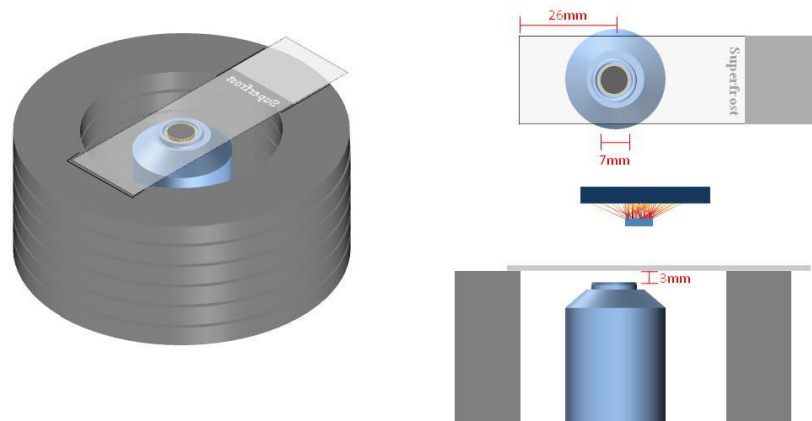
Figure 2-3 Schematic for direct irradiation with α-particles
For direct irradiation with α-particles, cells are grown on slides and inverted above the source

2.2.3 Fluorescence Staining

All immunofluorescence and general FISH procedures were carried out on the bench. When generating FISH probes, work was conducted in a class two laminar flow hood to prevent contamination of DNA templates.

2.2.3.1 Immunofluorescence staining of DNA DSB markers

To visualise sites of DSB within individual nuclei, antibodies directed toward 53BP1 and the variant form of H2AX, phosphorylated at serine 139, were used. To that end, cells were cultured and irradiated as required and then allowed to incubate for repair of any induced damage for varying lengths of time. Samples were then washed three times for 3-5min in ice cold PBS then fixed for 5-10min in 4% paraformaldehyde solution in order to preserve the 3D structure of the nucleus. After fixation, cells were washed three times for 3-5min in PBS then permeabilised, to aid antibody penetration, with 5% saponin (w/v) and 5% triton X-100 (v/v) for 20min at room temperature and then incubated in blocking buffer (5% foetal bovine serum in PBS) for 1hr at RT. Cells were then incubated with primary antibody (diluted in blocking buffer), either to 53BP1 (mouse monoclonal anti-human 53BP1, Clone 19, 1:200) or to γ-H2AX (rabbit anti-human, γ-H2AX polyclonal, 1:100). Cells were then washed three times for 5min in PBS to remove unbound antibody, dipped into blocking solution then incubated with secondary antibodies; goat anti mouse IgG conjugated with

AlexaFluor 555 or goat anti rabbit conjugates with FITC for visualisation of 53BP1 and γ-H2AX respectively. Cells were subsequently washed three times for 5min in PBS to remove unbound secondary antibody, mounted and counterstained with vecatashield containing 4',6-diamidino-2-phenylindole (DAPI). Coverslips were overlayed and sealed to slides using clear nail varnish.

2.2.3.2 DiOC$_6$ (3,3′-dihexyloxacarbocyanine iodide) staining for measurements of cell morphology

To measure the dimensions of HBEp cells, cells were grown on coverslips in 35mm Petri dishes and incubated in 100nM DiOC$_6$ for 10min. DiOC$_6$ is a mitochondrial stain capable of providing a cytoplasmic outline for discrimination of the cell and nuclear membranes. To make a temporary chamber for visualisation of live cells, a rubber o-ring from a cryovial was mounted to a glass slide with silicone grease, the well was then filled with medium and a coverslip mounted to make a medium filled chamber. Cells were then visualised on a Confocal Laser Scanning Microscope whereby dimensions for cellular and nuclear width/depth were made using ImageJ software (NIH). Cellular and nuclear morphology was consistently ellipsoidal or oblate spheroid in shape, to quantify the dimensions three measurements were taken on each axis for the diameter and depth of the cell nucleus and cytoplasm. These were plotted into an Excel (Microsoft) spreadsheet to obtain an overall average for 20 cells.
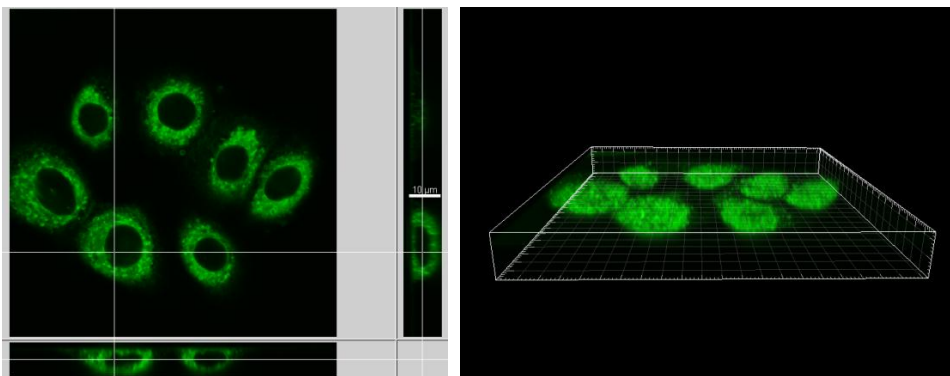
Figure 2-4 Confocal images of HBEp stained with DIOC^6
The nucleus can be discriminated by the lack of stain surrounded by DIOC^6 (green) (left panel). The same image stack was imported into Imaris for 3D visualisation showing the ellipsoid morphology of HBEp cells (right).

2.2.3.3 <u>Immunofluorescence-in-situ hybridisation (IF-FISH)</u>

One aim of this study was to visualise the spatial distribution of DSB within individual chromosome territories and to examine whether this altered with time after damage induction. To achieve this, the 'Immuno-FISH' method was employed which involves standard immunofluorescence followed by fixation of the antibodies before denaturation of chromosomes using a modified FISH protocol. Various optimisations of this assay were performed in both HBEp cells and AG01522 fibroblasts, using both commercial and home made FISH probes and which are described in the following sections.

2.2.3.3.1 Generating probes from whole chromosome templates.

Biotin-labelled DNA templates of chromosomes were generated through degenerate oligonucleotide (DOP)-PCR by mixing 10μl 10x DOP PCR buffer, 10μl AdenosineTp CytosineTp GuanineTp (2mM), 4μl ThymidineTp (2mM), 2010μl Biotin dUTp, 10μl DOP Primers (10μM), 35μl molecular grade water, 1μl Taq Supreme (2.5 units) and 10μl of template DNA (Gift from Dr Jo Bridger) in a sterile eppendorf tube. The sample was then loaded into a thermocycler for 3min at 94°C (x1) then 94°C for 1min, 62°C for 1min, 68°C for 1.5min (x30) ending at 68°C for 8min and then held at 4°C. Confirmation of DNA template amplification was performed by running the sample on a 1% agarose gel made with 0.5x Tris Buffer Elute and 2ul of 10mg/ml ethidium bromide. The sample appears as a 200-500Kb smear against a 1000kb ladder.

To generate DNA probes; 8μl of labelled template was mixed with 7μl Cot1 DNA, 3μl herring/salmon sperm DNA, 1.8μl 3M sodium acetate and 40μl ice old ethanol. The mixture was then incubated at -80°C for 30min, centrifuged at 500g at 4°C for 30min and the supernatant removed. The pellet was then washed with 200μl 70% ethanol for 15min at 500g at 4°C and subsequently air-dried before re-suspension overnight in hybridisation buffer comprising 2.4μl dextran sulphate (10%), 1.2μl 20X SSC (10%), 6μl formamide (50%), 0.12μl Tween-20 (1%) and 2.28μl dH$_2$0 (29%). DNA probes could then be stored at -20°C for up to 6 months.

2.2.3.3.2 IF-FISH

Cells were fixed using either 3:1 methanol and glacial acetic acid at -20°C or 4% paraformaldehyde in PBS, added dropwise to the surface for 5min. After fixation cells were washed three times for 3-5min in PBS before membrane permeabilisation with 5% saponin (w/v) and 5% Triton X-100 (v/v) in PBS for 20min at room temperature. Cells are then incubated in blocking buffer (5% foetal calf serum in PBS) for 1hr at RT. Cells were then incubated with primary antibody diluted in blocking buffer to 53BP1 (mouse monoclonal anti-human 53BP1, Clone 19, 1:200) for 1hr, washed three times for 5min each in PBS to remove unbound antibody then dipped into blocking solution before applying secondary antibody to 53BP1, goat anti-mouse IgG conjugated with AlexaFluor 555. Cells were washed again to remove unbound secondary antibody and incubated in 4% paraformaldehyde at RT for 10min to fix the antibodies and then washed three times in PBS. Cells were depurinated using 0.1M NaOH for 5min, washed with ice cold PBS then dehydrated in an ethanol series (70%, 90% and 100%) for 5min each before drying on a hot block at 75°C for 5min. Chromosomal DNA was denatured in 70% formamide in 2xSSC at 74°C for 2min and then immediately placed into an ice cold ethanol series for 1 min each. In parallel to this, probe DNA was denatured on a hot block at 90°C for 10min and then incubated at 37°C for 30min to allow re-annealing of repetitive sequences. Denatured chromosomal and probe DNA were then brought together and sealed under a coverslip using cow gum and left to hybridise for 72hr at 37°C in a humid dark environment.

    After hybridising, coverslips were removed using forceps and slides incubated in three washes of 50% formamide at 45°C in 2xSSC (3x5min), followed by three washes in 0.1xSSC at 60°C (3x5min). A blocking step was required using 4% Bovine Serum Albumin (BSA) in 2xSSC for 10min before indirectly detecting the biotin label on the probe DNA by incubating slides in streptavidin conjugated with Tetramethyl Rhodamine Iso-Thiocyanate (TRITC) (molecular probes) in 1% BSA for 1hr at RT. Slides were then washed in 4xSSC and 0.1% Tween20 at 42°C for 5min and mounted in vecatashield with 4',6-diamidino-2-phenylindole (DAPI) and sealed with coverslips using clear nail varnish.

2.2.4 Microscopy and image manipulation

To visualise cultured cells standard phase contrast microscopy was used. For the acquisition of fluorescence images a number of systems were evaluated. The two principal methods evaluated for the visualisation of fluorescently staining cells were widefield fluorescence microscopy and confocal laser scanning microscopy.

2.2.4.1 Phase Contrast

For routine monitoring of cultured cells and cell counts an inverted Olympus phase contrast microscope with 4 and 10x objectives was used. To acquire images a JuLi Cell analyser (Montreal-Biotech) microscope with 4x objective and 10x digital zoom was used. Images were transferred directly to the computer via memory card. A stage graticule was used to identify the pixel aspect ratio of 0.746pixels/μm.
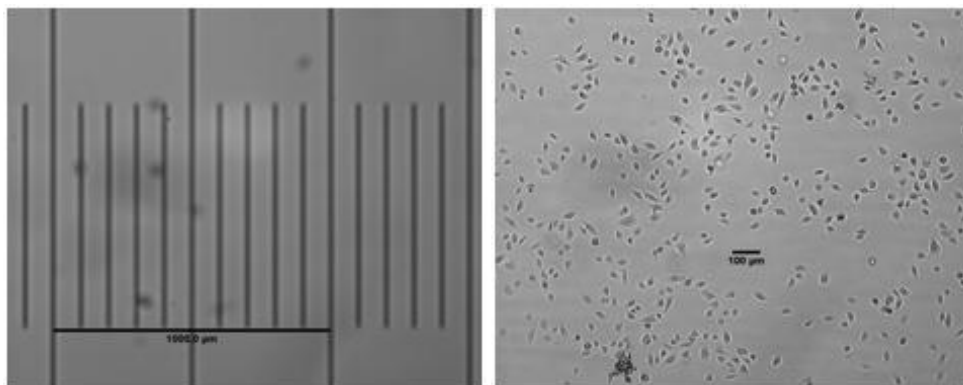
Figure 2-5 Phase contrast images of graticule and HBEp cells
Images taken from JuLi cell analyser showing calibration of scale using stage graticule (left) and primary human bronchial epithelial cells (right), bars show 1mm and 100μm respectivley.

2.2.4.2 Widefield fluorescence microscopy

A Zeiss Axiovert 200M microscope with 100x (NA1.4) Neofluor oil immersion objective and 14bit CCD monochrome camera was used with appropriate filter cubes (Zeiss). For fluorescence a UV arc lamp bulb (HBO100) and neutral density filter number 1 were used. Alignment of the UV light was checked prior to image capture for each experiment. Image acquisition was performed using Axiovision v4.6 software. For each experiment, exposure times for images were defined by sampling the

intensities of 10 images for each slide in an experiment to ensure no images were overexposed. Once exposure times were established, nuclei were sampled at random. Image stacks were acquired with 10 focal planes either side of a central slice defined by the operator. A typical image stack from slides with 70% confluent cells contains approximately 5 nuclei.
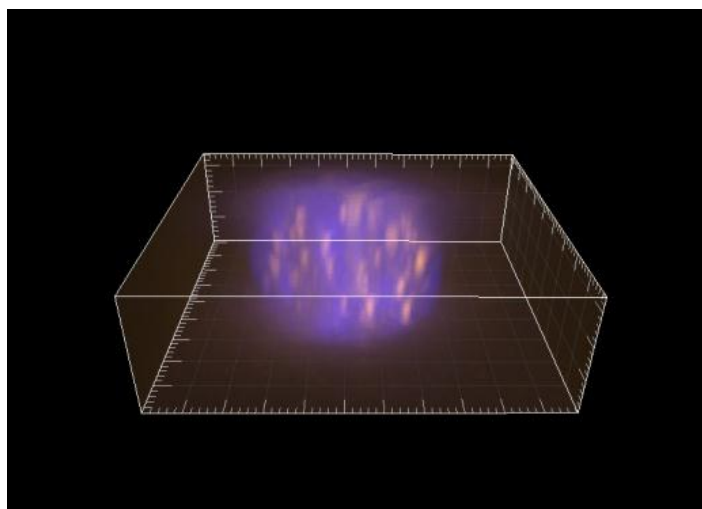
Figure 2-6 Widefield Image stack of 53BP1 foci in HBEp
Cropped image stack of HBEp after exposure to 2Gy γ-rays. Chromatin has been stained with DAPI (Blue) and 53BP1 labelled with AF555 (orange), graduated squares are equal to 2µm.

2.2.4.3 Confocal laser scanning microscopy

An Olympus EC-1 confocal laser scanning microscope (CLSM) was also tested for acquisition of 3D image stacks. A nikon 100x (NA1.4) oil immersion objective, Confocal scanner (Nikon), red green and blue lasers (Melles Griot) were used to acquire images in 'NIS elements' software. Prior to image acquisition several critical variables were tested and optimised.

To optimise image acquisition HBEp cells were irradiated with 2Gy γ- rays from the Brunel University high activity ^{60}Cobalt source and labelled for 53BP1 as described previously. The intensity of the resulting foci and the signal to noise ratio were evaluated in conjunction with the rate of data acquisition. Table 2-1 shows the optimal settings for acquisition of image stacks from the CLSM.

Table 2-1 Settings for optimal confocal image acquisition of foci

Setting	Description	Optimal setting
Average	Repeated scans of the same focal plane are average to provide a smoother image and reduce noise.	x4
Frame lambda	Acquires colours independently to negate the effects of overlapping excitation and emission wavelengths	off
Z-stack step size	Distance between focal planes	0.2µm
Density filters	Neutral density filters reduce the intensity of each laser	Red-No, Green-No, Blue-4
Pixel dwell time	The speed at which the laser scans, a long pixel dwell time will be more sensitive, shorter times are faster	minimum
Resolution	The dimensions of the image in pixels, can be up to 1024x1024	512x512

Images were saved as a Nikon .ics files and imported directly into Imaris for analysis. A typical image stack, containing only one nucleus, would take approximately 10min to capture, including the time taken to scan to the next field of view. This system was deemed inefficient in comparison to widefield due to the limit of only one nucleus per image stack and the relatively high photobleaching compared to the widefield system. The Confocal system also introduced higher signal to noise, often visualised as 'salt and pepper'. Although the system offers improved axial resolution, for the purpose of this investigation, the time constraints limit the viability of using CLSM for high throughput analysis.
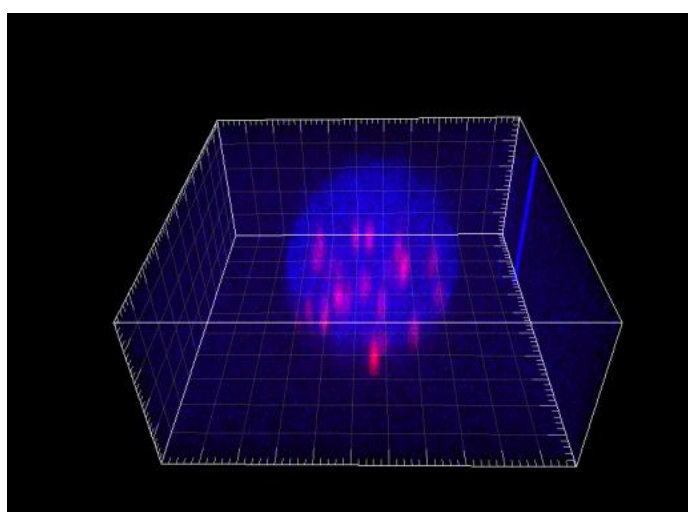
Figure 2-7 Confocal image stack of 53BP1 in HBEp.
Chromatin has been stained with DAPI (Blue) and 53BP1 labelled with AF555 (red), graduated squares are equal to 2µm

2.2.4.4 Deconvolution of widefield image stacks

Images acquired by CLSM or widefield microscopy enable objects to be visualised in three dimensions. With CLSM the axial resolution is improved by the pinhole aperture, objects appear more rounded and are likely to be more accurately represented. However, the system is relatively slow to acquire images and the high intensity of the laser rapidly bleaches the sample making quantification of fluorescence difficult.

In comparison, widefield microscopy is far more rapid and has reduced bleaching effects. However, 3D axial resolution is compromised by light from above and below the focal plane. The typical hourglass appearance shown in Figure 2-8 is due to light from multiple focal planes being transmitted to the focal plane being captured. Deconvolution reduces this effect through correction of pixel intensities.

Figure 2-8 Z-section of a nucleus with 53BP1 foci.
A single focus can clearly be seen with an elongated z-axis and flaring to the top and bottom. 5 other foci are also seen but are not central to this plane

Deconvolution was evaluated on widefield image stacks of HBEp cells in Imaris (Bitplane). Four deconvolution algorithms were evaluated to assess which, if any, were suitable for use in foci counting, for a detailed review of deconvolution methods see (Sibarita and Rietdorf, 2005). For comparison a similar sized nucleus with approximately the same number of foci was captured on a CLSM. Without deconvolution there is higher background on the foci channel, foci appear to be elongated along the z-axis but the

nucleus remains relatively spheroid. Iterative deconvolution removes background and effectively 'rounds off' the nucleus but has little or no impact on the shape of foci. Fast-iterative deconvolution has even more improved signal to noise for foci but nuclear morphology is not improved. The inverse filter algorithm was shown to have a dramatic effect on nuclear shape, as with previous algorithms foci morphology was not significantly altered but background was reduced. Finally, the nearest neighbour methods was tested, this had nominal impact on nuclear of foci morphology but showed some reduction in background (see Table 2-2), .

Table 2-2 Comparison of deconvolution algorithms.
Images taken on a widefield microscope in 3D (second row) were modified using four different deconvolution algorithms and compared to confocal images (top row).
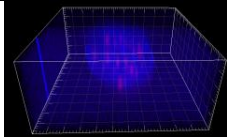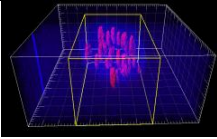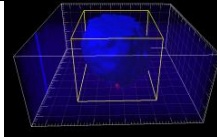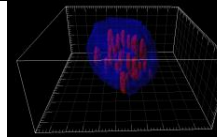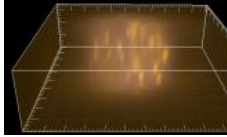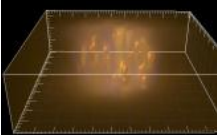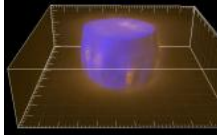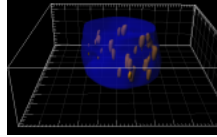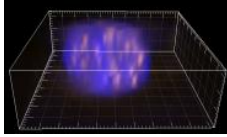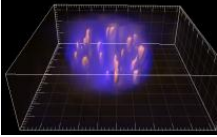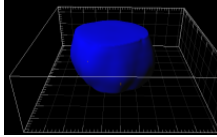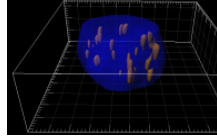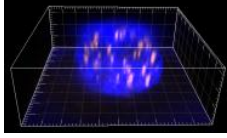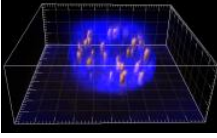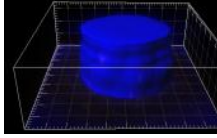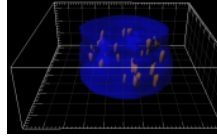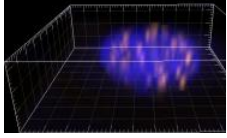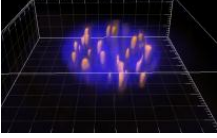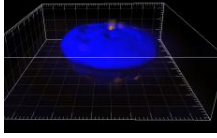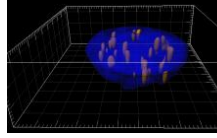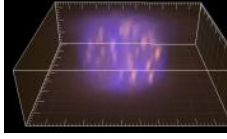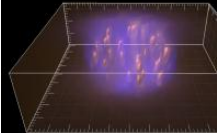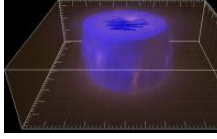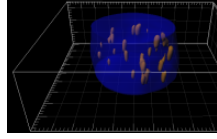
	Volume only	Volume & Surface for foci	Foci & nuclear surface	50% transp. nucleus
Confocal				
Raw				
Iterative				
Fast				
Inverse				
Nearest				

Image deconvolution was dismissed on the following grounds: Data is being manipulated and the exact function of each algorithm is too complicated to consider its effects on experimental data. As this investigation relies on the difference in pixel intensities for quantification of foci, it would be unfair to manipulate the data. For manual analysis of images the operator can become adept at identifying foci. Out of focus data is often easily discriminated from the focal plane and dismissed in 3D image stacks, therefore deconvolution was not a necessity. The remaining signal that could not clearly be identified were not significantly improved after deconvolution and as a result the benefit to deconvolution was considered nominal. Finally, the time, depending on the algorithm, it takes between 10 and 30min to deconvolve a single image stack. This effectively increased the time of an experiment to an impractical schedule.

2.2.4.5 Widefield live cell fluorescence

To visualise cells at high magnification glass bottom dishes (nunc) with coverslips bases (size 0.17) were used. Cells were seeded as for formal cell culture. To effectively visualise the early response to radiation cells were irradiated and transported on ice. For Live cell imaging an incubation chamber (Zeiss) was placed over the heated stage (37°C), 5% CO_2 was maintained through a heating regulator (Pecon), this requires 2-4hr to stabilise before use. Images stacks of 6µm depth at 1µm step size were taken using a Neofluor 63x oil immersion objective (Zeiss). Images were taken using FITC channels to observe fluorescence. Images were captured every 5min for 24hr or until fluorescence was eliminated. During the initial stages of time lapse imaging the focus will drift due to shifts in temperature. To maintain focus, the operator should observe the microscope and ensure the images are approximately within the focal range of the z-stack. Neutral density filter number 2 was used to preserve fluorescence and reduce photo-toxicity and capture times were kept to a minimum by using only a small portion of the cameras dynamic range.

2.2.5 Statistical analysis

Data was recorded into Excel (Microsoft) spreadsheets. The functions formulas were used to generate statistics, brackets would contain references to cells or arrays of cells used to generate the relevant statistic.

Statistic	Formula
Mean – Used to identify the typical number of foci in a nucleus from the population	=AVERAGE()
Standard Deviation – the average variance to the mean	=STDEV()
Frequency distribution – used to identify the number of nuclei with a specific number of foci	=FREQUENCY()
Students t-test – to test for significance between means	=TTEST()
Correlation – to identify	=CORRELL()

Where graphs show error bars this shows the standard deviation of the replicates.

Calculation of cell doubling time: Total population doublings (Td) is calculated based on the initial seeding (q1), resulting number of cells (q2) and the time between seeding (t2-t1).

$$Td = (t2 - t1) * \frac{\log 2}{\log\left(\frac{q2}{q1} \right)}$$

Calculation of nearest neighbour distance: The nearest neighbour distance is calculated based on proximity of units, which is calculated from the density (p), distance between each unit (r) and the number of measurements taken (N). The value 0.55397 is specific to the number of dimensions the units are distributed in (Clark and Evans, 1954, Clark and Evans, 1979).

$$R = \frac{rA}{rE} \qquad rA = \frac{\Sigma r}{N} \qquad rE = \frac{0.55397}{p^{1/3}}$$

3 Development of analysis methods for the quantification of radiation induced foci

3.1 Introduction

To reliably quantify radiation induced foci (RIF) there must be a clear definition of what actually constitutes a 'focus'. A RIF can be described as a peak of signal intensity, distinct from the background and therefore displaying a strong signal to noise (S:N) ratio. Factors that can reduce this S:N ratio include poor immunofluorescence staining (as a consequence of the antibody employed or poor technique), auto-fluorescence within the sample, the number and distribution of foci (whereby individual RIF overlap) and the optical system used. Further, counting of RIF is typically achieved by manual analysis either through the optical binoculars of a fluorescence microscope or by taking images and counting the RIF on a screen (Rothkamm and Lobrich, 1999, Paull et al., 2000, Riballo et al., 2004, Stiff et al., 2004, Desai et al., 2005, Torudd et al., 2005, Hamada et al., 2006, Krawczyk et al., 2006, Rube et al., 2008). Thus, additional factors that can influence the efficacy of RIF scoring include operator skill and/or image resolution.

Our understanding of the biology of RIF may reflect is growing such that it is now accepted that the number of foci quantified in each nucleus alone is a poor parameter of a cells response to DSBs and that a combination of number, size and signal intensity (at least) should be considered (Ishikawa et al., 2010). For instance, the 1:1 relationship between RIF:DSB is challenged whereby individual RIF may actually represent multiple proximal DSB or clustered DNA damage (Costes et al., 2007). In addition, given that DSB are the precursor lesion for the formation of chromosome exchanges then it is important that we understand the spatio-temporal aspects of each RIF, relative to each other, within individual nuclei if we are to gain insight into this important mechanism of genomic alteration. Thus, the aim of this chapter was to

develop a rapid, high-throughput method for the automated quantification of the number, size/volume and relative 3D distribution of RIF within individual nuclei.

3.2 Development of methodology for manual analysis of RIF

The scoring of foci directly through the binoculars of the microscope is the most rapid and simple method for scoring RIF. However, this method requires the operator to be experienced in 'true' RIF identification, is prone to error and is limited in effectual quality checking (both within and between laboratories). This is particularly relevant when the objective of each experiment is to accurately quantify and categorise the varying sizes of foci observed, in a single plane or across multiple focal planes, in samples that may be of varying S:N ratio. For instance, the likelihood that the same criteria will be consistently applied to appropriately assign foci according to the established size categorisation will vary between the same and different operators and also, will vary as the number of foci in each nuclei increases.

Greater accuracy can be achieved by manually analysing digital images of nuclei whereby RIF counting, categorisation and checking of scoring is based on measuring pixel size of saved images on a computer screen. The main issues that may impact on the resolution and therefore robustness and reproducibility of such scoring are outlined in the introduction, in addition to these limitations, the display adjustment on the analysis computers must be setup correctly to ensure the colours and brightness are optimal and consistent between experiments. For instance, if the contrast is too low, then dimmer foci might be omitted from the dataset despite clear signal being present on the original image. The optimal setup for a standard computer is to achieve the widest bit depth of 256 per pixel, commonly known as Truecolour (Microsoft) or Millions of colours (Macintosh) and is achieved by using a colour scale as described in Figure 3-1. Each square within the scale should be clearly distinct from its neighbour, if not then the brightness, contrast and hue must be altered.
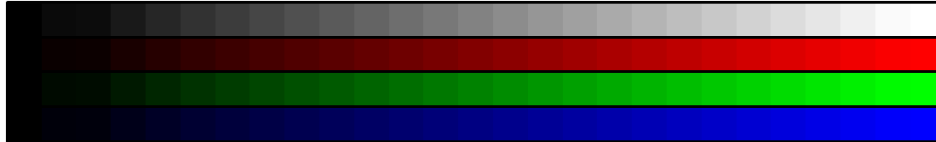
Figure 3-1 Colour scale used to adjust visual display units
The scale shown has 100% intensity for blue, green red and combined colours (white) at the far right. The intensities for each of these is then decreased by 5% until pixel values are zero (black). Each step should be clearly distinct to its neighbour.

3.2.1   Assessment of 2D & 3D images for quantification of foci

To assess if sufficient data could be obtained from single 2D images, as opposed to image sacks (3D), image stacks of HBEp cells and AGO1522 cell cultures irradiated with 2Gy γ-rays (dose rate ~0.33Gy/min) were captured on a widefield microscope at 0.5µm intervals. For 2D analysis; only the central focal plane was analysed. Counting only the central plane (2D) allowed for rapid scoring of foci but a large proportion of foci were difficult to classify as their outlines and signal intensity were fainter due to the narrow depth of field. For 3D analysis; the z-slice slider was moved to allow a general appreciation of the nucleus. The numbers of foci were then counted, working from the top of the image to the bottom. Figure 3-2 illustrates this point by comparing a single image of the nucleus compared to a maximum intensity projection in which multiple focal planes have been collapsed into a single image for visualisation only, these would normally be counted independently.
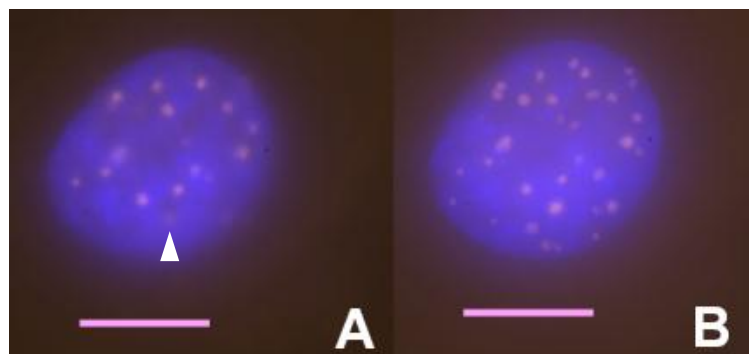
Figure 3-2 Comparison of 2D and 3D image
A representative image from a single focal plane of HBEp cells (A), a total of 13 foci were counted. Arrow indicates an example of a focus beyond the depth of field for that image. The same nucleus was then captured in 3D by acquiring a series of images from different focal planes. A maximum intensity projection (MIP) of the stack was then generated to show the proportion of foci from other focal planes (B). A total of 30 foci were counted.

Although it is not possible to categorise the out of focus (OOF) foci, labelled in Figure 3-2, it is possible for the user to make an estimate of what could be a focus just beyond the depth of field for that image. If these estimates are omitted the difference between manual 3D and 2D counts are nearly 4 fold. However, if included the count is consistently within 75% of the 3D count, see Figure 3-3.
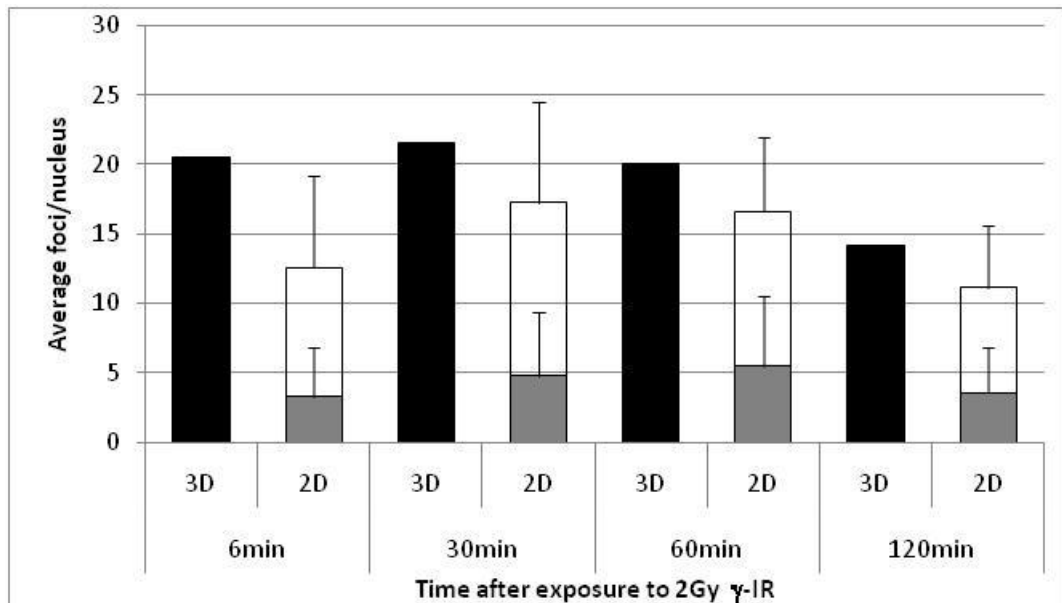
Figure 3-3 Comparison of foci scores form 2D and 3D analysis
Single images and image stacks were counted for AG01522 fibroblasts with 53BP1 foci immunofluorescently labelled. Black bars indicate the average number of foci per nucleus counted from a 3D image stack, grey bars indicate the average number of foci counted from the central focal plane of the same stacks omitting out of focus estimates, white bars show averages including estimates.

For the quantification and qualification of foci staining for 53BP1, manual 2D counting is sub-optimal in comparison to manual scoring of an image stack, as the estimated foci size cannot be measured. Therefore for accurate and reproducible counting of foci, including data on their size, 3D scoring is essential. Counting of maximum intensity projections is also viable but all axial data is lost and therefore if independent foci from different focal planes overlap, they are likely to be counted as a single focus.

3.2.2 Manual 3D quantification of foci size

To measure the size of foci the scale for the image must be known. This is measured in microns/pixel and can be calculated using a slide reticule. Most modern integrated microscopes utilise pre-calibrated software to allow for measurements to be taken directly from the images. The microscope used for manual analysis has a pixel resolution of 0.07µm/pixel at 100x magnification. After viewing a number of images and observing the relatively narrow range of foci diameters, three size integers were established corresponding to <0.5µm (small), 0.5-1.0µm (medium) and >1.0µm (large). To categorise RIF into size integers an acetate sheet with two scaled circles corresponding to 0.5µm and 1.0µm was used. Manual analysis for quantification of RIF was then conducted on coded slides using Axiovision software (Carl Zeiss v4.7) to view the images. RIF from multiple focal planes were counted and categorised according to size by scrolling up and down through the image stack, whereby the most in-focus area was used to determine size (diameter). Where RIF had indiscriminate edges or were not sharp enough to discern a boundary, they were classified as being "out-of-focus" (OOF).

To assess the reproducibility of the manual analysis method, HBEp cells irradiated with 2Gy γ-rays and fixed after 30min were scored for radiation induced 53PB1 foci using the manual 3D method described and then re-counted (blind).
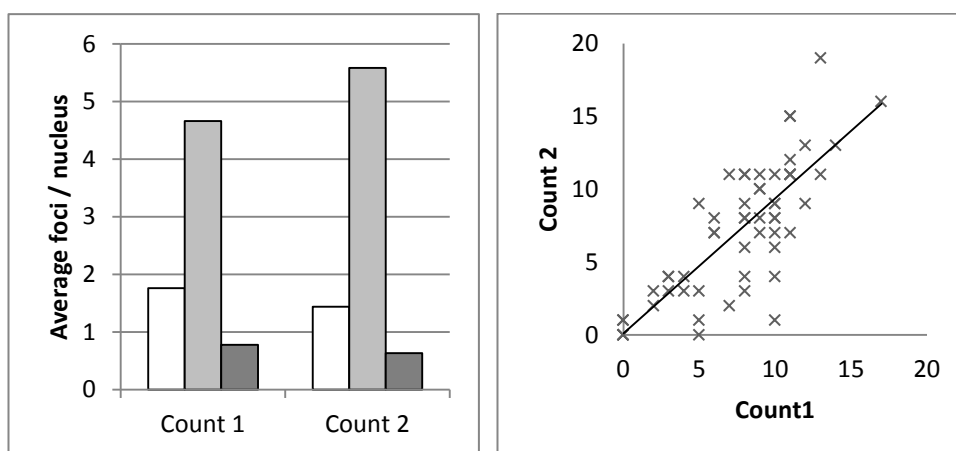
Figure 3-4 Reproducibility of manual scoring method
As part of a larger experiment, a single time point was copied and coded, to ensure no operator bias, and counted in parallel to the other time points (repeat of count).

53

A repeated count by the same operator yields similar results with a 1:1 relationship (correlation coefficient = 0.793) between initial and repeated counts, see Figure 3-4. Discrepancies in the averages are not statistically significant (P<0.05). Subtle factors like ambient light in the room will affect the relative intensity of foci on screen and cause changes in reproducibility. Comparisons between counts from different operators for the same images also show deviations, this can often be corrected by training the operator to recognise biological and microscopy artefacts such as debris under the coverslip or in the immersion oil, focal drift during acquisition, poor mounting of the sample, apoptotic nuclei and S-phase or dividing nuclei. With sufficient training, an operator can process a large number of images and allocate foci into size categories using the manual method. However, depending on training, inter-lab differences could vary greatly and data on size is limited to categories.
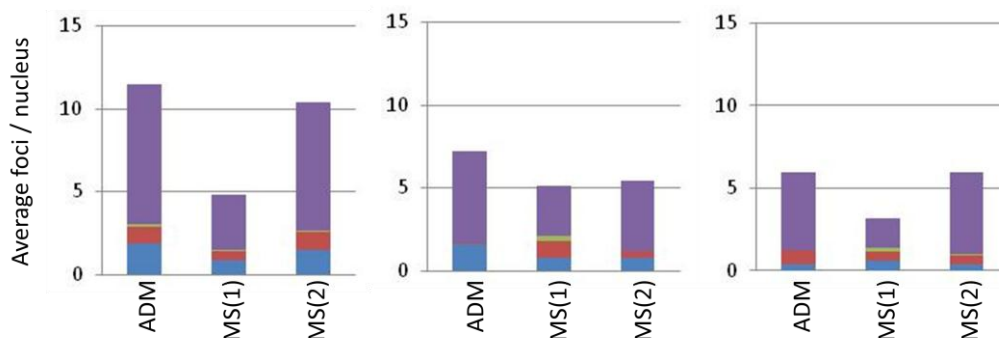
Figure 3-5 Comparisons of manual counts from different operators
Comparison between counts from an experienced user (ADM) and a new user (MS1). After identifying possible causes for deviations a second blind count was made (MS2).

3.3 Digital image analysis of radiation induced foci

To obtain more qualitative data and at a faster rate, several automated analysis methods were evaluated. The aim was to utilise software to automatically identify, count and measure foci within nuclei within a short time frame

3.3.1 Evaluation of pre-existing software

Images that had previously been captured and used for manual analysis were re-analysed and compared on the basis of data output, ease of use and speed of analysis. There have since been advances in the number of tools available but the applications investigated here encompass all the technology available for the purpose of foci counting at the time of study.

3.3.1.1 Imaris

Imaris (Bitplane, Switzerland) is software designed with an emphasis on rendering and measurement of 3D and time lapse microscopy images, as well as performing other tasks, such as object tracking (chapter 5). The software version available did not support batch processing and therefore the user must input multiple commands for each image. In addition, the only option for the identification of foci was through intensity thresholding. Once foci were identified, to calculate volume (size), foci were rendered using another "local" threshold. Rendering was not performed in real time and was time consuming, see Figure 3-6. Where foci were seen to overlap the user could manually isolate foci from each other. In more sensitive samples where background approximates what could be considered a focus signal, thresholding alone was not sufficient, see Figure 3-7. Furthermore, the software requirements limited the number of images that could be processed at any one time.
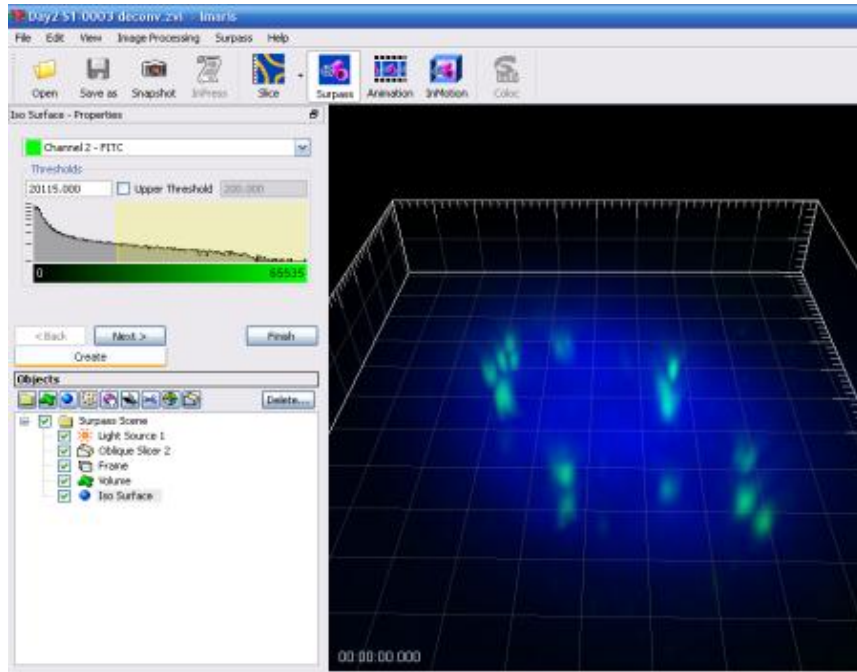
Figure 3-6 Screenshot from Imaris for foci counting
Iso-surface rendering in Imaris through application of intensity threshold (left), NB the
threshold is not applied to the image until the finish button is selected.
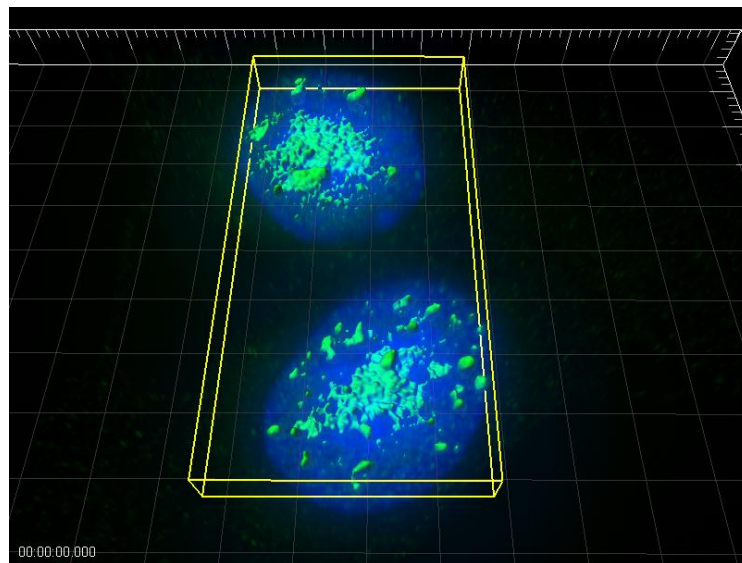
Figure 3-7 Rendering of 53BP1 foci in Imaris
Rendered image of two HBEp cells with chromatin coloured blue and 53BP1 foci in
green. This image illustrates that when the threshold is reduced to isolate the smaller foci
a large amount of noise is also identified.

To generate a single processed image took in excess of 15min/stack. This
method proves to be useful for generating high quality images and
quantitative data for single nuclei, such as live cell imaging data (chapter
5) (Asaithamby and Chen, 2009), but was not suited for high throughput
analysis and therefore was dismissed.
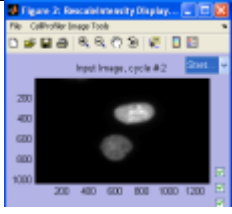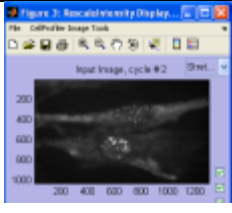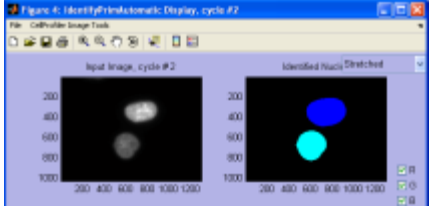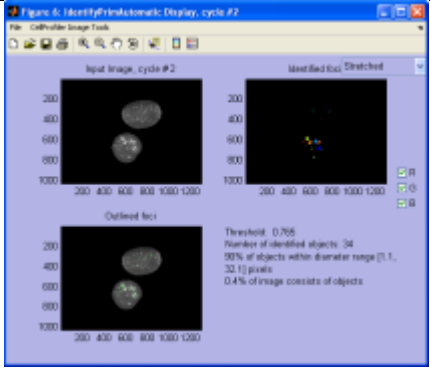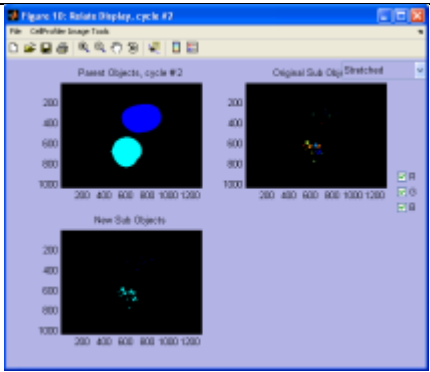
3.3.1.2 <u>Cell Profiler</u>

For the rapid throughput of images a more customised analysis package was tested. Cell profiler is a freely available image analysis tool with a user friendly interface which does not require any substantial knowledge of computing but will need a good understanding of image analysis (Carpenter et al., 2006). The system relies on the user generating or modifying "pipelines" whereby images are opened, objects identified and measured in a loop until an entire folder of images has been processed. An existing pipeline was modified to count foci in HBEp cells, Table 3-1 shows the modified pipeline.

The Otsu threshold (Otsu, 1979) was applied to identify the nucleus and subsequently used as a mask to exclude signal from outside the nucleus being scored as a focus. This threshold relies on stark contrast between signal and background and is well suited to the identification of DAPI signals but is likely to merge nuclei if they are too proximal. The Kapur (Maximum entropy) threshold (Kapur et al., 1985) appears to effectively identify most foci with minimal other processing. A range of data for multiple images can then be exported into a spreadsheet for further analysis. The advantages of Cell Profiler are that more data can be obtained and compared to manual analysis and significantly less user input is required compared to Imaris. However the main issue with this system that could not be resolved were that the pipelines were optimised for 2D images, which for this investigation has already been shown to be a sub-optimal measure of foci and the Kapur threshold often resulted in background being counted as foci therefore, the system was not sufficient to accurately count foci.

Table 3-1 Workflow of image processing using Cell Profiler

IMAGE(S)	PROCESS
	Raw image of nuclei opened (C:\...**c2**)
	Raw image of foci opened (C:\...**c1**)
	Otsu threshold applied to identify nucleus.
	The nuclear threshold region is then used to crop the foci image to exclude non-nuclear signals. The Kapur per object threshold is then applied to the cropped image to identify foci.
	Foci are then related to the nuclear 'parents' to identify how many foci per nucleus.

To aid identification, foci images ended in the identified c1 whilst DAPI images end in the identified c2.

3.3.1.3 Image J (formerly NIH image & Scion Image)

ImageJ supersedes NIH Image for Macintosh and Scion Image for Windows. It is an open source image analysis tool that supports user macros and development in addition to just being used to open images for analysis by eye (Bouquet et al., 2006, Markova et al., 2007, Su et al., 2010). Plug-ins have recently been released specifically for foci counting, but these lack the level of automation required for high throughput analysis or lack 3D processing (Du et al., 2011). A custom plugin was attempted using the macro function built into the programme. Several different segmentation 'plug-ins' were downloaded and tested to identify foci without user input, these are referred to as dynamic thresholds as their values are volatile (change with the histogram), see Figure 3-8.
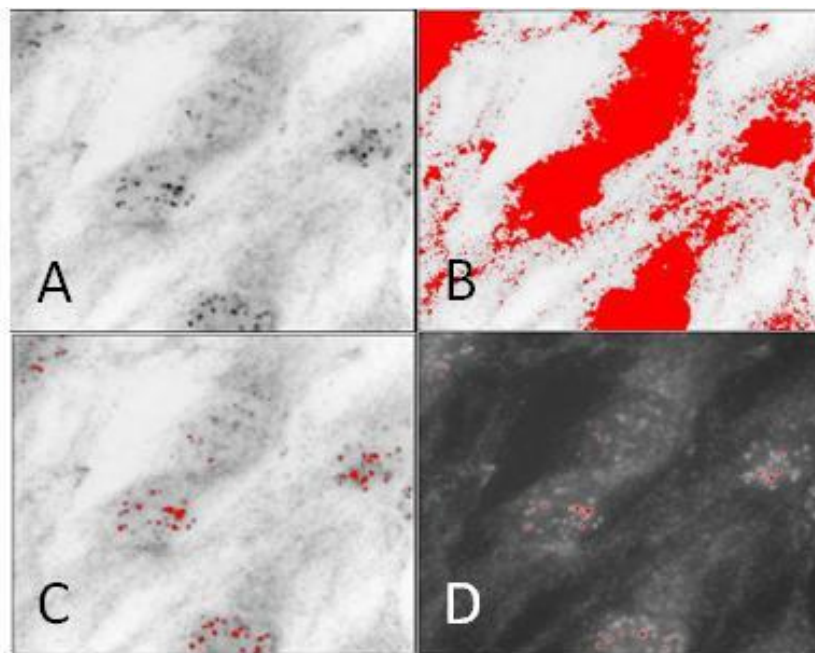
Figure 3-8 Comparison of three dynamic thresholds
Raw image has been inverted for clarity (A), red highlighting shows Otsu threshold (B), maximum entropy threshold (C) and threshold from background (D)

The Otsu threshold was found to reliably identify the nucleus (based on a DAPI image) with limited processing (as was shown with cell profiler). The maximum entropy threshold was also effective at identifying most foci, see Figure 3-8-C. The most useful aspect of ImageJ is the capability to write macros that enable the user to perform a series of actions as opposed to pre-determined processing steps. This allows for multiple image
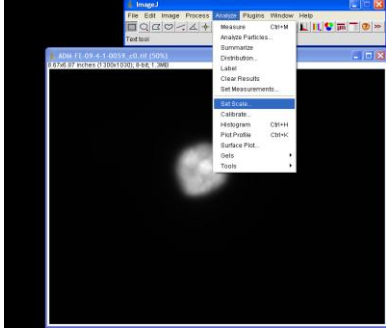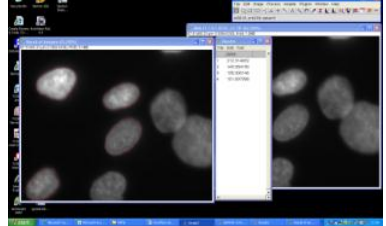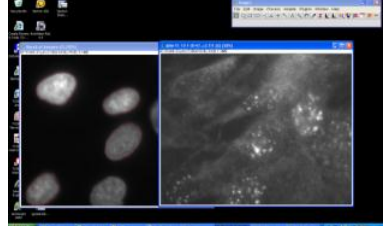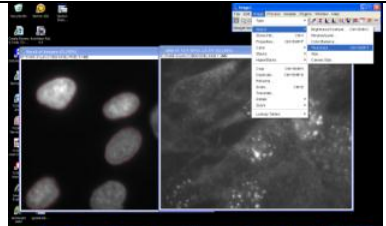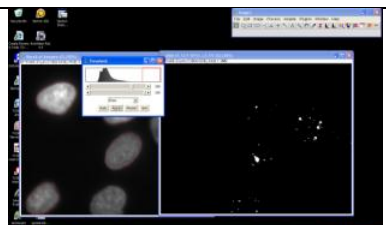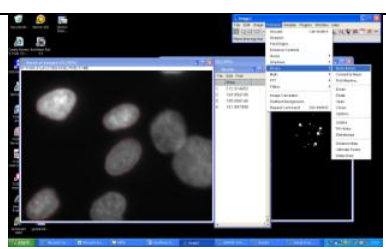
processing steps to be carried out as a workflow, see Figure 3-9 and Table 3-2. This workflow was made into a series of three macros which were given shortcuts on the menu tab thus cutting manual input to a minimum, see Figure 3-10. However, this still relied heavily on the user being present throughout to generate the results.
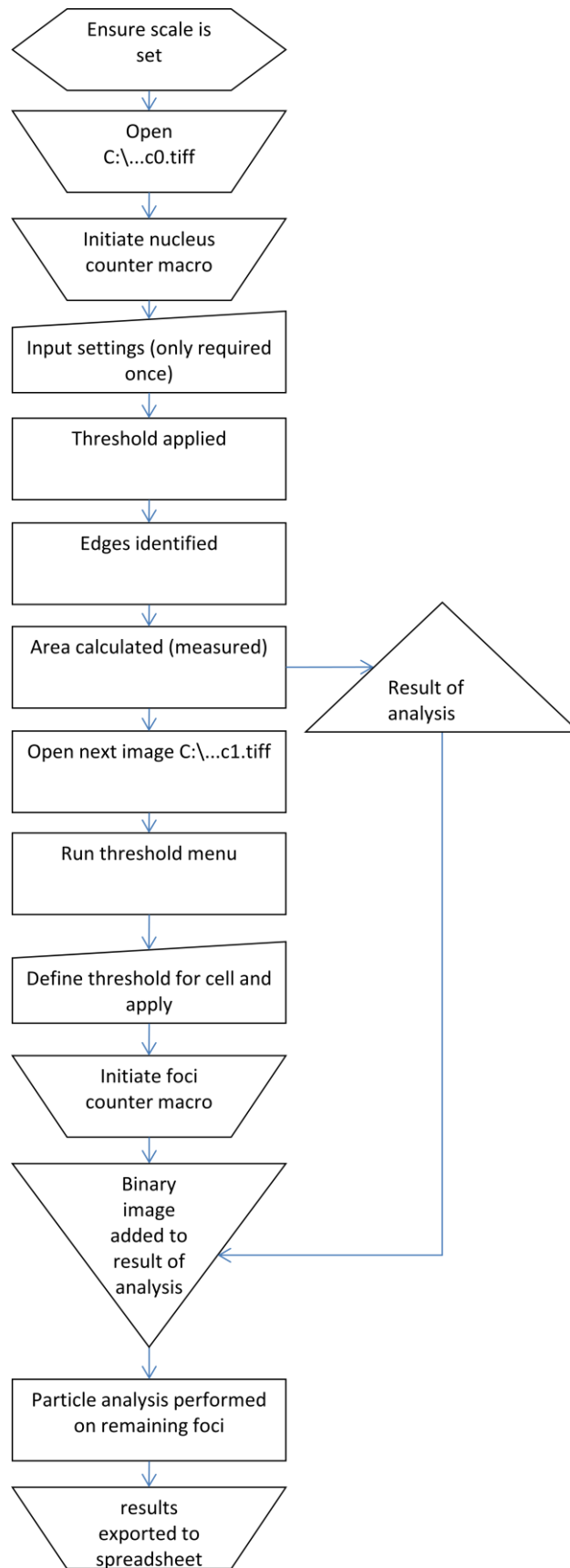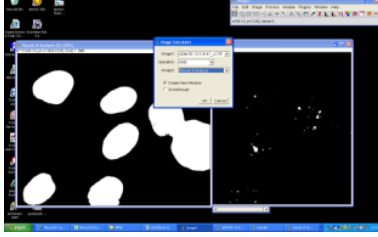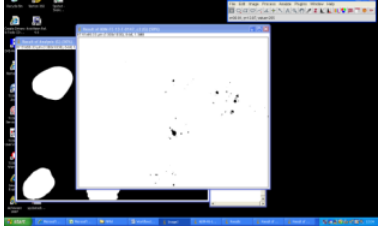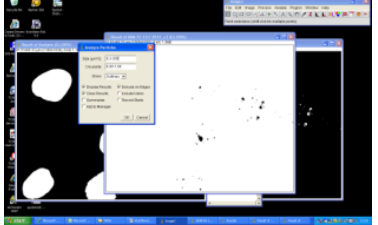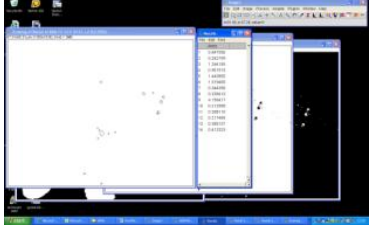
Figure 3-9 Workflow for ImageJ analysis method.
Typical flowchart shapes have been used, hexagon=preparation, trapezoids=manual operation, cut rectangle=manual input, up/downward triangles=extraction and merge.

Table 3-2 processing steps for ImageJ analysis

IMAGE(S)	PROCESS / DESCRIPTION
	Open DAPI image, name ending in identifier "...c0.TIF" Under analyse, set scale must be selected for any measurements; this need only be set at the beginning. Set Scale (14.856µm/pixel), ensure global is highlighted.
	Run the nucleus counter plugin to obtain nuclear area results. Areas are then copied into an excel spreadsheet.
	Open next is selected to open the image, which should be the same name but ending in the identifier "...c1.TIF".
	Image ↵ Adjust ↵ Threshold is selected to manually set the threshold for that image.
	Threshold is then applied to image to make it binary
	The Result of analysis window is made binary.

	Processes ↵ Image calculator is used to AND the two images (Result of analysis and threshold image)
	Combined image is inverted to make black spots for counting.
	Analyse ↵ Analyse particles is selected to measure the area and number of spots.
	Results are then exported into an excel spreadsheet, excluding those not inside a nucleus being measured. This step still requires user input

```
// START MACRO 1
run("Nucleus Counter", "smallest=20 largest=200 threshold=Otsu smooth=[Mean 3x3]");
run("Open Next");
run("Threshold...");
// OPERATOR SETS THRESHOLD AND INITIATES MACRO 2
selectWindow("Result of Analysis");
run("Make Binary");
run("Image Calculator...");
// OPERATOR SELECTS NUCLEAR IMAGE AND FOCI IMAGE FOR CONCATENATION
run("Invert");
run("Analyze Particles...", "size=0.20-50.00 circularity=0.00-1.00 show=Outlines display exclude
clear");
run("Image Calculator...");
// OPERATOR SELECTS DRAWING OF RESULT OF ANALYSIS AND NUCLEAR THRESHOLD
IMAGES FOR CONCATENATION AND INITIATES MACRO 3
close();
close();
close();
close();
run("Open Next");
```

Figure 3-10 Macros used in ImageJ for analysis
Forward slashes denote non-coding text, within this text are the macro numbers (1-3).
The three macros are run concurrently as at the end of each cycle the next image for
analysis is opened.

Despite being a faster method, the analysis was still limited by the restriction to 2D images and the accuracy of the threshold. To resolve the issue, a collaboration was initiated within Brunel University with Dr Simon Kent (Department of Information Systems and Computing). A new macro was generated that would automatically analyse the contents of a folder and save the results into another folder specified by the user. By cutting out the need for user to have any input, the speed of analysis was greatly increased. Batch processing also increased the speed at which images were opened as the graphics processing was greatly reduced. Unfortunately, the macro would often "fall over" and the results were often not an accurate count due to the threshold being incorrect or background being counted.

3.3.2 Development of in-house automated analysis system

The above mentioned collaboration was continued to develop a specific automated analysis system capable of identifying foci in 3D image stacks with high fidelity and exporting data on number, size and relative distribution with minimum user input.

3.3.2.1 Methodology

The approach taken to identify nuclei was based on Otsu's method of automatic image thresholding (Otsu, 1979) whereby a binary mask for each acquired image is created that effectively removes all information from outside the nucleus. A modified version of the sequential region labelling algorithm assigns x/y positional data for each nucleus within the image where the largest bounding rectangle in each image stack is used to crop the nucleus. Any nuclei below a thousand pixels, or lying on the boundary of an image, were excluded enabling image stacks of individual nuclei to be processed for the identification of RIF. This was achieved by converting each 2D greyscale image (Figure 3-11-A) within each nuclei stack into an intensity mesh (Figure 3-11-B), before combining all of the 2D parameters generated as a consequence of this, for the reconstruction of the 3D parameters for each RIF.
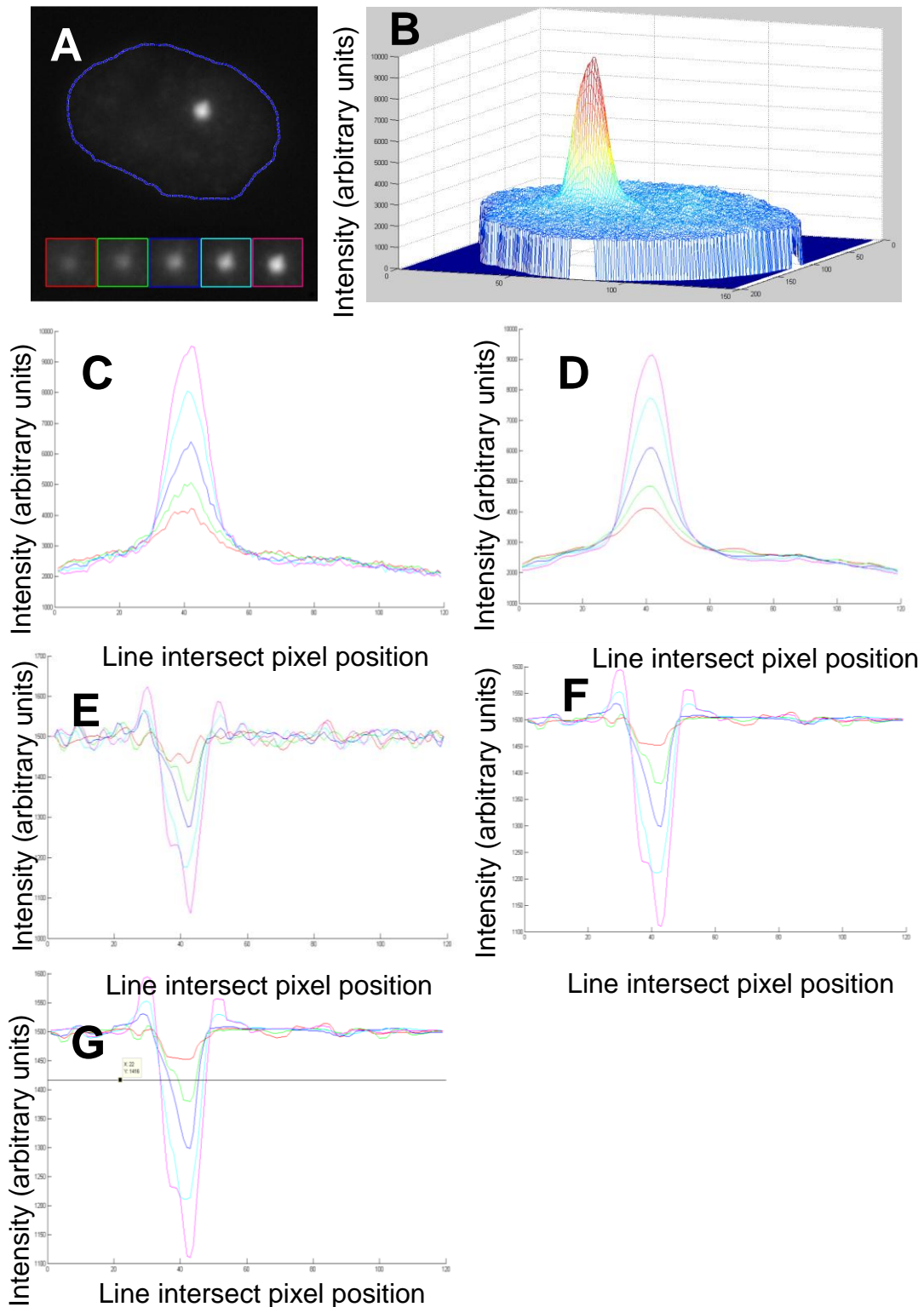
Figure 3-11 Image processing for automated analysis

A single slice (2D) grey-scale image showing a nucleus, blue dashed line, with a single RIF. The RIF has been highlighted to show its appearance in subsequent slices and are colour-coded to C-G (A). The same image is shown as a 3D intensity mesh in (B). The intensity mesh is also shown for a single axis with coloured lines for the most central focal plane (n=magenta) and the 4 focal planes at 0.5um intervals beneath (C). The same intensity mesh after filtering (D) shows reduced noise. A laplacian operator is applied (E) to identify boundaries and a normalisation value of 1500 is added to ensure RIF values do not fall below zero. A final filtering step removes noise (F). Finally a maximum entropy threshold is applied to identify RIF (G).

A modified Hessian operator was applied to remove high-frequency noise (Figure 3-11A), which gives the effect of smoothing the plots to allow accurate RIF dimensions to be extracted. This step does not effect the mask outline made from the DAPI channel but does remove the noise (Figure 3-11 C and D). Next, the Laplacian transform operator converts the smoothed image such that intensity peaks are translated into troughs or concavities (Figure 3-11 E). Although there are fluctuations in curvature of the plot these can easily be distinguished from the RIF. Any noise which escapes the smoothing phase would have been amplified by the application of the Laplacian operator therefore, to remove any artificially enhanced noise from the 'Laplacian' image, the Crimmins filter was used. This brightens pixels that are significantly darker than their neighbours, whilst it darkens those that are lighter than their neighbours (Figure 3-11 D). The maximum entropy threshold, derived from the data of the whole image stack, is then used to identify the RIF. The resulting binary image then undergoes the morphological closing operation "filling the gaps" in the individual foci.

In order to accurately determine the relative position of RIF within each nucleus, the centre of each RIF needed to be identified. To achieve this, a sequential region labelling algorithm, similar to the nucleus isolation algorithm described in the appendix, was applied. In the main, RIF are of irregular shape, meaning the centroid (centre of homogenous mass) cannot be determined by the intersection of a bounding rectangle (Figure 3-12) as this may incorrectly position the centre of mass of the RIF near the "tail" of the RIF. To account for this, an ellipse was used to bound the RIF whereby ellipse orientation and eccentricity are determined by calculating on the moments of the region. Details of the algorithms used to calculate orientation and eccentricity are outlined in the Appendix.
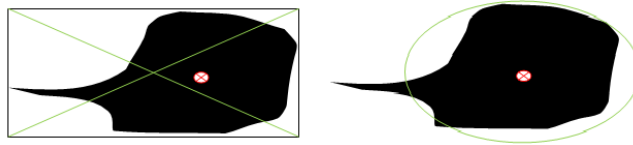
Figure 3-12 Bounding methods for irregular shaped foci
Example of irregular shaped RIF with a bounding rectangle (left) and ellipse (right).The
centre of the RIF is shown with a crossed ellipse.

The 3D parameters of each RIF are related to each other through the
application of a custom algorithm that checks whether RIF lie directly
above or below each other, in neighbouring slices in the image stack. If
two RIF lie above each other at slices N and N+1 and the centre of any of
the RIF lies within the area of the other focus, then these two RIF should
be considered as a part of the whole in 3D. If the RIF lie above each other
at slices N and N+1 but neither has its centre within the area of the other
focus then these two RIF would be considered independent of each other.
Where RIF overlap but are separated by a slice with no RIF they are also
considered independent (Figure 3-13).

Figure 3-13 Diagram illustrating the two foci overlaying each other
Centre of the upper focus lies within the area of the focus below (A) and centre of the
upper focus lies outside the area of focus below (B).

The 3D reconstruction process designed also keeps track of the weighted
average of the z-coordinate for every focus, together with x and y-
coordinates. Since the weighted average utilizes the same concept as
centroid, the output of the procedure is a weighted 3D focus coordinate.
Two Excel spreadsheets (Microsoft) are automatically generated with data
for each focus on each row. Spreadsheet 1 ends in the identifier 'coord'
and contains information on foci size, intensity and coordinates.
Spreadsheet 2 ends in the identifier 'dist' and lists the distance from each
focus in a nucleus to all other foci within that nucleus.

3.3.2.2 Application of automated in-house analysis system

Figure 3-14 details the workflow performed for each experiment. Initially a sample of images is selected from each experiment and used to test the settings for the number of filtering iterations required (Figure 3-14 step A & B). Within this test batch, the optimal settings may vary from image to image, therefore the final settings used for each was determined by the minimum number of filtering iterations that could be used without introducing artefacts. For instance, if too few filtering iterations were used, excessive noise termed as "salt and pepper" (Figure 3-14 (2)) will be seen. Increasing the pre-laplacian filtering iterations dramatically reduced the noise and also smoothed the outline of foci to become more circular (Figure 3-14 (3)). Post-laplacian filtering had a limited effect of reducing the background noise but had less of an impact on the outline of foci. Alteration of the laplacian sensitivity had no effect on the images analysed and so was not changed from its minimum setting. A comparison of the effects of the different filtering steps is shown in Figure 3-15. Once the settings were established the entire experiment was processed (Figure 3-14 - C)
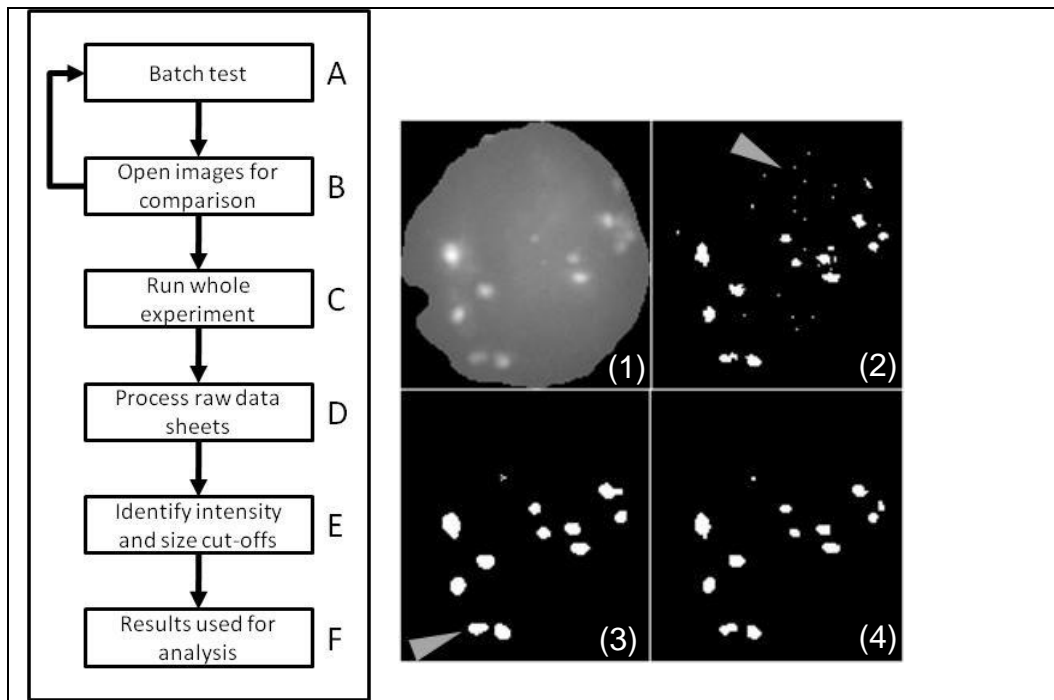
Figure 3-14 Workflow for image processing and analysis
Left shows the process for analysis of images for one experiment. Right identified examples of a raw image for 53BP1 (1), a binary image with insufficient thresholding, an arrow identifies the salt & pepper noise (2), the effects of excessive filtering can result in loss of morphology of foci (3) a compromise between these extremes must be made (4)

A sample of ~10% of all images is used to batch test the software and identify the optimum filtering settings (A). Once processed, the resulting binary images are compared to the originals (B). If the settings result in sub-optimal identification of RIF the batch is re-tested with modified settings, otherwise the entire experiment is processed with those settings (C). The spreadsheets with raw data are then organised and formulas applied to generate statistics (D). Original images, binary images and predetermined size categories are used to identify cut-off values (E) results are then plotted as graphs (F).

This raw data is further processed to categorise RIF by size, volume, intensity, 3D position within nuclei and also distance between each RIF within individual nuclei.

Figure 3-15 Effects of filtering steps for in house automated analysis
Pre-Laplacian, Laplacian and post-Laplacian filtering effects on an image of a single nucleus with 53BP1 foci showing intermediate laplacian image.

3.3.2.3 Analysis of results

Images from a single slide are stored in a folder, as described in section 3.3.2.1. For each folder of images two sheets are generated in an Excel workbook, one for the data on each focus x, y and z position, names "coord", and another sheet with the distances between each focus, named "dist". In both sheets, each row of data relates to a single focus, the image number or name is derived from the folder name it originated from.

To count the number of foci in each nucleus and their relative size a cumulative count of nuclei is made to allow identification of each nucleus independently. This is achieved in Excel, in Column "O" / cumulative nucleus count (Figure 3-16), the first row of data, in this example cell O-3, has the value 1, the cell below contains the formula "=IF(OR(C4<>C3,

B4<>B3), P3+1, P3)". If the image name or nucleus number are not equal to the lines above, the previous nucleus number is reported, if either are different, the nucleus number is incremented by 1. The parameters for the experiment are input to define integer sizes and minimum intensity and focus size (Figure 3-16, Column V). This measurement can be in pixels, microns, voxels or cubic microns. The parameters for size were extrapolated from the arbitrary size integers used in manual analysis, assuming a focus is roughly equivalent to a sphere, the equivalent volume was calculated.

Table 3-3 Conversions of focus diameter to volumes

Diameter (μm)	Radius^3	Volume (μm^3)*	Vol in Voxels
0.5	0.015625	0.065449847	26.714
1.0	0.125	0.523598776	213.71

*The volume of a focus is a theoretical estimate based no foci being spherical.

For the minimum size, a volume of 3 voxels was chosen, this equates to $0.00735\mu m^3$, which is well beyond the limits of resolution and can therefore be assumed to be too small to quantify. The size of each focus is reported in Column P, providing it meets the minimum intensity and size requirement, using the formula: "=IF((AND(K4>W2,I4>W3)),I4)". For comparison to manual data the size of each focus is binned into one of three sizes integers, the total number of small, medium and large foci can then be retrieved from the columns created by finding the maximum number and sum for each respective column. To obtain frequency distributions it is necessary to identify the number of foci per nucleus. In column "X" / nucleus number, a list of nuclei is made up to the maximum number for that sheet. The number of small, medium and large foci for each nucleus is calculated and the statistics are then reported in column "V" on the average number, standard deviation, average size and variance.

IMAGE	NUC NUM	NUC VOL	NUC WIDTH	NUC HEIGHT	NUC DEPTH	FOC NUM	FOC VOL	OVEREXP	INTENSITY	X	Y	Z	Cumulative	Size	Small	Medium	Large
FE-17-andy-	1	835626	238	209	22	1	528		8535	151.02841	68.52841	7.07955	1	528	0	0	1
FE-17-andy-	1	835626	238	209	22	2	200		6117	186.565	65.145	7.71	1	200	0	1	0
FE-17-andy-	1	835626	238	209	22	3	191		5828	204.12565	90.02094	7.27225	1	191	0	1	0
FE-17-andy-	1	835626	238	209	22	4	26		5355	124.	138.	6.	1	26	0	1	0
FE-17-andy-	1	835626	238	209	22	5	60		5521	136.	137.	7.	1	60	0	1	0
FE-17-andy-	1	835626	238	209	22	6	68		4637	111.5	142.5	7.5	1	68	0	1	0
FE-17-andy-	1	835626	238	209	22	7	135		5098	61.45185	73.15556	9.2963	1	135	0	1	0
FE-17-andy-	1	835626	238	209	22	8	375		7169	36.78133	71.42667	10.78133	1	375	0	0	1
FE-17-andy-	1	835626	238	209	22	9	16		4359	171.	34.	13.	1	16	1	0	0
FE-17-andy-	2	594792	196	185	22	1	80		7574	154.95	57.525	4.525	2	80	0	1	0
FE-17-andy-	2	594792	196	185	22	2	53		4277	75.	15.	6.4717	2	53	0	1	0
FE-17-andy-	2	594792	196	185	22	3	674		10452	149.41543	60.72107	8.41098	2	674	0	0	1
FE-17-andy-	2	594792	196	185	22	4	13		4462	160.	123.	7.	2	13	1	0	0
FE-17-andy-	2	594792	196	185	22	5	87		5135	59.57471	33.	8.57471	2	87	0	1	0
FE-17-andy-	2	594792	196	185	22	6	194		6032	155.34536	128.	10.03608	2	194	0	1	0
FE-17-andy-	3	622182	181	201	22	1	846		9861	87.23404	38.28251	7.47636	3	846	0	0	1
FE-17-andy-	4	574398	185	183	22	1	407		7439	111.77887	24.11057	7.42998	4	407	0	0	1
FE-17-andy-	4	574398	185	183	22	2	397		7577	45.87406	128.70025	7.57935	4	397	0	0	1
FE-17-andy-	4	574398	185	183	22	3	379		6695	88.88391	138.36412	11.46438	4	379	0	0	1
FE-17-andy- (1)	1	350438	138	153	22	1	40		4430	56.	48.	7.45	5	40	0	1	0
FE-17-andy- (1)	1	350438	138	153	22	2	34		3966	24.	44.	9.44118	5	34	0	1	0
FE-17-andy- (1)	1	350438	138	153	22	3	28		3954	106.	117.	10.32143	5	28	0	1	0
FE-17-andy- (1)	1	350438	138	153	22	4	35		3653	38.	119.	11.54286	5	35	0	1	0
FE-17-andy- (1)	1	350438	138	153	22	5	17		3704	19.	85.	14.	5	17	1	0	0
FE-17-andy- (1)	1	350438	138	153	22	6	61		4647	42.	44.	15.57377	5	61	0	1	0
FE-17-andy- (1)	1	350438	138	153	22	7	116		5415	93.	80.	16.2069	5	116	0	1	0

Intensity		3233
Small		3
Medium		26
Large		213
Total nuclei		113
Total Small		216
Total Medium		368
Total Large		228
Average Small		1.911504
Average Medium		3.256637
Average Large		2.017699
Average Foci		7.18584
SD Small		1.966494
SD Medium		2.789581
SD Large		1.592293
SD Total		4.467239
Average Size		171.9628
SD		212.5192
Variance		45164.4

Nuclues No.	Small foci	Medium Foci	Large foci	Total
1	1	6	2	9
2	1	4	1	6
3	0	0	1	1
4	0	0	3	3
5	1	6	0	7
6	5	2	4	11
7	0	3	2	5
8	2	3	7	12
9	7	6	5	18
10	6	10	2	18
11	1	2	3	6
12	1	5	4	10
13	1	1	2	4
14	5	2	2	9
15	2	2	3	7
16	1	0	1	2
17	5	8	1	14
18	2	2	4	7
19	6	3	0	9
20	0	0	1	1
21	0	1	3	4
22	4	6	3	13
23	0	3	2	5
24	2	9	3	14
25	2	1	1	4
26	0	1	4	5

Figure 3-16 Example of coord data spreadsheet

Columns K though AB are added after analysis to extract pertinent information from the data.

NUCLEUS NUM	NUCLEUS AREA	FOCUS NUM	FOCUS AREA	OVER EXPOSED	INTENSITY	DISTANCE TO SPOT							
						1	2	3	4	5	6	7	8
1	64.7045	1	.2352		3008		1.59625	6.08195	6.02163	5.57545	5.8954	5.35854	4.8945
1	64.7045	2	.0686		3011	1.59625		4.48929	4.55807	4.38269	4.62265	4.2946	4.27229
1	64.7045	3	.147		2955	6.08195	4.48929		2.47388	3.93559	3.65075	4.40778	5.69802
1	64.7045	4	.0245		2755	6.02163	4.55807	2.47388		1.63267	1.23843	2.19135	3.69677
1	64.7045	5	.1176		3418	5.57545	4.38269	3.93559	1.63267		.49	.57723	2.12897
1	64.7045	6	.0882		3121	5.8954	4.62265	3.65075	1.23843	.49		1.05929	2.61354
1	64.7045	7	.1617		3259	5.35854	4.2946	4.40778	2.19135	.57723	1.05929		1.55425
1	64.7045	8	.0784		2673	4.8945	4.27229	5.69802	3.69677	2.12897	2.61354	1.55425	
2	82.9815	1	.0539		3257		.93915	5.75066	4.10202	5.01124	5.35854	6.16835	6.45975
2	82.9815	2	.3234		4416	.93915		4.97788	3.18173	4.07265	4.42719	5.22943	5.52246
2	82.9815	3	.0686		2913	5.75066	4.97788		2.46595	3.19556	3.68881	3.18173	3.08715
2	82.9815	4	.1176		3262	4.10202	3.18173	2.46595		1.30771	1.85995	2.21027	2.43495
2	82.9815	5	.0441		3230	5.01124	4.07265	3.19556	1.30771		.56436	1.19206	1.53522
2	82.9815	6	.196		3231	5.35854	4.42719	3.68881	1.85995	.56436		1.13088	1.50785
2	82.9815	7	.0196		2926	6.16835	5.22943	3.18173	2.21027	1.19206	1.13088		.37696
2	82.9815	8	.0735		3010	6.45975	5.52246	3.08715	2.43495	1.53522	1.50785	.37696	
1	110.152	1	.1274		3442		6.23354	2.46595	2.45898	5.26677	8.46769	6.72911	8.03782
1	110.152	2	.0882		3584	6.23354		7.52264	5.98572	6.89313	4.83811	7.87399	5.64575
1	110.152	3	.098		3098	2.46595	7.52264		1.66388	3.69876	8.30909	5.00586	7.46674
1	110.152	4	.1519		3726	2.45898	5.98572	1.66388		2.80786	6.71745	4.27229	5.9894
1	110.152	5	.0735		3577	5.26677	6.89313	3.69876	2.80786		5.46628	1.47167	4.25218
1	110.152	6	.1911		4056	8.46769	4.83811	8.30909	6.71745	5.46628		5.48864	1.50785
1	110.152	7	.1078		3410	6.72911	7.87399	5.00586	4.27229	1.47167	5.48864		4.06
1	110.152	8	.0392		3443	8.03782	5.64575	7.46674	5.9894	4.25218	1.50785	4.06	

Figure 3-17 Example of 'dist' data spreadsheet
Rows have been shaded to show three nuclei and the foci associated with them.

74

3.3.2.4 <u>Validation of system</u>

To validate the application of the in-house automated analysis system, digital images that had previously been analysed using manual analysis techniques were re-analysed in a non-biased manner using the in-house automated analysis system. Figure 3-18 shows excellent concordance between manual and automated scores for both 3D and 2D methods. However, slightly elevated scores in shams are seen at both 2hr and 4hr time points compared to manual analysis.

The major difference between manual and automated scores is in the categorisation of foci sizes, as all foci are categorised using automated analysis we see a larger proportion of medium and large sized foci i.e no foci is categorised as OOF (Figure 3-18). The data supports earlier comparisons of 2D and 3D scoring; twice as many foci are scored after exposure to radiation using 3D methods compared to 2D, for both automated and manual analysis. The trend in distribution of RIF/nucleus for both sham and irradiated cells, between automated and manual methods also correlates well (Figure 3-19). This validation was carried out using 3 independent experiments encompassing ten different times points (data not shown) in which auto-analysis consistently scores comparable values to that determined manually, demonstrating that the autoanalysis system is capable of discriminating RIF at peak induction levels at least up to 2Gy γ-rays in HBEp cells at a fraction of the time (data not shown).

The frequency distribution of RIF/nucleus is consistent for both manual and automated methods ranging from 0-5 RIF/nucleus and ~5-19 RIF/nucleus for sham and irradiated samples, respectively.
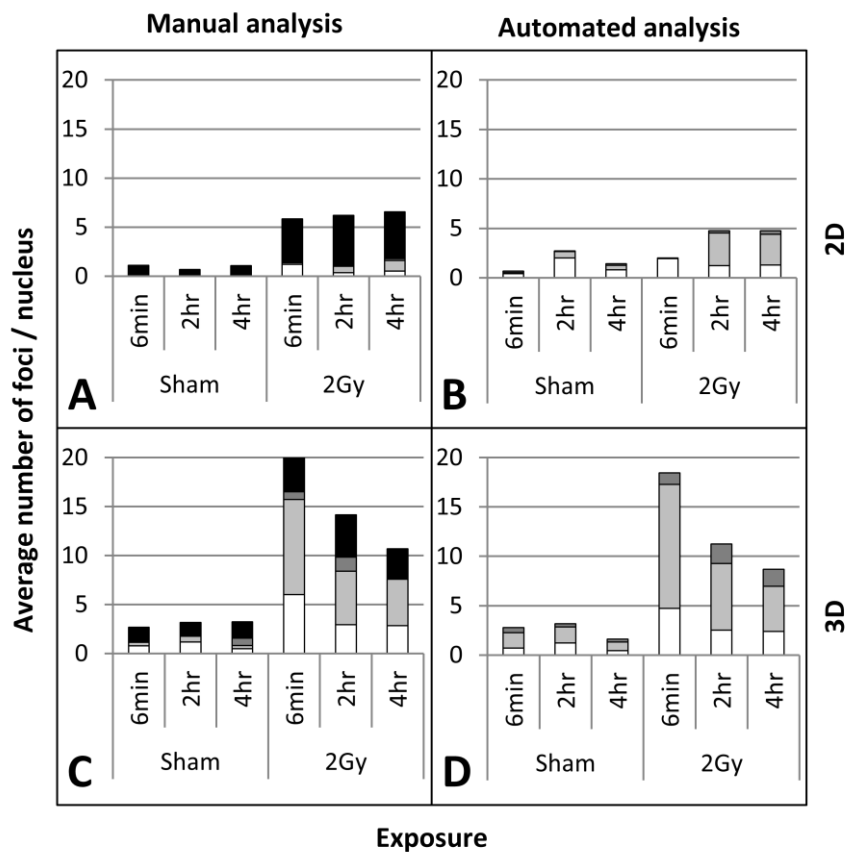
Figure 3-18 Validation of scores for automated analysis
Average number of RIF/nucleus with three size integers, <0.5μm (white), 0.5-10μm (grey) and >1μm (dark grey) and out-of-focus (black) scored by manual analysis (left panel) and automated analysis (right panel). Averages are from two independent experiments.
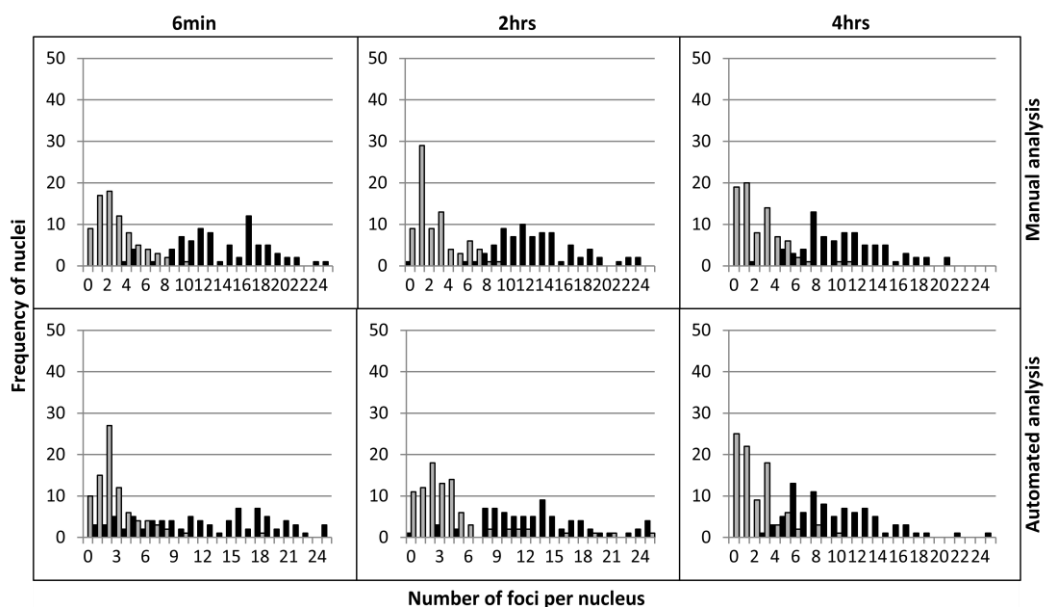
Figure 3-19 Frequency distributions for manual and automated analysis
Frequency distribution of foci/nucleus in HBEp cells exposed to 2Gy of γ-rays (black bars) or sham exposures (grey bars) and allowed to recover for 2hr (A&B) and 4hr (C&D). Analysis was performed manually (B&D) and with the automated method described (A&C)

To directly compare automated and manual counting results, correlation plots were generated from Figure 3-18 and Figure 3-19. Although the overall correlation approximates to a 1:1 ratio after 2Gy γ-ray, correlation coefficients are reduced by outliers (Figure 3-20).
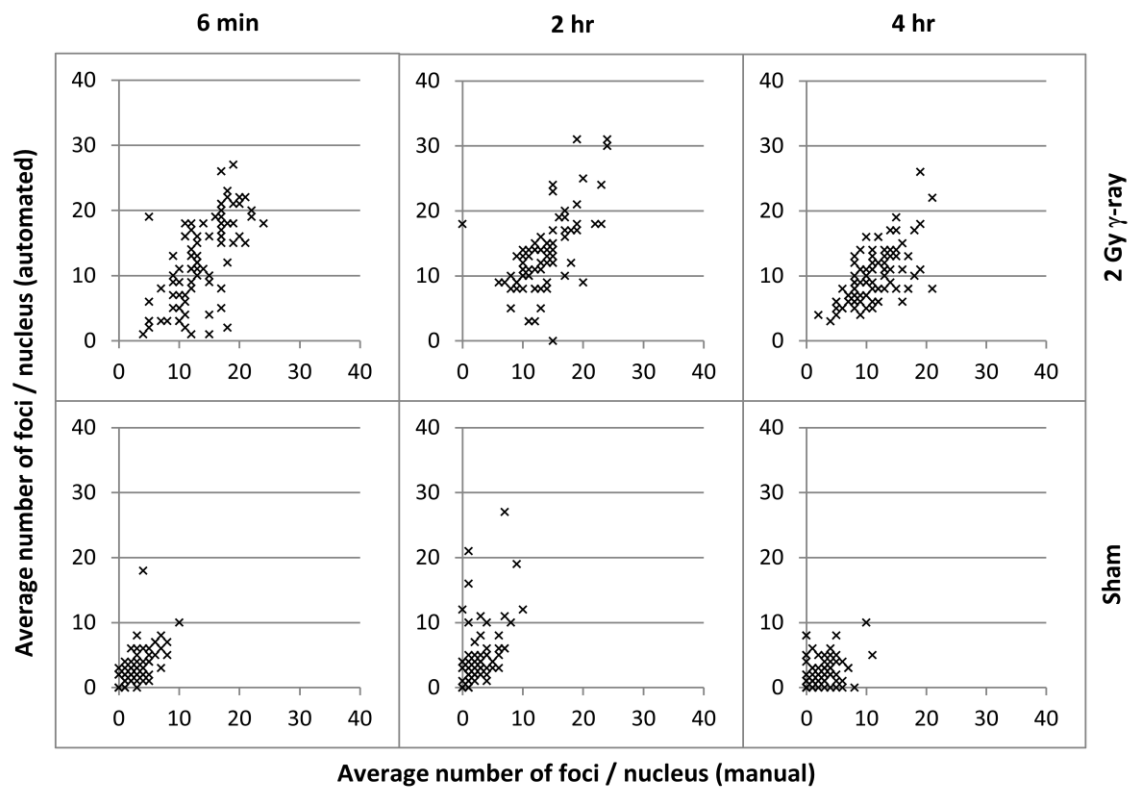
Figure 3-20 Correlation plots for manual and automated RIF analysis
Manual counts including estimates from out of focus category (x-axis) and automated counts for the same nuclei (y-axis) are shown. 100 nuclei were analysed for each graph.

The range of error was greater in irradiated samples compared to sham due to the presence of more RIF/nucleus. Correlation plots are skewed toward more foci being counted in the automated method but there is no significant difference between the means derived from the two methods (P<0.05).

3.3.3 Application of auto-analysis for DDR protein co-localisation studies in HBEp cells

53BP1 is known to localise into discrete foci after exposure to DNA DSB inducing agents (Anderson et al., 2001, Ward et al., 2003, Suzuki et al., 2010) and has been shown to co-localise with a variety of repair associated proteins, including γH2AX. To assess the degree of co-localisation in HBEp cells after exposure to γ-rays and, to assess the usefulness of the in-house autoanalysis system for quantifying co-localisation, cells were exposed to 2 Gy γ-rays and simultaneously labelled with 53BP1 and γ-H2AX (see section 2.2.3.1). To prevent cross-reactivity between 53BP1 and γH2AX (rabbit monoclonal (clone JBW103 Molecular probes) antibody), secondary antibodies from the same species were used. Specifically, fluorescent conjugated (488 nm) goat anti-rabbit secondary was used in conjunction with fluorescent conjugated (555 nm) goat anti-mouse IgG for γ-H2AX and 53BP1 respectively. Digital images, specifically maximum intensity projections (MIP), of ~500 nuclei were acquired using Zeiss Axioskop Metapher system. Negative controls were tested by applying only secondary antibodies to fixed and permeated cells, which showed no cross reactivity between species and no non-specific binding (data not shown).

To quantitatively assess the level of co-localisation of 53BP1 and γ-H2AX, intensity correlation scatter plots were generated in ImageJ (Figure 3-21). Red/Green scatter plots show the distribution of co-localised (yellow) pixels and their relative frequency is shown as a hot/cold scatter plots. The pixels with higher intensities (which are more likely to be foci) have been identified using a box on the frequency plots. The "Manders Coefficients" plug-in for imageJ suggested a good co-localisation of 53BP1 and H2AX (r=>0.8). However visual examination of the colour scatter plots and frequency distribution plots shows a large proportion of the signal is in the lower intensity range. This is likely to be a consequence of the poor signal to noise ratio in the γ-H2AX images coupled with the background homogenous staining of 53BP1 in undamaged nuclei (Figure 3-21). The majority of pixels, shown as yellow (colour plots) and white-hot regions

(frequency plots), have intensities associated with background. This is likely to skew the results toward a higher correlation coefficient that does not represent the co-localisation of foci (Manders et al., 1993). However, it is clear that there are more co-localised pixels of higher intensities in irradiated samples (top right of colour plots), compared to that seen in shams, which may suggest an increase (not quantifiable) in co-localisation.
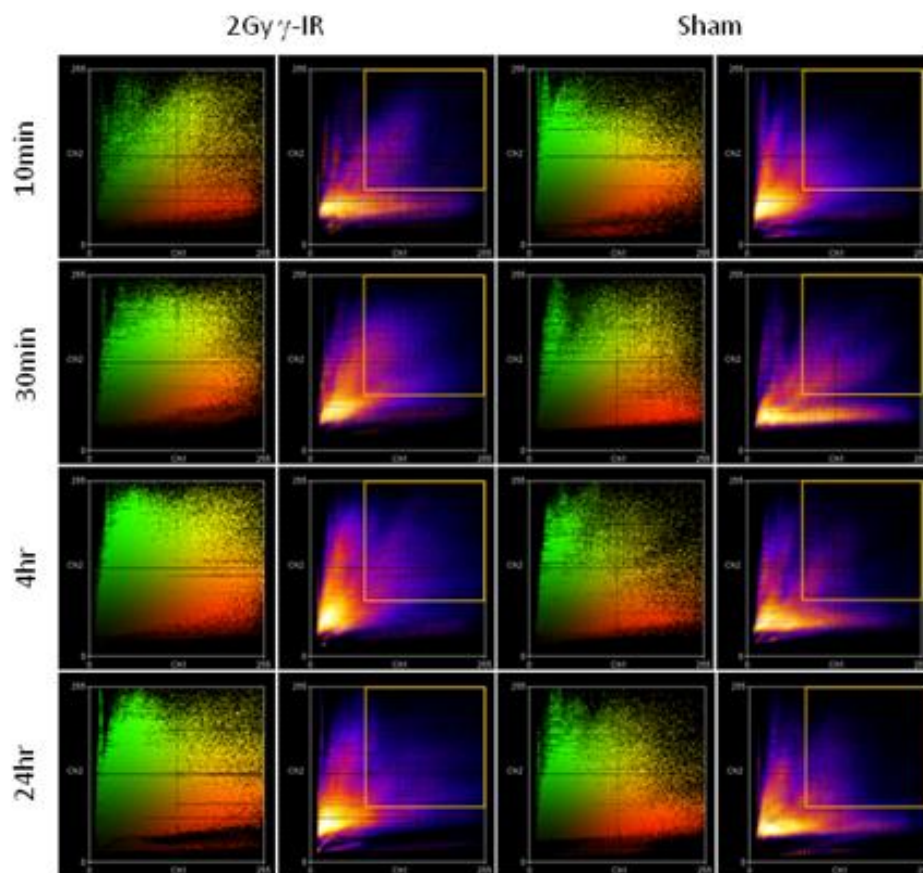
Figure 3-21 Correlation plots for co localisation of 53BP1 and γ-H2AX
Colour (red/green) and frequency (hot/cold) of 53BP1 (Ch1/red) and γ-H2AX (Ch2/green). Yellow boxes have been overlaid to show the region for co-localised foci. ~300 nuclei per time point were analysed.

To obtain a more quantitative evaluation of co-localisation it is necessary to segregate signal (foci) from noise (background). Current co-localisation analysis tools rely on a single intensity threshold to achieve this, and as we have shown, this is an ineffective method for identification of foci. Therefore we utilised the resulting binary images from the in-house auto analysis system to determine co-localisation.

Automated foci analysis for 53BP1 and γ-H2AX was carried out independently, the resulting binary images for each independent channel were then imported to ImageJ (Figure 3-22 A&B). Foci were identified using the "analyse particles" function and the results of the log copied into MS Excel for each time point. This provides the same data that is output from the automated analysis system (Figure 3-16 and 3-17).

A method was then developed to identify co-localised regions by combining the binary images into a colour composite where 53BP1 (red), γ-H2AX (green) and co-localised signal (yellow) can be identified (Figure 3-22 C). To quantify the co-localised signal; the image was converted from RGB format to 8 bit (greyscale), resulting in the three colours (red, green and yellow) being converted to intensities of 76, 150 and 227 respectively (Figure 3-22 D). A fixed intensity threshold was then applied to analyse particles of greater than 2 pixels in size and intensities over 227 (yellow) (Figure 3-22). Once imported into excel the average number of foci, average focus area and average total area was calculated for analysis.
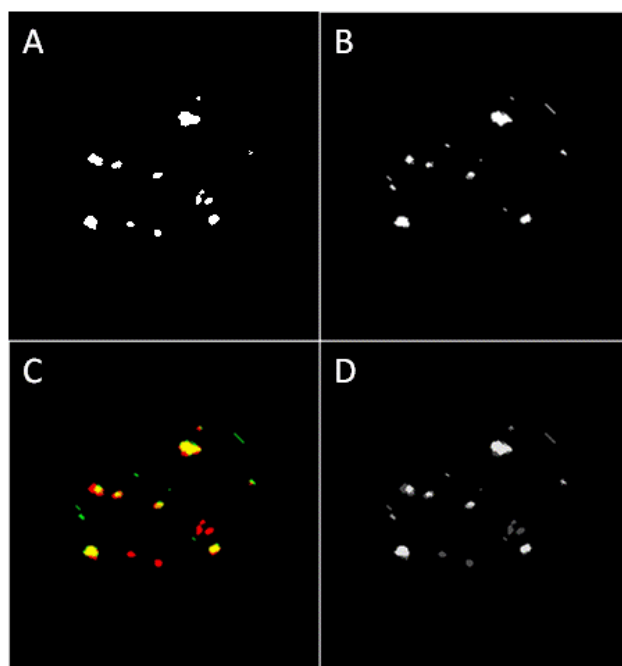
Figure 3-22 Binary images from 53BP1 and γ-H2AX co-localisation
HBEp cells 4hr after exposure to 2Gy γ-rays. Binary images are the result of image processing for automated analysis for 53BP1 (A) and γ-H2AX (B). A coloured merged composite is used to identify co-localised regions as yellow (C), an 8 bit greyscale image was then derived from the composite to allow thresholding to be applied.

The utilisation of the in-house automated analysis system to perform co-localisation analysis facilitates correlation analysis and measurement of foci numbers in relation to co-localised foci. Additionally, this validates the use of the automated analysis system within the context of a different microscope setup with different image acquisition (maximum intensity projections) and with different DSB markers.

3.4 Discussion

The quantification and measurement of RIF is a rapidly developing field. The benefits and limitations of the RIF assay have been reviewed (Löbrich et al., 2010) but there has yet to be a standardisation in the method for automated foci analysis. Of those systems available, the majority utilise filtering processes to enhance contrast between signal (foci) and noise (background). The 'top hat' filter is commonly used in conjunction with smoothing filters to improve contrast for foci analysis (Qvarnstrom et al., 2004, Jucha et al., 2010, Roch-Lefevre et al., 2010, Ivashkevich et al., 2011, Valente et al., 2011). This then allows a threshold to be applied to segment foci from the background. The application of a fixed threshold alone is possible but there must be consistent contrast between foci and background for this to be really effective (Cai et al., 2009). It is more practical to use a dynamic threshold that changes automatically with each image based on the frequency distribution of pixel intensities (histogram) (Hou et al., 2009). The alternative method for foci analysis is identification of the centres of foci from peaks of intensity (maxima) used in conjunction with water-shedding to identify the periphery of foci (Costes et al., 2007), but this can lead to unnecessary segmentation of larger foci and over estimates from noisy backgrounds. This has been rectified with more complex algorithms (Barber, 2007) but requires significantly more processing power and time. For instance, application of this methodology was tested in 3D, but proved to be too time consuming for rapid throughput as the processing requirements were too great (version 4.0 of in-house auto analysis system).

Peaks of intensity within cells could be derived from a multitude of factors that would not be considered foci based on biological or technical knowledge, these factors are listed in Table 3-4.

Table 3-4 Factors that can affect foci scores

Cells	Rolled by coverslip	Sausage shaped cells
	Necrotic	Irregular / broken outline
	Overlapping	Visible as non-ellipsoid outline
Staining	Background	Homogenous / regular pattern
	Debris	Very bright not unique to nucleus
Microscope	Oil aberration	Blurred image
	Depth of field	Out of focus information

The approach taken here was to identify nuclei using the dynamic Otsu threshold, which was then used as a mask to exclude non-nuclear signal from the foci image. Image contrast was then enhanced using a Laplacian filter with smoothing processes, which reduces the risk of amplifying noise and generating artefacts. Finally, the maximum entropy threshold, based on the histogram of all the images in a stack (global), is applied to segment foci from background in what has been described as pseudo 3D processing (Ivashkevich et al., 2011). The rationale for including all images from the stack for the threshold calculation instead of calculating the threshold for each image separately is based on following: noise gets accumulated into the histogram from all the images and given that it is of the same average value across, becomes more distinct as a class. As well as noise, the signal (foci) curvature spikes also get accumulated in the global histogram making the separation between noise and signal bigger. This makes the maximum entropy threshold class separation more precise. If the histogram were based on every individual image, in images with no distinct foci, the maximum entropy method will segment the noise into two classes: strong and weak noise, so the stronger noise would be mistaken for foci. However when the common threshold value based on the global histogram is applied to the whole stack, the images that did not have distinct foci would be subject to the same threshold as used in images containing foci. This prevents the noise from being exaggerated in slices without foci. There is also the functionality to combine histograms

from entire folders of results to further increase the strictness of the threshold, which extends the range of intensities that can be analysed within an experiment. The two filtering methods discussed (top hat and laplacian) are not mutually exclusive, in fact a combination of laplacian and top hat filtering has been used to identify similar objects in images from chest X-rays (Shi et al., 2011).

The development of each version of the in-house software involved improvements to the users interface, accuracy in counting, implementation of devices to allow operator input to account for differences in image quality and the ability to switch between foci and counterstained channels (depending on which was acquired first), see Table 3-5.

Table 3-5 Key development steps for automated analysis software

Version	Date	Developments
1.1	March 20th	Initial tests show good identification of foci but processing times are high, only 2D processing available.
2.0	April 25th	Version update includes specific processer requirements (user defines memory and processors).
3.0 3.1	May 5th & 12th	Separate 2D and 3D systems for processing of 3D image stacks.
4.0	June 16th	Development of CHARM algorithm (Barber, 2007) to count foci in 3D, decidedly too time consuming so further development of thresholding technique for 3D data.
5.0	June 29th	Final working version includes capability to analyse both 3D and 2D images, at 512MB or 1024MB with up to two processor cores.

A key aspect of development was the definition of folder structure. This is critical to the way in which images are opened and saved. The format used involves a hierarchical structure of folders allowing the operator to perform analysis in batches. Although less relevant at the time of analysis, this folder structure acts as an archive to allow other users easy access to specific time points and experiments.
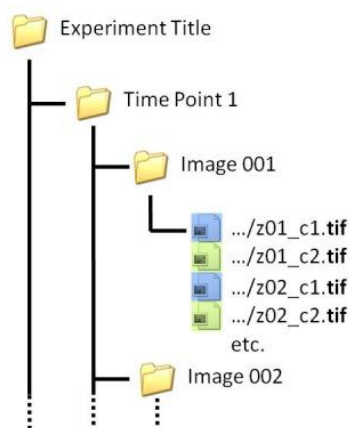
Figure 3-23 Hierarchical structure of images in folders for analysis
Each experiment folder has sub-folders for the variables (dose or time) within this folder
are image folders, which contain all the images for an individual stack (counterstain and
foci). In three channel images one channel must be temporarily removed for automated
analysis.

At each stage of development validity checks using binary images and
comparisons of overall scores were made, these checks appear to be
standard for systems involving the quantification of foci (Barber, 2007), but
detailed validation in relation to size is not (Bocker and Iliakis, 2006).
Ongoing validation has shown excellent correlation between the average
number of foci per nucleus, trends in induction and decline of foci over
time and the frequency distributions for nuclei. There is also good
concordance between measurements of focus size, but comparisons
between manual and automated size proportions should be considered
cautiously as the measurements are different. In the manual counting
method, each focus is only considered on a single focal plane and only the
diameter is measured, for automated methods the volume is extrapolated
based on the three dimensional periphery of the focus, the size integers
applied to the automated score assume foci to have an even and regular
outline, which we know to be incorrect. A more accurate method for
comparison between the methods would require more complex modelling
of foci.

The main benefit of this analysis tool is the rapid turnaround of
data. A single experiment with 10 slides and 100 nuclei per slide takes
approximately a week to categorise all the foci into size integers if manual
analysis methods are used. Although replicate counts have shown this to

be a reproducible method, it is still subject to bias and error. However, the same data can be obtained and with more depth of information and consistency within 2hr (depending on hardware) with minimal operator input using the in house automated analysis package. Prior to automated analysis, any foci with indiscriminate edges or insufficient intensity were classed as foci that were possibly out-of-focus. As this category does not provide data on size and accounts for such a large proportion of foci, quantification of foci size was difficult. With automated methods there was no ambiguity and foci size was a more accurate and consistent measurement as the size is obtained from a measurement of pixels (continuous data).

Some differences between manual and automated scores were observed (Figure 3-20) but these were identified to be due to outliers in the data caused by e.g. the bounding of two nuclei (data not shown) and possibly replicating cells. The population of HBEp cells used here are only semi-synchronous (chapter 4) and no marker for stage of the cell cycle was used even though it has been shown that nuclei undergoing cell division during irradiation show a larger number of foci than non-replicating cells(Nakamura et al., 2010). Thus, this variance in the automated determination of RIF could be reduced by application of additional cell cycle markers (Rothkamm et al., 2003, Sakaue-Sawano et al., 2008), enabling the operator to choose which foci to count or capture, or ask specific questions relating to the stage of the cell cycle and RIF frequency. In addition to this, the range of nuclear sizes (as a consequence of different stages in the cell cycle) could be masking more subtle changes and trends, especially when averages are used. Therefore, a normalisation to nuclear area could be used in future versions of the software.

The added information obtained through image analysis is not fully utilised in this application. Analysis of the DAPI channel offers information on the density of chromatin and has been used to show the distribution of RIF in relation to regions of dense chromatin (Costes et al., 2007, Falk et al., 2008). Conversely, the DAPI channel is frequently only used as a mask to define the nucleus, this is often not required in 3D as the

background 53BP1 staining is often sufficient to segment the nucleus. Therefore, reducing image capture and analysis to a single channel could increase acquisition and processing times with only a slight increase in error. The addition of multi channel analysis may also be beneficial for co-localisation investigations as presently the operator must run the analysis independently for each channel. Currently the software automatically outputs data into an Excel spreadsheet, modification of the software to ask the operator which measurements are required could be a useful tool as some measurements are currently ignored (circularity, mean intensity, integrated optical density etc).

Manual analysis of RIF by eye is still the benchmark for reliable quantification of foci number, but is not a feasible method for the detailed analysis of foci size and ultimately, dynamics. The use of image analysis software to apply a manual intensity threshold to an image stack provides sufficient data for detailed analysis of foci, but this is simply not practical for the large volumes of data required. This drawback, coupled with the fact that the intensity threshold alone is not sufficient to accurately identify all foci within an image stack means a more systematic approach is required. Here we have shown a method to rapidly identify, categorise and report data of 53BP1 foci from primary HBEp cells. An experiment with 10 slides and 100 images per slide would have taken between 8 and 15 days to analyse, using the systems shown this time has been reduced to less than 2 hours (depending on hardware), with minimal user input. In addition to speed, this methodology can easily be incorporated into other modular systems or java based code. The resulting images and spreadsheet data can then be used to identify number of foci, area, spatiotemporal positioning and with additional analysis co-localisation.

The development of any automated analysis system relies on the operators initial input of parameters, this is by no means a caveat, indeed the final development of foci automated analysis software should incorporate a form of iterative or reinforcement learning, whereby the operator is presented with a sample image of what the algorithm believes is correct segmentation, the operator can then correct the image and the algorithm automatically adapts. MatLab software already has this

functionality available but requires significant programming.

       The RIF assay has a multitude of variables that all contribute to the statistics and final value of 'foci per nucleus'. The analysis method is the final variable that seems to have little consistency between labs, making comparisons difficult. The software presented is by no means comprehensive but may contribute towards the development of standardisation in the field of RIF analysis.

4 Characterisation of radiation-induced damage in primary human bronchial epithelial cells

4.1 Introduction

Lung cancer is the most common cause of cancer mortality in males and the second most common cause in women (Travis et al., 1995, Baird et al., 2005), principally due to lack of early diagnosis. There are two main histological types of lung cancer namely; small cell lung cancers (SCLC) and non-small cell lung cancers (NSCLC). SCLC account for approximately 20% of all lung cancer cases and typically arise from the cells of the upper airways. The remaining 80% are NSCLC, further sub-categorised into squamous cell carcinoma (35%) which originate from the cells that line the airway, adenocarcinomas (27%) associated with the mucus producing cells and, large cell carcinomas (10%) which are also known as undifferentiated carcinomas (Baird et al., 2005).

The highest risk factor for lung cancer is cigarette smoking, but with increasing public awareness individuals smoking habits are changing (Peto et al., 2000) and it is suggested that world-wide 25% of lung cancers cannot be attributed to tobacco use (Sun et al., 2007). For instance, exposure to asbestos is associated with mesothelioma, which is a distinct form of lung cancer to SCLC and NSCLC in its epidemiology, accounting for 1% of all lung cancer cases (Britton et al., 2007). Possibly the greatest non-smoking risk factor for lung carcinogenesis is exposure to Radon gas and its daughters. The lungs and bronchioles constitute the main target tissue for inhaled radiation, such as that received from Radon gas. The microenvironments of the airway have varying constituent cell types but within the bronchioles of the lower airway there are three main cell types; columnar ciliated cells, mucus secreting goblet cells and basal cells (see Figure 4-1). It is now understood that much of the epidemiology of lung cancers can be attributed to geographical location in addition to smoking whereby a causal association between domestic exposure to Radon gas

and SCLC has been detected (Darby et al., 2005). Therefore, understanding the biology of radiation-induced lung cancers is becoming ever more important.
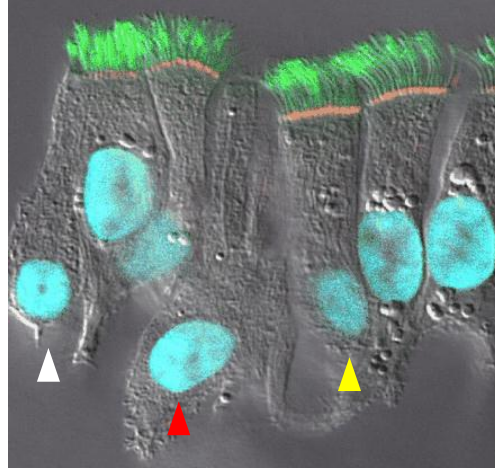
Figure 4-1 Image of different cell types of the bronchioles
Phase contrast microscopy image of human bronchi with nucleus stained blue with DAPI, actin filaments labelled red and cilia in green (Kreda et al., 2005). Diagram has been modified to illustrate the three main cell types associated with the lower bronchi with arrows: white – Basal cell, red – Goblet cell, yellow – Ciliated cell.

This chapter aims to characterise the radiobiological responses of human bronchial epithelial (HBEp) cells in vitro. Specifically, the induction and decline of radiation-induced 53BP1 foci will be evaluated using the manual and automated image analysis systems described in chapter 3.

The general growth characteristics and induction of foci after exposure to ionising radiation can then be used as a 'benchmark' for comparison to responses in immortalised HBEp cells with green fluorescent protein (GFP) and 53BP1 fusion protein (GFP-53BP1) cell lines. These cell lines enable conclusions to be drawn over the dynamics of individual foci over time within specified nuclei.

4.2 Results

4.2.1 <u>General growth characteristics of primary human bronchial epithelial cells</u>

Normal primary human bronchial epithelial (HBEp) cells were obtained commercially as single cell suspensions from Lonza, USA. Lonza is an FDA approved cell bank that obtains human tissue samples according to ethical guidelines with fully informed donor consent. Samples are screened prior to shipping for infectious agents including mycoplasma, HIV and Hepatitis. Accordingly, all cell culture was carried out using standard health and safety protocols in a class II microbiological cabinet. For this study, two different donors were studied. Donor 1 was a 19 year old Caucasian male and Donor 2, a 52 year old Hispanic female. The first seeding after shipping is defined as second passage (p2), from explants to cell suspension is classified as first passage (p1).

HBEp cells were maintained at 37°C in a 5% CO_2 / 95% air humidified environment with fresh media changes every 48hrs with a serum-free defined medium (Lonza) containing bronchial epithelial cell basal medium, bovine pituitary extract (0.2%), insulin (0.1%), hydrocortisone (0.1%), gentamicin sulfate and amphotericin-b (0.1%), retinoic acid (0.1%), transferrin (0.1%), epinephrine (0.1%) and human epithelial growth factor (0.1%). This regime maintains optimal growth conditions for HBEp cells, minimises terminal differentiation and also reduces the risk of fibroblasts outgrowth within the population (Lechner and LaVeck, 1985). Cell debris is a common characteristic within cultures and is caused by precipitates of the pituitary extract but do not require filter removal. To maintain logarithmic cell growth and to further minimise terminal differentiation, HBEp cells were routinely passaged between 80-90% confluence. Indeed it is a limiting feature of these primary cells that they cannot be allowed to reach 100% confluence, as this can lead to changes in cell characteristics, to be discussed later. From a cryopreserved state, HBEp cells seeded at the recommended density of $3x10^3$cells/cm^2 typically took 80-100hrs to reach 80-90% confluence, depending on donor and passage number.

Early passage (p2-p5) HBEp cells in log phase of growth were observed to have typical "cobblestone" appearance with minimal cytoplasm and were ~25µm in diameter (Figure 4-2 white arrow). Another population of more spherical larger cells is observed, which has more extensive cytoplasm that spreads over the vessel surface (Figure 4-2 black arrow), taking on the appearance of fried eggs. These two populations have been hypothesised to be the basal and goblet cells of the bronchial airway, respectively.
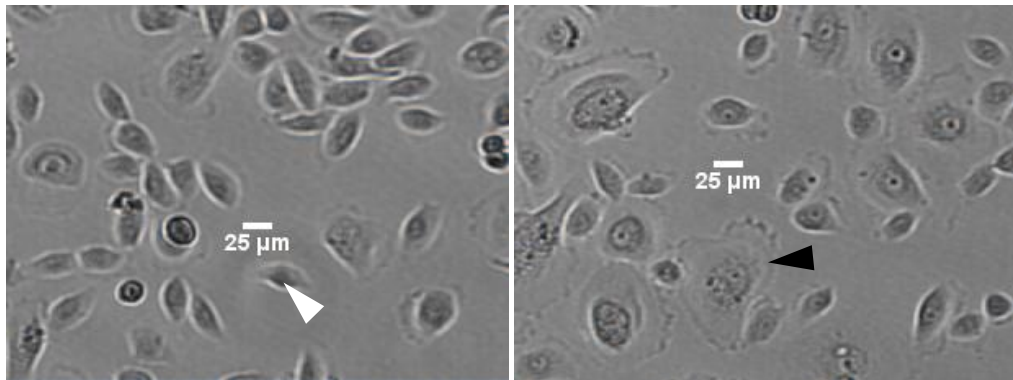
Figure 4-2 Phase contrast images of HBEp cells
Cells isolated from donor 1 at passage 3 (left) and passage 10 (right). White arrow indicates a typical basal cell morphology consistent with early passage cells, black arrow indicates a larger goblet cell typical of later passage cultures. Cells contrast well under phase illumination due to the depth of the cells (5.8µm).

At later passage (p5 onwards) the proportions of cells within the population gradually change from the smaller (basal type) to the larger (goblet type) cells which becomes even more striking as the cells enter the plateau phase of their growth (beyond p9). Cultures that were permitted to grow beyond 90% confluence, or when media was not replenished at the required 2 day intervals, showed an increased proportion of larger 'goblet' cells in subsequent passages. In addition, the larger 'goblet' cells were found to be more adherent and often required more time in trypsin to facilitate passage. A representative growth curve for Donor 2 shows the doubling time to be approximately 30hrs (Figure 4-3) and 24hrs for donor 1 (data not shown).
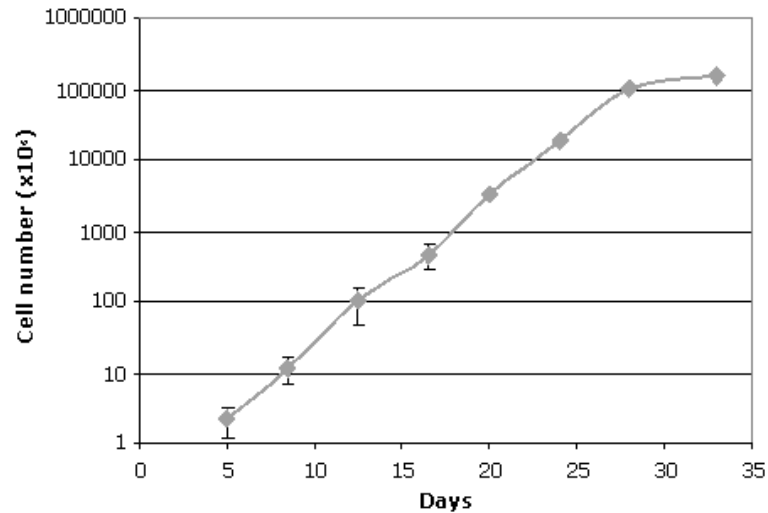
Figure 4-3 Cumulative growth curve for donor 2 HBEp cells (D2)
Exponential growth is observed over a period of 30 days (p2-p8), reaching a plateau at
p9.

The stage of cell cycle at the time of irradiation is known to be an
important factor in the DSB response (Hall and Giaccia, 2006) as a
consequence of varying radiosensitivities at different stages of the cell
cycle (Wojcik et al., 1996, Rothkamm et al., 2003, Edelmann et al., 2005).
Therefore, it is optimal to irradiate synchronised populations of cells
enabling radiobiological responses at different stages of the cell cycle to
be determined. However, given the constraints highlighted regarding the
requirement of HBEp cells to be maintained under stringent conditions in
log growth phase, such synchronisation was not possible. Furthermore,
the isolation of phase-specific cells by flow cytometry or magnetic bead
separation was not deemed practical, given the small numbers of cells
available for any experiment. With these caveats in mind, we analysed
HBEp cells at various stages of confluence in log growth by flow cytometry
to assess the proportion of cells that were outside the G1 phase of the cell
cycle to ascertain the optimal irradiation time after seeding.

Table 4-1 Distribution of HBEp cell cycle stages at varying confluence (data courtesy of Dr Matthew Themis)

% Confluence	%G_0/G_1	%S	%G_2/M
30	62	17	16
50	70	19	11
55	63	17	17
60	71	16	12
70	65	13	14
90	80	11	8
100	91	4.9	2.7

Table 4-1 shows that only 10-20% of cells are non-G1 when sampled at 90% confluence. A population of cells which are seeded at a normal density of 3.5×10^3 cells/cm^2 then cultured for a period of ~72hrs are generally around 90% confluence. Accordingly, for all irradiations, cells were seeded onto sterilised glass slides, within individual quadriPERM® chambers, at a density of 3.5×10^3 cells/cm^2 and cultured in 7ml complete medium until ~90% confluent. In all cases, a control flask (T25 or T75) of HBEp cells was cultured in parallel to ensure growth characteristics and morphology were consistent.

4.2.2 Immunofluorescence detection of DNA DSB in HBEp cells

53BP1 is known to localise into discrete foci after exposure to ionising radiation and other DNA DSB inducing agents and is recognised as a reliable marker for the in situ detection of DSB in individual nuclei (Schultz et al., 2000, Anderson et al., 2001). In this study we employed the mouse monoclonal (BD Clone 19 IgG2b) antibody from BD Scientific that is specific for human 53BP1 protein and detected this with goat anti-mouse fluorescence conjugated (Alexa Fluor 555) secondary antibodies (polyclonal anti-IgG2b whole antibody) to assess the induction and decline of DSBs.

In the absence of radiation exposure, HBEp cell nuclei show a homogenous staining pattern for 53BP1 signal, interrupted by a single area of reduced signal intensity (Figure 4-4). These regions of reduced intensity are of variable size but are consistently positioned in the middle of the nucleus, are of relatively circular margins and are believed to be the nucleolus. The nucleolus is a non-bound sub-structure of the nucleus containing larger proportions of proteins and RNA involved in protein synthesis and although not devoid of DNA (contains Nucleolar Organising Regions of the acrocentric chromosomes), it is chromatin poor relative to the remainder of the nucleus (Recher et al., 1970).
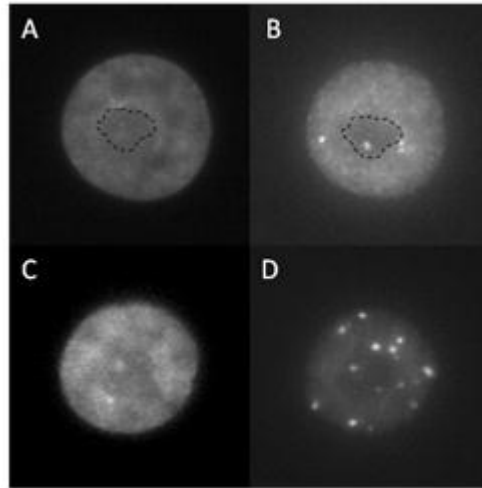
Figure 4-4 DAPI and 53BP1 foci in shams and irradiated HBEp cells
HBEp nuclei fixed 10min after exposure to sham (A & B) or 2Gy γ-rays (C & D). DAPI signal (left panels) shows chromatin with regions of decreased intensity. 53BP1 signal (right panels) appears homogenous throughout nucleus with the exception of the nucleolus (dashed line) for shams (B) and to a lesser extent for irradiated (D).

Within minutes of exposure to ionising radiation, regions of punctuate and intense 53BP1 signal are observed (Figure 4-4). The homogenous distribution of 53BP1 protein (Figure 4-4-B) rapidly re-localises to form discrete 53BP1 foci (Figure 4-4-D) consistent with the recruitment of 53BP1 to sites of DSB and involvement in DSB damage processing and repair. Interestingly, throughout this study, 53BP1 foci were rarely observed within the nucleolus and it is speculated that the lack of chromatin within the nucleolus may be relevant to the formation of 53BP1 foci.
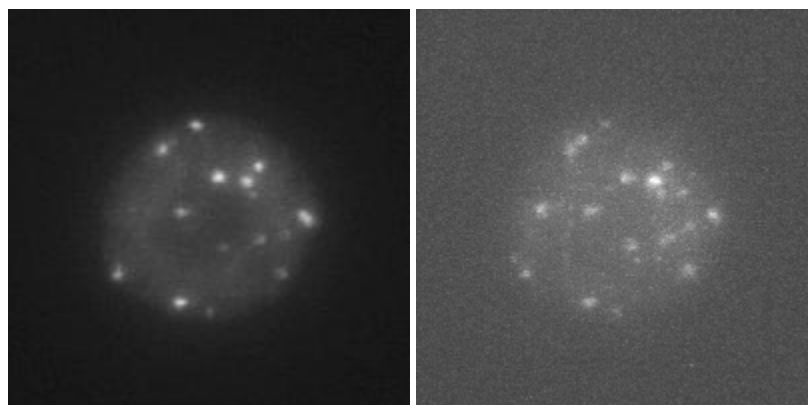
Figure 4-5 HBEp cells stained for 53BP1 and γ–H2AX.
Representative image showing the difference in signal: noise ratio for detection of p8 HBEp cell nuclei fixed and stained for 53BP1 (left) and γ-H2AX (right) after exposure to 2Gy γ-rays. (to generate similar images image gain was increased for γ-H2AX images).

Fluorescence signal specific for γ-H2AX foci was also observed within 10 minutes after exposure to γ-rays (Figure 4-5). Similar to that observed for 53BP1, the foci become more intense and punctuate with time after irradiation, however in contrast to 53BP1; the signal quality of γ-H2AX was consistently poorer in terms of signal to noise. Additionally, the phosphorylation of γ-H2AX and formation of discrete foci is known to occur in the absence of exposure to a clastogenic agents (Olive, 2009), which could be the result of endogenous breaks or non-DSB breaks (Vilenchik and Knudson, 2003, Harper et al.).

Additionally, it was noted that nuclei with condensed chromatin, believed to be entering mitosis, lacked 53BP1 staining whilst γ-H2AX foci were still present.
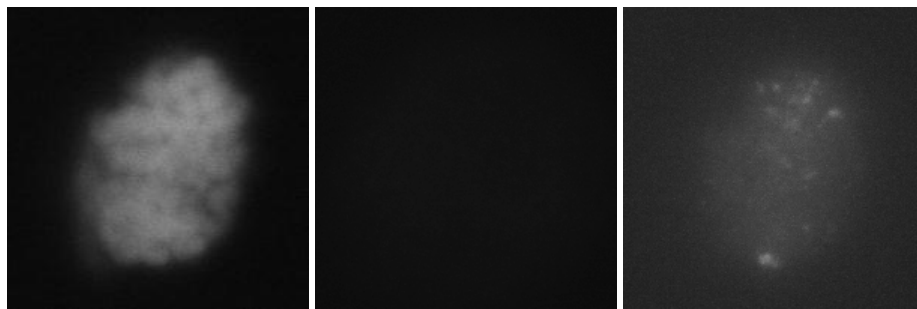
Figure 4-6 53BP1 and γH2AX signal in condensed chromatin
Condensed chromatin of dividing HBEp (left) as visualised using DAPI is associated with a lack of 53BP1 staining (centre) whilst γ-H2AX foci persist (right).

The combination of 53BP1 being excluded from G2/S/M in unirradiated cells (Giunta et al., 2010, Nakamura et al., 2010, Lukas et al., 2011) and the non-synchronous nature of HBEp populations, together with the excellent S:N ratio obtained, highlights 53BP1 as an excellent marker of DSB. In contrast, non-radiation induced γ-H2AX foci have been shown to form (McManus and Hendzel, 2005) during these phases, and although 53BP1 foci have been shown to form in the absence of DSBs they are not retained (Soutoglou and Misteli, 2008). Accordingly, 53BP1 was deemed the most appropriate marker for identification of DSBs in HBEp cells, and was utilised as the primary maker.

4.2.3 Induction and decline of radiation induced foci in HBEp cells exposed to low LET radiation

To assess the radiobiological response of HBEp cells to γ-rays, fractions of passage 4 to 8 HBEp cells were seeded onto sterilised glass slides as described in section 2.2.1.5 and irradiated when ~ 90% confluent with 0-2Gy of ^{60}Cobalt γ-rays (dose rate 0.31-0.33Gy/min). Cells were transported to and from the irradiation source in a 37°C portable incubator and immediately returned to a humidified 95% air/ 5% CO_2 incubator at 37°C within 15min of exposure. Cells were allowed to recover for varying lengths of time prior to 3D cell fixation using 4% paraformadehyde. Cells were stained as described in section 2.2.3 and imaged in 3D stacks (0.5μm z-step size for 11μm depth) using the Cell Observer as described in section 2.2.4.2. Qualification of DNA damage foci was achieved by scoring image stacks taken from random fields of view using methods which are described in detail in Chapter 3.

4.2.3.1 Induction and decline of RIF over 24 hrs after 2 Gy γ-rays

Figure 4-7 shows the average number of 53BP1 foci observed in HBEp cells using the manual 3D scoring method, described in Chapter 3. In shams, a background average of ~2 53BP1 foci/nucleus was consistently observed from ~1 hr after exposure over a 24 hr period. A slightly higher average of ~5 53BP1 foci was seen at earlier times after sham exposure which may reflect the stress of transportation to and from the radiation source, overall though, levels of damage are consistent with published studies that also used bronchial epithelial cells and normal human fibroblast cell types, which show a background level of 2-5 53BP1 foci/nucleus (Asaithamby and Chen, 2009, Gerashchenko and Dynlacht, 2009, Lee et al., 2009). Thus, our in-house procedure for irradiation and manual detection of foci is robust and in-line with expectation.

A significant increase in the average number of 53BP1 foci was observed within 6 min (~20 foci) of exposure to 2 Gy γ-rays compared to sham-irradiated cells fixed at the same time (~5 foci) ($p<0.05$) with peak induction of 53BP1 foci (22 foci/nucleus) being observed 30 min after

exposure, Figure 4-7. The peak induction of 53BP1 foci appears to lag by 30 mins from the time of irradiation and may be due to the rapid repair of simple DSBs within shorter time frames in addition to the kinetics for recruitment of 53BP1 to the sites of DNA damage. This peak induction average is equivalent to ~11 foci/Gy and is only slightly lower than that observed in other epithelial cell types (Costes et al., 2007, Groesser et al., 2011). Pulse field gel electrophoresis (PFGE) data suggests more DSBs are induced than are visualised using foci analysis, as 1Gy γ-rays from a [60]Cobalt source with an LET of approximately 0.2 keV/μm is estimated to produce between 20 and 40 DSBs. However, it has also been shown that measurements of DSBs by PFGE exaggerate the number of DSBs (Rydberg, 2000, Leatherbarrow et al., 2006). It has also been suggested that for lower doses this method still lacks sensitivity (Prise et al., 2001).
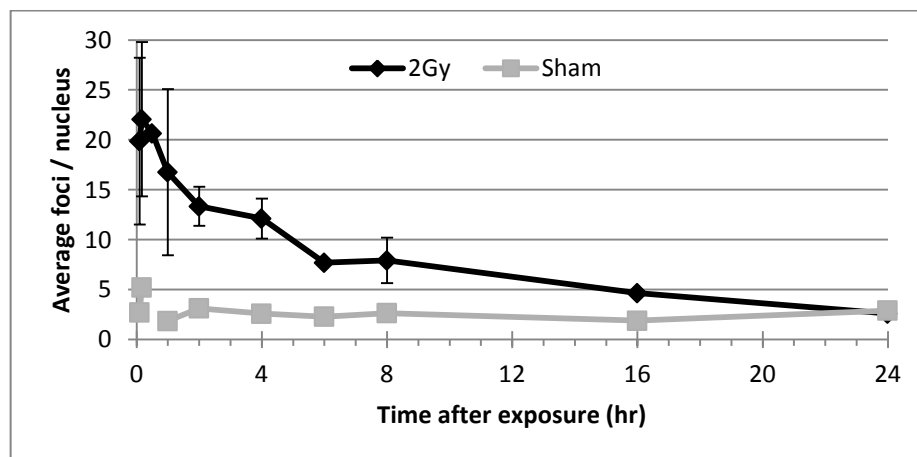
Figure 4-7 Induction and decline of 53BP1 foci in HBEp cells
HBEp cells were exposed to 2Gy γ-rays cells and labelled for 53BP1. Foci were scored manually from 3D image slices. Error bars show SD of mean for replicate experiments.

The decline in average number of 53BP1 foci from 30min after exposure appears to have two phases (Figure 4-7). Initially, there is a rapid decline from ~22 foci/nucleus to 8-10 foci/nucleus up to ~6 hrs after exposure, before flattening to a gradual decline over the next 6-12 hrs and reaching background levels of ~2 foci/nucleus, 24 hrs post irradiation. It is expected that the majority of DSBs are repaired within 4 hrs of exposure (Leatherbarrow et al., 2006) possibly reflecting the steeper decline in the number of 53BP1 foci over this time-frame. If so, this may suggests that

the residual foci observed after this time could constitute more complex damage that cannot be repaired as easily and therefore as rapidly. Further, this two phase decline may be indicative of independent repair kinetics or pathways (Goodarzi et al., 2010), whereby different pathways are utilised for fast repair of simple lesions and a slower repair, occurring over longer time frames. Overall, this trend of induction and two phase decline in 53BP1 foci in HBEp cells is consistent with previously published data in a range of different cell types, al-be-it with fewer total numbers of foci compared to others.

As part of our automated foci analysis system validation process, the same 3D image stacks that comprise Figure 4-7 were processed using the automated analysis method described in Chapter 3. No normalisation of the data was required and as Figure 5-7 shows, both the trend in induction/decline and the average number of 53BP1/nucleus foci was consistent when analysed by both the 3D automated (a) and 3D manual (b) foci analysis methods. In addition, neither the standard deviation of the mean, which reflects the range in distribution of 53BP1 foci, in each nucleus or, the standard deviation between experiments were reduced by automated analysis. Taken together, these data highlight the robustness of the in-house automated analysis system and shows potential capability for the accurate processing of large data-sets to be carried out in a fraction of the time.
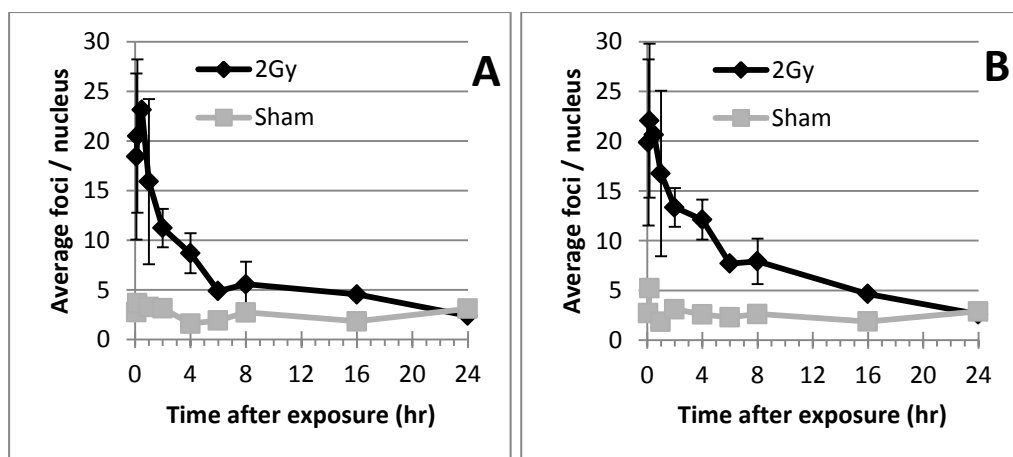
Figure 4-8 Comparison of automated and manual 3D scores
Induction and decline of 53BP1 foci as counted using automated (A) or manual (B) 3D scoring methods. (Error bars represent replicates)

The large standard deviation for the average number of foci reflects the large distribution of foci that is commonly observed in all foci analysis studies, see Figure 4-9.
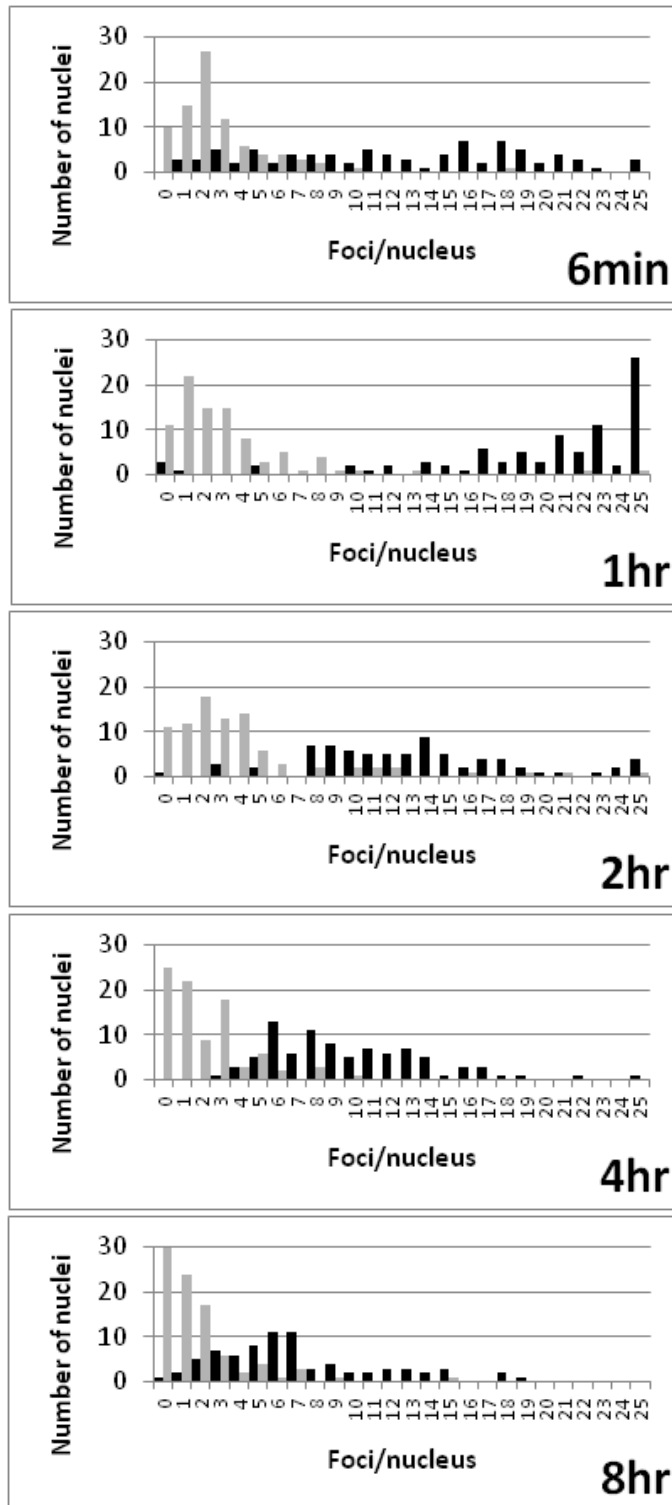
Figure 4-9 Frequency distribution of 53BP1 foci in HBEp cells
Frequency distribution for 53BP1 foci at varying times after exposure to 2Gy γ-rays (black bars) or sham conditions (grey bars). Data is from a single experiment with 100 nuclei scored automatically for each time point.

In cells exposed to sham conditions, the modal number of foci is consistently between 0 and 2 but the range of this distribution appears larger at earlier time points (6 min and 1hr), possibly indicative of stress induced damage from transport of cells. After exposure to 2 Gy γ-rays the range of 53BP1 foci observed from 6 min to 4 hrs varies little from 0 to 25 and only slightly reduces to 0 to19 after 8 hrs; however the modal number does alter over this time frame from 25 to 14 within 1 hr, then from 14 to 6 within 4hrs. Interestingly, even after 8 hrs, when the majority of low LET induced DSBs should be repaired, there is still a large range in the distribution with >20% of nuclei having more than 10 foci.

From the data presented, four critical times after radiation exposure were identified; initial induction (10 min), peak induction (30 min), decline (4 hr) and restored sham levels (24 hrs). These time points were investigated further using the co-localisation analysis method described in chapter 3. Maximal induction of foci was seen at 30min for 53BP1 (22 foci/nucleus) and γ-H2AX (17 foci/nucleus) declining to sham levels by 24hrs. Although 53BP1 foci levels at 24hrs are higher than expected (2-4 foci, Figure 4-7), the number of residual foci at 24hrs is comparable to shams for the same time point, see Figure 4-10. The induction of γ-H2AX foci is shown to approximate that of 53BP1 and is within the standard deviation of the mean for 53BP1.
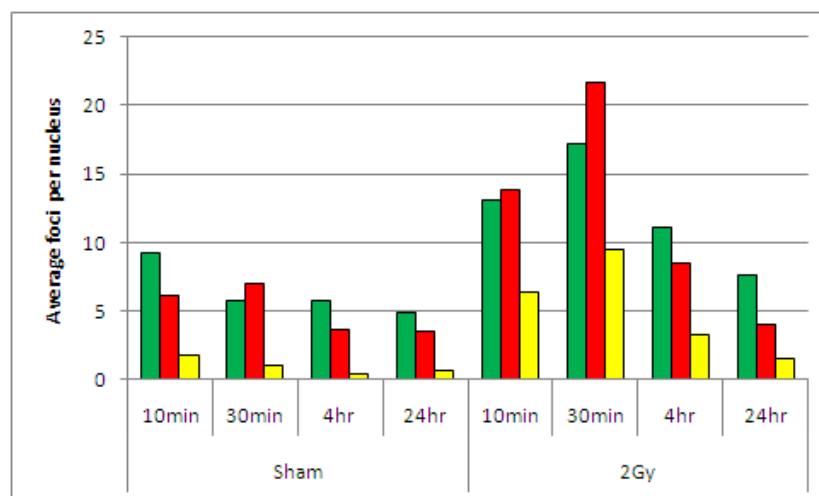
Figure 4-10 Induction and decline of 53BP1 and γ-H2AX
Induction and decline of average number of 53BP1 (red) and γ-H2AX (green) foci per nucleus in HBEp cells exposed to 2 Gy γ-rays and sham conditions.

The co-localisation of γ-H2AX foci and Rad51 has been shown to vary with time after irradiation (Bocker and Iliakis, 2006). For γ-H2AX and 53BP1 observations show co-localisations to reach 87% in tissues 2 hrs after exposure to 0.5 Gy (Suzuki et al., 2010). The data generated here is lower than this and could be due to the non-synchronous growth of cells. For instance, in nuclei with condensed chromatin, 53BP1 foci were consistently absent but γ-H2AX foci persisted, see Figure 4-6 and it is known that 53BP1 signal detection will vary at different stages of the cell cycle (Nakamura et al., 2010, Lukas et al., 2011).

4.2.3.2 Effect of dose on the induction and persistence of 53BP1 foci

To quantify the induction of radiation-induced 53BP1 foci in HBEp cells after exposure to doses of <2 Gy of ionizing radiation, DSBs were quantified 30 min and 8 hrs after exposure to 0.25, 0.3, 0.5, 1.0 and 2.0 Gy γ-rays. The latter dose of 2.0 Gy is used for comparison to previous data. HBEp cells were cultured on glass slides to 90% confluence, transported to ^{60}Cobalt source at 37°C and irradiated as described in section 2.2.2. Immediately after irradiation, cells were returned to an incubator humidified at 95% air/5% CO_2 for either 30min or 8hrs before fixation with 4% paraformaldehyde and then immunofluorecently stained as described in section 2.2.3. 53BP1 foci were scored using both the manual and automatic 3D methods to enable further validation of the automated analysis systems at lower radiation doses.

A significant induction of 53BP1 foci was seen for all doses (P<0.05) compared to shams. Specifically, an average of two 53BP1 foci/nucleus was detected in sham-exposed cells, which is consistent with previous data. After irradiation the average number of foci increased to 4.39, 5.78, 3.34, 7.84 and 19.0 for HBEp cells exposed to 0.25, 0.3, 0.5, 1 and 2Gy respectively, 30mins after exposure. Linear regression of the 30min time point shows good correlation with a linear dose response from the background level of 2 foci in shams. By 8hrs all doses have returned to sham levels, except after 2Gy where numbers of foci are still elevated (3 fold).
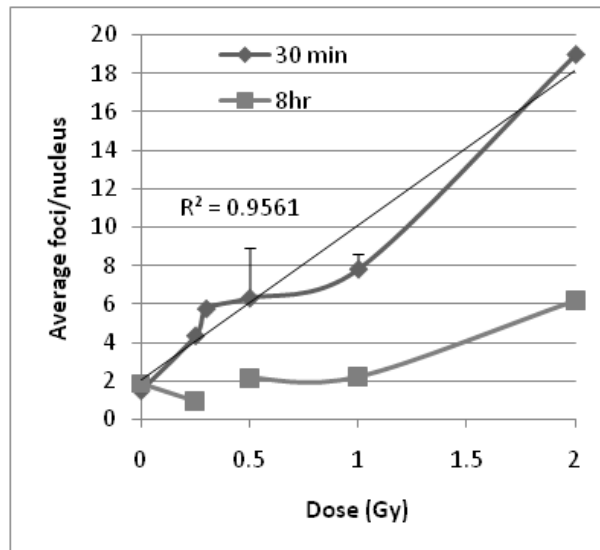
Figure 4-11 Dose response for HBEp cells after 2Gy γ-rays.
HBEp cells were fixed 30min (diamonds) and 8hrs (squares) after irradiation. Linear regression has been applied to peak induction time to assess initial dose response. Dose of 0 Gy=Sham.

To identify more subtle shifts in the induction of foci, the frequency distribution at 30 min was also investigated. For moderate doses, the majority of nuclei exposed to sham conditions have between 0 and 3 foci per nucleus. This is consistent with previous work at 2 Gy. After exposure to 0.25 Gy and 0.5 Gy the distributions shift to the right showing induction of 53BP1 foci and more nuclei have >9 foci but this is subtle compared to that observed after exposure to 1 Gy. No difference in the distribution of 53BP1 foci was seen by 8 hrs (data not shown). For shams, the modal average number of foci is consistently 0.
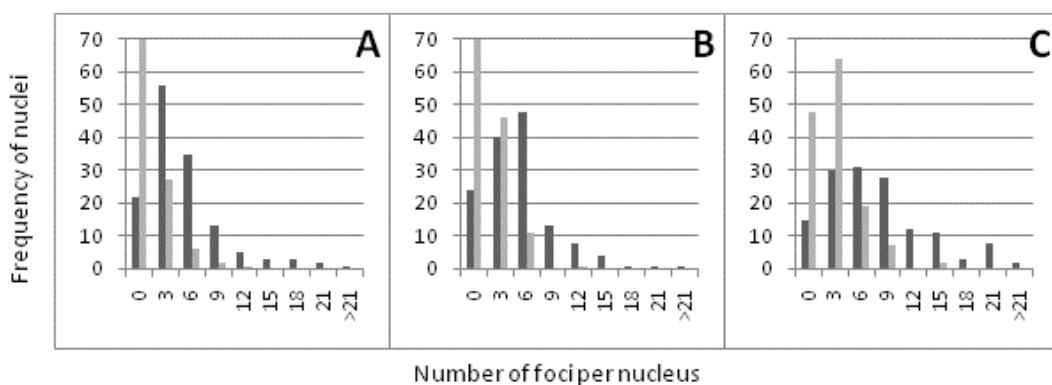
Figure 4-12 53BP1 foci induction at low and moderate doses of γ-rays
HBEp cells were exposed to 0.25Gy (A), 0.5Gy (B) and 1Gy (C) γ-rays and scores shown as frequency distribution. Shams are shown as grey bars and black bars for irradiated.

For the time points investigated, a near linear dose increase in the induction of 53BP1 foci is observed (Figure 4-11), however further sampling time points are needed to validate this.

4.2.4 Induction of 53BP1 foci after exposure to high-LET α-particles

4.2.4.1 Optimisation of irradiation setup using high LET α-particles

To assess the radiobiological response of HBEp cells to single α-particles the fluence must first be calculated based on the dimensions of the nucleus. Preliminary tests to measure nuclear and cellular dimensions on Mylar were unsuccessful due to the poor optical qualities of Mylar. Using the methodology described in section 2.2.3.2 nuclei were visualised by staining with the cytoplasmic stain $DiOC_6$ (Figure 4-13) and measurements taken for cellular and nuclear diameter and height.
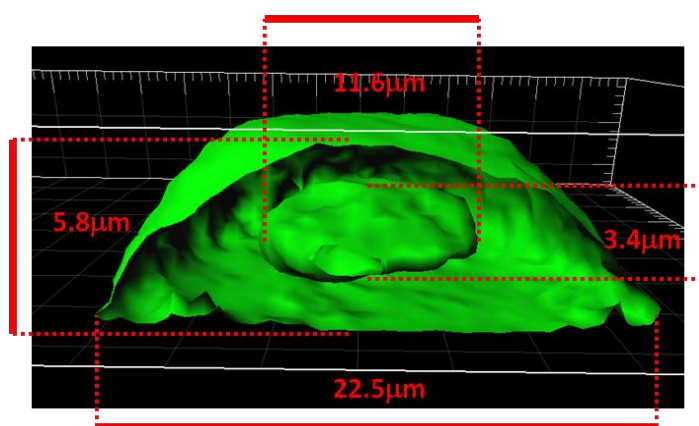
Figure 4-13 Three dimensional rendering of HBEp cell
Cytoplasm was stained with $DiOC_6$ (green) enabling dimensions of cell and nucleus to be determined. The average of diameter and depth of HBEp cells are shown in red. (Volume of ellipsoid = $[4/3]\pi r1r2r3$)).

The objective was to expose cells to an incident LET within the range of 120-150keV/μm and to visualise the track length along the x-y axis of the nucleus by subsequent 53BP1 staining. To do this using the Gray Laboratory source required the Mylar dish to be irradiated at a 20° angle from the base of the irradiation rig (Figure 4-16) and the temporary removal of the majority of the cell medium.
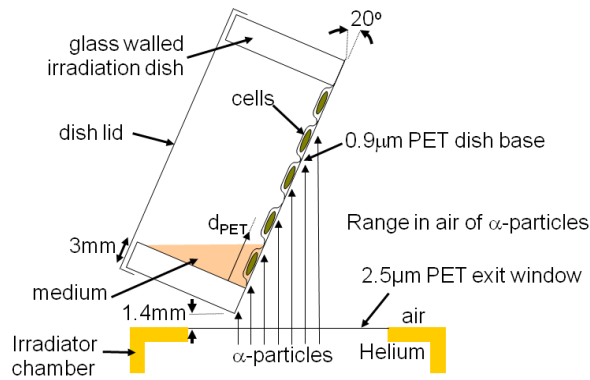
Figure 4-14 Schematic for irradiation with α-particles
Setup for irradiation of HBEp cells cultured on Mylar dishes (cells not to scale). α-particles are in a near-parallel beam through a helium chamber to the dish (image courtesy of Dr Mark Hill).

The range of α-particles in air is very limited (~4cm), α-particles also have a limited ability to penetrate the Mylar base and both of these factors will influence the incident LET at the base of the cells (see Figure 4-15). Thus, the angled design of the irradiation setup, coupled with the use of 2.5µm PET, will increase the incident LET that the majority of the cells are ultimately exposed to.
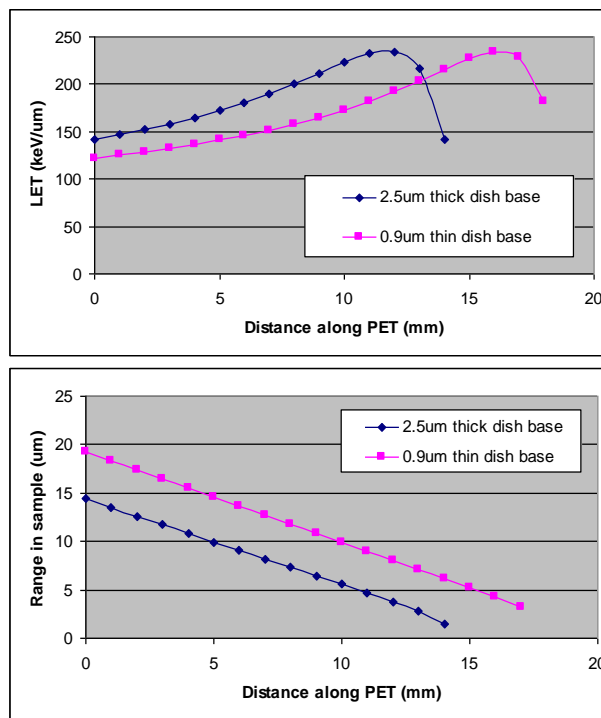
Figure 4-15 LET data for α-particle penetration depths
LET and range of α-particles in relation to distance from point of irradiation on the side of mylar dishes (image courtesy of Dr Mark Hill).

106

Accurate dosimetry measurements carried out after the irradiation process showed that the fraction of dish and therefore the fraction of exposed cells, that received α-particle tracks was limited to only a 2mm strip at the very edge of the dish. The proximity of this 'working area' to the edge of the dish made subsequent microscopic analysis of 53BP1 staining difficult. Images were acquired using confocal microscopy for all nuclei observed to possess 53BP1 α-particle-induced tracks with image stacks taken at 0.2μm internals, see Figure 4-17.
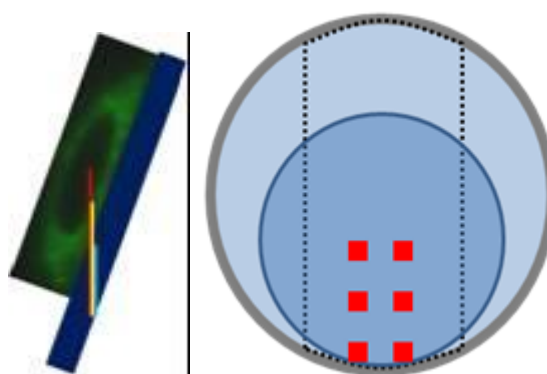
Figure 4-16 Scale drawing of the penetrating abilities of α-particles
In samples at 20° angle there is a relative increase to PET depth. Blue bar represents the PET dish base. Red, yellow and light blue lines represent maximum range of α-particles at 0, 5 and 10mm from the base of the dish. Right: working area for analysis (inner blue circle) is limited by shielding (dashed lines), red squares indicate where images were acquired NB only the bottom two squares were exposed to α-particles.

From the working areas imaged (Figure 4-14 - red squares) it was concluded that the majority of cells on the dish would have been exposed to either a very high incident LET (>200 keV/μm) or nothing (distance of cells beyond the α-particle range).

4.2.4.2 Induction of 53BP1 foci after exposure to high LET α-particles
Fractions of passage 4 to 8 HBEp cells were seeded onto Mylar dishes (PET) as described in section 2.2.2.2.1 and irradiated at ~ 90% confluence with a fluence of 1 α-particle/nucleus, as calculated by Dr Mark Hill and David Stevens, Gray Cancer Institute, Oxford.
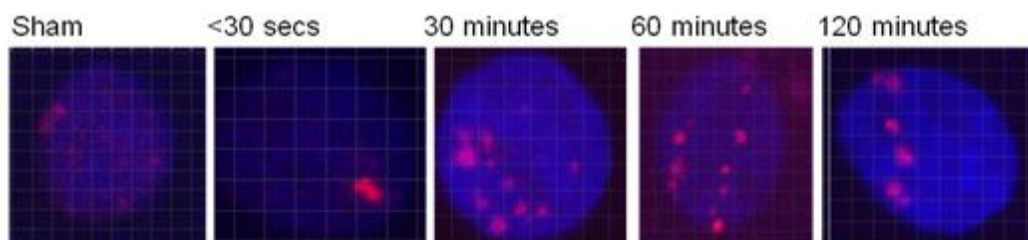
Figure 4-17 α-particle tracks in HBEp cells
Confocal images of HBEp cells labelled for 53BP1 after exposure to a fluence of 1 α-particle/nucleus. Nuclei (blue) can be seen at varying times after irradiation with 1 or 2 tracks of individual 53BP1 foci (red).

General observations show formations of 53BP1 foci in tracks to occur within 30min and that discernible tracks were still visible 4hrs after irradiation (Figure 4-17). The fluence of irradiated cells varied, with some nuclei containing two tracks whilst others contained none, consistent with expectations. It was also noted that the number of foci per track declined with time (Figure 4-18).

The average number of foci per nucleus was calculated using the manual 3D analysis method detailed in chapter 3, size integers were also evaluated (data shown in section 5.2). In cells exposed to sham conditions a very low background of <1 foci is seen, which is not consistent with data from low LET irradiations (Figure 4-18), although this could reflect the lack of transportation that is required directly after γ-ray exposure. A significant induction in the number of 53BP1 foci was observed within 1 min of exposure to ~1 high-LET α-particles, reaching a peak by 30 mins of 5.1 foci/nucleus, reducing to 2.8 foci/nucleus after 4 hrs. A linear extrapolation of this trend suggests the number of foci may return to normal between 16 and 24 hrs.

Revisions to the experiment to account for the high incident LET, including the use of 0.9 μm Mylar were implemented, but further technical complications occurred which meant this data-set could not be verified or indeed extended to assess later time points.
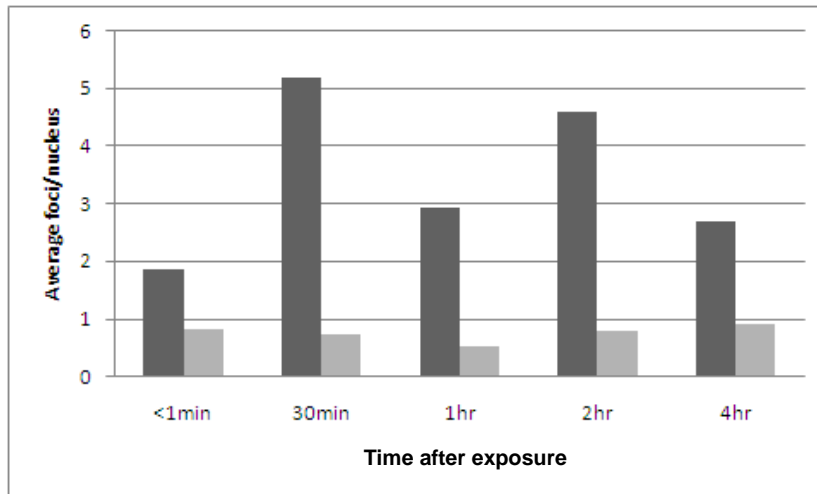
Figure 4-18 Average number of foci /nucleus after ~1 α-particle
Induction of 53BP1 foci in HBEp cells irradiated with ~1 α-particle (dark grey bars) and sham conditions (light grey bars). Significant induction (P<0.05) is seen between shams and irradiated at all times.

4.2.5 DNA DSB in 53BP1-GFP HBEp cells after exposure to low-LET γ-rays

To visualise the real time kinetics of the induction of RIF, immortalised HBEp cells transfected with 53BP1 protein fused to Green Fluorescent Protein (GFP) were monitored after exposure to 2 Gy γ-rays. HBEp cells with 53BP1-GFP, kindly supplied and previously characterised by Asaithamby (Asaithamby and Chen, 2009), were cultured at 37°C and 5% CO_2. The growth characteristics were observed to be similar to those of normal primary HBEp cells and the cell morphology was also similar but it was noted that more cellular debris was present (Figure 4-19).
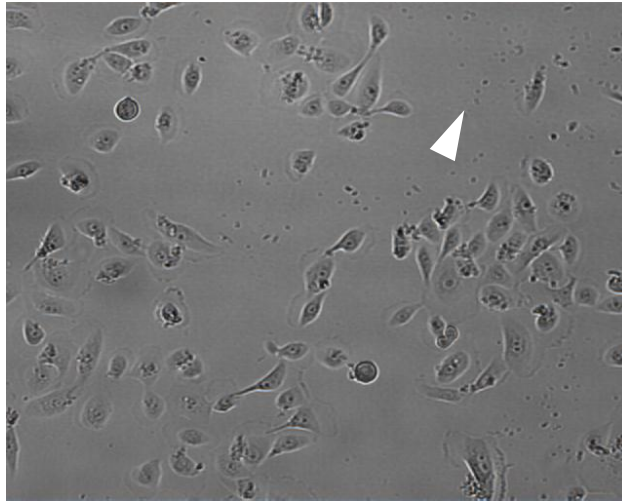
Figure 4-19 Phase contrast image of HBEp cells transfected with 53BP1-GFP
White arrow indicates 'normal' debris associated with culture of transfected cells in selection media.

For live cell microscopy, transfected cells were seeded onto glass bottom dishes, as described in 2.2.4.5. To enable observation of early time points, cells were transported and irradiated on ice. This presented a technical limitation as the change in temperature would often cause condensation to form on the glass dish and the surface to change in size; both factors which directly influenced the ability to focus on cells. Additionally, irradiation on ice may have introduced a lag in the cellular response of 53BP1 as the cellular metabolism returns to normal kinetics (Markova et al., 2007).

To observe 53BP1-GFP foci in live cells a compromise between image capture and preservation of cellular integrity was optimised. Initial time-lapse experiments showed increasing numbers of foci with time, believed to be the result of photo-toxicity and, within 5 hrs, fluorescence signal was lost through photo-bleaching. To resolve these issues neutral density filters were used to minimise fluorescence exposure and only the lower intensity range (most sensitive range) of the camera was utilised to minimise exposure times. Finally, image stacks were reduced to 5 slices at 1μm intervals from the central focal plane once every 5min for the duration of the experiment (17-20 hrs). For shams, cells were exposed to the same conditions but without exposure to radiation. Irradiated and sham experiments were conducted with 24 hrs of each other to minimise possible differences originating from population doublings. Figure 4-20 shows maximum intensity projections for a single nucleus at 10 min, 30 min and 1 hr and hourly after that until 17 hrs. Foci counts at these times show a good correlation with fixed cell data, with the majority of foci seen within 30 min before subsequent decline in number and corresponding increase in size by 8 hrs (Figure 4-20).

In an effort to correlate live and fixed cell data, the number of foci per nucleus was counted for each image in the time lapse for 4 nuclei over duration of the experiment (Figure 4-21). It was noted that nucleus 1 (Figure 4-21 A) shows nominal induction after irradiation but a steady increase in the number of foci up to 7-8 hrs, followed by a gradual decline. For nucleus 2 and 3 ((Figure 4-21 B and C), the trend for induction and decline more closely represents that seen in fixed cell data. However the peak for induction appears to plateau for a longer period, with the decline in number of foci only seen after 4hrs. Nucleus 4 (Figure 4-21 D), shows nominal induction after irradiation, which declines to sham levels within 3 hrs. The responses of these nuclei illustrate the range of responses seen within a population of cells, in particular that the induction of foci is not consistent in all nuclei. Thus, the number of foci for each time point was averaged to more directly reflect the average assessments made from fixed cell data (Figure 4-22).
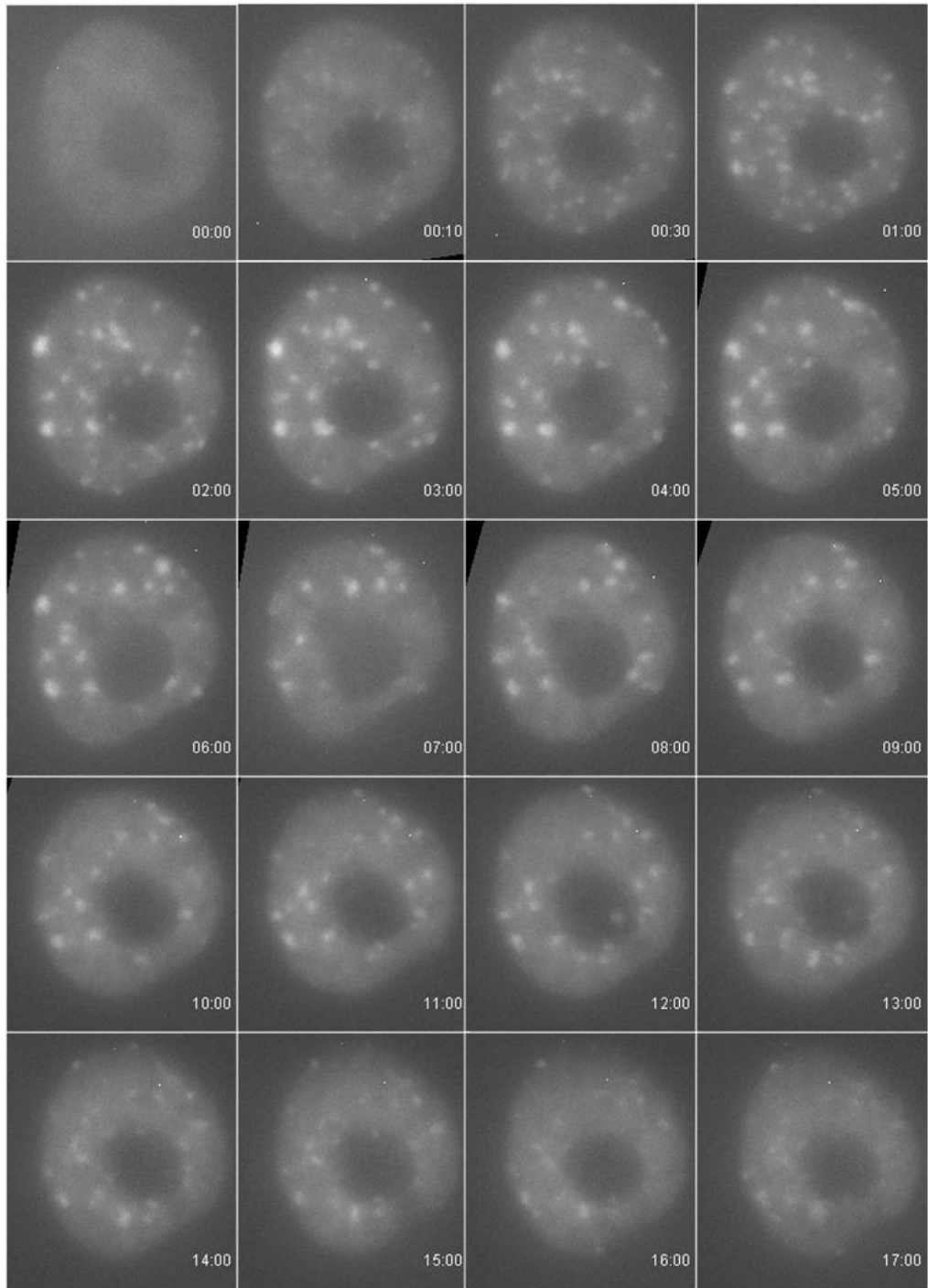
Figure 4-20 Time-lapse images of HBEp cells with 53BP1-GFP
HBEp cells were transfected with 53BP1-GFP visualised at 5min timer intervals, times
indicated are in hrs and mins.
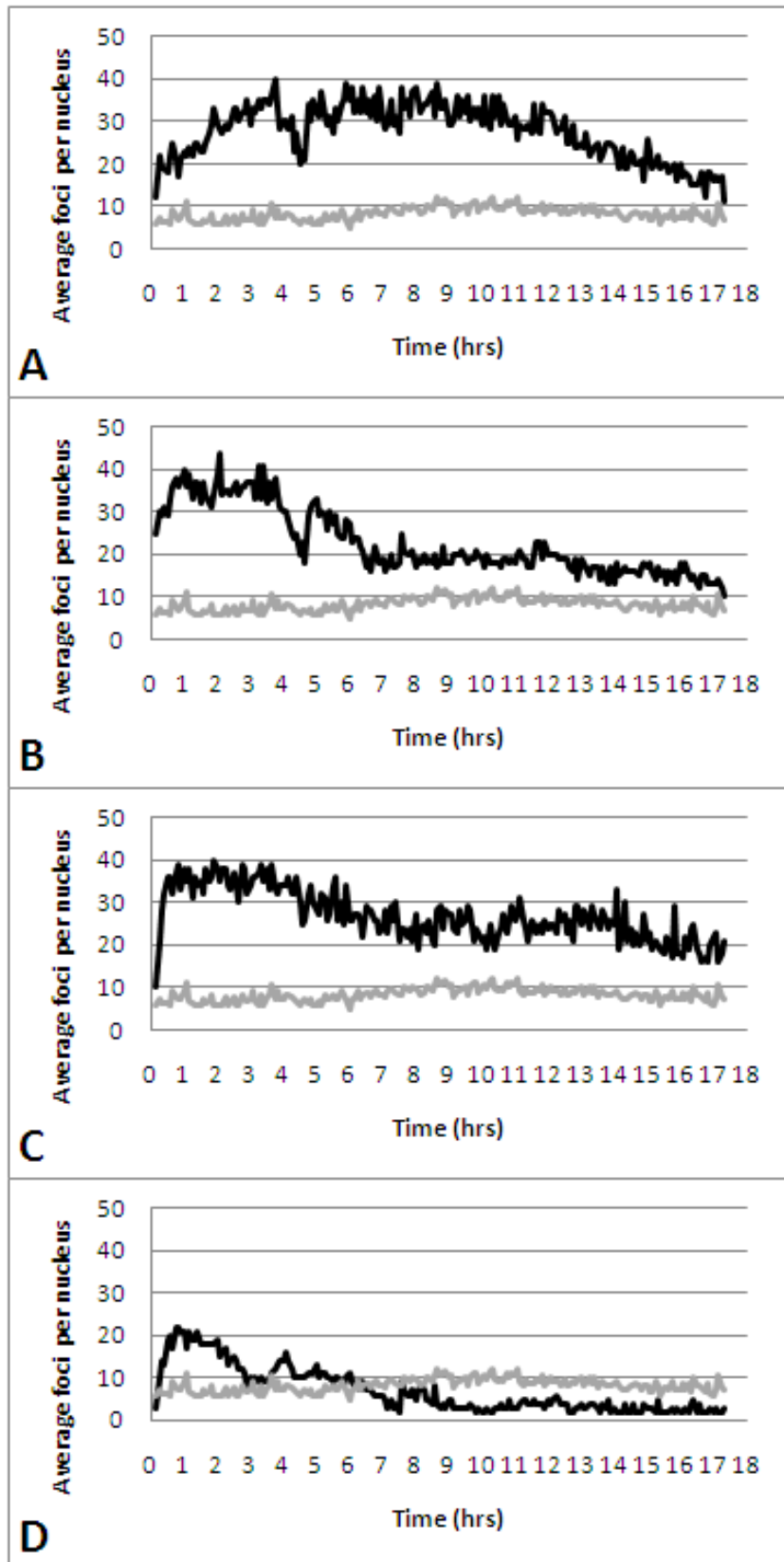
Figure 4-21 Numbers of 53BP1 foci in live cells at 5min intervals
The number of 53BP1 foci were counted in each image over the duration of the time lapse for four nuclei (black lines), the number of foci for shams was taken as an average for the four nuclei (grey lines).
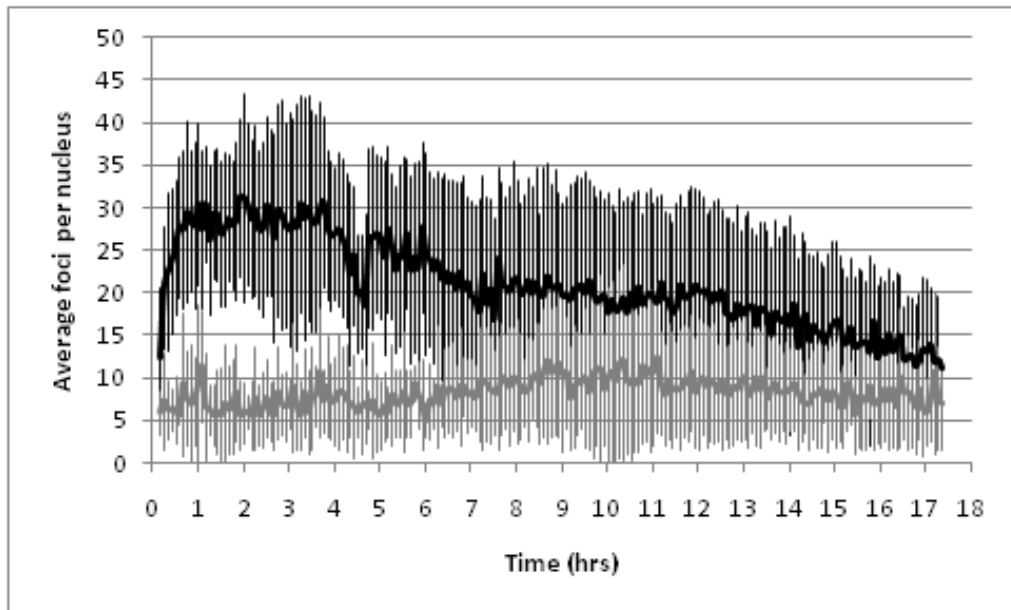
Figure 4-22 Average number of foci per nucleus in live cells
Average number of GFP-53BP1 foci in immortalised HBE cells after 2 Gy γ-rays (black line) or sham conditions (grey line), error bars show standard deviation of the mean taken from three nuclei.

The average number of foci per nucleus (taken for 4 nuclei) shows a more familiar trend for induction and decline of 53BP1 foci. After irradiation the number of foci increased, reaching a peak induction of 31 foci at 1hr:55mins after exposure compared to 4 foci per nucleus in shams. This then declines to 11 foci per nucleus at 17hr:20mins for irradiated and 7 for shams. Assuming linear extrapolation of the irradiated time points, foci would return to sham levels by 20hrs. There is also a subtle increase in the number of foci in shams from ~6 foci at the start of the experiment to ~10 foci after 10hrs of observation. This is likely to be due to photo-toxicity but may be compounded by the cell cycle, as varying degrees of sensitivity at different stages of the cell cycle may contribute to the sensitivity of cells to UV from the microscope. Thus, direct comparisons between GFP-53BP1 and fixed cell data suggest more damage in the GFP cell line. However it should be noted that other investigations have shown the background number of YFP-53BP1 foci to be more comparable to fixed cell data (Asaithamby and Chen, 2009) suggesting YFP to be more stable than GFP.

114

4.3 Discussion

Many studies use a variety of immortalised cell lines to monitor responses to ionising radiation. However, radiobiological responses of these are likely to differ at the genomic, cellular and tissue level when compared to normal cells (Coggle et al., 1986, Bao et al., 1997, Parada et al., 2004). These limitations can be reduced through use of primary cells e.g PBL, however again, different cell types, even from the same microenvironment, are known to differ (Fisher et al., 1991) meaning the responses in radiation target tissues will not be fully explored. Therefore to generate novel radiobiological data that has the potential to contribute to the understanding of how target cells respond to particular qualities and doses of radiation, it is important to study primary normal cells from relevant target tissues.

   In this study, normal human bronchial epithelial (HBEp) cells were used however the use of primary cells has several key limitations. Population doublings in culture technically limit the duration over which cultures can be experimented on. For HBEp cells, significant morphological changes were observed in cells that were grown to later passages (p9) and as a result, cells could only be used for experimentation between passage 4 and 8. Indeed, when cells were grown in aged medium where pituitary extracts has precipitated, morphological changes were also observed. The stage of the cell cycle at the time of irradiation will also determine the fate of a cell in response to radiation (Lukas et al., 2003, Rothkamm et al., 2003, Giunta et al., 2010) and given that most cells of the airway do not go through continuous cell growth, it was optimal to irradiate at the G_0/G_1 phase of the cell cycle. Synchronisation of primary cells through chemical blocks (e.g. Aminopterin, Thmidine, Colchicine etc.) was deemed excessively non-physiological and likely to confound the response to radiation, additionally, there was no guarantee that all cells would synchronously re-enter the cell cycle. Serum starvation is a more physiological method of synchronising cells to induce quiescence but the culture methods used for HBEp cells do not use serum, rather they grow in a specialised, defined medium. Continued culture at 100% confluence can

cause contact inhibition, resulting in a quiescent state, but again this was not deemed practical as HBEp cells cells grown to 100% confluence were shown to have significant morphological changes. Accordingly, it was elected to define what stage of the cell cycle the majority of HBEp cells were in at time of irradiation and to apply the same culture regime for all experiments to ensure reproducibility; flow cytometric analysis showed that ~90% of the cell population were in $G_{0/1}$ phase of the cell cycle when irradiated at ~ 90% confluence.

Protein 53BP1 and γ-H2AX were utilised as a markers of DNA double strand breaks (DSBs). The distribution of 53BP1 in un-irradiated cells shows a lack of protein within the nucleolus region compared to the rest of the nucleus. Investigations have shown nucleoli to increase in size and number after irradiation (Dezawa et al., 1999, Ibragimova et al., 2001) but no such measurements were made in this investigation. However, it was noted that this region rarely contained foci, or contained foci mostly at the periphery of the nucleoli. This observation could be due to either less damage being present, possibly due to less DNA content meaning less of a target or, alternatively, it has been proposed that the lack of foci may reflect the higher proportions of proteins within the nucleolus having a protective effect on the DNA, sequestering free radicals (Sak et al., 2000, Falk et al., 2010). Of course it is also possible that the increased presence of proteins in this area do not allow repair machinery access and so DSBs may exist but foci do not form due to steric hindrance.

The accurate quantification and measurement of foci is critical to ensure consistency when comparing results to published works. For instance, significant differences in the induction and decline of foci may not be the result of radiobiological factors but the method used to identify/score them. The method developed in chapter 3 and employed in this study has been rigorously validated and has been demonstrated to be reproducible between experiments.

For HBEp cells exposed to sham conditions an average of 2 foci per nucleus was observed, consistent with literature (Asaithamby and Chen, 2009, Gerashchenko and Dynlacht, 2009, Lee et al., 2009). This

average is effectively 'evened out' by cells that were dividing at the time of irradiation and also G_2/S phase nuclei, as demonstrated by analysis of the modal average (0 foci at 4 and 8hrs) and distribution of foci which ranges from 0-20 (Figure 4-9). The large proportion of un-irradiated nuclei with one or two foci has been suggested to be the result of endogenous DSBs, resulting from stalled replication forks or other lesions (Branzei and Foiani, 2010, Harper et al., 2010). Persistent 53BP1 foci associated with previous damage believed to be linked to DNA lethal lesions and to poor cell survival (Banath et al., 2010). Other possible explanations as to the range and presence of 53BP1 foci in shams are that 53BP1 has been implicated in maintaining the integrity of the fragile regions (Lukas et al., 2011) and also in the promotion of mobility for telomeres (Dimitrova et al., 2008).

After irradiation the homogenous 53BP1 background staining is reduced as most of the 53BP1 proteins re-localise into discrete foci at the sites of DSBs. After 2Gy [60]Cobalt γ-rays (0.31-0.33 Gy/min) a statistically significant increase in the average number of RIF per nucleus occurs within 6 min (20 foci), peaking to 22 foci 30 min after irradiation, which is consistent with similar investigations measuring peak induction of RIF (Rogakou et al., 1999, Schultz et al., 2000, Rappold et al., 2001, Torudd et al., 2005) but is slightly lower than expected for similar cell types (Costes et al., 2007, Asaithamby and Chen, 2009, Groesser et al., 2011). This lag between damage and peak foci induction has also been recorded in other cell types using a variety of imaging techniques, and can vary between 20 min and 1 hr (Schultz et al., 2000, Anderson et al., 2001, Banath et al., 2010). This consistency between cell types and optical systems suggests the lag is not entirely due to optical sensitivity but may be due to the kinetics for the recruitment of the 53BP1, which is suggested to be downstream of other factors such as MDC1 (Goodarzi and Jeggo, 2009). The duration of a lag phase is likely to be dependent on dose and quality of radiation as higher doses and LET radiation will have more ionisation events which may lead to faster sequestering of 53BP1. At high enough doses there may even be saturation of damage where insufficient protein is available.

After peak induction, the average number of 53BP1 foci declines. This decline appears to have two phases, which could be due to the number of DSBs declining at this rate (foci dispersal = DSB repair) or it could be that some foci are not dispersed as rapidly and so the dispersion kinetics of 53BP1 do not mimic the repair kinetics. It has been suggested that there are two phases to the repair of DSBs (Goodarzi and Jeggo, 2011) and that 53BP1 is used primarily in the slow method for repair. After an initial rapid decline in the number of RIF from 22 foci at 30 min to 8 at 8 hrs, the rate of decline is reduced taking a further 16 hrs to reach sham levels. This may be the result of ineffective dispersion of 53BP1 from larger foci, however, there is evidence suggesting removal of 53BP1 to be an active and rapid process (McManus and Hendzel, 2005).

Through live cell analysis it is possible to observe the kinetics of 53BP1 foci in real time in vitro. In the analysis carried out in section 4.2.5 a compromise was made to enable the long term visualisation of foci to reflect the time-course in Figure 4-7. Image stacks with relatively large step sizes were used to preserve the biological validity of the experiment. Unfortunately, although not in the original design, these images were analysed as maximum intensity projections due to problems with the computer hardware at the image analysis (Imaris) processing step. These factors combined to restrict the axial detail and therefore limited some of the more detailed conclusions that could be drawn. Due to time limitations only 4 nuclei of immortalised HBEp cells with stably transfected 53BP1-GFP expression were analysed, yet more foci were observed than in previous fixed data using primary cells and even other investigations using the same cells (Asaithamby and Chen, 2009). It is likely that the elevated frequency of 53BP1 foci for shams is most likely to be the result of the small sample size used in combination with UV-induced DSB as the number of 53BP1 foci was also observed to increase in un-exposed cells during the course of the experiment highlighting phototoxicity issues from the fluorescence microscope.

In cells irradiated with 2 Gy γ-rays, the lag between exposure and peak induction was increased to ~1 hr (Figure 4-22), as opposed to 30 min

for fixed cell data (Figure 4-7). This increase in response time has been hypothesised to be the result of transporting cells on ice, which will slow the cellular metabolism and subsequently the kinetics for 53BP1 foci may be delayed (Markova et al., 2007). Indeed, it was noted that the foci intensities appeared to lag behind the induction, which may be indicative of protein dynamics for signal expansion. Additionally, the decline in the number of foci was also delayed compared to fixed cell data, with numbers of foci not beginning to decline until 4hrs post irradiation. Once again this can be attributed to the effects of transit on ice and the continual observation using UV, which may be propagating the presence of 53BP1 foci through the induction of additional DNA lesions. The different responses of individual foci have been observed in similar investigations but no mechanism has been suggested (Cao et al., 2010). A linear decline in the number of foci then occurs over the remainder of the experiment, with a trend suggesting the average number of foci to return to sham levels 20 hrs after irradiation, consistent with previous data. Thus, the two phase decline in the average number of foci was not apparent in live cell studies. Clearly the sample size for this form of analysis is limited and additional experiments need to be conducted to generate more detailed conclusions.

Utilisation of sensitive optics and computer aided analysis has enabled the detection of RIF at very low doses (Ishikawa et al., 2010, Roch-Lefevre et al., 2010). It appears there may be a threshold for response at very low doses (<0.1 Gy), this may be due to the background level of foci masking any visible response or that the response is not initiated until a threshold dose is delivered. After exposure to doses lower than 2 Gy (0.25-1.0 Gy γ-rays) a linear dose response is seen (R^2=0.9561) in HBEp cells. This linear scale originates from the background level of 2 foci per nucleus in shams, increasing at a rate of ~10 foci per Gy.

The variance of the average number of foci per nucleus is likely to be spread by the absence of 53BP1 staining in nuclei with condensed chromatin (Giunta et al., 2010, Lukas et al., 2011) The restriction of 53BP1 foci to G_0/G_1 cells is likely to spread the distribution of average foci scores

as nuclei with damage and labelled DSBs may not recruit 53BP1 (FitzGerald et al., 2009). The increased sensitivity of nuclei during replication is believed to result in a small proportion of nuclei with higher than average numbers of foci, commonly referred to as 'S-phase' cells, indicating they were most likely in the S/M phase of the cell cycle at irradiation (Dickey et al., 2009). The combination of these factors is likely to have spread the distribution and lowered the overall average number of foci scored.

In summary, an average of 22 53BP1 foci are induced HBEp cells 30 min after 2 Gy γ-rays with a rapid decline over a 6 hr period to 10 foci per nucleus before restoration to sham levels at 24 hrs. These kinetics closely match similar observations in other, non-primary, cell types (Leatherbarrow et al., 2006, Asaithamby and Chen, 2009, Groesser et al., 2011)

5 Spatiotemporal relationship of foci number and size

5.1 Introduction

The number of radiation induced foci (RIF) has been linked to the number of DSBs within a cell nucleus and their induction and decline has been closely investigated by numerous researchers (Schultz et al., 2000, Anderson et al., 2001, Rothkamm and Lobrich, 2003, Leatherbarrow et al., 2006, Markova et al., 2007, Su et al., 2010). With the development of more sophisticated imaging and analysis tools more labs are now measuring foci size as well as number, and it has become clear that the size of RIF increases with time after exposure (Aten et al., 2004, Desai et al., 2005, Krawczyk et al., 2006). Whether this increase is foci size is a consequence of the accumulation or propagation of protein, irrespective of the repaired nature of DSBs (Kruhlak et al., 2006, Yamauchi et al., 2008, Suzuki et al., 2010), due to the clustering of multiple, proximal, DSBs (Lisby et al., 2003, Aten et al., 2004, Lisby and Rothstein, 2004, Costes et al., 2007) or due to complexity of DSB lesion initially-induced, is under debate. What does appear clear is that larger RIF are typically more persistent and are closely associated with cell lethality (Banath et al., 2010), therefore, these arguments may not be exclusive.

The spatiotemporal dynamics of chromatin in mammalian cells has been shown to be limited in live cells (Kruhlak et al., 2006, Soutoglou et al., 2007). This observation suggests DSBs are incapable of movement and therefore the illegitimate rejoining of chromatin must be the result of chromatin already in contact before the break, referred to as "contact first". Alternatively, chromatin has been hypothesised to be actively recruited to centres for repair, as they do in *Saccharomyces cerevisiae* (Savage, 2002, Lisby et al., 2003), referred to as "breakage first". These two theories are not mutually exclusive, and 53BP1 has been shown to promote mobility of DSBs (Nelms et al., 1998, Dimitrova et al., 2008), suggesting that the larger foci could be encompassed in clouds of mobility promoting proteins to aid rejoining of separated chromatin.

There have been two principal methods for the measurement of foci sizes. The simplest form is to measure the diameter of foci (Schettino et al., 2010, Suzuki et al., 2010). A more accurate method for the measurement of foci is the identification of area or volume, which requires more accurate segmentation of the foci across the boundary; methods for such identification and segmentation of foci are detailed in chapter 3. The accurate measurement of focus size and determination of their relative distribution throughout a cell nucleus should enable scientists to generate new theories on the dynamics of foci. The purpose of this chapter is to identify any trends in focus size and relative distribution in order to contribute to understanding the processes that lead to the illegitimate repair of DSBs.

5.2 Quantification of relative foci size

The relative size of 53BP1 foci was observed to increase in HBEp cells with time after exposure to ionising radiation. This phenomenon has been described by numerous authors, in particular, this concept has been explored to evaluate the possibility that multiple RIF cluster as a function of DSB repair (Aten et al., 2004). The purpose of this work was to characterise any difference in the number of different sized foci at different times after exposure to ionising radiation. Measurements of foci size were made using the in-house automated analysis system and manual analysis methods described in chapter 3.

5.2.1 Semi-quantitive analysis of focus size

In brief, foci were categorised based on their diameter (extrapolated from volume for automated analysis) into three size integers; small (<0.5µm diameter), medium (0.5-1.0 µm diameter) and large (>1.0 µm diameter). General observations of HBEp cells exposed to 2 Gy γ-rays shows that foci at shorter times after irradiation (30 min) have many small punctuate foci whilst later times have fewer large foci (Figure 5-1).
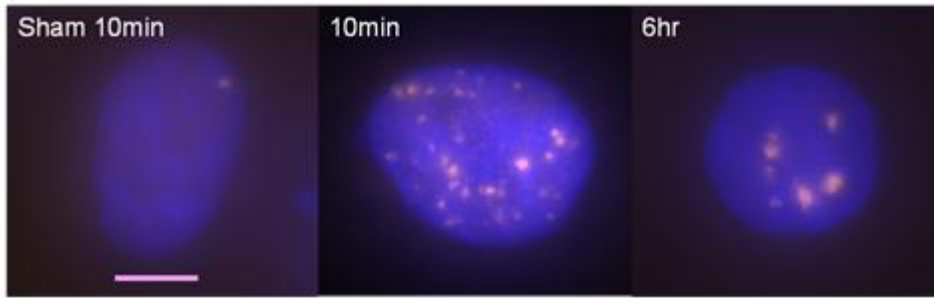
Figure 5-1 Typical staining patterns for 53BP1 in HBEp cells
HBEP cells after exposure to 2Gy γ-IR, fixed in 3D and stained for 53BP1 (red) and chromatin (blue)

Quantification of this change in size was achieved using the manual and automated methods described in chapter 3. There is a clear increase in the number of all three size integers after exposure to γ-rays and by 24hr the average number of foci/nucleus has returned to sham levels. However, the proportions of foci sizes at this time do not correlate to shams and on average, residual foci at later times appear to be larger than equivalents not exposed to radiation.
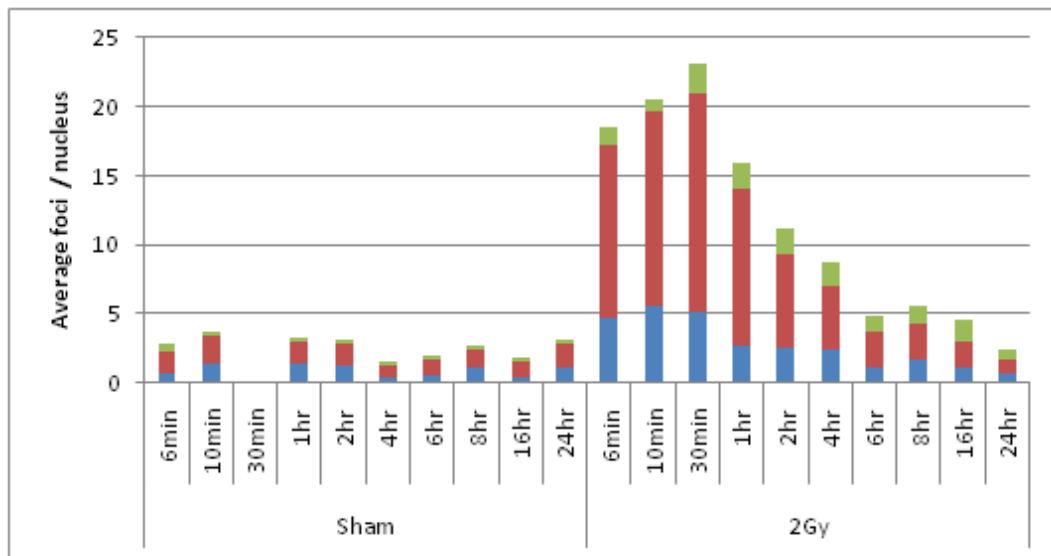
Figure 5-2 Induction and decline of foci by size category
Average number of small, medium and large foci per nucleus in HBEp cells after 2Gy γ-rays or sham exposure, as scored using automated analysis methods. No significant difference between automated and manual results were observed (P<0.05).

The data shows there is no significant difference in foci size with time in shams for these experiments (Figure 5-2), therefore the averages for all time points for each size integer were pooled in shams to generate a

123

single average for all time points. This is depicted as a line for each size which are 0.916 0.449 and 0.317 foci/nucleus for small, medium and large sized foci, respectively. To make comparisons between size integers, data has been presented as clustered columns for each time point (Figure 5-3).
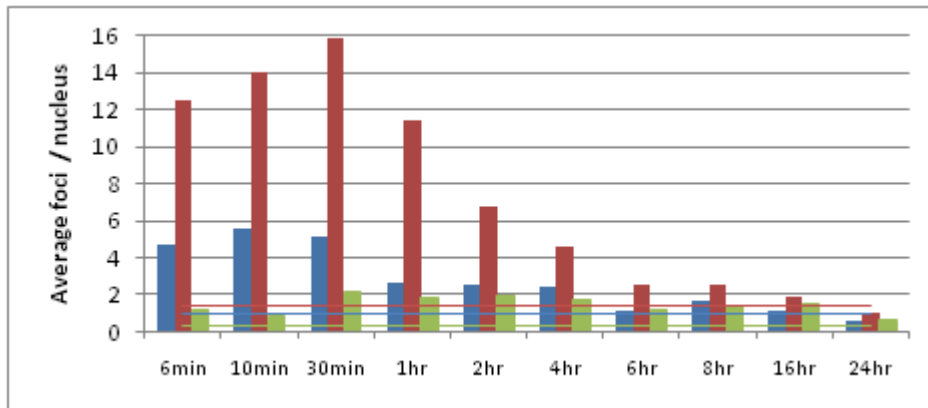
Figure 5-3 Average number of foci by size category over 24hr
Small (blue), medium (red) and large (green) foci have been categorised based on extrapolation of volume size. Coloured lines show average size proportions for shams.

After exposure to 2 Gy γ-rays, a maximal induction of small foci is seen within 10 min (5.6 foci/nucleus), which then declines rapidly from 30 min (5.3 foci/nucleus) to 1 hr (2.6 foci/nucleus) after irradiation. The peak induction of medium sized foci lags behind the peak for small foci and is 15.9 foci per nucleus at 30 min, declining to 11.4 after 1 hr and 2.5 within 8 hr. The average number of large foci in shams is negligible but significantly, large foci increased in most time points after exposure to γ-rays. To identify trends between size integers, each size integer must be normalised to account for the change in number of foci per nucleus over time. The simplest method to normalise the data is to show it as a proportion of the total number of foci. As with previous data, shams have been pooled for comparison.
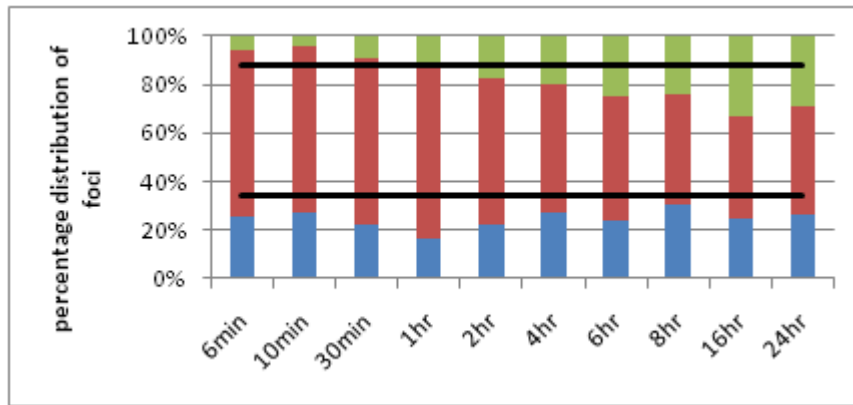
Figure 5-4 Proportional distribution foci by size after 2Gy γ-rays
Proportions are of total foci for that time point. Black bars represent proportions of small (below bottom line), medium (between lines) and large (above top line).

In shams, only 12% of foci are categorised as large (above top line), small (below bottom line) and medium (between lines) foci account for 34% and 54% of all foci respectively. This distribution shifts after irradiation with a decline in the proportion of small and a relative increase in proportion of medium sized foci up to 1 hr (Figure 5-4). After 2 hr, the proportion of large foci is seen to increase above shams levels, increasing with time, reaching a maximal of 33% by 16 hr, declining to only 28% after 24 hr. The trend for an increase in the proportion of large foci with time, coupled with the relative decline in the proportion of small and medium sized foci suggests one of two scenarios is occurring. Either; the majority of small and medium foci are dispersing whilst others grow into larger foci, or smaller and medium sized foci are clustering together to form larger foci.
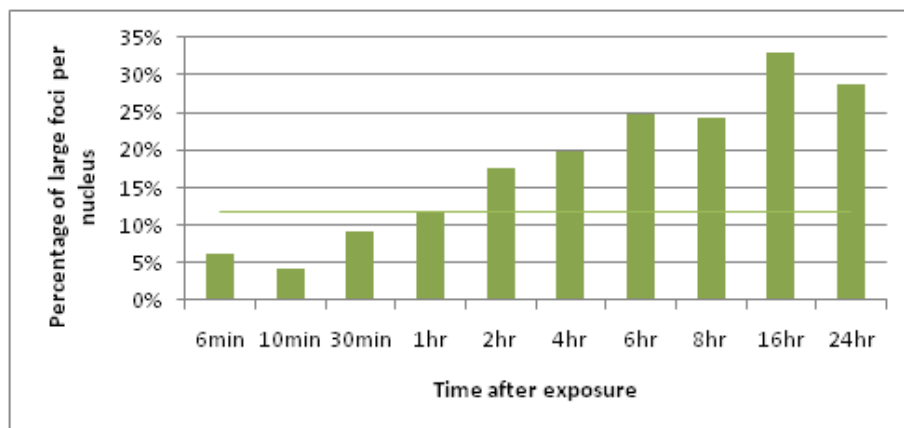
Figure 5-5 Percentage of large foci/nucleus after 2Gy γ-rays.
The proportion of large foci, as a percentage of total foci for that time point, is shown to increase with time. Data from shams has been pooled for comparison (line).

125

To assess the effect of dose, the number of 53BP1 foci were quantified 30 min and 8 hr after exposure to 0.25, 0.5 and 1 Gy γ-rays. These times were selected based on the 2 Gy data presented above. For all size categories there is a significant induction in the number of 53BP1 foci above sham levels (Figure 5-6). The relative number of medium foci is seen to increase with dose, in what appears to be a linear response from sham levels at 0.6 foci per nucleus. The number of large foci is also seen to have a dose response suggesting there is no threshold for the induction of medium and large foci with dose. The majority of RIF are apparently repaired 8hr after irradiation as the numbers of all size integers decreases to ~ sham levels (0.25 Gy) or slightly elevated above sham (0.5 and 1 Gy) (Figure 5-6).
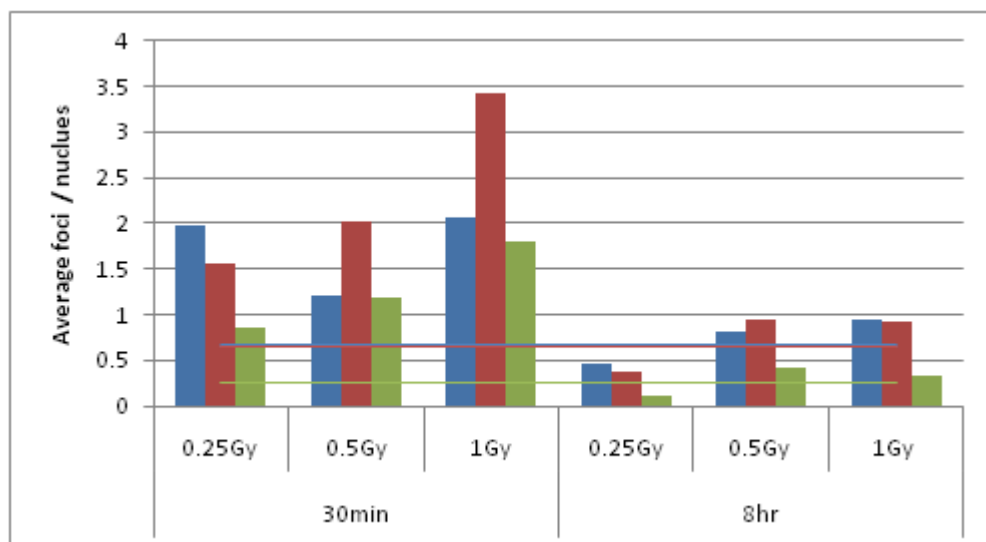
Figure 5-6 Dose response by size category
HBEp cells fixed 30min and 8hr after exposure to moderate doses of γ-rays. Time points were selected based on peak induction for medium and large foci at 2Gy. Average numbers for shams are shown as lines.

To identify changes in the proportions of each size integer it is therefore desirable to use higher doses as to induce sufficient number of large and medium sized foci for analysis.

To assess the effect of radiation quality, HBEp cells were exposed to a fluence of ~1 α-particle per nucleus and fixed immediately (<1min), 30min, 1hr, 2hr and 4hr after exposure (for details see chapter 4). Immediately after exposure to high LET α-particles only small foci are

seen to be induced above sham levels (Figure 5-7). As a proportion of the total number of foci per nucleus at each time, the proportion of small foci appears to decline whilst the proportion of medium foci increases from 30 min to 2hr (Figure 5-7). The proportion of large foci is only seen to increase 4hr after irradiation. This data correlates with induction of 53BP1 foci after low LET radiation, suggesting the increase in focus size after exposure to IR is independent of radiation quality, but it is unlikely that large foci from low and high-LET radiations are equivalent.
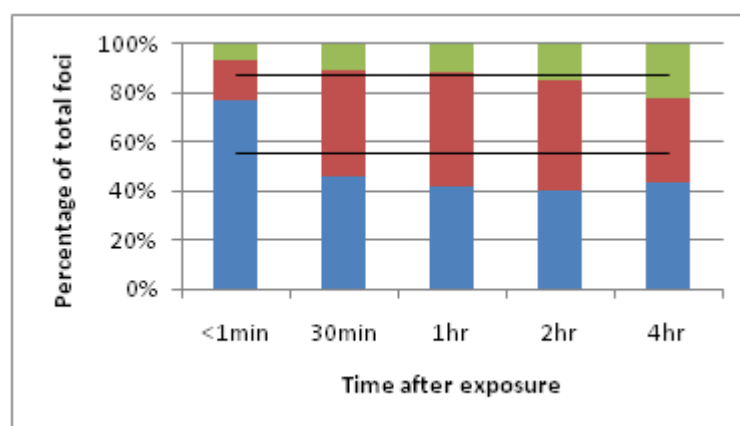
Figure 5-7 Proportional distribution of foci sizes after ~1α-particle/nucleus
Proportions of foci were determined from average foci scores for each time point as scored using the manual 3D scoring method. Lines represent sham distributions (below bottom=small, above top = large and between = medium).

5.2.2 Quantitative analysis of focus size

One key benefit to automated analysis over manual categorisation of foci size is that automated results are not qualitative but are continuous and can generate quantitative data of the foci area and/or volume depending on the mode of image acquisition (2D, MIP or 3D stack). This is possible, in part, due to the accurate identification of a focus boundary (chapter 3) whereby the edge of a focus is more consistently and accurately defined.

A comparative quantification of the co-localisation experiment performed in chapter 3 was carried out to measure the area of both 53BP1 and g-H2AX in MIP images, at selected times after irradiation (Figure 5-8). Both 53BP1 and γ-H2AX foci show significant increases in their relative areas compared to sham after irradiation ($P<0.05$), however it is only the 53BP1 foci that subsequently increase their area with time (Figure 5-8).
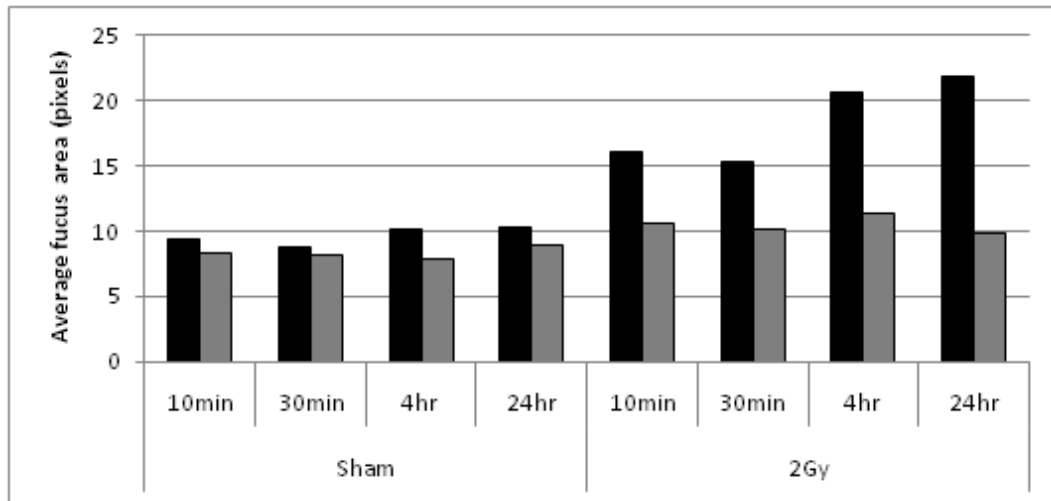
Figure 5-8 Average focus area for 53BP1 and γ-H2AX
Average area of 53BP1 (black bars) and γ-H2AX foci (grey bars) is shown after 2Gy γ-rays or sham conditions.

Specifically, the average area for 53BP1and γ-H2AX foci in sham nuclei is 9.6 and 8.3 pixels respectively. After exposure to 2 Gy γ-rays the average area for 53BP1 increases to ~15 pixels at 10 min and 30 min, and ~21 at 4hr and 24hr. For γ-H2AX foci, the average area is significantly increased in all irradiated samples from 8 pixels to 11 pixels, but no increasing trend is observed over time. Manual thresholding of the same data for co-localisation analysis reveals similar results but with larger relative foci sizes (data not shown).

A more detailed quantification of foci volume (based on 3D stacks) shows a similar trend to that observed with semi-quantitative methods, where an increase in the volume of foci is only apparent after 8hr (Figure 5-9). Up to 8hr after irradiation the average volume of 53BP1 foci is highly variable with no significant difference between shams and irradiated samples. After 8hr, there is an increase in the average volume of foci and by 16hr the average volume is 156 voxels, compared to an average of only 73 voxels for shams at the same time (Figure 5-9). This is consistent with the proportional increase in the number of large foci at the same time (Figure 5-4).
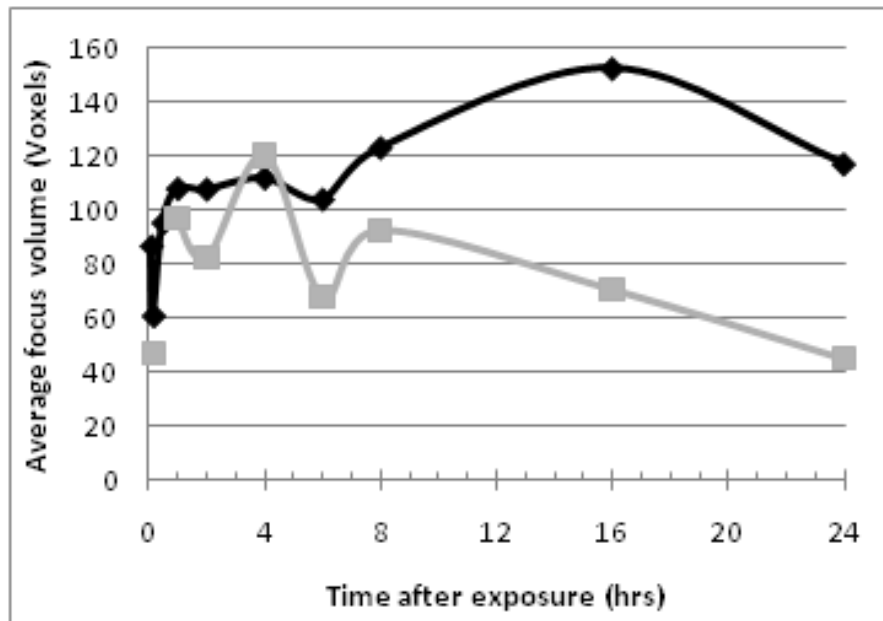
Figure 5-9 Average 53BP1 focus volume in voxels
Focus volume is measured in voxels at varying times after 2Gy γ-rays (black line) or sham conditions (grey line) as measured using automated analysis.

Overall therefore, 53BP1 foci increase in volume as a function of time after irradiation. A number of biological explanations may account for this (see section 5.1), including the clustering of independent small/medium foci such that they are ultimately resolved as large. Although this interpretation is not supported by the lack of area increase observed with γ-H2AX (Figure 5-8), it is noted that the γ-H2AX data-set is limited and not verifiable in this study, furthermore, the data generated from the in-house automated analysis system lends itself to being exploited to address this question. However, data obtained on area and volume must be interpreted with caution; only trends can be identified as the lack of replicates prevents statistical analysis of significance.

5.3 Assessing evidence for clustering of foci

To assess for evidence of clustering of individual 53BP1 foci, a number of approaches were employed. Firstly, the relative x,y,z positions of foci were measured in fixed cells to assess if there is a change in the relative distance between foci over time. Secondly, the position of foci relative to chromosome territories was assessed to identify trends in foci distribution relative to nuclear structures, at various times after irradiation, thirdly, the

composition of larger foci was examined to determine if the proportion of larger foci contained multiple peaks of intensity possibly indicative of multiple DSBs and fourthly, 53BP1 foci were monitored in real-time by live cell microscopy after irradiation.

5.3.1   <u>Measurement of relative foci positioning in fixed HBEp</u>
         <u>cells</u>

Data extracted from automated analysis (see chapter 3) provides the spatial coordinates (x, y and z) for each focus which can then be used to determine the relative distances of each focus to all other foci within that nucleus. These distances can then be used to assess trends in the relative distribution of all foci over time. To compare these measurements at different times, two variables must be considered firstly, that the number of foci is not fixed and that a non-linear change in the number of foci is seen with time after exposure, therefore, as the number of foci increases/decreases it becomes more likely that foci will be more proximal/distant to each other. The second factor that must be considered is the density of foci, determined by the number of foci and the area of the nucleus.

      To determine the relative distribution of foci a nearest neighbour method was adapted (Clark and Evans, 1954, Clark and Evans, 1979). The nearest neighbour was estimated to be the smallest distance measurement extracted from the x, y, and z coordinates, excluding zero values. This can then be normalised to a unit area to generate an observed distribution of distances between foci (rA). The expected distances are obtained by dividing the observed number of foci by the area the occupy and the distances that could be expected (rE). The ratio of observed to expected then identifies the randomness of a distribution (R value). Numbers closer to 0 represent very clustered distributions whilst number closer to 1 represent randomness. Where objects are maximally spaced the R value will reach 2.1491.
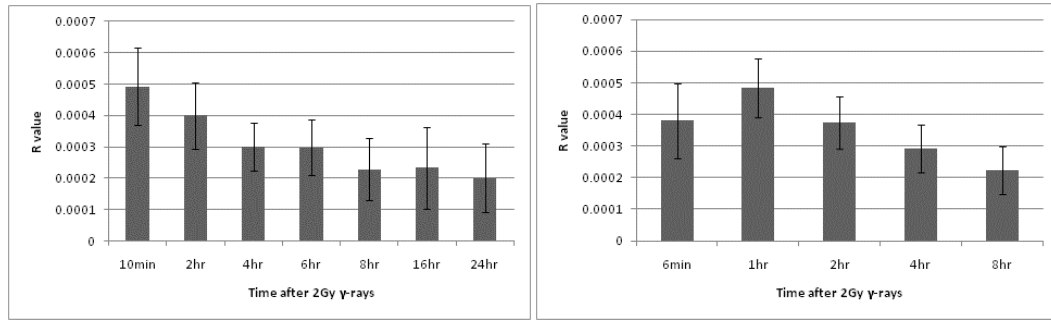
Figure 5-10 Nearest neighbour analysis
R-values from two independent experiments where HBEp cells were irradiated with 2Gy
γ-rays and allowed to recover for the indicated times, error bars show standard deviation
of the mean R-value.

For all experiments and time points the R-value was very low due to the
very low number of foci voxels per nucleus, compared to the significantly
larger volume of the nucleus (Figure 5-10). Thus, according to Clark et al
1954 the R-value depicted indicates a high degree of aggregation. In two
independent experiments, the R-value was seen to decrease as a function
of time after irradiation, with a slight increase only being observed
between 6 mins and 1 hr possibly reflecting peak induction of 53BP1 foci.
After 24hr R-values match shams (data not shown).

This slight change in R-value over time may suggest an increase in
clustering with time after irradiation. However, this method neglects to
incorporate the volume of foci when considering the nearest neighbour. As
the measurement is taken from the centre of homogenous mass, larger
foci may therefore be more proximal than assumed here, as the distance
from edge to edge may be different to centre to centre measurements.

5.3.2 Assessing peaks of intensity within larger foci for evidence of clustering

The automated analysis system developed in chapter 3 has been shown
to be effective at identifying the outline of foci, including the frequently
irregular outlines of larger foci. To assess for evidence of clustering, the
larger foci were examined in more detail to determine if their constitution
could provide evidence of clustered smaller foci. To do this, an automated
analysis system developed by Dr Costes (Lawrence Berkley National

132

Laboratory, USA) (Costes et al., 2006) , which identifies foci using a different algorithm to the in-house system, was used to re-analyse sets of 3D image stacks to ask whether more information could be extracted on each focus. The method developed by Costes et al (2006) often identifies multiple peaks of intensity within large foci, which are then discriminated through the process of water-shedding. Due to this different approach the system can potentially count more foci in the same data-set compared to the in-house system (see Figure 5-11) and may be able to discriminate more subtle differences between signal intensities of large foci.
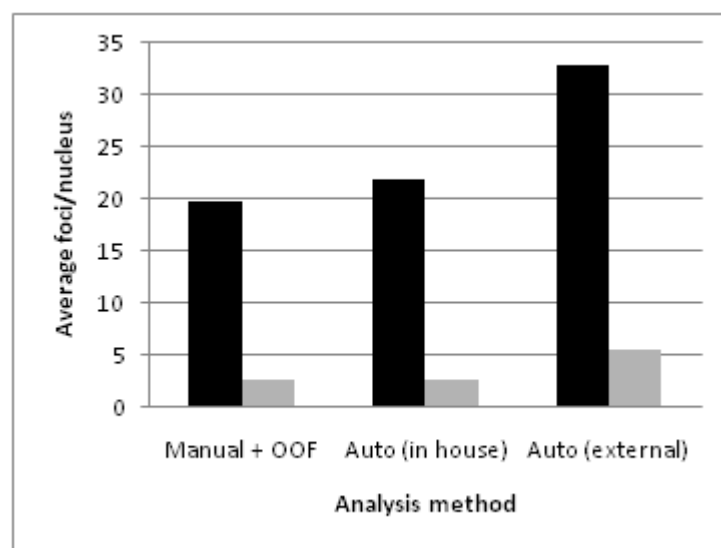
Figure 5-11 Comparison of automated analysis methods
The average number of foci per nucleus in HBEp cells after 2 Gy γ-rays (black bars) or sham conditions (grey bars) as counted the 'in house' system or with Dr Costes system. . Both are compared to manual analysis counts for comparison.

A comparison of analysis systems using the same 3D images, confirms that more foci are detected using Costes et al analysis software (Figure 5-11). This increase in foci number is believed to be due to large foci being resolved as multiple smaller foci in close proximity, see Figure 5-12. In the example shown, the largest foci (red arrow) is shown to consist of 4 peaks of intensity and in another large focus (green arrow) two sub-foci and a third that is very proximal are clearly seen.

133
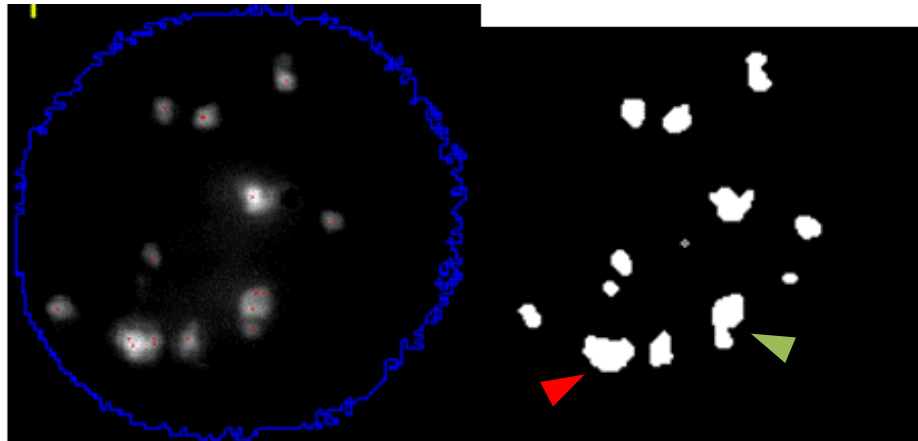
Figure 5-12 determining composition of large foci with differing analysis methods
Processed images from Costes et al (2006) (left) and in-house (right) analysis systems.
Red spots indicate peaks of intensity whilst the in-house system generates a binary
image for comparison. Arrows indicate where larger foci have been resolved as multiple
smaller foci.

To quantify the number of large foci (as counted using the in-house
system) that could be discriminated as consisting of smaller sub-foci, and
also to assess whether this altered as a function of time, all large foci at
selected time points were manually analysed (Figure 5-13).
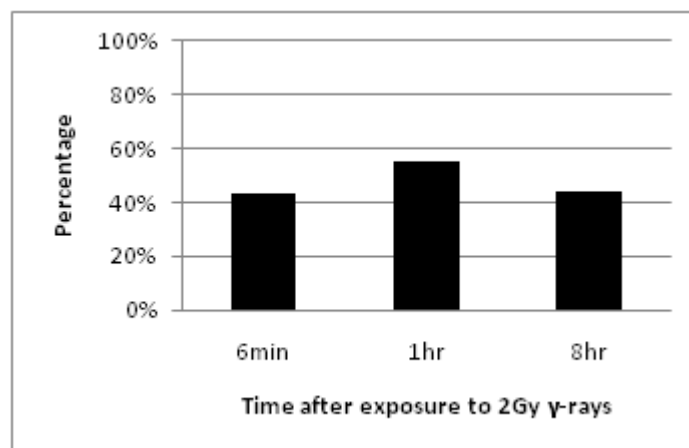
Figure 5-13 Breakdown of large foci made of clusters
The percentage of large foci consisting of two or more smaller foci is shown for three
important time points, based on possible timescales for clustering of individual foci.

43% of the large foci present could be resolved into two or more smaller
foci within 6 min of irradiation, however this was not seen to alter with time
(55% and 44% at 1hr and 8hr after irradiation) (Figure 5-13). The lack of a
significant change in the proportions of large foci consisting of smaller foci
does not support the hypothesis that larger foci counted using the in -

134

house system are made of foci that formed into clusters 8hr after radiation, suggesting the increase in foci size by this time was not a consequence of clustering. Indeed, further analysis of all data-sets re-analysed by the Costes et al (2006) system, revealed that the increase in the number of foci counted was actually in the small category with no significant change to the number of large foci counted (Figure 5-14). In both irradiated and shams the Costes et al (2006) system scored more small sized foci. One notable characteristic of the system is that almost twice as many small foci are counted in shams compared to the in-house system, which could be indicative of the systems parameters being overly sensitive to background. What this analysis comparison does tell us however, is that large foci may indeed comprise complex, clustered lesions that reflect initially-induced damage.
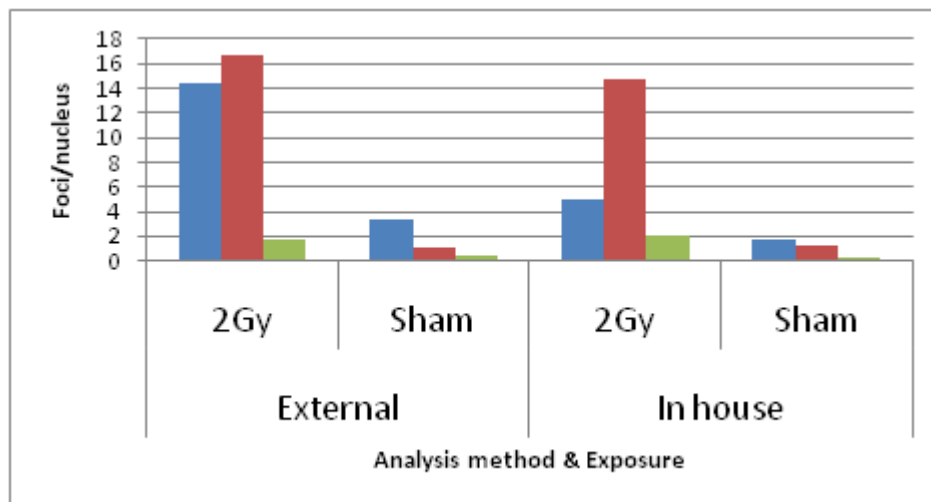
Figure 5-14 Size distributions for auto-analysis methods
Relative proportions of small (blue), medium (red) and large (green) foci are shown in HBEp cells 1hr after exposure to 2Gy γ-rays, determined from 3D image stacks.

5.3.3 Relative distribution of RIF to chromosome territories over time

The density of chromatin, as visualised by DAPI stain intensity or histone content, has been used to identify trends in the distribution of foci relative to chromatin rich and chromatin-poor regions. For fixed cells, some cells display distinctly variable chromatin staining patterns, such as the HeLa and NIH3T3 cell lines (Goodarzi et al., 2009), for those cell types that do

not have variable densities, the density of chromatin can be artificially altered using buffered salt solutions (Falk et al., 2008). In the HBEp cell type the chromatin signal is generally homogenous, with a single region of decreased intensity in the centre of most nuclei, believed to be the nucleolus (discussed in chapter 4). As we did not wish to artificially modify the cell homeostasis by exposing primary cells to non-physiological conditions no effort was made to assess foci distribution relative to density of chromatin. Instead, the distribution of RIF in relation to chromosome territories was investigated. To achieve this, a combination of immunofluorescence and Fluorescence In-Situ Hybridisation (FISH), commonly referred to as Immuno-FISH (IF-FISH) was carried out.

5.3.3.1 <u>Optimisations for low LET radiation and IF-FISH staining</u>
In our system, the quantification of 53BP1 foci relies on preservation of epitopes, therefore IF was conducted first to allow measurement of fluorescence loss, relative to an initial measure before FISH. HBEp cells were grown to 80% confluence and irradiated with 2Gy γ-rays. After 1hr cells were fixed and labelled for 53BP1. Four separate fields of view were then imaged using a stage vernier scale and measured for fluorescence intensity at each stage of the FISH protocol (without use of DNA probe).
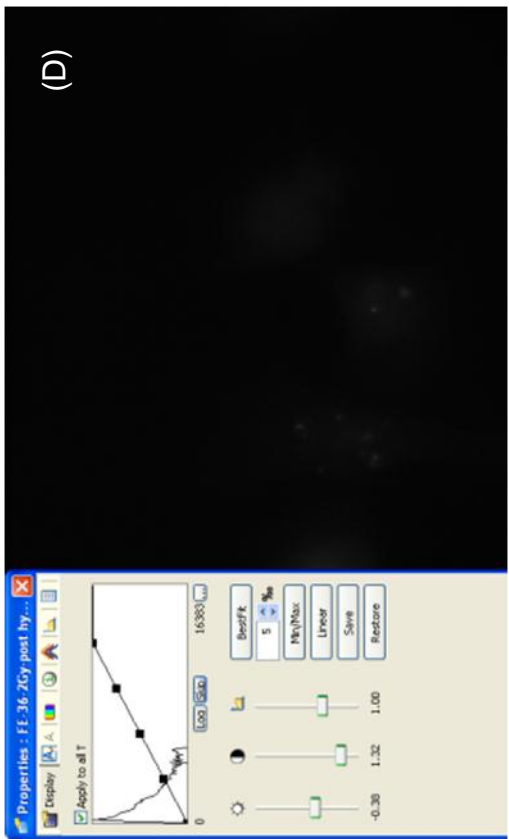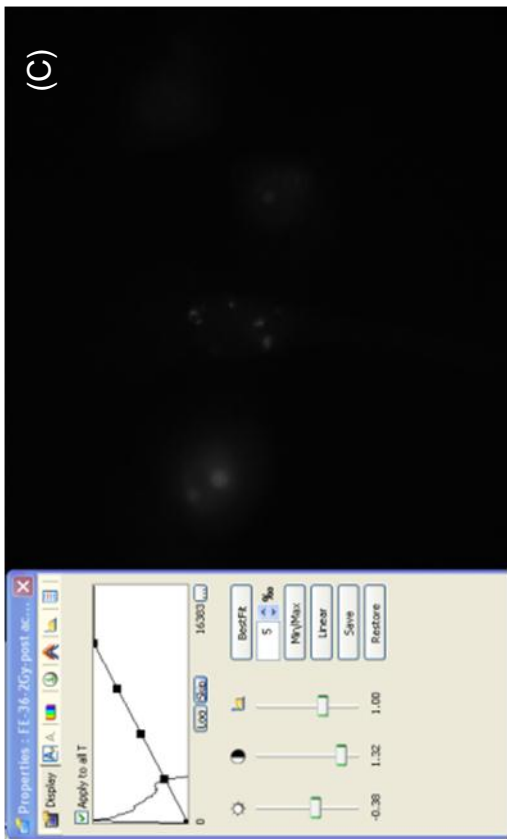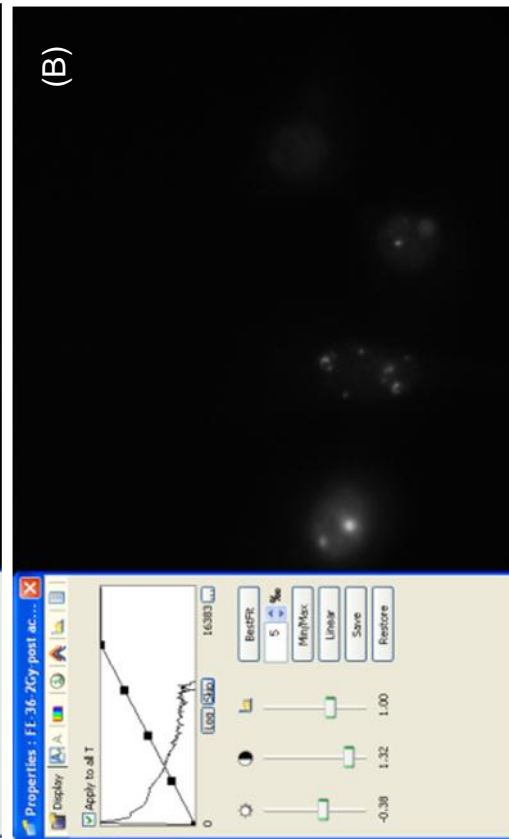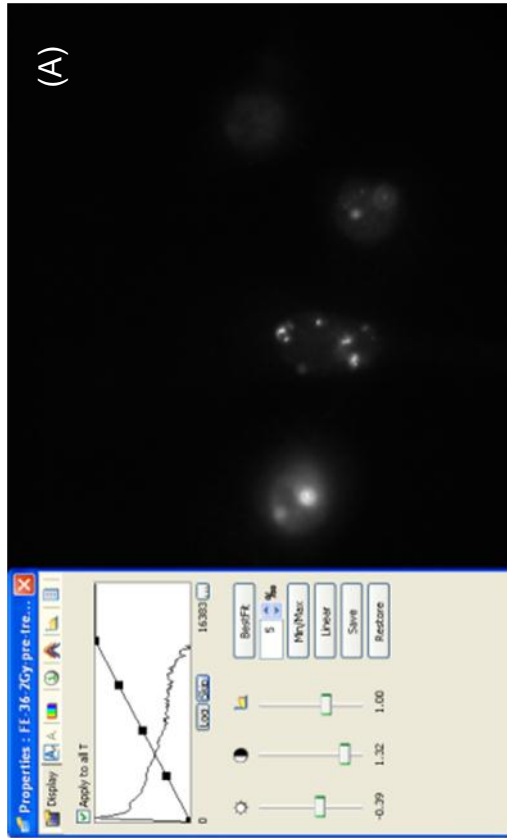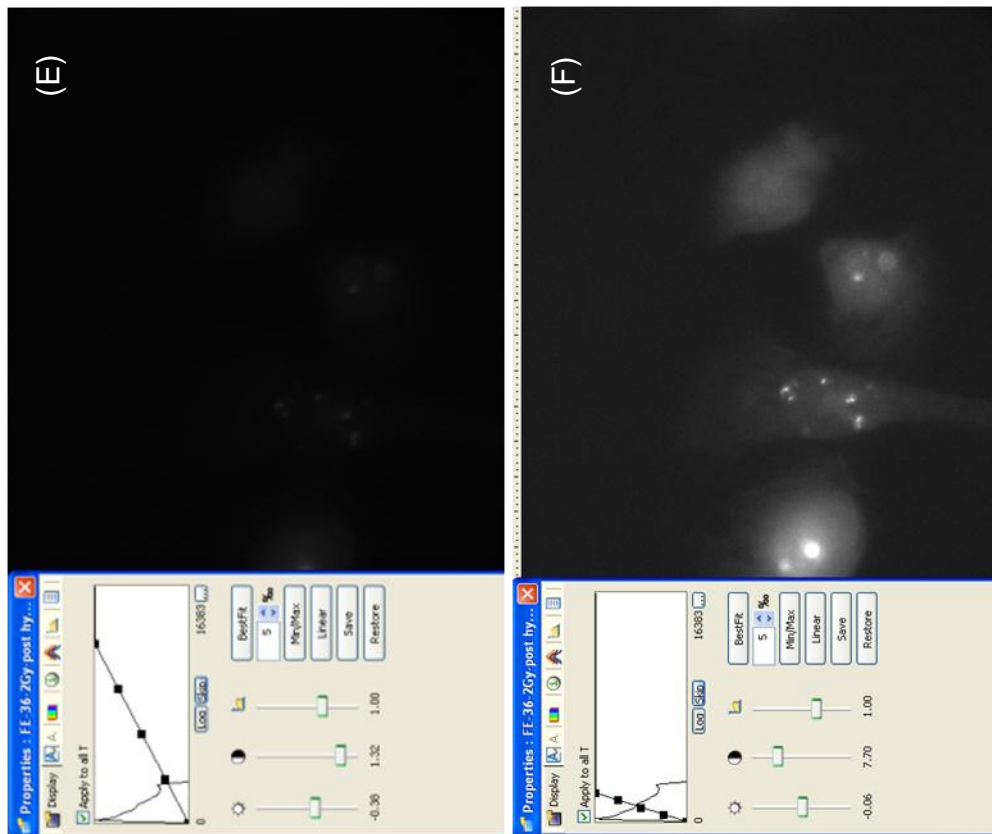
Figure 5-15 Observations of fluorescence intensity after FISH
Images with histograms of HBEp cells fixed 1hr after exposure to 2Gy γ-rays. Images were taken before FISH protocol (A), after membrane permeabilisation (B), after genomic DNA denaturation (C), after hybridisation (D) and post-hybridisation washes (E). Although there a significant loss of intensity, the signal for foci was preserved and could be visualised through the protocol with adjustment of the display (F).

The disruption of lipids and depurination during permeabilisation has the greatest effect on fluorescence, which is likely to be compounded by PBS washes, the high temperatures and salt stringency of the denaturing steps also reduced fluorescence (Figure 5-15). The effects of fluorescence loss can be recovered, to a degree, through increased acquisition time or increased gain but with reduction in signal to noise (Bernas et al., 2005). The results shown here confirm there is sufficient residual fluorescence to effectively identify foci.

Initial optimisations of this assay were conducted in human dermal fibroblasts (AG01522) which were fixed using either methanol and acetic acid (3:1) at -20°C (2D), or using 1-4% paraformadehyde (3D). The main optimisations aimed to balance between the preservation of IF whilst enabling penetration of antibodies and whole chromosome probes (WCP). A number of permabilisation steps were optimised using Saponin to

sequester cholesterol and detergents (TritonX-100) to remove lipids and also post IF fixation to preserve the IF signal during FISH protocols whilst limiting cross linking that reduced penetration of WCP. Comparisons between commercially available and home-made whole chromosome probes were also tested whereby different WCP probe length was seen to impact to efficacy of protocol (data not shown).
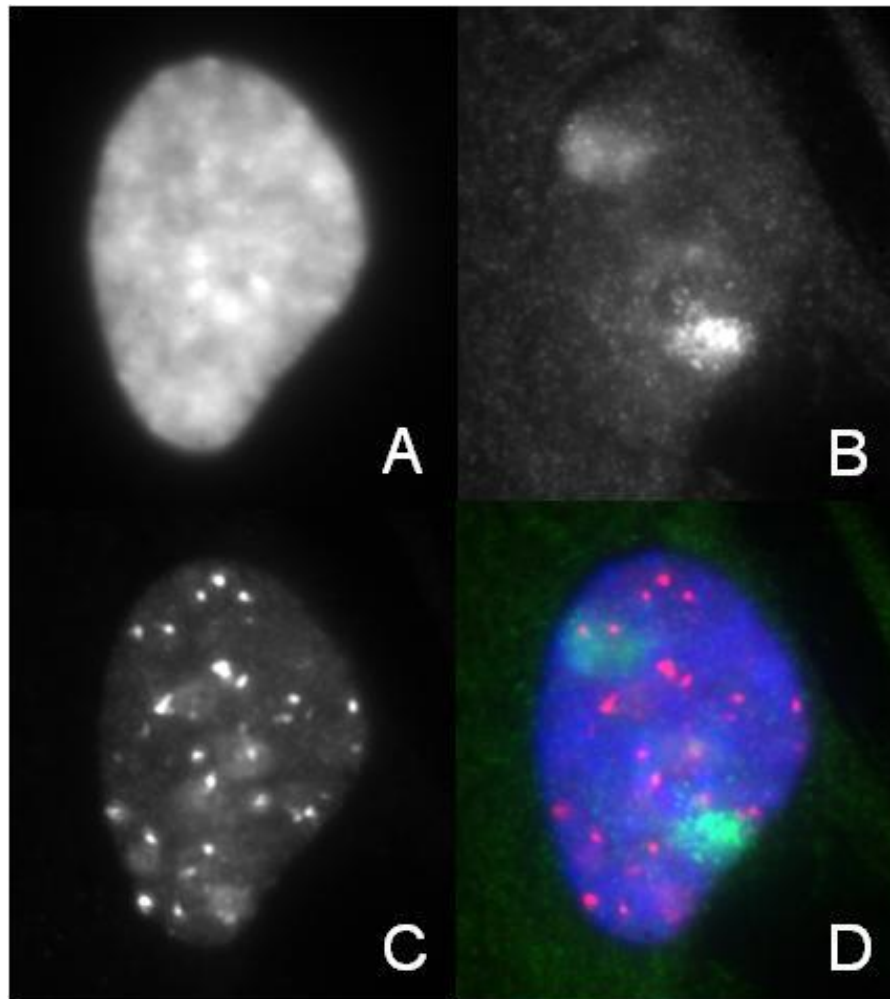
Figure 5-16 53BP1 and chromosome 4 labelled human dermal fibroblast
Human dermal fibroblast cell 30min after 2Gy γ-rays. Chromatin has been stained with DAPI (A), chromosome 4 labelled with DNA probe (B) and 53BP1 labelled with fluorescent antibodies (C) and a pseudo coloured composite (D).

Initial optimisations showed proof of principal for labelling chromosome territories and 53BP1 immunofluorescence (Figure 5-16 and 5-16), however initial analysis was limited to the success of the FISH signal as not all cells had sufficiently clear chromosome territories. The total area occupied by the chromosome territories was deemed an important factor in the design of the assay. To effectively assess the relative distribution of foci within individual chromosome territories required a sufficient number of foci to be induced within that territory. Therefore, cells were fixed at specific (early) time points and the larger chromosomes were selected for CT labelling (e.g. chromosome 4) (Figure 5-16).

Using the information gained from AGO1522 fibroblasts, the modified protocol was tested using HBEp cells that had been irradiated with 2Gy γ-rays and fixed 30min after exposure to obtain maximum number of foci. As with the AG01522 Fibroblasts, it was noted that not all nuclei were labelled for chromosome territories, additionally, the 53BP1 signal was less punctuate in HBEp cells compared to fibroblasts (Figure 5-17). Further optimisations specific to the HBEp cells involving harsher permeabilisation steps and weaker post IF fixations were subsequently carried out.
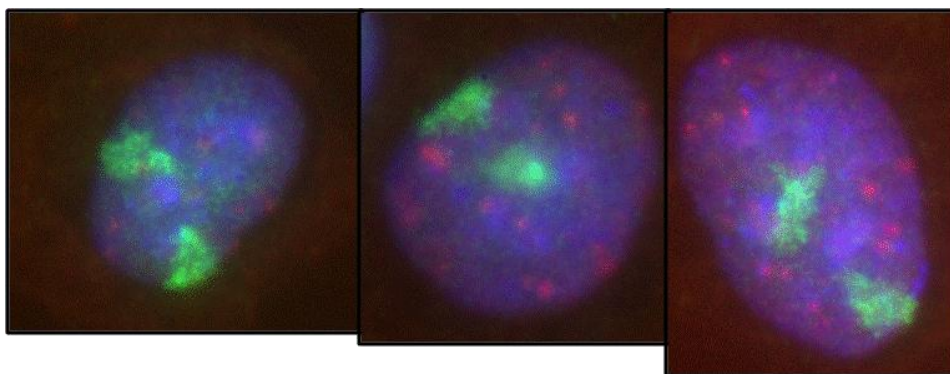
Figure 5-17 53BP1 and Chromosome 4 labelled HBEp cells
HBEp cells 30min after exposure to 2Gy γ-rays, chromatin (blue), 53BP1 foci (red) and Chromosome 4 (green) have been pseudo coloured for visualisation.

Manual analysis of the distribution of 53BP1 foci inside, on the periphery of, or on the outside the chromosome territories revealed that a large number of nuclei would need to be scored to effectively see a change in the distribution, particularly at later times where there are fewer foci. To

assess this in more detail, HBEp cells were exposed to 2Gy γ-rays and fixed 10min, 6hr, 16hr and 24hr after irradiation. Optimised IF-FISH protocols were carried out and images automatically captured using the Zeiss Metapher system with settings for the capture of three channels (DAPI -blue, 53BP1-red and whole chromosome probe (WCP) –green) in a MIP. For all time points it was noted that not only had the intensity of 53BP1 foci been reduced but fewer foci were observed compared to previous assays. In addition, the localisation of 53BP1 was seen to be dependent on phase of the cell cycle whereby 53BP1 signal appeared excluded in those nuclei entering mitosis (revealed by condensed DAPI signals). The condensed chromatin of mitotic nuclei, were often clearly labelled with whole WCP but were absent of 53BP1. Conversely, nuclei with the brightest 53BP1 foci often had little or no chromosome territory signal, see Figure 5-188.

Figure 5-18 Exclusion of 53BP1 and WCP signal in DAPI intense nuclei
Images of HBEp cells stained for chromatin with DAPI (left), chromosome 8 WCP (centre) and antibodies to 53BP1 (right) 10min after 2Gy γ-rays.

The mutually exclusive presence of chromosome territories and 53BP1 foci in this experiment reduced the number of nuclei that could be analysed. Only nuclei with one or more chromosome territories and two or more 53BP1 foci were therefore considered for analysis. The percentage of cells analysed that fit these criteria are shown in Figure 5-19.
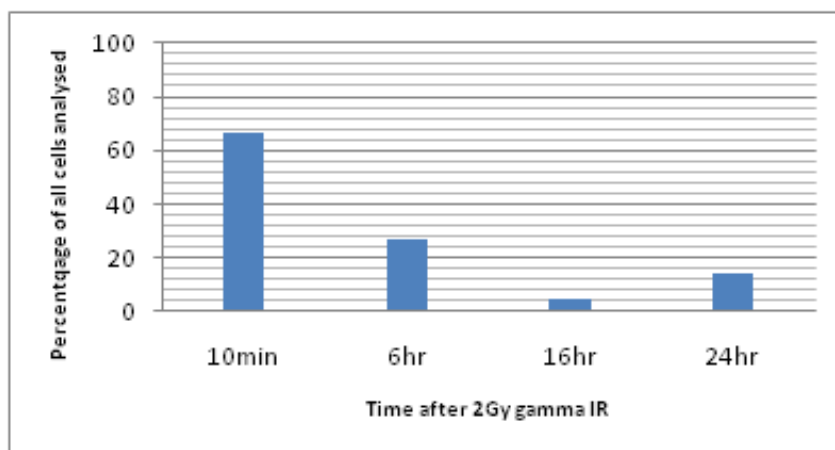
Figure 5-19 Nuclei with chromosome territories and more than 2x 53BP1 foci.
The percentage of nuclei that were suitable for analysis of was determined by the presence of WCP signal and at least 2 53BP1 foci, as determined through manual inspection of MIP images.

The number of nuclei that can be effectively analysed at 16 and 24 hr after radiation is expected to be low as it is known that at these time points an average of 2 foci per nucleus is normal. Therefore any shift in the proportions of foci in relation to chromosome territories would be difficult at later time points. In addition to this caveat, it was noted that CT labelling was not uniform across time points, see Figure 5-19. There was also a notable difference in CT area between time points, see Figure 5-20.
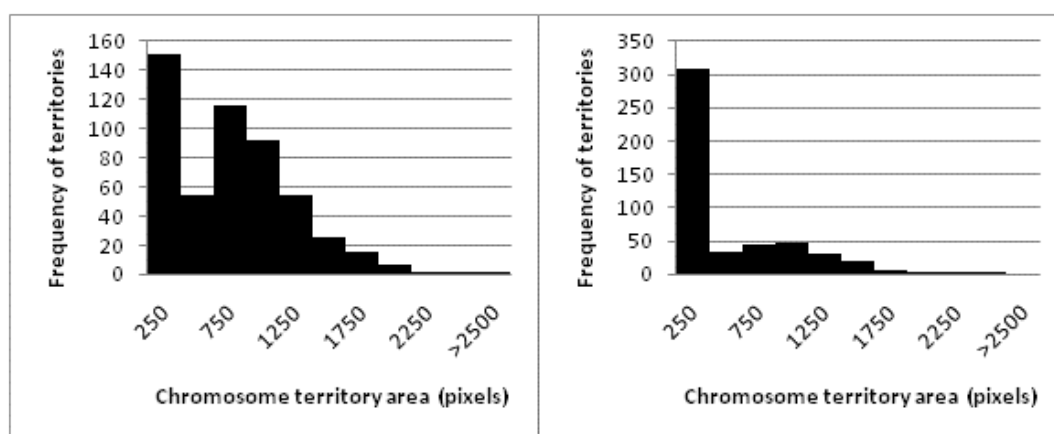
Figure 5-20 Frequency of chromosome territories area
HBEp cells fixed 10min (left) and 6hr (right) after irradiation and labelled for chromosome 4.

This observation could be a result of ineffective FISH labelling but it was also noted that automated capture of nuclei relied on the automated identification of nuclei, which was dependent on the intensity of the DAPI

142

signal. Signal intensities appeared to vary more drastically in the 6 hr time point compared to 10 min, which resulted in a proportion of less brightly stained nuclei not being included for analysis. Despite this, even with the increased number of nuclei scored for each time point, the number of nuclei with chromosome territories and > 2 foci was too low to discern any valuable statistics on trends for foci in relation to CTs. To illustrate this, the total area for chromosome territories as a fraction of the nucleus was used to estimate the area of foci signal seen based on the total foci signal. The deviation of expected foci area in CTs to the observed was compared using the Chi square test. In both instances the observed proportion of foci area significantly deviated from expected. The percentage area the CTs occupy in the nucleus is typically around 10% for chromosome 4 in HBEp cells. Within 10min of irradiation only six 53BP1 foci per nucleus are observed. As stated, this is lower than expected due to the protocol for duel labelling of 53BP1 foci and CTs. Therefore, only 0.6 53BP1 foci would be expected per CT per nucleus. This very low ratio at peak induction does not allow for trends to be observed at later time points.

5.3.3.2 Optimisations for high-LET irradiation and IF-FISH staining

The linear pattern of energy deposition associated with α-particles offers several advantages for the investigation of foci clustering. Aten et al (2004) utilised the linear nature of the energy deposition to determine evidence of clustering as there is limited movement of foci from the axis of irradiation but there is a change along the axis with time. For the investigation of RIF in relation to CTs, this linear deposition of energy means a CT can be considered qualitatively as hit or not at any time point. This definitive identification of foci location relative to CTs makes statistical observations more viable (compared to γ-rays), additionally the more complex damage induced by α-particles will result in more foci being present at longer times after irradiation.

After testing the effects of the FISH protocol on the Mylar dishes, the glue used to hold the PET to the dish often failed with treatments involving higher temperature. Furthermore, the working area for counting

sufficient number of cells also restricted analysis and finally, the optical quality of the images that result from imaging through Mylar were too poor for high throughput analysis. To resolve these issues and generate α-particle tracks for IF-FISH assays, cells were grown on glass slides as described previously but were irradiated by inverting the slides over a plutonium source (see section 2.2.2), see Figure 5-21. Slides were irradiated at a distance of 3mm from the source approximately central to the slides working area for 10 seconds.
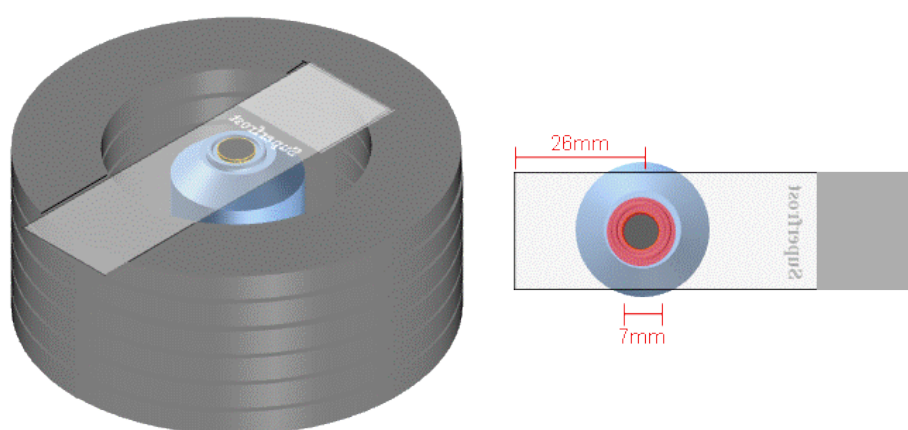
Figure 5-21 Setup for direct irradiation with α-particles on slides.
Slides are inverted of the source (black disc) on acrylic rings (grey rings) to produce a working area of α-particle tracks traversing the nuclei at an angle (red ring).

No increase in cell necrosis or change in cell morphology was observed by trypan blue staining suggesting time in air during the irradiation process was not excessively toxic to the cells, but it was noted that the slide would become dry in 30 seconds under the air flow of a laminar flow hood.

To achieve radiation tracks along the x-y axis only cells within a 3 mm ring (estimated from CR39s) around the site of irradiation were exposed to α-particles at shallow angles. This ring is limited by the range of the α-particles in air and the depth of the cells. The area directly over the source has a higher dose rate and more α-particles traversing at multiple angles and so would not be suitable to generate x-y tracks. After exposure cells were fixed at varying times, and stained for 53BP1 foci then subsequently scanned to identify the region on the slide where nuclei with

144

tracks could be observed. In a 14mm x 3mm area only 27 nuclei were found to have tracks, see Figure 5-22. The area only contained 100 nuclei, which is roughly equivalent to 5% confluence.
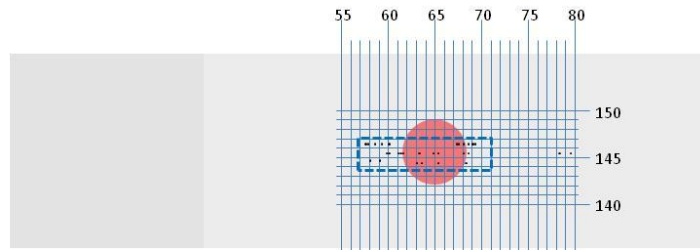
Figure 5-22 Line scans for nuclei containing α-particle tracks.
Working area map shows frequency of nuclei across the slide.

Of the successfully irradiated nuclei most contained very clear α-particle tracks consisting of many foci along the length of the nucleus, as shown in Figure 5-23 and which are consistent with the staining patterns observed by other studies (Aten et al., 2004, Desai et al., 2005, Jakob et al., 2009).
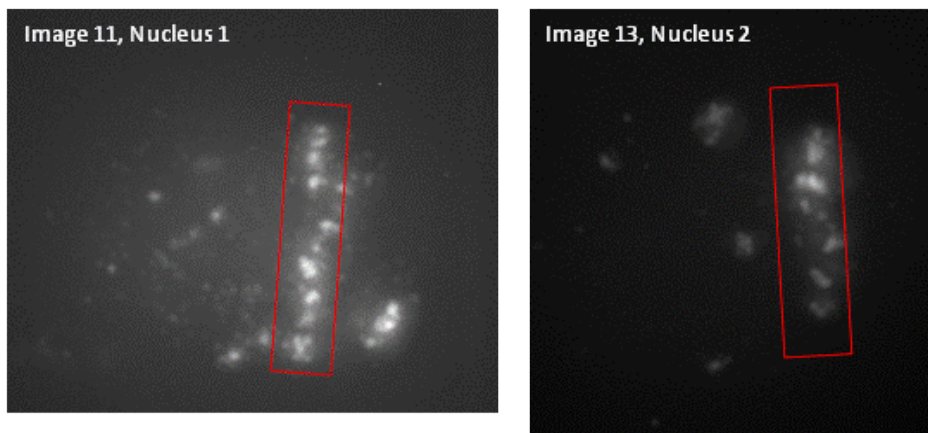
Figure 5-23 A-particle tracks from inverted irradiation technique
HBEp cells irradiated with α-particles from a Plutonium-238 labelled for 53BP1 foci. α-particle track traversals have been highlighted in red.

This method shows successful irradiation of HBEp cells with α-particles to generate tracks of damage but due to insufficient numbers of cells, no statistical analysis of foci was achievable. Due to technical limitations and time constraints application of the optimised methodology for labelling of chromosome territories and 53BP1 was not conducted, but the tools to achieve this have now been established.

145

5.3.4 Assessing for evidence of clustering using immortilised HBEp cells stably transfected with GFP-53BP1 protein

The methods outlined above utilised fixed cell data to ask questions on DSB dynamics and to ascertain whether large 53BP1 foci, observed 8hr after radiation, could originate through the clustering of individual DSB foci that remain un-repairable by that time. To address the questions of foci dynamics more directly, HBEp-3KT cells stably transfected with GFP-tagged 53BP1 were used. Details on the growth characteristics and the induction and decline of 53BP1 foci over time are given in chapter 4. Using the 'live cell' setup for investigations into RIF has several advantages over standard immunofluorescence, but comparisons to data from primary cells is difficult due to difficulty in obtaining replicates (one time lapse video per experiment) and differences between the cell types (effects of plasmid, selection, immortalisation and observation using UV). Therefore, for this part of the study the dynamic relationship of individual foci relative to each other was assessed. Figure 5-24 illustrates this by showing selected images of a zoomed area of a nucleus showing three foci that can be seen to cluster and merge over time. In addition, examples of foci that apparently de-clustered were also observed and also what appears to be shuttling of proteins (image 5.50) between persistent foci, see Figure 5-24. One focus appears to persist for a 9 hr time frame (right of frame in Figure 5-24), whilst two smaller foci, induced at a later times (05:10), appear to fuse and then migrate to the persisting focus.
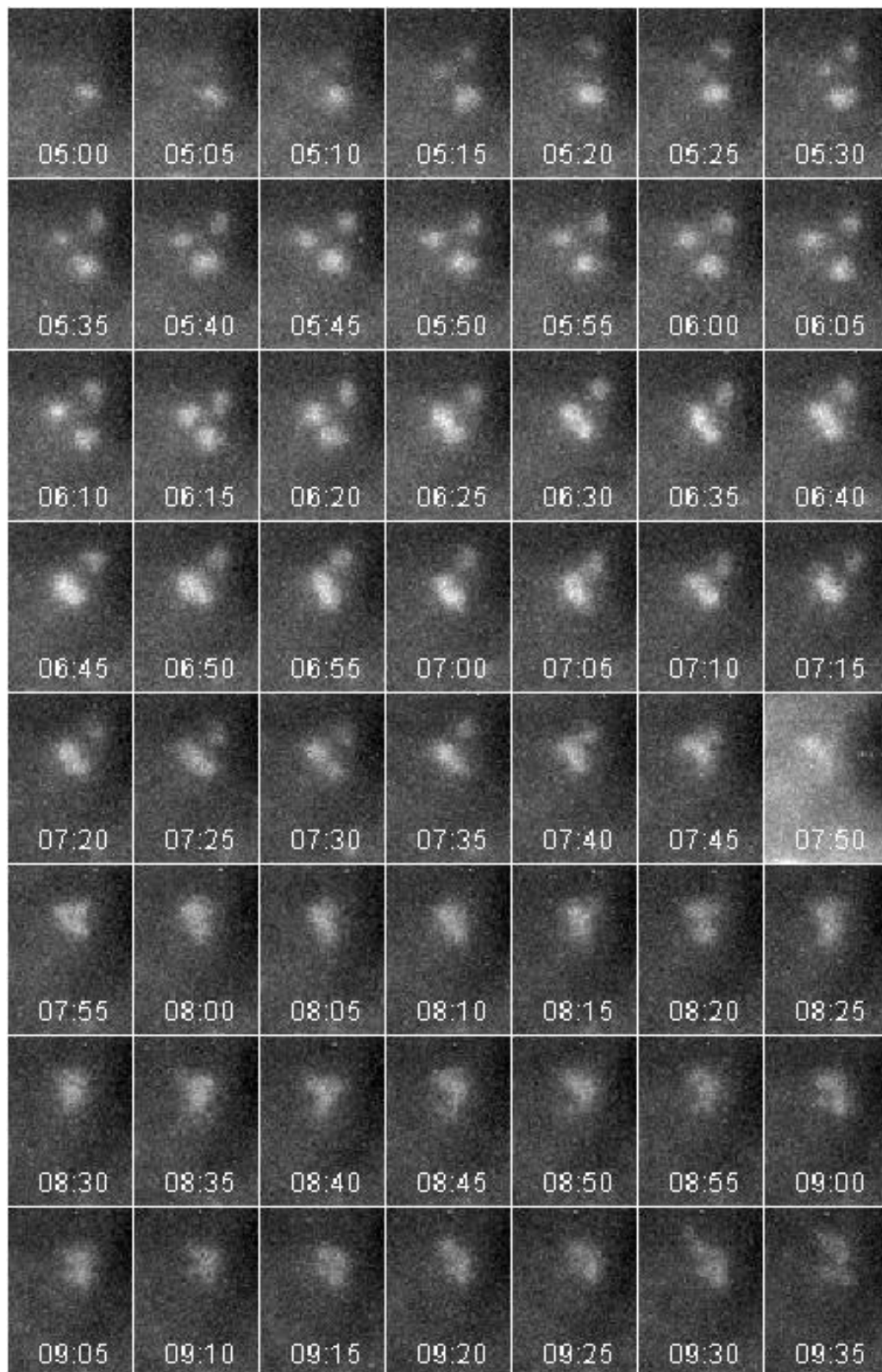
Figure 5-24 53BP1-GFP foci clustering
5hr:35min after irradiation three proximal foci are seen, by 6:25 two have merged, by 7:50 all three have merged. The timescales for this apparent clustering is consistent with the increase in large foci data.

147

To assess for evidence of clustering, the number of occurrences where two or more foci combine (fuse) and the number of times a single focus was seen to split into more foci (branches) was monitored in HBEp cells expressing 53BP1-GFP. Manual counts of fusions and branches were made for nuclei throughout the time course (Figure 5-25). It was noted that more fusions occurred than branches but a proportion of these were in fact foci that fused and later branched. Confirmation of this using Imaris (Bitplane) showed that the number of fusions and branches is approximately equal.
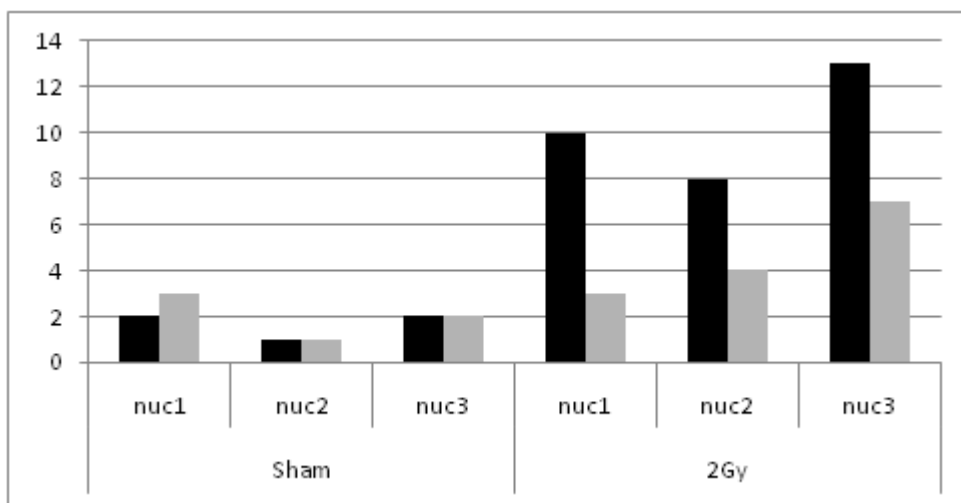
Figure 5-25 Fusion and branches of foci in HBEp GFP-53BP1 cells
Fusions (black bars) were counted when two or more foci combine in a single image, branches (grey bars) were counted when two distinct foci were observed to originate from a single focus.

To assess if the fusion or clustering of foci was a directed event, cells with 53BP1-GFP were irradiated with 1Gy γ-rays and then allowed to recover for 4 hr under observation. The 'primary' induced foci were then used as a reference for foci induced from a second dose of 1 Gy (2 Gy fractionated). The hypothesis for this experiment was to examine whether 'new' RIF would migrate to existing sites of DSB, effectively as a means to access existing complexes of repair proteins. However no evidence for this was found, indeed very little interaction between primary and secondary induced foci occurred, instead the majority of the RIF appeared to be relatively fixed in a 3D location with evidence of shuttling of proteins between the different foci, see Figure 5-26.
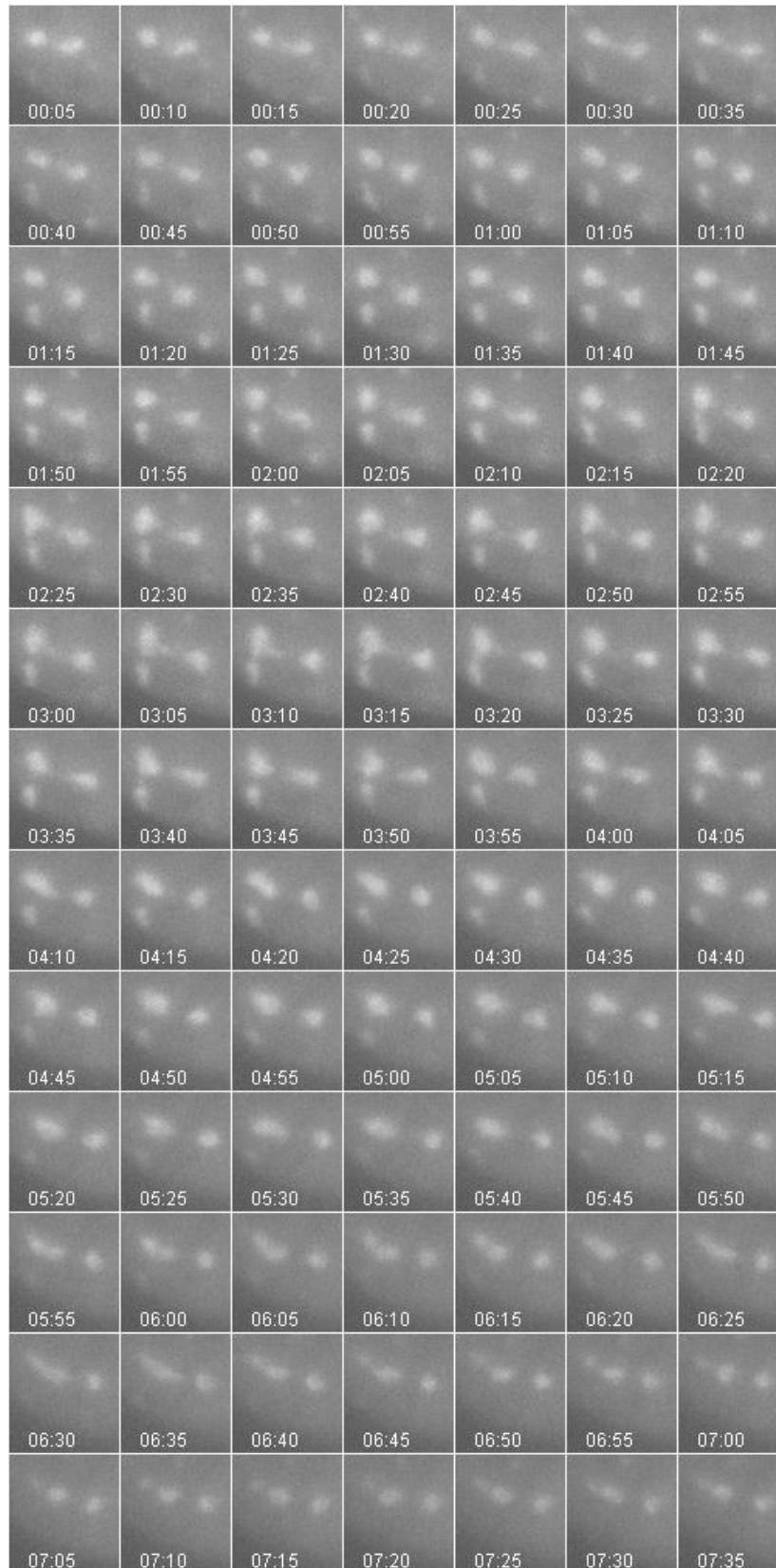
Figure 5-26 Shuttling of 53BP1 proteins in live cells
Residual foci from first dose of 1Gy γ-rays are seen at 00:05, two new foci resulting from
a second dose of 1Gy are seen at 01:00. 'Shuttling' between two 53BP1 appears at 00:30
to 00:40 and from 03:00 to 03:20 'shuttling' between three foci is seen. Each image
square is $=8\mu m^2$

149

It is remarkable that RIF induced in proximity (<4 μm) appear relatively fixed over the duration of this time course, see supplementary data. To quantify any degree of movement for all foci within the nucleus, the Bitplane tracking module of Imaris was used, in particular, to monitor the spatiotemporal distribution of foci based on a Brownian motion algorithm, which links independent points in a time series based on a distance constraint. To prevent results being biased by the rotation and migration of the cell the nucleus was aligned using the stack registration plug-ins for imageJ. For visualisation, the tracks of RIF were colour-coded to a time-scale to allow the operator to see the track length and duration (Figure 5-27 and Figure 5-28). In irradiated nuclei, RIF induction is seen at early time points (blue, 0-2hr) and continues into the later times (yellow, 12-14hr). These foci are not seen to make large scale movements and in fact appear relatively fixed within the nucleus. Some directional movement is observed at the periphery of 'nucleus 1' but this is most likely the result of the nucleus growing in size over the time course (see supplementary data). As has been seen in fixed cells, the nucleolus is devoid of foci in nuclei 1, 2 and 3 (Figure 5-27 and 5-28) and as expected, there are fewer foci in shams. Here, the foci that do appear occur at later time points (yellow, 12-14hr) and have very short track lengths (Figure 5-28) compared to irradiated foci, which is more likely to be a function of their duration than mobility. These foci also appear to be smaller and less bright than the foci observed in irradiated samples.

To quantify the observations of foci movement, the mean squared displacement was calculated for all foci within the nucleus over the duration of the experiment. This figure normalises movement into positive values to estimate the average movement of a focus, see Figure 5-29.
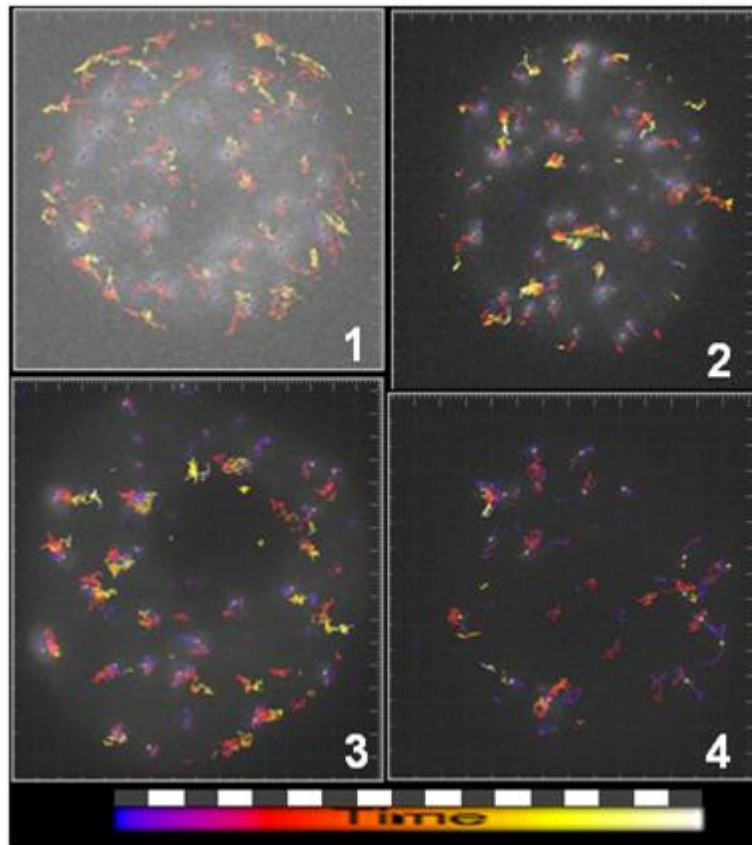
Figure 5-27 Automated tracking of foci after 2Gy γ-ray
53BP1-GFP foci tracks are colour labelled corresponding to time. Grey and white bars
above colour time scale correspond to 1hr each.
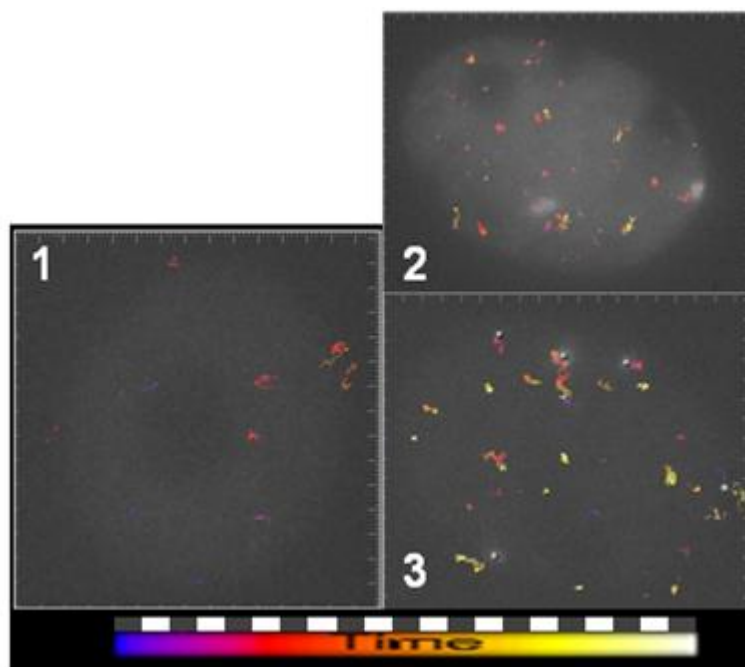
Figure 5-28 Automated tracking of foci after sham exposure
53BP1-GFP foci tracks are colour labelled corresponding to time. Grey and white bars
above colour time scale correspond to 1hr each. Image numbers correspond to nucleus
number in Figure 5-29
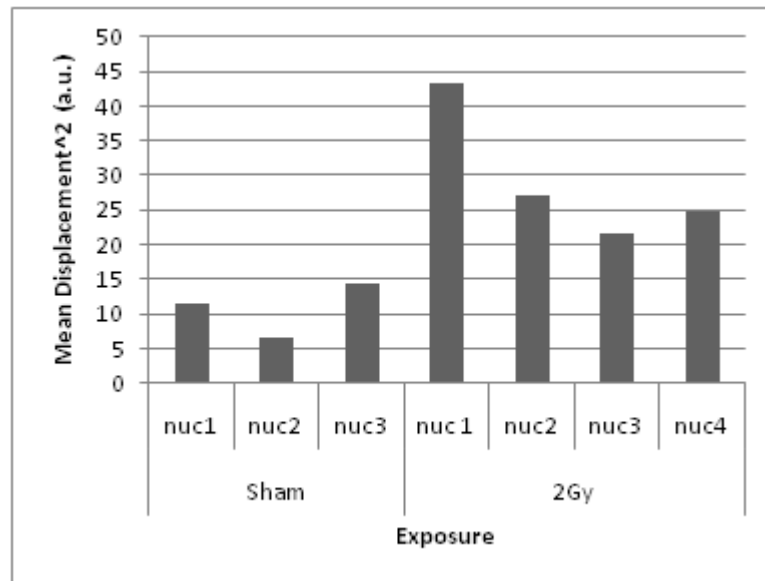
Figure 5-29 Automated tracking, mean displacement^2.
Average mean squared displacement for all tracks within each nucleus is shown in arbitrary units.

From this analysis it does appear that there is more movement of RIF in irradiated nuclei compared to shams, consistent with the possibility that RIF do cluster for repair. However, it is difficult to fully interpret these data as the foci in shams do not persist long enough to have large enough movements, likewise, in 'nucleus 1' although the track lengths for foci are increased, the nucleus was also observed to grow in size and, so foci would move relative to their original position. By contrast, it is also possible that the measurement of all foci within the nucleus bias's results toward there being less movement, as some foci are repaired rapidly in situ. Therefore, further image analysis is needed on specific foci that appear to have more directed movement, i.e. those which are in close proximity and those that are longer lived.

5.4 Discussion

The spatial deposition of damage, including DNA DSB, in a cell nucleus is known to be related to the structure of the radiation track (LET), dose, cellular geometry and the organisation of chromatin (chapter 1). Similarly, the cellular responses to this damage are governed by orchestrated processes that act within these sites (spatial) over varying periods of time (temporal). Thus to understand more fully the radiobiological response of cells to DSB and, the biological fate of these responses e.g. cell death, chromosome exchange etc, then an understanding of the spatiotemporal aspects for repair of DSB is required. The investigation of spatiotemporal aspects of RIF has, until recently, been limited by the analysis tools that are available. However with advances in fluorescence microscopy and digital image processing, many researchers are now able to quantitatively assess a whole array of relevant measures. For instance, the number and size of RIF which are observed at specific times after radiation exposure (van Veelen et al., 2005, Cai et al., 2009, Ishikawa et al., 2010, Schettino et al., 2010) may be informative in determining the actual composition of RIF. This field of research is being advanced through the application of fluorescence proteins and the development of 'live cell' microscopy which is enabling observations of RIF in real time (Falk et al., 2007, Asaithamby and Chen, 2009, Jakob et al., 2009).

An important observation through this development, of which there is now an established consensus in a range of cell types for both high and low LET radiation, is that RIF are larger at later times after irradiation compared to those RIF which are initially-induced (Aten et al., 2004, Krawczyk et al., 2006, Scherthan et al., 2008, Asaithamby and Chen, 2009, Ishikawa et al., 2010). The data generated in this study and presented in Figure 4-17 and 5-1 are also in agreement with this. Using primary HBEp cells we quantitatively assessed the size of 53BP1 foci after 2Gy-γ-rays (diameter, area and volume) and found that the size of RIF increased approximately 8 hrs after exposure (the proportion of large at 30mins and 8hrs were 9% and 24% of the respectively). In un-irradiated nuclei an average of 2 foci was present and proportionally, the majority of

these endogenous foci were either small or medium sized. Interestingly, by 24 hrs the average number of RIF (2 foci/nucleus) had reached sham levels, suggesting all the RIF have been resolved, but the relative proportions of foci sizes were not consistent with each other, with more large foci being observed in the irradiated samples. Thus, large 53BP1 foci initially-induced after exposure to 2 Gy γ-rays were persisting suggesting these RIF comprise complex lesions that have yet to be repaired. The long term consequences of large, persisting foci have been associated with cellular senescence (Rodier et al., 2009) and also cell death (Banath et al., 2010).

For the three size categories (small <0.5µm, medium 0.5-1.0µm, large >1.0µm diameter) investigated, an apparent staggered peak for induction for each was observed; with peak induction of small foci reached within 10min, medium foci at 30 min and large foci taking up to 16hrs after exposure to 2 Gy γ-rays to peak. This lag in response time for each size category has been shown in other cell types and is believed to be due to the kinetics of the marker or repair pathway. For instance, 53BP1 has consistently been shown to have a lag time before peak induction, depending on experimental setup (Anderson et al., 2001, Leatherbarrow et al., 2006, Asaithamby and Chen, 2009) that is hypothesized to be due to 53BP1 being downstream of several other factors for recruitment, such as γ-H2AX, which has also been shown to have an initial lag in response (Leatherbarrow et al., 2006, Kato et al., 2008, Rube et al., 2008). Furthermore, the induction of large foci (in contrast to those which appear over time) appear to be dependent on dose, as 30min after exposure to 0.25, 0.5 and 1Gy γ-rays the number of large foci increased at approximately 0.75 large foci/Gy (relative to sham levels). By contrast, the induction of medium foci appeared to follow a more logarithmic trend increasing from 1.5 to 2 to 3.4 after exposure to the same doses. This possible dose effect for larger foci may suggest the initial induction of large foci is reflective of the complexity of damage induced, which even at low doses of low-LET γ-rays, will result in a number of isolated clustered, complex lesions (Goodhead, 1989).

It has been hypothesised that there are two pathways for DSB repair; a fast pathway (<30min) that is capable of repairing simple lesions independently of the signalling cascade and a slower repair pathway that utilises signal transduction to repair more complex lesions (Jeggo and Lobrich, 2006, Goodarzi et al., 2010). If so then more complex damage, as is induced with high-LET radiation may invoke a different pathway for repair than would be used for simple lesions. Therefore, with high-LET radiation where a large amount of complex damage is induced we might expect to see a greater lag in 53BP1 response as the complex lesions require the formation of signalling proteins, compared to γ-rays. However data shown here suggests 53BP1 may actually have faster kinetics after exposure to high-LET α-particles, as 53BP1 foci were seen to form within 1 min of exposure. This result may be due to the rapid method for irradiation, where cellular metabolism is less likely to decrease due to temperature changes (Markova et al., 2007) during transportation for irradiation with γ-rays, but could equally be due to a more rapid response being evoked by the greater level of damage. The relative increase in focus size with α-particle irradiation shares the same staggered increase for small medium and large foci as was observed for low-LET radiations, which is consistent with general observations of high-LET RIF (Aten et al., 2004, Desai et al., 2005, Krawczyk et al., 2006).

One hypothesis for the apparent growth in RIF size is suggested to be the result of clustering of multiple foci (and by proxy DSBs) into larger foci which may act as centres for repair or 'repair factories' (Lisby et al., 2003, Aten et al., 2004, Lisby and Rothstein, 2004, Krawczyk et al., 2006). Consequently, this hypothesis supports the breakage and reunion model for chromosome exchange formation as it invokes a model whereby DSB from multiple chromosomes could come into close proximity with each other. Contrary to this hypothesis, others have suggested the increase in RIF size is a consequence of signal amplification due to re-localising of repair proteins at persisting lesions, or due to expansion of chromatin at the DSB site (Nelms et al., 1998, Kruhlak et al., 2006).

To address this, two novel approaches were undertaken to examine

evidence for clustering of RIF at later times after irradiation. In fixed cells; the relative positioning of foci (nearest neighbour analysis) was assessed to identify if a trend in the distance between foci exists and the composition (in terms of intensity) of large foci was examined in detail.

Observations of the larger foci showed a notable proportion consisted of multiple very proximal foci or a single large focus with multiple peaks of intensity. It was reasoned that, if larger foci were the result of multiple smaller foci accumulating over time then the proportion of large foci that were actually made of smaller foci would increase with time. By employing a different automated foci analysis system (Costes et al., 2007), we identified that ~40% of large foci consisted of two or more smaller foci. However this figure did not change with time and therefore did not provide evidence that larger foci at later times were formed via the clustering of smaller foci.

The nearest neighbour analysis method assesses the distance between foci, whereby decreasing nearest neighbour values over time could be suggestive of clustering. However, the distances between foci at the doses examined are very small compared to the total volume of the nucleus and the lower number of foci at later time points results in very low comparative 'R-value', suggesting foci are always clustered. This is unlikely as the distribution of DSBs from low LET γ-rays is known to be random, therefore, rather than consider absolute values it was more pertinent to assess trends. In the data presented in Fig 5-10 there is a consistent decline in the R-value, suggesting more clustering of foci with time, which could be the result of foci being in closer proximity at later times after irradiation. However, the conclusions drawn from clustering of foci are limited as the methods used do not account for focus size (which has been shown to increase with time). Therefore, at later time points the distance between foci centres may not have changed significantly but the distance between foci surfaces may have changed. Thus, more complex algorithms or simulations are required to define any significant change in the proximity of foci over time. This is particularly relevant since the dynamics of endogenous foci (observed in sham nuclei) remain to be understood.

The technical limitations associated high-LET α-particle exposure on Mylar at defined LETs, for subsequent multiple sample processing were challenging, however in collaboration with Queens University, Belfast, methods were optimised that enabled the irradiation of HBEp cells with high-LET α-particles on glass slides. In parallel, an IF-FISH method for the visualisation of RIF and chromosome territories was optimised for HBEp cells grown on glass slides. The objective being that the spatial organisation of RIF could be assessed over time within the context of relevant nuclear substructures (i.e. chromosomes). For instance, valuable information could be obtained that could correlate the fixed cell findings of Aten et al (2004) with the proposed model of sequential exchange as a mechanism for the characteristic formation of complex chromosome exchanges after exposure to high-LET α-particles (Anderson et al., 2002, Anderson et al., 2006). This experimental strategy has been carried out by Falk et al (2007), who observed a reduced number of RIF in gene-rich (more open chromatin) chromosomes compared to gene-poor (more condensed chromatin) chromosomes, after exposure to low-LET radiation, inferring that the condensed state of chromatin effectively protected DNA from the indirect (ROS) effects of low-LET exposure. What is clear from Falk etal 2007 and also from optimisations carried out in this study, was that the number of RIF in any individual CT was too low after γ-rays, to enable effective time-course studies to be carried out (unless very high doses were used). Thus, the use of high-LET radiation to assess for evidence of RIF clustering within this context was regarded more favourable compared to low-LET since if a CT is 'hit' by an α-particle then it would be likely to contain many DSB and more complex damage that would persist for longer increasing, the likelihood of observing dynamic changes in its spatial organisation (Aten et al., 2004, Desai et al., 2005, Jakob et al., 2009). In addition, the linear deposition of the energy also facilitates more simplistic one dimensional analysis of radiation tracks, when cells are irradiated at angles, compared to sparsely ionising radiation. Unfortunately due to time constraints, the application of this assay for studying the spatial and temporal dynamics of RIF within (and

between) chromosome territories, could not be carried out.

Studies performed using live cells transfected with 53BP1-YFP-fusion proteins have enabled quantitative measurements to be taken for foci after irradiation to assess if foci are capable of directed movement. The principal measurement to determine significant movement used was the mean squared displacement. When considered on a global scale (all foci) no evidence for directed movement (above Brownian motion) was observed (Jakob et al., 2009). However, measurements of specific foci has shown that some foci were capable of directed movement, but only over very small distances (<1 µm) (Falk et al., 2007). In the data presented in this study, measurement of the mean squared displacement for all foci was notably higher in irradiated nuclei (compared to shams). Whether this was a true reflection of dynamic movement of foci or whether this is more likely to be a result of persisting foci being more likely to move as a consequence of unrelated cellular functions, is unclear. Rarely, foci were observed to have migrated over short (2µm) distances and 'fused' with other foci. These rare foci fusion events occurred at various times after exposure (Figure 5-24) and were associated with the overall growth of the resulting focus size. Thus, evidence for clustering and the formation of large foci was observed. In addition to 53BP1 foci fusions, foci were also seen to branch, where they would split into two or more smaller foci, although these were less common than the fusion events (Figure 5-25). It should be pointed out that as the analysis of these live cell images was technically limited to 2D, it is not possible to discriminate between a genuine fusion and branching event from two foci passing over one another (lack of z-resolution).

By fractionating the total dose delivered, 53BP1 foci from the initial dose could be hypothesised to attract newly forming proximal RIF into these regions. Thus real time visualisation of subsequently induced foci could show a relative movement with subsequent foci fusion events. The data presented however shows that foci induced in close proximity remained relatively fixed, indeed for all live cell experiments, evidence was seen where 53BP1 protein appeared to 'shuttle' between fixed foci. This is consistent with the fact that 53BP1 is not chromatin bound and is capable

of being recruited to other DSBs.

Overall therefore, the data presented in this study is in accordance with other investigations using live cell microscopy and quantification of spatiotemporal dynamics of RIF. 53BP1 foci were seen to have limited movement within the 3D structure of the nucleus (<1 µm) and there was no evidence for directed large scale movements, in keeping with that proposed previously (Nelms et al., 1998, Costes et al., 2006, Kruhlak et al., 2006, Falk et al., 2007). The larger foci observed could result from either the labelling of initially induced complex damage, that is not immediately resolved, complex damage that may continue to signal thought the duration of the DSBs presence and therefore any expansion in size is the result of signal expansion or finally, 53BP1 proteins may cluster when proximal DSBs are present.

6 Conclusions

53BP1 was selected as the primary marker of DNA DSBs as it has been shown to rapidly localize to the sites of DSB and the trend in RIF induction and decline has been hypothesized to parallel the induction and decline in DSBs (Schultz et al., 2000). The main limitation of using 53BP1 as a marker of DSBs is that beyond certain doses (3-5 Gy) saturation of damage occurs and insufficient 53BP1 protein is present within the nucleus (Torudd et al., 2005). However, for the doses used in this investigation this marker was considered optimal.

The RIF assay is becoming an increasingly popular method for the identification of foci at a range of doses and for a range of applications. To quantify the induction, decline and spatiotemporal dynamics of 53BP1, a series of analysis methods were developed, ultimately leading to the generation of a novel analysis technique for quantification of RIF from image stacks. This system can rapidly analyse 2D images or 3D image stacks, requires minimal processing power and generates continuous data on individual foci for subsequent detailed analysis. The applications of the software are not limited to foci detection and could theoretically be used to identify other nuclear staining patterns (e.g. cell cycle markers). The main benefit to the use of this system is the time it affords the operator; what could take an experienced operator 8 hrs can now be achieved within 30 min, allowing for more experiments with greater detail and improved statistics. However, it is important to recognise that any automated analysis system relies on the operator to input the appropriate settings for the identification of foci and if this was not performed by a skilled individual who fully understands the process then there is a risk of generating erroneous data. To minimise this and to ensure maximum exploitation of the automated analysis system developed in Chapter 4, a detailed user manual has been compiled (to follow). This software also has potential for further development through the addition of extra user interface options such as; thumbnail previewing, co-localisation and counter stain selection (quantification or exclusion).

Using the methods described in chapters 2 and 3 the induction and decline of radiation induced 53BP1 foci in primary cells, which are the target for 50% of our collective annual radiation exposure, have been characterised. A detailed understanding of how these primary cells behave in culture has enabled evaluation of the processing of 53BP1 foci after exposure to differing radiation qualities and doses. HBEp cells were found to respond in a similar manner to previous investigations using epithelial cells (Leatherbarrow et al., 2006, Asaithamby and Chen, 2009, Groesser et al., 2011) in that that the induction of RIF occurs rapidly (<5min) and reaches a peak induction after ~30min. The subsequent decline to basal levels of ~2 foci/nucleus occurs within a 24hr period, but the size of these residual foci does not correspond to shams (endogenous foci) that were fixed at the same time. This suggests that either complex lesions are not repaired and foci persist or, that residual foci signal observed is not associated with DSBs but rather reflects some other, as yet undefined phenomena.

Through measurement of foci sizes after varying doses and radiation qualities the increase in focus size has been quantified with time. The data suggests a threshold for the induction of large foci at lower doses, which further supports the hypothesis that larger foci contain more complex lesions that may constitute multiple DSBs. Additionally, the staggered induction times for small, medium and large sized foci may suggest interplay between the size categories. Through two novel approaches using fixed cells and through monitoring of live cells after exposure to γ-rays, evidence has been evaluated for the dynamics of 53BP1 foci. Although there is no evidence for directed movement of foci as a whole, there is evidence that suggests some proximally located foci may be capable of limited movement, in the region of 1μm whilst other proximally located foci can appear fixed. The lack of evidence for large scale directed movement of foci, supports the argument for the ICN model, where intermingling of chromosomes and looping out of chromatin for functional purposes if the underlying mechanism for sequential chromosomal exchange aberrations.

7 Supplementary data
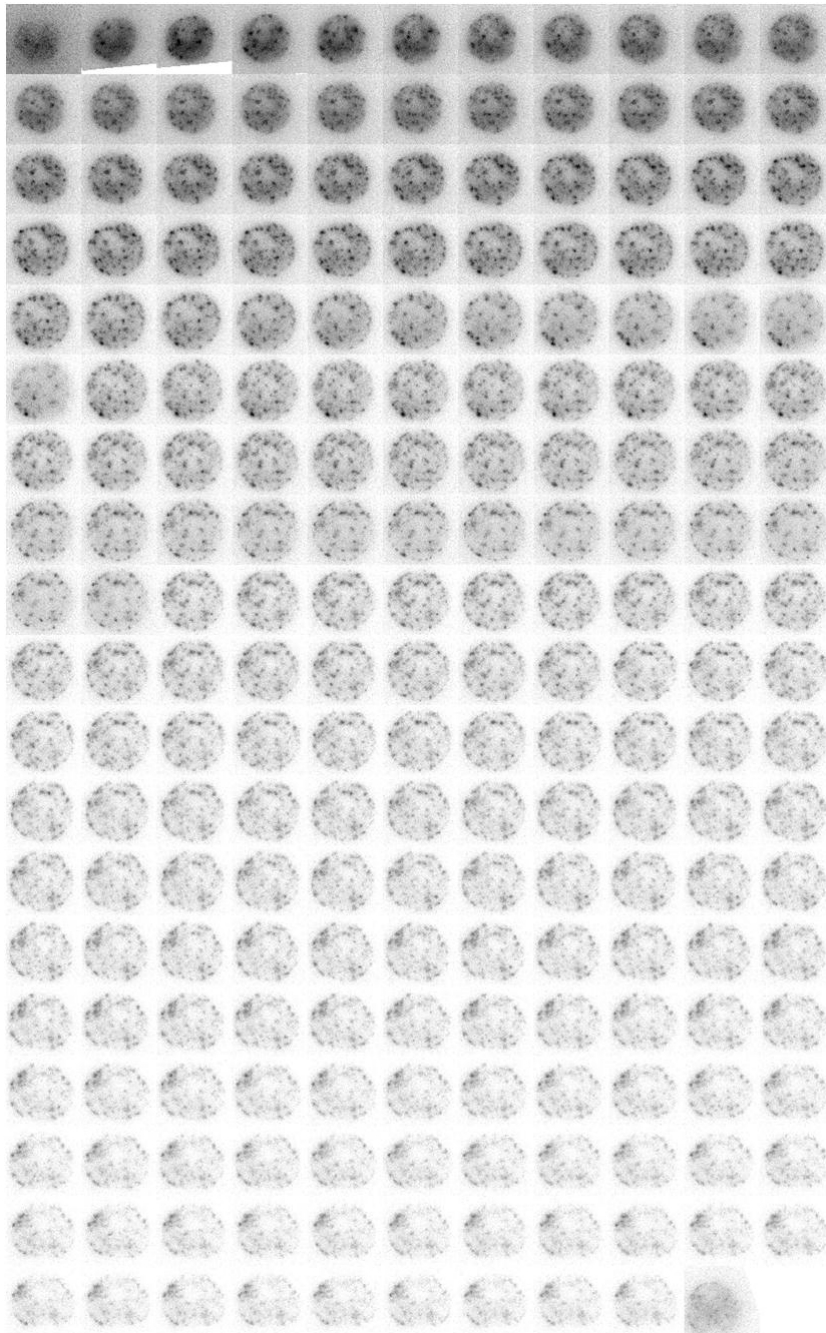
Figure 7-1 Time lapse of 53BP1 in HBE (nucleus 1) 2Gy γ-rays
(all subsequent images have been inverted for clarity)
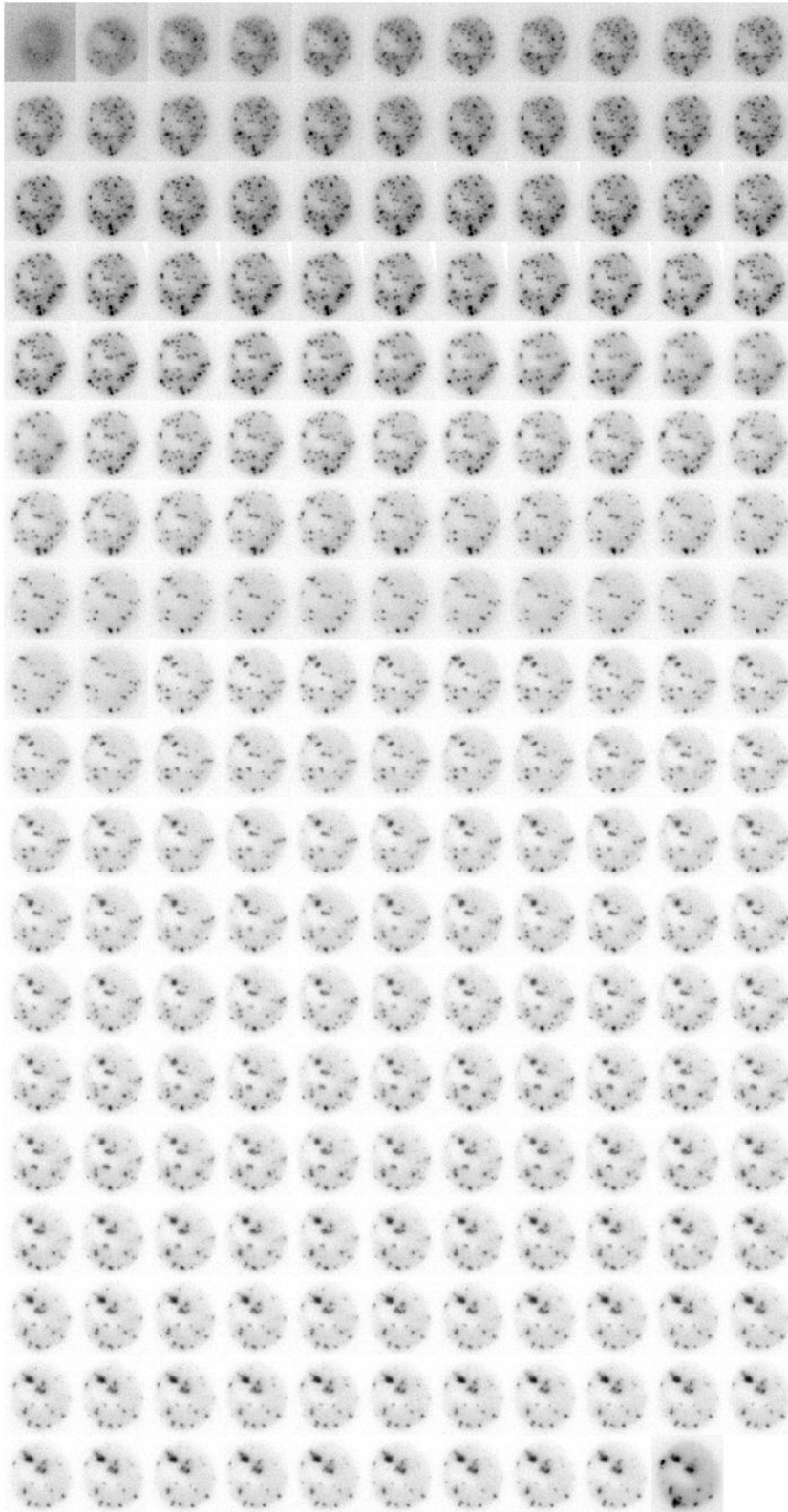
Figure 7-2 Time lapse of 53BP1 in HBE (nucleus 2) 2Gy γ-rays
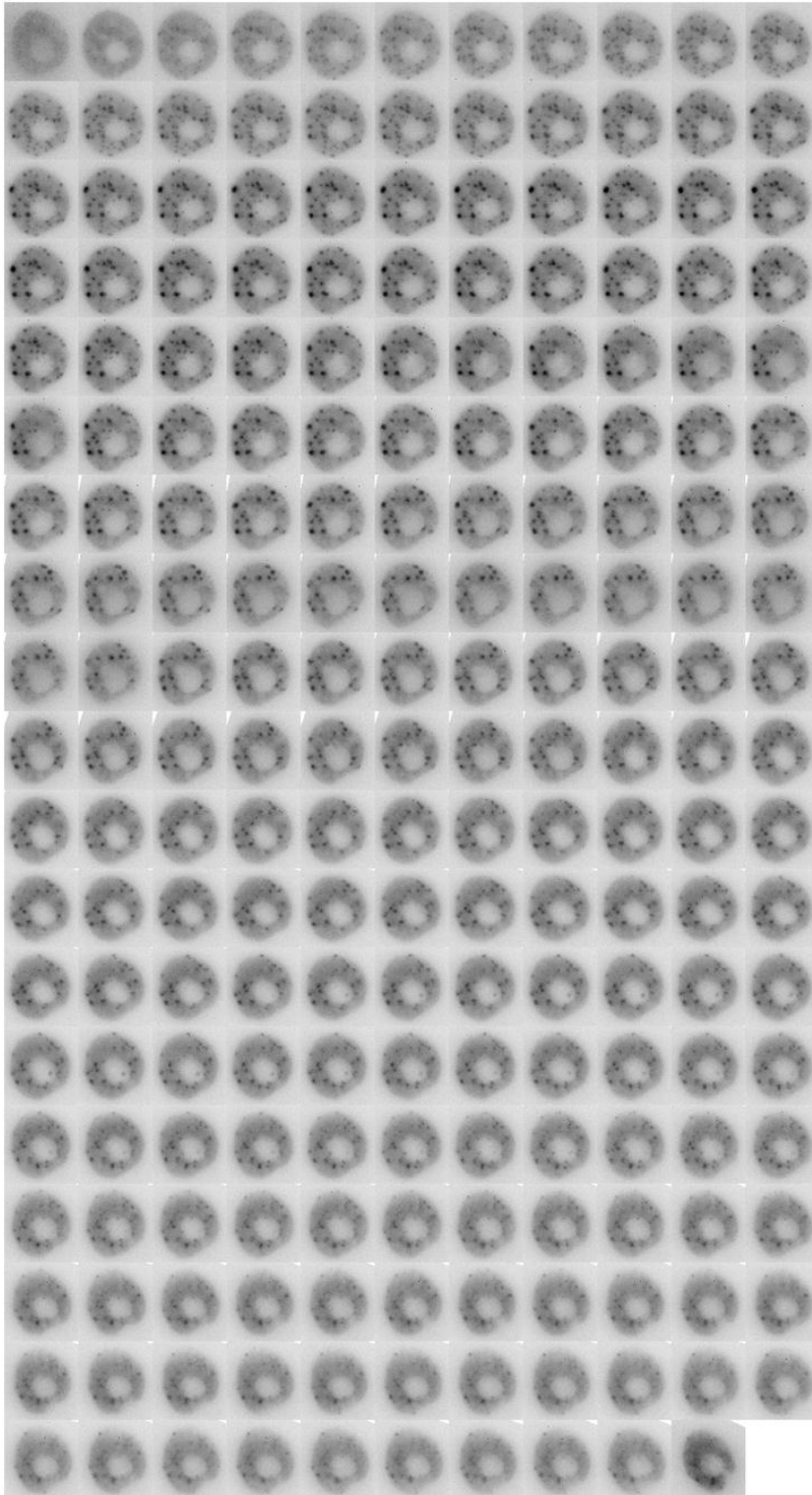
Figure 7-3 Time lapse of 53BP1 in HBE (nucleus 3) 2Gy γ-rays
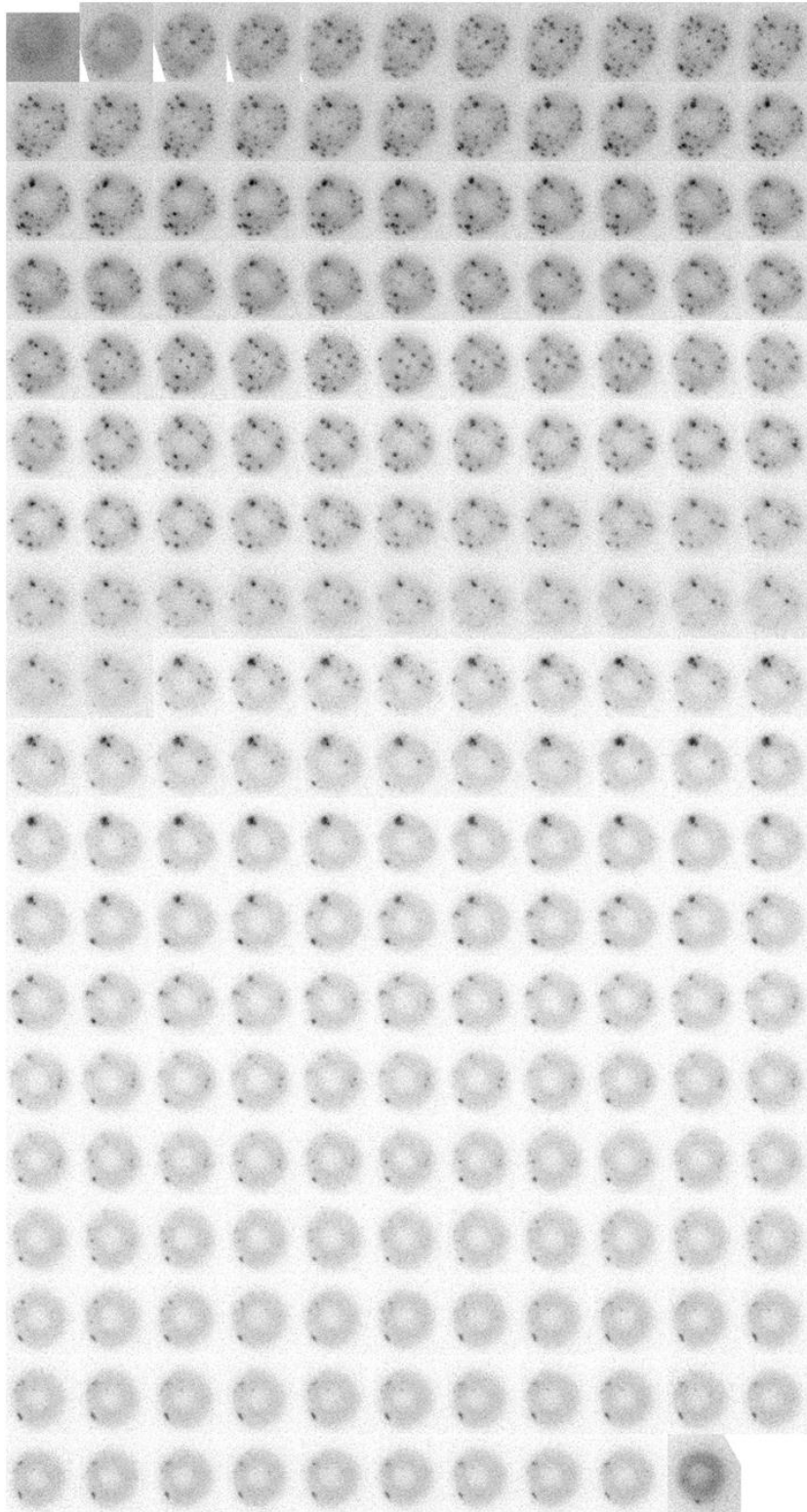
Figure 7-4 Time lapse of 53BP1 in HBE (nucleus 4) 2Gy γ-rays
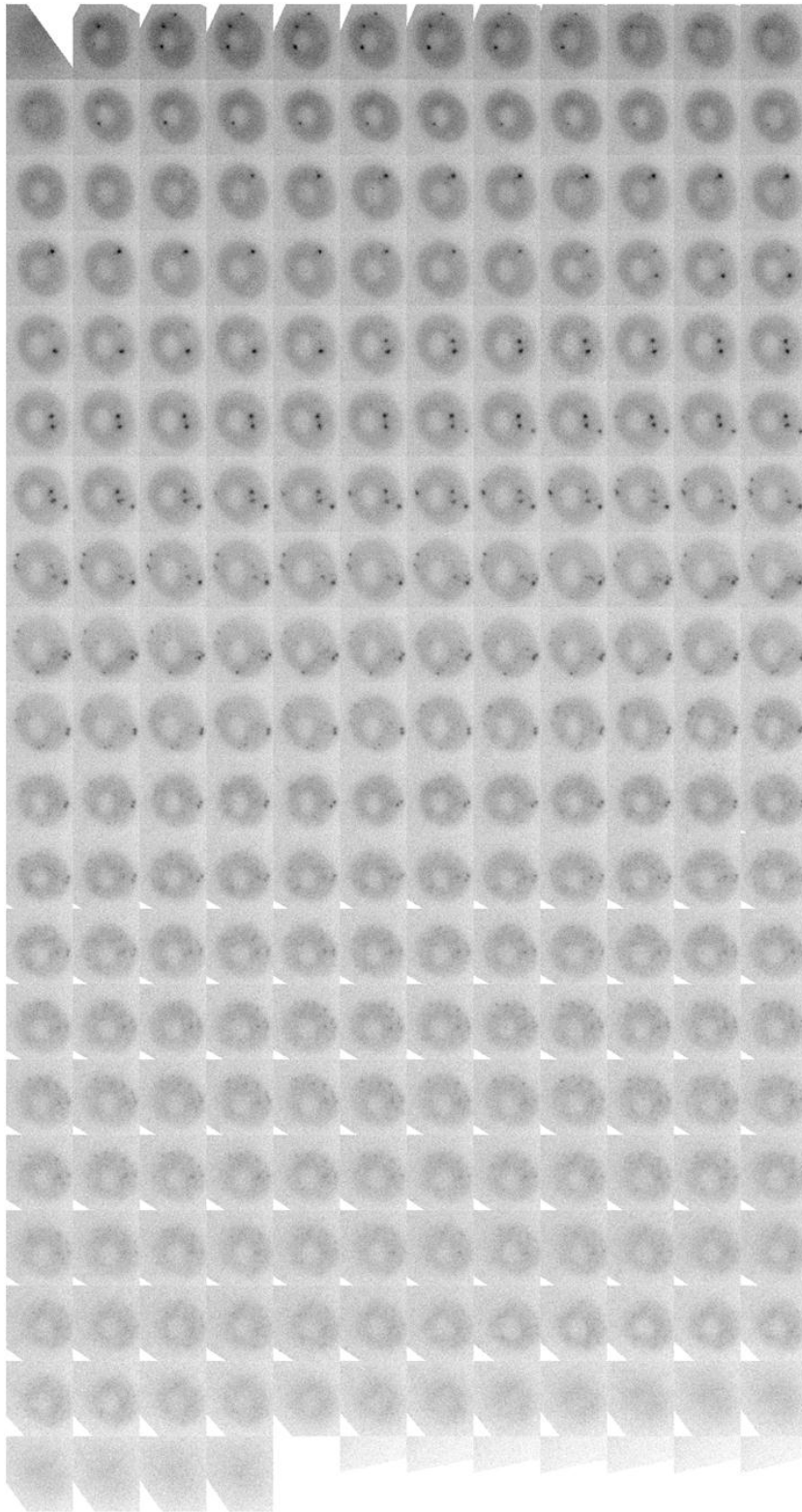
Figure 7-5 Time lapse of 53BP1 in HBE (nucleus 1) sham exposure

166
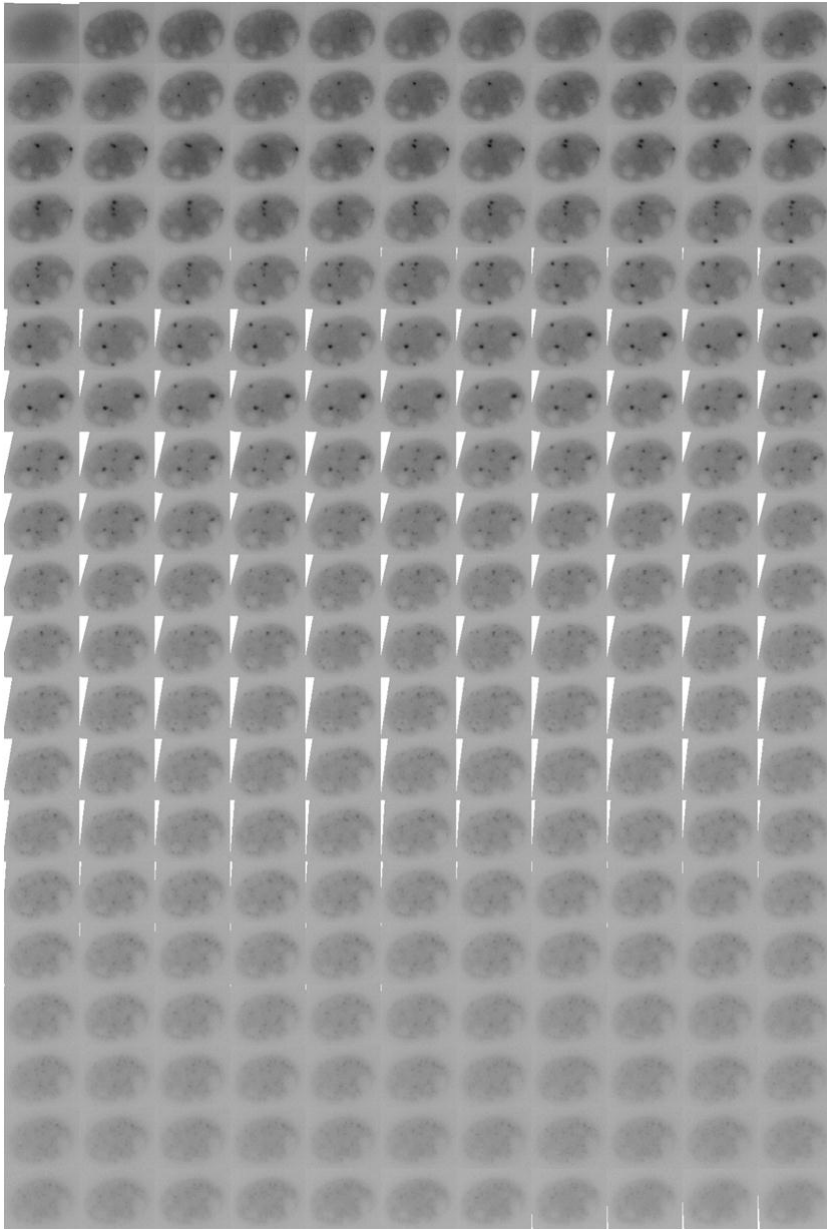
Figure 7-6 Time lapse of 53BP1 in HBE (nucleus 2) sham exposure
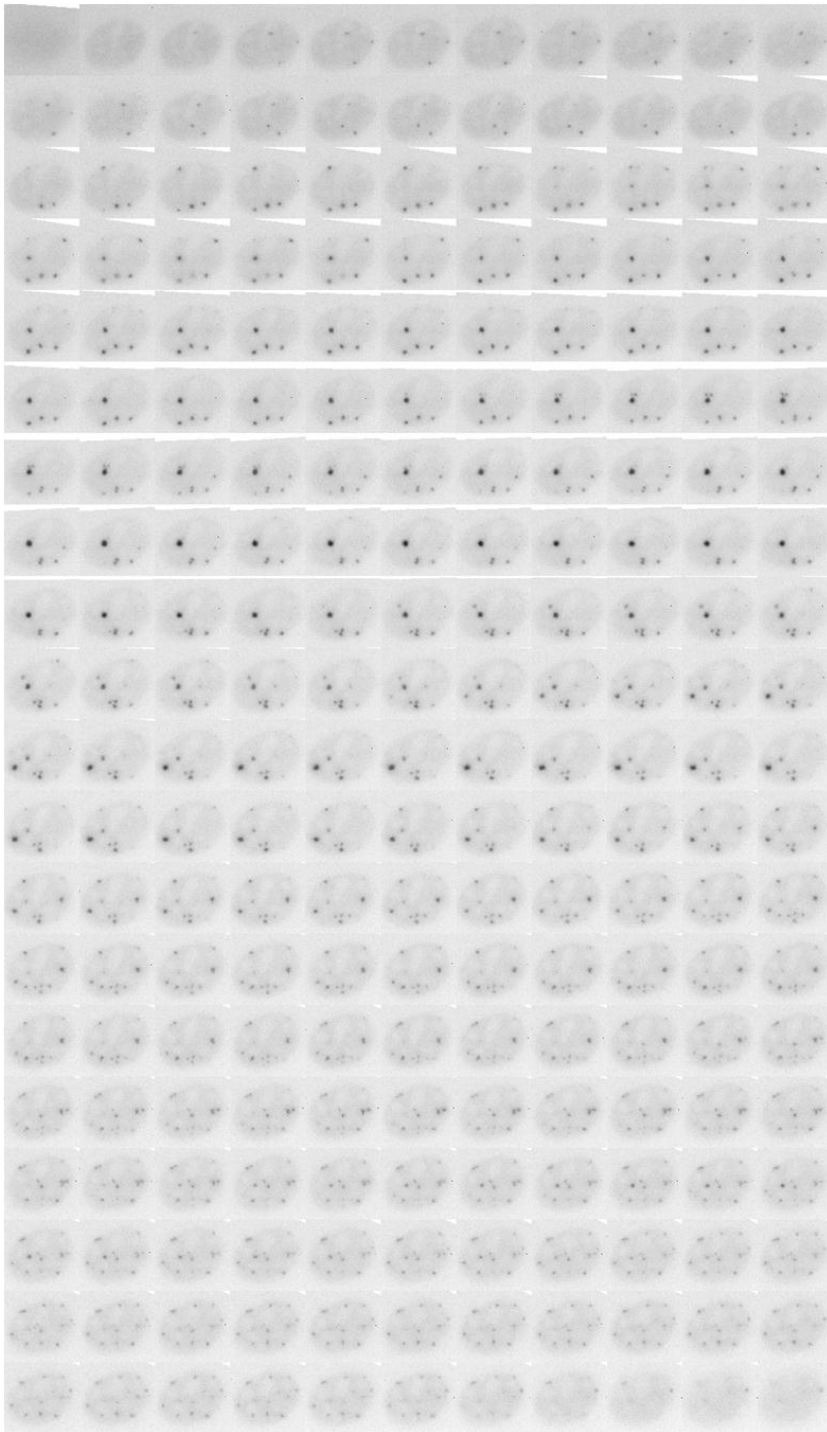
Figure 7-7 Time lapse of 53BP1 in HBE (nucleus 3) sham exposure

8 Appendix

The concept of moments originally comes from physics and statistics but can also be applied to the pixel distribution of the gray-scale image. The moment of the order p, q for a binary region is defined by the following formula:

$$m_{pq} = \sum_{(u,v) \in R} u^p v^q,$$

Where R is a set of region pixels for which the moment is calculated. The area of that region can be expressed as the zero order moment:

$$A(R) = |R| = \sum_{(u,v) \in R} 1 = \sum_{(u,v) \in R} u^0 v^0 = m_{00}(R)$$

Coordinates of the gravity centre of the spot region (centroid) can be found by formulas:

$$\bar{x} = \frac{m_{10}(R)}{m_{00}(R)} = \frac{1}{|R|} \sum_{(u,v) \in R} u^1 v^0$$

$$\bar{y} = \frac{m_{01}(R)}{m_{00}(R)} = \frac{1}{|R|} \sum_{(u,v) \in R} u^0 v^1$$

In order to calculate position independent parameters such as rotation angle and eccentricity of the ellipse the Central moments are used. The central moments are similar to the ordinary moments, except that they are calculated around the region Centroid $(\bar{x}, \bar{y})$:

$$\mu_{pq}(R) = \sum_{(u,v) \in R} (u - \bar{x})^p (v - \bar{y})^q$$

The rotation angle of the ellipse is the angle between X-axis and major ellipse axis (Fig.16). It is expressed via central moments of different orders:

$$\theta_R = \frac{1}{2} tan^{-1} \left(\frac{2 * \mu_{11}(R)}{\mu_{20}(R) - \mu_{02}(R)} \right)$$
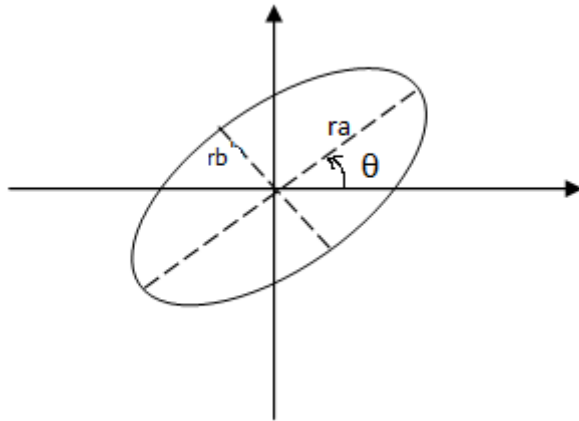
Figure 8-1 Illustration of rotation angles for an elipse

Ellipse with rotation angle θ, major and minor radii r_a and r_b

Eccentricity of the ellipse is calculated as follows:

$$Ecc(R) = \frac{a_1}{a_2} = \frac{\mu_{20}+\mu_{02}+\sqrt{(\mu_{20}-\mu_{02})^2+4*\mu_{11}^2}}{\mu_{20}+\mu_{02}-\sqrt{(\mu_{20}-\mu_{02})^2+4*\mu_{11}^2}},$$

where $a_1 = 2\lambda_1$, $a_2 = 2\lambda_2$ are multiples of eigenvalues λ_1, λ_2 of the symmetric matrix

$$A = \begin{pmatrix} \mu_{20} & \mu_{11} \\ \mu_{11} & \mu_{02} \end{pmatrix}$$

The minor and major radii of the approximation ellipse can be express via its eccentricity:

$$r_a = 2 * \left(\frac{\lambda_1}{|R|}\right)^{1/2} = \left(\frac{2a_1}{|R|}\right)^{1/2}$$

$$r_b = 2 * \left(\frac{\lambda_2}{|R|}\right)^{1/2} = \left(\frac{2a_2}{|R|}\right)^{1/2}$$

This localisation algorithm uses the above to return the number of RIF in a slice, their centre coordinates, theirs areas, rotation, angle and radii, which are then used to reconstruct foci in 3D.

9 References

Anderson, L., Henderson, C. & Adachi, Y. (2001) Phosphorylation and rapid relocalization of 53BP1 to nuclear foci upon DNA damage. *Molecular and cellular biology,* 21**,** 1719-29.

Anderson, R. M., Papworth, D. G., Stevens, D. L., Sumption, N. D. & Goodhead, D. T. (2006) Increased complexity of radiation-induced chromosome aberrations consistent with a mechanism of sequential formation. *Cytogenetic and genome research,* 112**,** 35-44.

Anderson, R. M., Stevens, D. L. & Goodhead, D. T. (2002) M-FISH analysis shows that complex chromosome aberrations induced by alpha -particle tracks are cumulative products of localized rearrangements. *Proceedings of the National Academy of Sciences of the United States of America,* 99**,** 12167-72.

Arents, G., Burlingame, R. W., Wang, B. C., Love, W. E. & Moudrianakis, E. N. (1991) The nucleosomal core histone octamer at 3.1 A resolution: a tripartite protein assembly and a left-handed superhelix. *Proceedings of the National Academy of Sciences of the United States of America,* 88**,** 10148-52.

Asaithamby, A. & Chen, D. J. (2009) Cellular responses to DNA double-strand breaks after low-dose γ-irradiation. *Nucleic acids research,* 37**,** 3912-23.

Aten, J. A., Stap, J., Krawczyk, P. M., Van Oven, C. H., Hoebe, R. A., Essers, J. & Kanaar, R. (2004) Dynamics of DNA Double-Strand Breaks Revealed by Clustering of Damaged Chromosome Domains. *Science,* 303**,** 92-5.

Avery, O. T., Macleod, C. M. & Mccarty, M. (1944) STUDIES ON THE CHEMICAL NATURE OF THE SUBSTANCE INDUCING TRANSFORMATION OF PNEUMOCOCCAL TYPES : INDUCTION OF TRANSFORMATION BY A DESOXYRIBONUCLEIC ACID FRACTION ISOLATED FROM PNEUMOCOCCUS TYPE III. *The Journal of experimental medicine,* 79**,** 137-58.

Baird, J., Belchamber, C., Bellamy, D. & Blake, D. (2005) Lung cancer: The diagnosis and treatment of lung cancer.

Banath, J. P., Klokov, D., Macphail, S. H., Banuelos, C. A. & Olive, P. L. (2010) Residual gammaH2AX foci as an indication of lethal DNA lesions. *BMC cancer,* 10**,** 4.

Bao, S., Harwood, P. W., Wood, B. H., Chrisler, W. B., Groch, K. M. & Brooks, A. L. (1997) Comparative clastogenic sensitivity of respiratory tract cells to gamma rays. *Radiation research,* 148**,** 90-7.

Barber, P. L., R. Pierce, G. Rothkamm, K. Vojnovic, B. (2007) Gamma-H2AX Foci Counting: Image processing and control software for high-content screening.

Beels, L., Bacher, K., Smeets, P., Verstraete, K., Vral, A. & Thierens, H. (2011) Dose-length product of scanners correlates with DNA damage in patients undergoing contrast CT. *European Journal of Radiology,* In Press, Corrected Proof.

Bekker-Jensen, S., Lukas, C., Melander, F., Bartek, J. & Lukas, J. (2005) Dynamic assembly and sustained retention of 53BP1 at the sites of DNA damage are controlled by Mdc1/NFBD1. *The Journal of cell biology,* 170**,** 201-11.

Bernas, T., Robinson, J. P., Asem, E. K. & Rajwa, B. (2005) Loss of image quality in photobleaching during microscopic imaging of fluorescent probes bound to chromatin. *Journal of biomedical optics,* 10**,** 064015.

Bocker, W. & Iliakis, G. (2006) Computational Methods for Analysis of Foci: Validation for Radiation-Induced γ-H2AX Foci in Human Cells. *Radiation Research,* 165.

Boei, J. J., Fomina, J., Darroudi, F., Nagelkerke, N. J. & Mullenders, L. H. (2006) Interphase chromosome positioning affects the spectrum of radiation-induced chromosomal aberrations. *Radiation research,* 166**,** 319-26.

Bolzer, A., Kreth, G., Solovei, I., Koehler, D., Saracoglu, K., Fauth, C., Muller, S., Eils, R., Cremer, C., Speicher, M. R. & Cremer, T. (2005) Three-dimensional maps of all chromosomes in human male fibroblast nuclei and prometaphase rosettes. *PLoS Biol,* 3**,** e157.

Botuyan, M. V., Lee, J., Ward, I. M., Kim, J., Thompson, J. R., Chen, J. & Mer, G. (2006) Structural Basis for the Methylation State-Specific Recognition of Histone H4-K20 by 53BP1 and Crb2 in DNA Repair. *Cell,* 127**,** 1361-1373.

Bouquet, F., Muller, C. & Salles, B. (2006) The Loss of γH2AX Signal is a Marker of DNA Double Strand Breaks Repair Only at Low Levels of DNA Damage. *Cell Cycle,* 5**,** 1116-1122.

Bourton, E. C., Plowman, P. N., Smith, D., Arlett, C. F. & Parris, C. N. (2011) Prolonged expression of the γ-H2AX DNA repair biomarker correlates with excess acute and chronic toxicity from radiotherapy treatment. *International Journal of Cancer***,** n/a-n/a.

Boyle, S., Gilchrist, S., Bridger, J. M., Mahy, N. L., Ellis, J. A. & Bickmore, W. A. (2001) The spatial organization of human chromosomes within the nuclei of normal and emerin-mutant cells. *Hum Mol Genet,* 10**,** 211-9.

Branco, M. R. & Pombo, A. (2006) Intermingling of chromosome territories in interphase suggests role in translocations and transcription-dependent associations. *PLoS Biol,* 4**,** e138.

Branzei, D. & Foiani, M. (2010) Maintaining genome stability at the replication fork. *Nat Rev Mol Cell Biol,* 11**,** 208-19.

Bridger, J. M., Herrmann, H., Munkel, C. & Lichter, P. (1998) Identification of an interchromosomal compartment by polymerization of nuclear-targeted vimentin. *Journal of cell science,* 111 (Pt 9)**,** 1241-53.

Britton, M. G., Darlison, L., Entwisle, J. & Greenstone, M. (2007) BTS statement on malignant mesothelioma in the UK, 2007. *Thorax,* 62 Suppl 2**,** ii1-ii19.

Cai, Z., Vallis, K. A. & Reilly, R. M. (2009) Computational analysis of the number, area and density of gamma-H2AX foci in breast cancer cells exposed to (111)In-DTPA-hEGF or gamma-rays using Image-J software. *International journal of radiation biology,* 85**,** 262-71.

Calini, V., Urani, C. & Camatini, M. (2002) Comet assay evaluation of DNA single- and double-strand breaks induction and repair in C3H10T1/2 cells. *Cell Biol Toxicol,* 18**,** 369-79.

Calsou, P., Delteil, C., Frit, P., Drouet, J. & Salles, B. (2003) Coordinated assembly of Ku and p460 subunits of the DNA-dependent protein kinase on DNA ends is necessary for XRCC4-ligase IV recruitment. *J Mol Biol,* 326**,** 93-103.

Cao, Z., Kuhne, W. W., Steeb, J., Merkley, M. A., Zhou, Y., Janata, J. & Dynan, W. S. (2010) Use of a microscope stage-mounted Nickel-63 microirradiator for real-time observation of the DNA double-strand break response. *Nucleic acids research,* 38**,** e144.

Carpenter, A. E., Jones, T. R., Lamprecht, M. R., Clarke, C., Kang, I. H., Friman, O., Guertin, D. A., Chang, J. H., Lindquist, R. A., Moffat, J., Golland, P. & Sabatini, D. M. (2006) CellProfiler: image analysis software for identifying and quantifying cell phenotypes. *Genome Biol,* 7**,** R100.

Carter, T. H., Kopman, C. R. & James, C. B. (1988) DNA-stimulated protein phosphorylation in HeLa whole cell and nuclear extracts. *Biochemical and biophysical research communications,* 157**,** 535-40.

Chappell, C., Hanakahi, L. A., Karimi-Busheri, F., Weinfeld, M. & West, S. C. (2002) Involvement of human polynucleotide kinase in double-strand break repair by non-homologous end joining. *The EMBO journal,* 21**,** 2827-32.

Clark, P. J. & Evans, F. C. (1954) Distance to Nearest Neighbor as a Measure of Spatial Relationships in Populations. *Ecology,* 35**,** 445-453.

Clark, P. J. & Evans, F. C. (1979) Generalization of a Nearest Neighbor Measure of Dispersion for Use in K Dimensions. *Ecology,* 60**,** 316-317.

Coggle, J. E., Lambert, B. E. & Moores, S. R. (1986) Radiation effects in the lung. *Environ Health Perspect,* 70**,** 261-91.

Costes, S. V., Boissiere, A., Ravani, S., Romano, R., Parvin, B. & Barcellos-Hoff, M. H. (2006) Imaging features that discriminate between foci induced by high- and low-LET radiation in human fibroblasts. *Radiation research,* 165**,** 505-15.

Costes, S. V., Ponomarev, A., Chen, J. L., Nguyen, D., Cucinotta, F. A. & Barcellos-Hoff, M. H. (2007) Image-based modeling reveals dynamic redistribution of DNA damage into nuclear sub-domains. *PLoS computational biology,* 3**,** e155.

Cremer, T., Kurz, A., Zirbel, R., Dietzel, S., Rinke, B., Schrock, E., Speicher, M. R., Mathieu, U., Jauch, A., Emmerich, P., Scherthan, H., Ried, T., Cremer, C. & Lichter, P. (1993) Role of chromosome territories in the functional compartmentalization

of the cell nucleus. *Cold Spring Harb Symp Quant Biol,* 58**,** 777-92.

Croft, J. A., Bridger, J. M., Boyle, S., Perry, P., Teague, P. & Bickmore, W. A. (1999) Differences in the localization and morphology of chromosomes in the human nucleus. *The Journal of cell biology,* 145**,** 1119-31.

Darby, S., Hill, D., Auvinen, A., Barros-Dios, J. M., Baysson, H., Bochicchio, F., Deo, H., Falk, R., Forastiere, F., Hakama, M., Heid, I., Kreienbrock, L., Kreuzer, M., Lagarde, F., Makelainen, I., Muirhead, C., Oberaigner, W., Pershagen, G., Ruano-Ravina, A., Ruosteenoja, E., Rosario, A. S., Tirmarche, M., Tomasek, L., Whitley, E., Wichmann, H. E. & Doll, R. (2005) Radon in homes and risk of lung cancer: collaborative analysis of individual data from 13 European case-control studies. *BMJ,* 330**,** 223.

Defazio, L. G., Stansel, R. M., Griffith, J. D. & Chu, G. (2002) Synapsis of DNA ends by DNA-dependent protein kinase. *The EMBO journal,* 21**,** 3192-3200.

Delara, C. M., Jenner, T. J., Townsend, K. M., Marsden, S. J. & O'neill, P. (1995) The effect of dimethyl sulfoxide on the induction of DNA double-strand breaks in V79-4 mammalian cells by alpha particles. *Radiation research,* 144**,** 43-9.

Desai, N., Davis, E., O'neill, P., Durante, M., Cucinotta, F. A. & Wu, H. (2005) Immunofluorescence detection of clustered gamma-H2AX foci induced by HZE-particle radiation. *Radiation research,* 164**,** 518-22.

Dezawa, M., Fujii, K., Kita, K., Nomura, J., Sugita, K., Adachi-Usami, E. & Suzuki, N. (1999) Increase in nucleoli after x-radiation of fibroblasts of patients with Gorlin syndrome. *J Lab Clin Med,* 134**,** 585-91.

Dickey, J. S., Baird, B. J., Redon, C. E., Sokolov, M. V., Sedelnikova, O. A. & Bonner, W. M. (2009) Intercellular communication of cellular stress monitored by gamma-H2AX induction. *Carcinogenesis,* 30**,** 1686-95.

Dimitrova, N., Chen, Y. C., Spector, D. L. & De Lange, T. (2008) 53BP1 promotes non-homologous end joining of telomeres by increasing chromatin mobility. *Nature,* 456**,** 524-8.

Du, G., Drexler, G. A., Friedland, W., Greubel, C., Hable, V., Krã¼Cken, R., Kugler, A., Tonelli, L., Friedl, A. A. & Dollinger, G. (2011) Spatial Dynamics of DNA Damage Response Protein Foci along the Ion Trajectory of High-LET Particles. *Radiation research*.

Edelmann, M., Gamarra, F., Da Silva, A. K., Hornung, V., Castro, M., Passlick, B., Huber, R. M. & Bergner, A. (2005) Cell cycle effects of radiation on human bronchial epithelium and lung carcinoma cells in monolayer cultures and a three-dimensional co-culture system. *Radiation research,* 164**,** 391-9.

Elcock, L. S. & Bridger, J. M. (2010) Exploring the relationship between interphase gene positioning, transcriptional regulation and the nuclear matrix. *Biochem Soc Trans,* 38**,** 263-7.

Eliezer, Y., Argaman, L., Rhie, A., Doherty, A. J. & Goldberg, M. (2009) The direct interaction between 53BP1 and MDC1 is required for the recruitment of 53BP1 to sites of damage. *The Journal of biological chemistry,* 284**,** 426-35.

Falk, M., Lukasova, E., Gabrielova, B., Ondrej, V. & Kozubek, S. (2007) Chromatin dynamics during DSB repair. *Biochimica et biophysica acta,* 1773**,** 1534-45.

Falk, M., Lukasova, E. & Kozubek, S. (2008) Chromatin structure influences the sensitivity of DNA to gamma-radiation. *Biochimica et biophysica acta,* 1783**,** 2398-414.

Falk, M., Lukasova, E. & Kozubek, S. (2010) Higher-order chromatin structure in DSB induction, repair and misrepair. *Mutation Research/Reviews in Mutation Research,* 704**,** 88-100.

Finch, J. T. & Klug, A. (1976) Solenoidal model for superstructure in chromatin. *Proceedings of the National Academy of Sciences of the United States of America,* 73**,** 1897-901.

Fisher, D. R., Hui, T. E. & James, A. C. (1991) Model for Assessing Radiation Dose to Epithelial Cells of the Human Respiratory Tract from Radon Progeny. *Radiation protection dosimetry,* 38**,** 73-80.

Fitzgerald, J. E., Grenon, M. & Lowndes, N. F. (2009) 53BP1: function and mechanisms of focal recruitment. *Biochem Soc Trans,* 37**,** 897-904.

Frank, K. M., Sekiguchi, J. M., Seidl, K. J., Swat, W., Rathbun, G. A., Cheng, H. L., Davidson, L., Kangaloo, L. & Alt, F. W. (1998) Late embryonic lethality and impaired V(D)J recombination in mice lacking DNA ligase IV. *Nature,* 396**,** 173-7.

Gardiner, K. (1995) Human genome organization. *Curr Opin Genet Dev,* 5**,** 315-22.

Gerashchenko, B. I. & Dynlacht, J. R. (2009) A tool for enhancement and scoring of DNA repair foci. *Cytometry. Part A : the journal of the International Society for Analytical Cytology,* 75**,** 245-52.

Giunta, S., Belotserkovskaya, R. & Jackson, S. P. (2010) DNA damage signaling in response to double-strand breaks during mitosis. *The Journal of cell biology,* 190**,** 197-207.

Goodarzi, A. A., Jeggo, P. & Lobrich, M. (2010) The influence of heterochromatin on DNA double strand break repair: Getting the strong, silent type to relax. *DNA repair,* 9**,** 1273-1282.

Goodarzi, A. A. & Jeggo, P. A. (2009) 'A mover and a shaker': 53BP1 allows DNA doublestrand breaks a chance to dance and unite. *F1000 Biol Rep,* 1**,** 21.

Goodarzi, A. A. & Jeggo, P. A. (2011) Irradiation induced foci (IRIF) as a biomarker for radiosensitivity. *Mutation Research/Fundamental and Molecular Mechanisms of Mutagenesis,* In Press, Corrected Proof.

Goodarzi, A. A., Noon, A. T. & Jeggo, P. A. (2009) The impact of heterochromatin on DSB

repair. *Biochem Soc Trans,* 37**,** 569-76.

Goodhead, D. T. (1989) The initial physical damage produced by ionizing radiations. *International journal of radiation biology,* 56**,** 623-34.

Groesser, T., Chang, H., Fontenay, G., Chen, J., Costes, S. V., Helen Barcellos-Hoff, M., Parvin, B. & Rydberg, B. (2011) Persistence of gamma-H2AX and 53BP1 foci in proliferating and non-proliferating human mammary epithelial cells after exposure to gamma-rays or iron ions. *International journal of radiation biology*.

Gu, Y., Jin, S., Gao, Y., Weaver, D. T. & Alt, F. W. (1997) Ku70-deficient embryonic stem cells have increased ionizing radiosensitivity, defective DNA end-binding activity, and inability to support V(D)J recombination. *Proceedings of the National Academy of Sciences of the United States of America,* 94**,** 8076-81.

Hall, E. J. & Giaccia, A. J. (2006) *Radiobiology for the Radiologist,* Toronto, Lippincott Williams and Wilkins.

Hamada, N., Schettino, G., Kashino, G., Vaid, M., Suzuki, K., Kodama, S., Vojnovic, B., Folkard, M., Watanabe, M., Michaela, B. D. & Prisea, K. M. (2006) Histone H2AX Phosphorylation in Normal Human Cells Irradiated with Focused Ultrasoft X Rays: Evidence for Chromatin Movement during Repair. *Radiation Research,* 166**,** 31-38.

Harper, J. V., Anderson, J. A. & O'neill, P. (2010) Radiation induced DNA DSBs: Contribution from stalled replication forks? *DNA repair,* 9**,** 907-913.

Heussen, C., Nackerdien, Z., Smit, B. J. & Bohm, L. (1987) Irradiation damage in chromatin isolated from V-79 Chinese hamster lung fibroblasts. *Radiation research,* 110**,** 84-94.

Holley, W. R. & Chatterjee, A. (1996) Clusters of DNA induced by ionizing radiation: formation of short DNA fragments. I. Theoretical modeling. *Radiation research,* 145**,** 188-99.

Hou, Y., Lavaf, A., Huang, D., Peters, S., Huq, R., Friedrich, V., Rosenstein, B. S. & Kao, J. (2009) Development of an Automated γ-H2AX Immunocytochemistry Assay. *Radiation Research,* 171**,** 360-367.

Huyen, Y., Zgheib, O., Ditullio Jr, R. A., Gorgoulis, V. G., Zacharatos, P., Petty, T. J., Sheston, E. A., Mellert, H. S., Stavridi, E. S. & Halazonetis, T. D. (2004) Methylated lysine 79 of histone H3 targets 53BP1 to DNA double-strand breaks. *Nature,* 432**,** 406-411.

Ibragimova, N. V., Tugolukova, L. V., Kravtsov, V. & Nikiforov, A. M. (2001) [The number of nucleoli in peripheral blood lymphocytes of the Chernobyl accident liquidators]. *Tsitologiia,* 43**,** 941-3.

Ishikawa, A., Yamauchi, M., Suzuki, K. & Yamashita, S. (2010) Image-based quantitative determination of DNA damage signal reveals a threshold for G2 checkpoint activation in response to ionizing radiation. *Genome integrity,* 1**,** 10.

Ivashkevich, A. N., Martin, O. A., Smith, A. J., Redon, C. E., Bonner, W. M., Martin, R. F. & Lobachevsky, P. N. (2011) [gamma]H2AX foci as a measure of DNA damage: A computational approach to automatic analysis. *Mutation Research/Fundamental and Molecular Mechanisms of Mutagenesis,* 711**,** 49-60.

Jakob, B., Splinter, J., Durante, M. & Taucher-Scholz, G. (2009) Live cell microscopy analysis of radiation-induced DNA double-strand break motion. *Proceedings of the National Academy of Sciences of the United States of America,* 106**,** 3172-7.

Jeggo, P. A. & Lobrich, M. (2006) Contribution of DNA repair and cell cycle checkpoint arrest to the maintenance of genomic stability. *DNA repair,* 5**,** 1192-8.

Johnson, C. A., Goddard, J. P. & Adams, R. L. (1995) The effect of histone H1 and DNA methylation on transcription. *Biochem J,* 305 (Pt 3)**,** 791-8.

Jucha, A., Wegierek-Ciuk, A., Koza, Z., Lisowska, H., Wojcik, A., Wojewodzka, M. & Lankoff, A. (2010) FociCounter: A freely available PC programme for quantitative and qualitative analysis of gamma-H2AX foci. *Mutation research,* 696**,** 16-20.

Kapur, J. N., Sahoo, P. K. & Wong, A. K. C. (1985) A new method for gray-level picture thresholding using the entropy of the histogram. *Computer Vision, Graphics, and Image Processing,* 29**,** 273-285.

Karran, P. (2000) DNA double strand break repair in mammalian cells. *Curr Opin Genet Dev,* 10**,** 144-50.

Kato, T. A., Okayasu, R. & Bedford, J. S. (2008) Comparison of the induction and disappearance of DNA double strand breaks and gamma-H2AX foci after irradiation of chromosomes in G1-phase or in condensed metaphase cells. *Mutation research,* 639**,** 108-12.

Kornberg, R. D. (1974) Chromatin structure: a repeating unit of histones and DNA. *Science,* 184**,** 868-71.

Kozubek, S., Lukasova, E., Jirsova, P., Koutna, I., Kozubek, M., Ganova, A., Bartova, E., Falk, M. & Pasekova, R. (2002) 3D Structure of the human genome: order in randomness. *Chromosoma,* 111**,** 321-31.

Krawczyk, P. M., Stap, J., Van Oven, C., Hoebe, R. & Aten, J. A. (2006) Clustering of double strand break-containing chromosome domains is not inhibited by inactivation of major repair proteins. *Radiation protection dosimetry,* 122**,** 150-3.

Kreda, S. M., Mall, M., Mengos, A., Rochelle, L., Yankaskas, J., Riordan, J. R. & Boucher, R. C. (2005) Characterization of wild-type and deltaF508 cystic fibrosis transmembrane regulator in human respiratory epithelia. *Molecular biology of the cell,* 16**,** 2154-67.

Kruhlak, M. J., Celeste, A., Dellaire, G., Fernandez-Capetillo, O., Muller, W. G., Mcnally, J. G., Bazett-Jones, D. P. & Nussenzweig, A. (2006) Changes in chromatin structure

and mobility in living cells at sites of DNA double-strand breaks. *The Journal of cell biology,* 172**,** 823-34.

Kurz, A., Lampel, S., Nickolenko, J. E., Bradl, J., Benner, A., Zirbel, R. M., Cremer, T. & Lichter, P. (1996) Active and inactive genes localize preferentially in the periphery of chromosome territories. *The Journal of cell biology,* 135**,** 1195-205.

Lassmann, M., Hanscheid, H., Gassen, D., Biko, J., Meineke, V., Reiners, C. & Scherthan, H. (2010) In vivo formation of gamma-H2AX and 53BP1 DNA repair foci in blood cells after radioiodine therapy of differentiated thyroid cancer. *Journal of nuclear medicine : official publication, Society of Nuclear Medicine,* 51**,** 1318-25.

Leatherbarrow, E. L., Harper, J. V., Cucinotta, F. A. & O'neill, P. (2006) Induction and quantification of gamma-H2AX foci following low and high LET-irradiation. *International journal of radiation biology,* 82**,** 111-8.

Lechner, J. F. & Laveck, M. A. (1985) A serum-free method for culturing normal human bronchial epithelial cells at clonal density. *Methods in Cell Science,* 9**,** 43-48.

Lee, J. H., Cheong, H. M., Kang, M. Y., Kim, S. Y. & Kang, Y. (2009) Ser1778 of 53BP1 Plays a Role in DNA Double-strand Break Repairs. *The Korean journal of physiology & pharmacology : official journal of the Korean Physiological Society and the Korean Society of Pharmacology,* 13**,** 343-8.

Lee, J. H., Goodarzi, A. A., Jeggo, P. A. & Paull, T. T. (2010) 53BP1 promotes ATM activity through direct interactions with the MRN complex. *The EMBO journal,* 29**,** 574-85.

Li, Z., Otevrel, T., Gao, Y., Cheng, H. L., Seed, B., Stamato, T. D., Taccioli, G. E. & Alt, F. W. (1995) The XRCC4 gene encodes a novel protein involved in DNA double-strand break repair and V(D)J recombination. *Cell,* 83**,** 1079-89.

Lisby, M., Mortensen, U. H. & Rothstein, R. (2003) Colocalization of multiple DNA double-strand breaks at a single Rad52 repair centre. *Nature Cell Biology,* 5**,** 572-577.

Lisby, M. & Rothstein, R. (2004) DNA damage checkpoint and repair centers. *Current opinion in cell biology,* 16**,** 328-34.

Lobrich, M., Cooper, P. K. & Rydberg, B. (1996) Non-random distribution of DNA double-strand breaks induced by particle irradiation. *International journal of radiation biology,* 70**,** 493-503.

Lobrich, M. & Jeggo, P. A. (2007) The impact of a negligent G2/M checkpoint on genomic instability and cancer induction. *Nature reviews. Cancer,* 7**,** 861-9.

Löbrich, M., Shibata, A., Beucher, A., Fisher, A., Ensminger, M., Goodarzi, A. A., Barton, O. & Jeggo, P. A. (2010) γH2AX foci analysis for monitoring DNA double-strand break repair: Strengths, limitations and optimization. *Cell Cycle,* 9**,** 662-669.

Lukas, C., Falck, J., Bartkova, J., Bartek, J. & Lukas, J. (2003) Distinct spatiotemporal

dynamics of mammalian checkpoint regulators induced by DNA damage. *Nature cell biology,* 5**,** 255-60.

Lukas, C., Savic, V., Bekker-Jensen, S., Doil, C., Neumann, B., Pedersen, R. S., Grofte, M., Chan, K. L., Hickson, I. D., Bartek, J. & Lukas, J. (2011) 53BP1 nuclear bodies form around DNA lesions generated by mitotic transmission of chromosomes under replication stress. *Nature cell biology,* 13**,** 243-53.

Mahajan, K. N., Nick Mcelhinny, S. A., Mitchell, B. S. & Ramsden, D. A. (2002) Association of DNA polymerase mu (pol mu) with Ku and ligase IV: role for pol mu in end-joining double-strand break repair. *Molecular and cellular biology,* 22**,** 5194-202.

Mahy, N. L., Perry, P. E. & Bickmore, W. A. (2002a) Gene density and transcription influence the localization of chromatin outside of chromosome territories detectable by FISH. *The Journal of cell biology,* 159**,** 753-63.

Mahy, N. L., Perry, P. E., Gilchrist, S., Baldock, R. A. & Bickmore, W. A. (2002b) Spatial organization of active and inactive genes and noncoding DNA within chromosome territories. *The Journal of cell biology,* 157**,** 579-89.

Manders, E. M. M., Verbeek, F. J. & Aten, J. A. (1993) Measurement of co-localization of objects in dual-colour confocal images. *Journal of Microscopy,* 169**,** 375-382.

Markova, E., Schultz, N. & Belyaev, I. Y. (2007) Kinetics and dose-response of residual 53BP1/gamma-H2AX foci: co-localization, relationship with DSB repair and clonogenic survival. *International journal of radiation biology,* 83**,** 319-29.

Maser, R. S., Monsen, K. J., Nelms, B. E. & Petrini, J. H. (1997) hMre11 and hRad50 Nuclear Foci Are Induced during the Normal Cellular Response to DNA Double-Strand Breaks. *Molecular and Cellular Biology,* 17**,** 6087-6096.

Masters, B. R. (2010) The Development of Fluorescence Microscopy. *eLS.* John Wiley & Sons, Ltd.

Mcmanus, K. J. & Hendzel, M. J. (2005) ATM-dependent DNA damage-independent mitotic phosphorylation of H2AX in normally growing mammalian cells. *Molecular biology of the cell,* 16**,** 5013-25.

Mehta, I. S., Elcock, L. S., Amira, M., Kill, I. R. & Bridger, J. M. (2008) Nuclear motors and nuclear structures containing A-type lamins and emerin: is there a functional link? *Biochem Soc Trans,* 36**,** 1384-8.

Miles, J., Appleton, J., Rees, D., Green, B., Adlam, K. & Myers, A. (2007) Indicative Atlas of Radon in England and Wales. Didcot, Health Protection Agency and British Geological Survey.

Mimori, T., Hardin, J. A. & Steitz, J. A. (1986) Characterization of the DNA-binding protein antigen Ku recognized by autoantibodies from patients with rheumatic disorders. *The Journal of biological chemistry,* 261**,** 2274-8.

Misteli, T. & Soutoglou, E. (2009) The emerging role of nuclear architecture in DNA

repair and genome maintenance. *Nat Rev Mol Cell Biol,* 10**,** 243-54.

Mochan, T. A., Venere, M., Ditullio, R. A., Jr. & Halazonetis, T. D. (2004) 53BP1, an activator of ATM in response to DNA damage. *DNA repair,* 3**,** 945-52.

Nakamura, A. J., Rao, V. A., Pommier, Y. & Bonner, W. M. (2010) The complexity of phosphorylated H2AX foci formation and DNA repair assembly at DNA double-strand breaks. *Cell Cycle,* 9**,** 389-397.

Nakano, H. & Shinohara, K. (1994) X-ray-induced cell death: apoptosis and necrosis. *Radiation research,* 140**,** 1-9.

Nelms, B., Maser, R., Mackay, J., Lagally, M. & Petrini, J. H. (1998) In Situ Visualization of DNA Double-Strand Break Repair in Human Fibroblasts. *Science,* 280**,** 590-592.

Neugut, A. I., Murray, T., Santos, J., Amols, H., Hayes, M. K., Flannery, J. T. & Robinson, E. (1994) Increased risk of lung cancer after breast cancer radiation therapy in cigarette smokers. *Cancer,* 73**,** 1615-20.

Nevaldine, B., Longo, J. A., Vilenchik, M., King, G. A. & Hahn, P. J. (1994) Induction and repair of DNA double-strand breaks in the same dose range as the shoulder of the survival curve. *Radiation research,* 140**,** 161-5.

Niimura, Y. & Gojobori, T. (2002) In silico chromosome staining: reconstruction of Giemsa bands from the whole human genome sequence. *Proceedings of the National Academy of Sciences of the United States of America,* 99**,** 797-802.

Oleinick, N. L., Balasubramaniam, U., Xue, L. & Chiu, S. (1994) Nuclear structure and the microdistribution of radiation damage in DNA. *International journal of radiation biology,* 66**,** 523-9.

Olins, A. L. & Olins, D. E. (1974) Spheroid Chromatin Units (ν Bodies). *Science,* 183**,** 330-332.

Olive, P. L. (2009) Endogenous DNA breaks: gammaH2AX and the role of telomeres. *Aging (Albany NY),* 1**,** 154-6.

Otsu, N. (1979) A Threshold Selection Method from Gray-Level Histograms. *Systems, Man and Cybernetics, IEEE Transactions on,* 9**,** 62-66.

Oudet, P., Gross-Bellard, M. & Chambon, P. (1975) Electron microscopic and biochemical evidence that chromatin structure is a repeating unit. *Cell,* 4**,** 281-300.

Parada, L. A., Mcqueen, P. G. & Misteli, T. (2004) Tissue-specific spatial organization of genomes. *Genome Biol,* 5**,** R44.

Paull, T. T., Rogakou, E. P., Yamazaki, V., Kirchgessner, C. U., Gellert, M. & Bonner, W. M. (2000) A critical role for histone H2AX in recruitment of repair factors to nuclear foci after DNA damage. *Current Biology,* 10**,** 886-895.

Peto, R., Darby, S., Deo, H., Silcocks, P., Whitley, E. & Doll, R. (2000) Smoking, smoking

cessation, and lung cancer in the UK since 1950: combination of national statistics with two case-control studies. *BMJ,* 321**,** 323-9.

Petrini, J. H. & Stracker, T. H. (2003) The cellular response to DNA double-strand breaks: defining the sensors and mediators. *Trends Cell Biol,* 13**,** 458-62.

Prise, K. M., Pinto, M., Newman, H. C. & Michael, B. D. (2001) A Review of Studies of Ionizing Radiation-Induced Double-Strand Break Clustering. *Radiation research,* 156**,** 572-576.

Pryde, F., Khalili, S., Robertson, K., Selfridge, J., Ritchie, A. M., Melton, D. W., Jullien, D. & Adachi, Y. (2005) 53BP1 exchanges slowly at the sites of DNA damage and appears to require RNA for its association with chromatin. *Journal of cell science,* 118**,** 2043-55.

Qvarnstrom, O. F., Simonsson, M., Johansson, K. A., Nyman, J. & Turesson, I. (2004) DNA double strand break quantification in skin biopsies. *Radiother Oncol,* 72**,** 311-7.

Radulescu, I., Elmroth, K. & Stenerlow, B. (2004) Chromatin organization contributes to non-randomly distributed double-strand breaks after exposure to high-LET radiation. *Radiation research,* 161**,** 1-8.

Ramirez, R. D., Sheridan, S., Girard, L., Sato, M., Kim, Y., Pollack, J., Peyton, M., Zou, Y., Kurie, J. M., Dimaio, J. M., Milchgrub, S., Smith, A. L., Souza, R. F., Gilbey, L., Zhang, X., Gandia, K., Vaughan, M. B., Wright, W. E., Gazdar, A. F., Shay, J. W. & Minna, J. D. (2004) Immortalization of Human Bronchial Epithelial Cells in the Absence of Viral Oncoproteins. *Cancer research,* 64**,** 9027-9034.

Rappold, I., Iwabuchi, K., Date, T. & Chen, J. (2001) Tumor Suppressor p53 Binding Protein 1 (53BP1) Is Involved in DNA Damage–signaling Pathways. *The Journal of Cell Biology,* 153**,** 613-620.

Recher, L., Whitescarver, J. & Briggs, L. (1970) A cytochemical and radioautographic study of human tissue culture cell nucleoli. *The Journal of cell biology,* 45**,** 479-92.

Redon, C. E., Nakamura, A. J., Gouliaeva, K., Rahman, A., Blakely, W. F. & Bonner, W. M. (2010) Q[gamma]-H2AX, an analysis method for partial-body radiation exposure using [gamma]-H2AX in non-human primate lymphocytes. *Radiation Measurements,* In Press, Corrected Proof.

Riballo, E., Kuhne, M., Rief, N., Doherty, A., Smith, G. C., Recio, M. J., Reis, C., Dahm, K., Fricke, A., Krempler, A., Parker, A. R., Jackson, S. P., Gennery, A., Jeggo, P. A. & Lobrich, M. (2004) A pathway of double-strand break rejoining dependent upon ATM, Artemis, and proteins locating to gamma-H2AX foci. *Molecular cell,* 16**,** 715-24.

Roch-Lefevre, S., Mandina, T., Voisin, P., Gaetan, G., Mesa, J. E., Valente, M., Bonnesoeur, P., Garcia, O. & Roy, L. (2010) Quantification of gamma-H2AX foci in human lymphocytes: a method for biological dosimetry after ionizing radiation exposure. *Radiation research,* 174**,** 185-94.

Rodier, F., Coppe, J. P., Patil, C. K., Hoeijmakers, W. A., Munoz, D. P., Raza, S. R., Freund, A., Campeau, E., Davalos, A. R. & Campisi, J. (2009) Persistent DNA damage signalling triggers senescence-associated inflammatory cytokine secretion. *Nature cell biology,* 11**,** 973-9.

Rogakou, E. P., Boon, C., Redon, C. & Bonner, W. M. (1999) Megabase Chromatin Domains Involved in DNA Double-Strand Breaks In Vivo. *The Journal of Cell Biology,* 146**,** 905-915.

Rogakou, E. P., Pilch, D. R., Orr, A. H., Ivanova, V. S. & Bonner, W. M. (1998) DNA Double-stranded Breaks Induce Histone H2AX Phosphorylation on Serine 139. *The Journal of Biological Chemistry,* 273**,** 5858-5868.

Rollini, P., Namciu, S. J., Marsden, M. D. & Fournier, R. E. K. (1999) Identification and characterization of nuclear matrix-attachment regions in the human serpin gene cluster at 14q32.1. *Nucleic acids research,* 27**,** 3779-3791.

Roots, R. & Okada, S. (1975) Estimation of life times and diffusion distances of radicals involved in x-ray-induced DNA strand breaks of killing of mammalian cells. *Radiation research,* 64**,** 306-20.

Rothkamm, K., Kruger, I., Thompson, L. H. & Lobrich, M. (2003) Pathways of DNA Double-Strand Break Repair during the Mammalian Cell Cycle. *Molecular and cellular biology,* 23**,** 5706-5715.

Rothkamm, K. & Lobrich, M. (1999) Misrejoining of DNA double-strand breaks in primary and transformed human and rodent cells: a comparison between the HPRT region and other genomic locations. *Mutation research,* 433**,** 193-205.

Rothkamm, K. & Lobrich, M. (2003) Evidence for a lack of DNA double-strand break repair in human cells exposed to very low x-ray doses. *Proceedings of the National Academy of Sciences of the United States of America,* 100**,** 5057-62.

Rube, C. E., Grudzenski, S., Kuhne, M., Dong, X., Rief, N., Lobrich, M. & Rube, C. (2008) DNA double-strand break repair of blood lymphocytes and normal tissues analysed in a preclinical mouse model: implications for radiosensitivity testing. *Clinical cancer research : an official journal of the American Association for Cancer Research,* 14**,** 6546-55.

Rydberg, B. (2000) Radiation-induced heat-labile sites that convert into DNA double-strand breaks. *Radiation research,* 153**,** 805-12.

Rydberg, B., Heilbronn, L., Holley, W. R., Lobrich, M., Zeitlin, C., Chatterjee, A. & Cooper, P. K. (2002) Spatial distribution and yield of DNA double-strand breaks induced by 3-7 MeV helium ions in human fibroblasts. *Radiation research,* 158**,** 32-42.

Rydberg, B., Holley, W. R., Mian, I. S. & Chatterjee, A. (1998) Chromatin conformation in living cells: support for a zig-zag model of the 30 nm chromatin fiber. *J Mol Biol,* 284**,** 71-84.

Sachs, R. K., Shuryak, I., Brenner, D., Fakir, H., Hlatky, L. & Hahnfeldt, P. (2007) Second cancers after fractionated radiotherapy: Stochastic population dynamics effects. *Journal of Theoretical Biology,* 249**,** 518-531.

Saenko, V., Ivanov, V., Tsyb, A., Bogdanova, T., Tronko, M., Demidchik, Y. & Yamashita, S. (2011) The Chernobyl Accident and its Consequences. *Clinical Oncology,* 23**,** 234-243.

Sak, A., Stuschke, M., Wurm, R. & Budach, V. (2000) Protection of DNA from radiation-induced double-strand breaks: influence of replication and nuclear proteins. *International journal of radiation biology,* 76**,** 749-56.

Sakaue-Sawano, A., Kurokawa, H., Morimura, T., Hanyu, A., Hama, H., Osawa, H., Kashiwagi, S., Fukami, K., Miyata, T., Miyoshi, H., Imamura, T., Ogawa, M., Masai, H. & Miyawaki, A. (2008) Visualizing spatiotemporal dynamics of multicellular cell-cycle progression. *Cell,* 132**,** 487-98.

Savage, J. R. (2002) Reflections and meditations upon complex chromosomal exchanges. *Mutation research,* 512**,** 93-109.

Savic, V., Yin, B., Maas, N. L., Bredemeyer, A. L., Carpenter, A. C., Helmink, B. A., Yang-Iott, K. S., Sleckman, B. P. & Bassing, C. H. (2009) Formation of dynamic gamma-H2AX domains along broken DNA strands is distinctly regulated by ATM and MDC1 and dependent upon H2AX densities in chromatin. *Molecular cell,* 34**,** 298-310.

Scherthan, H., Hieber, L., Braselmann, H., Meineke, V. & Zitzelsberger, H. (2008) Accumulation of DSBs in gamma-H2AX domains fuel chromosomal aberrations. *Biochemical and biophysical research communications,* 371**,** 694-7.

Schettino, G., Ghita, M., Richard, D. J. & Prise, K. M. (2010) Spatiotemporal investigations of DNA damage repair using microbeams. *Radiation protection dosimetry,* 143**,** 340-343.

Schultz, L. B., Chehab, N. H., Malikzay, A. & Halazonetis, T. D. (2000) p53 Binding Protein 1 (53BP1) Is an Early Participant in the Cellular Response to DNA Double-Strand Breaks. *The Journal of Cell Biology,* 151**,** 1381-1390.

Shi, Z., Zhao, M., He, L. & Wang, Y. (2011) A Combinational Filtering Method for Enhancing Suspicious Structures in Chest X-rays. *Journal of Information and Computational Science,* 8**,** 997-1005.

Sibarita, J.-B. & Rietdorf, J. (2005) Deconvolution Microscopy Microscopy Techniques. Springer Berlin / Heidelberg.

So, S., Davis, A. J. & Chen, D. J. (2009) Autophosphorylation at serine 1981 stabilizes ATM at DNA damage sites. *The Journal of cell biology,* 187**,** 977-990.

Soutoglou, E., Dorn, J. F., Sengupta, K., Jasin, M., Nussenzweig, A., Ried, T., Danuser, G. & Misteli, T. (2007) Positional stability of single double-strand breaks in mammalian cells. *Nature cell biology,* 9**,** 675-82.

Soutoglou, E. & Misteli, T. (2008) Activation of the cellular DNA damage response in the absence of DNA lesions. *Science,* 320**,** 1507-10.

Stiff, T., O'driscoll, M., Rief, N., Iwabuchi, K., Lobrich, M. & Jeggo, P. A. (2004) ATM and DNA-PK Function Redundantly to Phosphorylate H2AX after Exposure to Ionizing Radiation. *Cancer Research,* 64**,** 2390-2396.

Strahl, B. D. & Allis, C. D. (2000) The language of covalent histone modifications. *Nature,* 403**,** 41-5.

Stucki, M., Clapperton, J. A., Mohammad, D., Yaffe, M. B., Smerdon, S. J. & Jackson, S. P. (2005) MDC1 directly binds phosphorylated histone H2AX to regulate cellular responses to DNA double-strand breaks. *Cell,* 123**,** 1213-26.

Su, Y., Meador, J. A., Geard, C. R. & Balajee, A. S. (2010) Analysis of ionizing radiation-induced DNA damage and repair in three-dimensional human skin model system. *Experimental dermatology,* 19**,** e16-22.

Sun, H. B., Shen, J. & Yokota, H. (2000) Size-dependent positioning of human chromosomes in interphase nuclei. *Biophys J,* 79**,** 184-90.

Sun, S., Schiller, J. H. & Gazdar, A. F. (2007) Lung cancer in never smokers--a different disease. *Nature reviews. Cancer,* 7**,** 778-90.

Surralles, J., Darroudi, F. & Natarajan, A. T. (1997a) Low level of DNA repair in human chromosome 1 heterochromatin. *Genes Chromosomes Cancer,* 20**,** 173-84.

Surralles, J., Sebastian, S. & Natarajan, A. T. (1997b) Chromosomes with high gene density are preferentially repaired in human cells. *Mutagenesis,* 12**,** 437-42.

Suzuki, K., Nakashima, M. & Yamashita, S. (2010) Dynamics of ionizing radiation-induced DNA damage response in reconstituted three-dimensional human skin tissue. *Radiation research,* 174**,** 415-23.

Sy, S. M., Chen, J. & Huen, M. S. (2010) The 53BP1-EXPAND1 connection in chromatin structure regulation. *Nucleus,* 1**,** 472-474.

Takata, M., Sasaki, M. S., Tachiiri, S., Fukushima, T., Sonoda, E., Schild, D., Thompson, L. H. & Takeda, S. (2001) Chromosome instability and defective recombinational repair in knockout mutants of the five Rad51 paralogs. *Molecular and cellular biology,* 21**,** 2858-66.

Torudd, J., Protopopova, M., Sarimov, R., Nygren, J., Eriksson, S., Markova, E., Chovanec, M., Selivanova, G. & Belyaev, I. Y. (2005) Dose-response for radiation-induced apoptosis, residual 53BP1 foci and DNA-loop relaxation in human lymphocytes. *International journal of radiation biology,* 81**,** 125-38.

Travis, W. D., Travis, L. B. & Devesa, S. S. (1995) Lung cancer. *Cancer,* 75**,** 191-202.

Uziel, T., Lerenthal, Y., Moyal, L., Andegeko, Y., Mittelman, L. & Shiloh, Y. (2003)

Requirement of the MRN complex for ATM activation by DNA damage. *The EMBO journal,* 22**,** 5612-5621.

Valente, M., Voisin, P., Laloi, P., Roy, L. & Roch-Lefèvre, S. (2011) Automated gamma-H2AX focus scoring method for human lymphocytes after ionizing radiation exposure. *Radiation Measurements,* In Press, Corrected Proof.

Van Dekken, H., Pinkel, D., Mullikin, J., Trask, B., Van Den Engh, G. & Gray, J. (1989) Three-dimensional analysis of the organization of human chromosome domains in human and human-hamster hybrid interphase nuclei. *Journal of cell science,* 94 (Pt 2)**,** 299-306.

Van Veelen, L. R., Cervelli, T., Van De Rakt, M. W., Theil, A. F., Essers, J. & Kanaar, R. (2005) Analysis of ionizing radiation-induced foci of DNA damage repair proteins. *Mutation research,* 574**,** 22-33.

Van Vugt, M., Gardino, A., Linding, R., Ostheimer, G., Reinhardt, H., Ong, S., Tan, C., Miao, H., Keezer, S., Li, J., Pawson, T., Lewis, T., Carr, S., Smerdon, S., Brummelkamp, T. & Yaffe, M. (2010) A Mitotic Phosphorylation Feedback Network Connects
Cdk1, Plk1, 53BP1, and Chk2 to Inactivate the G2/M DNA
Damage Checkpoint. *PLoS Biology,* 8**,** 20.

Vilenchik, M. M. & Knudson, A. G. (2003) Endogenous DNA double-strand breaks: production, fidelity of repair, and induction of cancer. *Proceedings of the National Academy of Sciences of the United States of America,* 100**,** 12871-6.

Volpi, E. V., Chevret, E., Jones, T., Vatcheva, R., Williamson, J., Beck, S., Campbell, R. D., Goldsworthy, M., Powis, S. H., Ragoussis, J., Trowsdale, J. & Sheer, D. (2000) Large-scale chromatin organization of the major histocompatibility complex and other regions of human chromosome 6 and its response to interferon in interphase nuclei. *Journal of cell science,* 113 (Pt 9)**,** 1565-76.

Walker, A. I., Hunt, T., Jackson, R. J. & Anderson, C. W. (1985) Double-stranded DNA induces the phosphorylation of several proteins including the 90 000 mol. wt. heat-shock protein in animal cell extracts. *The EMBO journal,* 4**,** 139-45.

Wang, B., Matsuoka, S., Carpenter, P. B. & Elledge, S. J. (2002) 53BP1, a mediator of the DNA damage checkpoint. *Science,* 298**,** 1435-8.

Ward, I. M., Minn, K., Jorda, K. G. & Chen, J. (2003) Accumulation of checkpoint protein 53BP1 at DNA breaks involves its binding to phosphorylated histone H2AX. *The Journal of biological chemistry,* 278**,** 19579-82.

Watson, S., Jones, A., Oatway, W. & Hughes, J. (2005) Ioising Radiation Exposure of the UK population: 2005 Review. *RPD.* Oxford, Healt Protection Agency.

West, R. B., Yaneva, M. & Lieber, M. R. (1998) Productive and nonproductive complexes of Ku and DNA-dependent protein kinase at DNA termini. *Molecular and cellular biology,* 18**,** 5908-20.

Weterings, E., Verkaik, N. S., Bruggenwirth, H. T., Hoeijmakers, J. H. & Van Gent, D. C. (2003) The role of DNA dependent protein kinase in synapsis of DNA ends. *Nucleic acids research,* 31**,** 7238-46.

Wilson, K. A. & Stern, D. F. (2008) NFBD1/MDC1, 53BP1 and BRCA1 have both redundant and unique roles in the ATM pathway. *Cell Cycle,* 7**,** 3584-3594.

Wojcik, A., Aghamohammadi, S., Aillaud, M., Bosi, A., Dai, G., Olivieri, G., Salone, B., Savage, J. R. K., Shadley, J. D. & Streffer, C. (1996) Adaptive response to ionizing radiation in human lymphocytes: the problem of scoring aberrations in cells irradiated during asynchronous growth. *Mutation research,* 366**,** 137-143.

Woodcock, C. L., Grigoryev, S. A., Horowitz, R. A. & Whitaker, N. (1993) A chromatin folding model that incorporates linker variability generates fibers resembling the native structures. *Proceedings of the National Academy of Sciences of the United States of America,* 90**,** 9021-5.

Xie, A., Hartlerode, A., Stucki, M., Odate, S., Puget, N., Kwok, A., Nagaraju, G., Yan, C., Alt, F. W., Chen, J., Jackson, S. P. & Scully, R. (2007) Distinct roles of chromatin-associated factors MDC1 and 53BP1 in mammalian double strand break repair. *Mol. Cell.,* 28**,** 1045-1057.

Yamauchi, M., Oka, Y., Yamamoto, M., Niimura, K., Uchida, M., Kodama, S., Watanabe, M., Sekine, I., Yamashita, S. & Suzuki, K. (2008) Growth of persistent foci of DNA damage checkpoint factors is essential for amplification of G1 checkpoint signaling. *DNA repair,* 7**,** 405-17.

Yaneva, M., Kowalewski, T. & Lieber, M. R. (1997) Interaction of DNA-dependent protein kinase with DNA and with Ku: biochemical and atomic-force microscopy studies. *The EMBO journal,* 16**,** 5098-112.

Zgheib, O., Pataky, K., Brugger, J. & Halazonetis, T. D. (2009) An oligomerized 53BP1 tudor domain suffices for recognition of DNA double-strand breaks. *Molecular and cellular biology,* 29**,** 1050-8.

Zhang, Y. & Reinberg, D. (2001) Transcription regulation by histone methylation: interplay between different covalent modifications of the core histone tails. *Genes Dev,* 15**,** 2343-60.

Zirbel, R. M., Mathieu, U. R., Kurz, A., Cremer, T. & Lichter, P. (1993) Evidence for a nuclear compartment of transcription and splicing located at chromosome domain boundaries. *Chromosome Res,* 1**,** 93-106.